



Norwegian University of
Science and Technology

Characterization of BaTiO₃/La_{0.7}Sr_{0.3}MnO₃ Thin Films on SrTiO₃(111) Substrates

A Transmission Electron Microscopy Study

Theodor Secanell Holstad

Nanotechnology

Submission date: June 2016

Supervisor: Randi Holmestad, IFY

Co-supervisor: Thomas Tybell, IET
Per Erik Vullum, IFY

Norwegian University of Science and Technology
Department of Physics

Preface

This is a Master thesis conducted at NTNU in the Nanotechnology study program. It was carried out during the spring of 2016, and is a continuation of a project work carried out during the fall of 2015. The work done here is the result of a collaboration between the Oxide Electronics Lab at the Department of Electronics and Telecommunications and the TEM-group at the Department of Physics, both at NTNU.

The Oxide Electronics Lab has been studying thin film systems for several years in order to exploit the potential multiferroic properties of composite thin film structures in electronic devices. Professor Thomas Tybell, who has worked in this field for almost two decades, wants to investigate a system that has received little attention in the literature thus far: BTO/LSMO/STO(111). Earlier studies have been done mostly using STO(001) substrates. The purpose of this work is to characterize this system using TEM techniques. One important aspect of this characterization is to investigate the ferroelectric structure in the BTO layer at different thicknesses of this layer. The system has already been characterized by XRD at the Oxide Electronics Lab. In order to further characterize it, a TEM investigation is necessary.

The TEM-group obtained three new state-of-the-art TEM instruments in 2013, and has several competent operators. It receives material systems to investigate from among others the Oxide Electronics Lab. This is the nature of the collaboration between the two groups, and the background for the research presented in this work.

Throughout the work, I assume that the reader is familiar with basic material physics, vector calculus and Fourier analysis.

Trondheim, 2016-06-19

Theodor S. Holstad

Acknowledgment

I would like to thank Professor Randi Holmestad for her valuable insights, assistance and supervision during this work. I am very grateful for the opportunity to learn experimental physics under her guidance. My gratitude is also given to Professor Thomas Tybell for his theoretical expertise and for the critical questions he asked that pushed me on during the spring. Associate Professor II Per Erik Vullum is thanked for his understanding of the perovskite structure and for providing his expertise on experimental TEM-work, as well as all the time he spent teaching me how to prepare TEM specimens in the specimen preparation lab. Furthermore, all images shown in this work taken on the *Jeol-Jem ARM 200F* were captured by Associate Professor II Per Erik Vullum during a single session, and the 10-10-CS specimen was prepared by him using the *FEI Helios NanoLab DualBeam FIB* at NTNU NanoLab. Senior Engineers Ragnhild Sæterli and Bjørn Gunnar Soleim are thanked for their assistance and guidance during the experimental work on the TEM, and for their efforts to keep the instruments fully operational at all times.

The TEM work was carried out on the NORTEM JEOL 2100F and the NORTEM JEOL ARM 200F, TEM Gemini Centre, Norwegian University of Science and Technology (NTNU), Norway. This work is supported by the project NORTEM (Grant 197405) within the programme INFRASTRUCTURE of the Research Council of Norway (RCN). NORTEM was co-funded by the RCN and the project partners NTNU, UiO and SINTEF.

T. S. H.

Summary

In this work, an oxide thin film system was investigated by using transmission electron microscopy (TEM) techniques. It is of great interest to study such systems due to their current applications as well as potential future applications in electronic devices. One sample consists of a 10 nm BaTiO₃ thin film deposited on a 10 nm La_{0.7}Sr_{0.3}MnO₃ thin film deposited on a (111)-oriented SrTiO₃ substrate, in short BTO(10nm)/LSMO(10nm)/STO(111). The other sample is the same, except for having a BTO film of thickness 3 nm. BTO is a tetragonal perovskite with space group P4mm (99) and STO is cubic perovskite with space group Pm $\bar{3}$ m (221). LSMO is a rhombohedral perovskite with space group R $\bar{3}$ c (167) in bulk form. TEM specimens with cross-sectional and plan-view geometries were prepared using a mechanical polishing routine combined with precision ion polishing, and by a focused ion-beam (FIB) procedure. High-resolution TEM (HR-TEM), brightfield TEM (BF-TEM), scanning precession electron diffraction (SPED), scanning transmission electron microscopy electron energy loss spectroscopy (STEM-EELS), high angle annular dark-field STEM (HAADF-STEM), geometrical phase analysis (GPA) and selected area diffraction (SAD) were performed on the *Jeol-Jem 2100F* and the *Jeol-Jem ARM 200F*.

The data obtained in this work suggests that the BTO thin films are in a ferroelectric mono-domain state. Due to a large amount of edge dislocations, it was not possible to map the precise positions of the Ti columns and thus the ferroelectric polarization. Such dislocations occur naturally when there is misfit between a thin film and the substrate, and the thin film is relaxed. Since the crystallographic difference between ferroelectric domains in BTO is very small, it becomes very difficult to deconvolve the strain fields around dislocations from a potential ferroelectric domain structure.

The LSMO thin film was found to have undergone a reduction in symmetry from its bulk structure. This conclusion was reached based on the fact that additional super-reflections were observed in the SAD patterns. Based on the literature available on LSMO thin film systems deposited on STO(111), it was concluded that LSMO has undergone a monoclinic distortion. However, a precise determination of its space group is beyond the scope of this work. Furthermore, two domain states were found in LSMO.

The EELS analysis indicates that LSMO has a large amount of oxygen vacancies and a Mn oxidation state far below its bulk value. In addition, a tensile strain in the direction normal to the thin film interface was observed in the GPA analysis, which is inconsistent with X-ray

diffraction measurements done on the same system. This discrepancy is probably linked to the large amount of oxygen vacancies in LSMO, which may dramatically alter its behavior. The oxygen vacancies may have been created during the TEM specimen preparation in the FIB. Another explanation is that the oxygen vacancies were induced by the electron beam in the TEM, as this has been observed to occur in LSMO in several earlier studies. The oxygen vacancies are probably not ordered, since the observed super-reflections were not consistent with any known ordering, such as the Brownmillerite phases.

In conclusion, an important and interesting oxide thin film system has been characterized using TEM techniques. An important observation is the fact that there are many obstacles to extracting the relevant data. Firstly, misfit dislocations are not easily avoided, but make it difficult to map small changes in the positions of the Ti columns. Secondly, the electron beam and the specimen preparation may induce oxygen vacancies that dramatically alter the structure of LSMO. Hopefully, the findings in this work will give an insight into the structure-property relations of these systems, as well as an overview of the challenges associated with studying them. A recommendation for the future is to produce specimens using several different types of preparation techniques, to find out how these affect the specimen quality. It may be necessary to alter the parameters used during the thin film synthesis as well. For example, annealing the sample in an oxygen rich atmosphere after synthesis and after preparation in the FIB to reduce the amount of oxygen vacancies. Finally, using a low voltage and shorter exposure times in the TEM may help reduce the creation of oxygen vacancies in LSMO.

Sammendrag

I dette arbeidet ble et oksid tynnfilm-system undersøkt ved hjelp av transmisjons-elektronmikroskopi-teknikker (TEM). Det er av interesse å karakterisere slike systemer siden de anvendes i elektronikk i dag, og siden de har flere potensielle anvendelser i fremtidens elektronikk. En prøve besto av 10 nm BaTiO₃ deponert på 10 nm La_{0.7}Sr_{0.3}MnO₃ deponert på et (111)-orientert STO-substrat, BTO(10nm)/LSMO(10nm)/STO(111). Den andre prøven besto av BTO(3nm)/LSMO(10nm)/STO(111). BTO er en tetragonal perovskitt med romgruppe P4mm (99) og STO er en kubisk perovskitt med romgruppe Pm $\bar{3}m$ (221). LSMO er en rhomboedral perovskitt med romgruppe R $\bar{3}c$ (167) i bulk. TEM-prøver med tverrsnitt og plan-view geometrier ble produsert ved bruk av mekanisk polering kombinert med presisjons-ione-polering, og ved hjelp av en fokusert ione-stråle-teknikk (FIB). Høyoppløsnings-TEM (HR-TEM), skanning-presesjon-elektron-diffraksjon (SPED), lysfelt-TEM (BF-TEM), høyvinkel annulær-mørkefelt-STEM (HAADF-STEM), skanning-TEM-elektron-energi-tap-spektroskopi (STEM-EELS), utvalgt- område-elektron-diffraksjon (SAD) og geometrisk fase analyse (GPA) var blant teknikkene som ble brukt på *Jeol-Jem 2100F* og *Jeol-Jem ARM 200F*.

De eksperimentelle dataene antydte at BTO tynnfilmene består av et ferroelektrisk monodomene. Svært mange kantdislokasjoner ble observert, og dette medførte at det ikke var mulig å kartlegge posisjonene til Ti-kolonnene i BTO og dermed den ferroelektriske polariseringen. Slike dislokasjoner forekommer i relaxerte tynnfilmer som har en forskjellig gitterparameter fra substratet. Siden den krystallografiske forskjellen mellom to ferroelektriske domener i BTO er veldig liten, er det svært vanskelig å dekonvolere denne fra deformasjonsfeltene rundt dislokasjonene.

Siden ekstra superreflekser ble observert i diffraksjonsmønstrene, ble det konkludert med at LSMO-tynnfilmen har redusert symmetri i forhold til bulk. Basert på et litteratursøk på LSMO-tynnfilmer i tilsvarende systemer med STO(111)-substrater ble det konkludert med at LSMO har en monoklinsk symmetri. En presis bestemmelse av romgruppen til LSMO er utenfor rekkevidde i dette arbeidet. To forskjellige ferroelastiske domener ble observert i LSMO.

EELS analysen som ble gjennomført antydte at LSMO har en stor mengde oksygen-vakanser, og at oksidasjonstilstanden til Mn er lavere enn i støkiometrisk LSMO. I tillegg antydte GPA-analysen at enhetscellen til LSMO er forlenget i forhold til STO normalt på grenseflatene. Dette er ikke i samsvar med røntgen-diffraksjons-målinger gjort på tilsvarende systemer.

Denne avvikende målingen skyldes sannsynligvis den store mengden oksygen-vakanser i LSMO, siden det er kjent at slike vakanser kan endre egenskapene til LSMO dramatisk. Slike oksygen-vakanser kan oppstå som en konsekvens av FIB-prøveprepareringen. Oksygen-vakanser kan også forårsakes av elektronstrålen, og dette har blitt observert i LSMO i flere tidligere arbeider. Oksygen-vakansene antar sannsynligvis en uordnet struktur, siden de observerte super-refleksene ikke er konsistente med kjente super-strukturer, for eksempel en Brownmillerite-ordning av oksygen-vakansene.

Kort oppsummert har et viktig og interessant oksid tynnfilm-system blitt karakterisert ved bruk av ulike TEM-teknikker. Enkelte struktur-parametere er vanskelige å måle nøyaktig. For det første gjør dislokasjoner det vanskelig å kartlegge små endringer i posisjonene til Ti-kolonnene. For det andre, elektronstrålen og prøveprepareringen kan skape oksygen-vakanser som kan endre struktur-parameterene til tynnfilm-systemet betraktelig. Observasjonene gjort i dette arbeidet kan forhåpentligvis gi innsikt i struktur-parameterene til oksid-tynnfilmssystemet som har blitt studert, i tillegg til en innsikt i utfordringene som må løses dersom det skal karakteriseres videre i fremtiden. En anbefaling for fremtidige studier er å bruke flere forskjellige prøveprepareringsteknikker for å se hvordan disse påvirker prøvevaliteten. Det kan også bli nødvendig å endre parameterene brukt under tynnfilm-syntesen. For eksempel, å bake prøven i en oksygen-rik atmosfære etter tynnfilmsyntesen og etter FIB-prepareringen for å redusere antall oksygen-vakanser. I tillegg anbefales det å bruke lav spenning og kortere eksponeringstid når prøven studeres i TEM, slik at oksygen-vakanser ikke skapes i LSMO.

Abbreviations

- AFM - Antiferromagnetic
- ASTAR - Automatic crystallographic indexing and orientation/phase mapping tool
- BFP - Back-Focal Plane
- BTO- BaTiO₃
- CBED - Convergent Beam Electron Diffraction
- CCD - Charge Coupled Device
- CMOS - Complementary Metal-Oxide-Semiconductor
- CS - Cross-section
- DF - Dark Field
- DLF - Diamond Lapping Film
- DP - Diffraction Pattern
- DRAM - Dynamic Random Access Memory
- EDS - Energy-dispersive X-ray Spectroscopy
- EELS - Electron-Energy Loss Spectroscopy
- Fe-FET - Ferroelectric field effect transistor
- FEG - Field Emission Gun
- Fe-RAM - Ferroelectric Random Access Memory
- FIB - Focused Ion Beam
- FFP - Front-Focal Plane
- FFT - Fast Fourier Transform
- GPA - Geometrical Phase Analysis
- HAADF - High Angle Annular Diffraction
- HR-TEM - High-Resolution Transmission Electron Microscopy
- IFFT - Inverse Fast Fourier Transform
- LSMO - La_{0.7}Sr_{0.3}MnO₃

-
- MBE - Molecular Beam Epitaxy
 - MEMS - Microelectromechanical System
 - MFTJ - Multi-Ferroic Tunnel Junction
 - MOSFET - Metal-Oxide-Semiconductor Field-Effect-Transistor
 - Nb:STO - Nb-doped STO
 - NV-RAM- Non-Volatile Random Access Memory
 - PCA - Principal Component Analysis
 - PIPS - Precision Ion Polishing System
 - PLD - Pulsed Laser Deposition
 - PTO - PbTiO_3
 - PV - Plan-view
 - RHEED - Reflection High-Energy Electron Diffraction
 - ROI - Region of Interest
 - RPM - Rounds Per Minute
 - SADP - Selected Area Diffraction Pattern
 - SPED - Scanning Precession Electron Diffraction
 - STEM - Scanning Transmission Electron Microscopy
 - STO - SrTiO_3
 - STO(001) - (001) oriented SrTiO_3
 - STO(111) - (111) oriented SrTiO_3
 - TEM - Transmission Electron Microscopy
 - TMO - Transition Metal Oxide
 - VLM - Visible Light Microscopy
 - XRD - X-ray Diffraction

Contents

Preface	i
Acknowledgment	ii
Summary	iii
Sammendrag	v
Abbreviations	vii
1 Introduction	1
2 Theory	7
2.1 Transmission Electron Microscopy	7
2.1.1 Introduction	7
2.1.2 Microscope design	8
2.1.3 Aberrations and astigmatism	13
2.1.4 Imaging techniques	14
2.1.5 Energy dispersive spectroscopy	20
2.1.6 Electron energy loss spectroscopy	20
2.1.7 Geometrical phase analysis	23
2.2 Crystal structure and diffraction	26
2.2.1 Lattice translation vectors	26
2.2.2 Basis of the crystal structure	27
2.2.3 Lattice types	27
2.2.4 The reciprocal lattice	27
2.2.5 The Laue condition and the Ewald sphere	29
2.2.6 The structure factor and the atomic form factor	30
2.2.7 Diffraction patterns	31
2.2.8 Crystallographic properties of perovskites	32

2.2.9	Thin film crystal structure	33
2.2.10	Dislocations	34
2.3	Ferroelectricity	35
2.3.1	Ferroelectric crystals	35
2.3.2	Landau theory	35
2.3.3	Allowed domain structures in tetragonal thin films on (111) oriented substrates	36
2.3.4	Observing ferroelectric domains in thin film systems using TEM	39
2.4	Ferroelastic domains in LSMO	40
2.4.1	Orientation relationship between cubic and hexagonal axes	42
2.4.2	Ferroelastic domains seen from the $[1\bar{1}0]_c$ zone-axis	42
2.4.3	Ferroelastic domains seen from the $[11\bar{2}]_c$ zone-axis	43
2.4.4	Ferroelastic domain-walls in LSMO	43
2.5	Principal component analysis	47
3	Applications of oxide thin films	49
3.1	Fe-RAM	49
3.2	Ferroelectric field effect transistors (Fe-FETs)	51
3.3	Ferroelectric thin films in MEMS devices	51
3.4	Magnetoelectric coupling	51
3.5	Four-state NV-RAM based on a multiferroic tunnel junction	52
3.6	Polar metals	54
4	Methods	57
4.1	Thin film synthesis	57
4.2	TEM Specimen preparation	57
4.2.1	Tripod polishing	58
4.2.2	Preparing plan-view specimens using a tripod polisher	59
4.2.3	Preparing cross-sectional specimens using a tripod polisher and PIPS	60
4.2.4	Preparing a cross-sectional specimen using FIB	64
4.3	TEM methods	65
4.4	SADP simulations of ferroelastic domains in LSMO	66
4.4.1	Crystal structures	66

4.4.2	Simulation in E-MAPS	67
4.5	SADP simulations of ferroelectric domains in BTO	70
4.6	HyperSpy Analysis	74
5	Results and discussion	77
5.1	Crystal structures	77
5.2	Thin film quality	86
5.2.1	GPA strain analysis	86
5.2.2	Artefacts in GPA	90
5.2.3	Effect of the Pt/Pd (80/20)-alloy protection layer	91
5.2.4	Composition	92
5.2.5	Dislocations	93
5.2.6	Ion beam damage	99
5.3	EELS Analysis of Mn oxidation state and oxygen-vacancies in LSMO	102
5.4	Ferroelastic domain walls in LSMO	107
5.5	Ferroelectric domains in BTO	113
5.5.1	Mapping of the ferroelectric polarization	114
5.5.2	Dark-field imaging	114
6	Conclusions	117
7	Further work	119
	Bibliography	121
A	HyperSpy EELS-Analysis Code	133
B	Additional EELS data	135
C	Additional Image Stacks Analyzed in GPA	145

Chapter 1

Introduction

In society today, information and computer technology play important roles. Traffic lights, websites, hospital equipment, car keys, automatic doors, kitchen equipment, images, digital music and movies are just some examples of commodities that have been radically changed and improved as a consequence of this new technology. In science, information technology has created new fields such as numerical physics, capable of taking on problems thought to be impossible to solve just a few years ago. For example, density functional theory is a computational method used to simulate the electronic structure of many-body systems. This approach would not have been fruitful without computer technology. Progress of digital devices and computers is thus linked to progress within society and the natural sciences.

Key to this development was the invention of the transistor in 1947 by Bardeen, Brattain and Shockley [1]. This was among the most important scientific inventions in the 20th century. In 1959, Dawon Kahng and Martin Atalla at Bell labs invented the metal-oxide-semiconductor field-effect transistor (MOSFET), the basic building block in electronic circuits [2]. Several new industries arose out of these inventions. Among those were the semiconductor industry. Since its birth in the 1950s, the semiconductor industry has transformed society due to the rapid improvement of the computing power of integrated circuits. Gordon E. Moore, a co-founder of the Intel Corporation, predicted in 1965 that the number of components per integrated circuit would double every second year. Since then, it has doubled about every 18th month. This has since been known as Moore's law [3]. Today, the dimensions of transistors are reaching fundamental limits. When these limits are reached, quantum physical effects such as electron tunneling will affect device performance. For this reason it is necessary to investigate new material systems and designs. This means to not

just scale down the designs, but to invent new designs. This trend is known as “More than Moore” [4].

Since ferroelectricity was discovered in 1921, it has been speculated by many scientists that the two polarization states $+P$ and $-P$ might be used to encode the 0 and 1 of the Boolean algebra forming the foundation for memory and logic circuitry in computers [5]. Some actual applications for these materials are for example in capacitors in dynamic random-access memory (DRAM), where ferroelectric materials are used in thin-film form [5]. The principal advantage these materials offer is very high dielectric constants, typically in the range $\epsilon_r = 100 - 1000$ [5]. In comparison, for SiO_2 , used in electronics today, $\epsilon_{\text{SiO}_2} = 3.9$ [6]. However, the density of present day DRAMs is limited mainly by capacitor area per cell. This is because the resistors and transistors take up relatively little area. It is the capacitors that limit the chip bit-density [5]. If the dielectric constant is increased by a factor of e. g. 100, then the area of the capacitor can be reduced by a factor of 100 while still having the same capacitance. This can easily be seen in an ideal parallel-plate capacitor, where $C = \frac{\epsilon A}{d}$. Although the capacitance may have a more complex formula for more complex designs, it is still true that increasing the dielectric constant allows for reducing the capacitor area. Thus, the chip-bit density can be increased. Also, in non-volatile RAM (NV-RAM), the ferroelectrics serve not just as capacitors, but as the memory element [5]. Their advantages in this application are: low voltage (1.0 V) operation, small size (and thus low cost), radiation hardness and very high speeds [5].

Complex transition-metal oxides (TMO) are strongly correlated electron materials where the interactions between electronic spins, charges, orbitals and the lattice produce a multitude of self-organization and electronic phases. All these effects combined give rise to a large variety of nonlinear electronic phenomena and functionalities [7]. The research field on these complex oxide materials has been developing rapidly during the last two decades, and it is among the most exciting and challenging areas of research in condensed matter physics [7, 8, 9, 10, 11]. Among the interesting properties these materials display are e. g. ferroelectricity, magnetism, semiconductivity, ionic conductivity and superconductivity [7]. During this spring, it has been demonstrated that polar metals may be produced from these systems [12]. This has never been possible before due to charge screening in conductive materials. Furthermore, if two or more complex oxides are combined with atomic-scale resolution in a heterostructure to form new composite nanoscale materials, even more functional

properties are observed. For example, multiferroic materials where the magnetic properties can be controlled using electric fields due to magnetoelectric coupling. In the last few years, oxide heterostructures have therefore been investigated extensively in order to utilize these properties in new electronic architectures [7].

Perovskite thin film systems are among the most common examples of strongly correlated composite nanoscale materials. Perovskites have chemical composition ABX_3 , where A and B are cations and X is an anion, typically oxygen. In this work, thin film systems deposited by reflection high-energy electron diffraction (RHEED)-controlled pulsed laser deposition (PLD) have been studied using transmission electron microscopy (TEM)-techniques. One sample consists of a 10 nm $BaTiO_3$ thin film deposited on a 10 nm $La_{0.7}Sr_{0.3}MnO_3$ thin film deposited on a (111)-oriented $SrTiO_3$ substrate, BTO(10nm)/LSMO(10nm)/STO(111). The other sample is BTO(3nm)/LSMO(10nm)/STO(111). BTO is a tetragonal perovskite with space group $P4mm$ (99) and STO is a cubic perovskite with space group $Pm\bar{3}m$ (221). LSMO is a rhombohedral perovskite with space group $R\bar{3}c$ (167) in bulk form. TEM specimens with cross-sectional (CS) and plan-view (PV) geometries were prepared using a mechanical polishing routine combined with precision ion polishing (PIPS), and by a focused ion-beam (FIB) procedure. High-resolution TEM (HR-TEM), brightfield TEM (BF-TEM), scanning precession electron diffraction (SPED), scanning transmission electron microscopy electron energy loss spectroscopy (STEM-EELS), high angle annular dark-field STEM (HAADF-STEM), geometrical phase analysis (GPA) and selected area diffraction (SAD) were performed on the *Jeol-Jem 2100F* and the *Jeol-Jem ARM 200F*.

Since the substrate and the epitaxial thin films are both perovskites, their structure and symmetry properties are very similar. Thus far, most thin film systems have been deposited on STO(001). The Oxide Electronics Lab at NTNU has been investigating the properties of thin film systems on STO(111) [13, 14]. It is believed that the sixfold symmetry of the STO(111) surface will affect the properties of the thin film. To investigate the coupling between the symmetry properties of the substrate and the thin film and its influence on the ferroelectric domain structure is therefore of great interest. It has been predicted that there is no critical film thickness for domain pattern formation in (111) oriented epitaxial ferroelectric films [15].

Ferroelectric domains are strongly coupled to structural domains. There is a spatial symmetry reduction associated with the phase transition from the paraelectric to the ferroelec-

tric state. This structural symmetry reduction can be observed in the diffraction pattern as super-reflections. However, since the thin-films studied here are 10 nm and 3 nm thick, and since the domain size scales roughly with the square root of the film thickness [16], the expected domain size is only a few nanometers. Additionally, the displacement of the titanium atom and oxygen atoms from one domain to another is in the sub-Ångstrom range. Hence, in order to resolve it, a very high resolution is necessary. This means the TEM is a perfect instrument for observing these very small ferroelectric domains. In addition, high quality samples with a minimal amount of strain are needed.

It is also of interest to study the crystal structure, dislocation structure, the EELS fine structure of the different elements present, ferroelastic domains in LSMO as well as any other observations from which new aspects of the thin film system are revealed. The focus in this work has therefore not been limited to ferroelectricity, but to characterize the provided thin film samples as fully as possible with the available resources at the TEM Gemini Centre.

In this work, the theory chapter first goes through the basics of the TEM instrument, the design of its different main parts as well as giving a brief description of aberrations and astigmatism. Next, the different imaging techniques are presented, and the contrast mechanisms underlying them are explained. Then, the two spectroscopy techniques used in this work, energy-dispersive X-ray spectroscopy (EDS) and EELS, are presented. EDS is explained quite briefly, while a thorough presentation is given for EELS as it has been more central in this work. Finally, GPA is described briefly.

The subsequent section goes through the basics of crystal structure and diffraction. The next section goes through the definitions needed to explain ferroelectricity and the expected form of a ferroelectric domain structure in this thin film system. A comment on how these are expected to appear in the TEM is given. A section on ferroelastic domains then follows, before a section on principal component analysis (PCA) concludes the theory chapter.

The next chapter presents some relevant applications for ferroelectric and multiferroic composite oxide thin films. It demonstrates how useful oxide thin film systems already are in society today and how they may become even more useful tomorrow by being an important part of the “More than Moore” trend. Thus, the chapter gives additional motivation for characterizing these types of systems.

Then, the Methods chapter goes through all the specific settings used during the TEM experiments as well as the TEM specimen preparation. A section on how the thin films were

synthesized is included. This chapter also describes the different types of simulations performed, as well as how the EELS spectra were analyzed in HyperSpy.

The next chapter presents the experimental observations while a discussion of these is given simultaneously. The final two chapters contain a list of the main conclusions reached in this work as well as recommendations for future work, respectively.

Chapter 2

Theory

2.1 Transmission Electron Microscopy

The following section is based on the book by Williams and Carter [17].

2.1.1 Introduction

A TEM is a powerful tool used for characterization of nanoscale materials and devices. It can be used to determine both the structure and composition of materials, and thus plays a vital role in fields such as materials science, nanotechnology and biotechnology. The discovery of the wave particle duality by Louis de Broglie in 1925 made it clear that particles also behave like waves. With this in mind, it was theorized that it should be possible to use electrons instead of photons in microscopes. The reason for wanting to do so is that electrons have a much smaller wavelength than light, and hence they can resolve much smaller details. In 1927, two research groups, Davisson and Germer and Thomson and Reid, carried out electron-diffraction experiments, demonstrating the wave nature of these particles. In their papers, the idea of an electron lens was also conceived. In 1932, the first electron microscope was proposed by Knoll and Ruska. In their paper, they demonstrated images taken by the instrument, and for this they received the Nobel price in 1986. Within one year, the diffraction limit of visible light was surpassed by the resolution of electron microscopes.

The classical Rayleigh criterion for visible light microscopes (VLM), states that the smallest distance that can be resolved is approximately

$$\delta = \frac{0.61\lambda}{\mu \sin(\beta)}, \quad (2.1)$$

where λ is the wavelength of the radiation, μ is the refractive index of the viewing medium and β is the semi-angle of collection of the magnifying lens. If green light, which is in the middle of the visible spectrum ($\lambda = 550$ nm) is used, the resolution of a VLM is about 300 nm. This is much higher than the upper limit of the nano regime at 100 nm.

For an electron, the wavelength (in nm) is given by

$$\lambda = \frac{1.22}{E^{1/2}}, \quad (2.2)$$

where E is the energy of the electron in electron volts. 200 keV electrons move at relativistic velocities, and have a wavelength of about 0.00251 nm. With this in mind, one would expect a 200 kV TEM to be able to resolve sub-Ångstrom details. However, due to the low quality of electron lenses compared to optical lenses, there are some limitations on the TEM. This brings up the topic of the design of the TEM.

2.1.2 Microscope design

The first step in understanding results obtained from the TEM is to understand how the instrument itself is constructed. Electrons are transmitted through the specimen, and the various properties of these electrons before and after transmission are detected. The basic design of the TEM is shown in figure 2.1. The instrument is constructed as a column that is kept at a vacuum of a certain quality. It is convenient to divide the TEM into four components from top to bottom along this column: the electron gun, the illumination system, the objective lens/stage and the imaging system.

The electron gun

The electron gun can be one of two main types. A thermionic gun consists of a W or LaB₆ filament that is heated to make it easier to extract electrons using an electric field. If a material is heated to a high enough temperature, the electrons are given sufficient energy to overcome the barrier that keeps them from leaking out from the surface. This barrier is called the work function, Φ , and is typically on the order of a few eV. Richardson's law summarizes the physics of a thermionic gun,

$$J = AT^2 e^{-\frac{\Phi}{k_B T}}. \quad (2.3)$$

Here, k_B is Boltzmann's constant, A is Richardson's constant and T is the temperature. From this equation it is clear that when the needle is heated to a high temperature, the current J will increase as the thermal energy of the electrons exceeds Φ .

Alternatively, a field emission gun (FEG) may be used. In this latter type of gun, an electric field is used to extract electrons from a very fine W needle tip. The principle behind a FEG is that the strength of the electric field E is very high at sharp points. This can be explained by the fact that if a voltage V is applied to a spherical point of radius r , the electric field is

$$E = \frac{V}{r}. \quad (2.4)$$

It is possible to heat the needle, but this will reduce the coherency of the electrons. Furthermore, due to the sharpness of the FEG needle, the electric field is very strong and it is not necessary to heat it. If the FEG is kept at ultrahigh vacuum ($< 10^{-9}$ Pa), the FEG needle may in fact be kept at room temperature (cold-FEG). One of the advantages of a FEG is that the brightness (intensity per angle) is much higher than in a thermionic gun. Another advantage is that the coherency of the electrons is better, making a FEG instrument better for acquiring phase-contrast images. For this reason, the *Jeol-JEM 2100F* and *Jeol-JEM ARM 200F* were used in this work. A drawback to the FEG is that it is unable to image as large an area as a thermionic gun, because of the small size of the needle. Therefore, it may be preferable to use a thermionic gun when doing amplitude contrast imaging.

The illumination system

After being extracted from the filament, the electrons are formed into a beam by the illumination system. This system consists of a set of magnetic lenses, deflection coils and apertures. The illumination system transfers this beam of electrons to the specimen, giving either a broad beam or a focused beam entering the specimen, depending on whether the TEM is operated in STEM mode or traditional TEM mode. The parallelism of the beam is measured by the convergence angle, α . In SAD, BF-TEM and dark field TEM (DF-TEM), a parallel beam is required. In STEM and convergent beam electron diffraction (CBED), a convergent beam is required. In the parallel beam TEM mode, the first two condenser lenses (C_1 , C_2) are adjusted to illuminate the specimen with a parallel beam of electrons. As demonstrated in figure 2.2, the C_1 lens first forms an image of the gun crossover before the C_2 lens forms a parallel beam hitting the specimen.

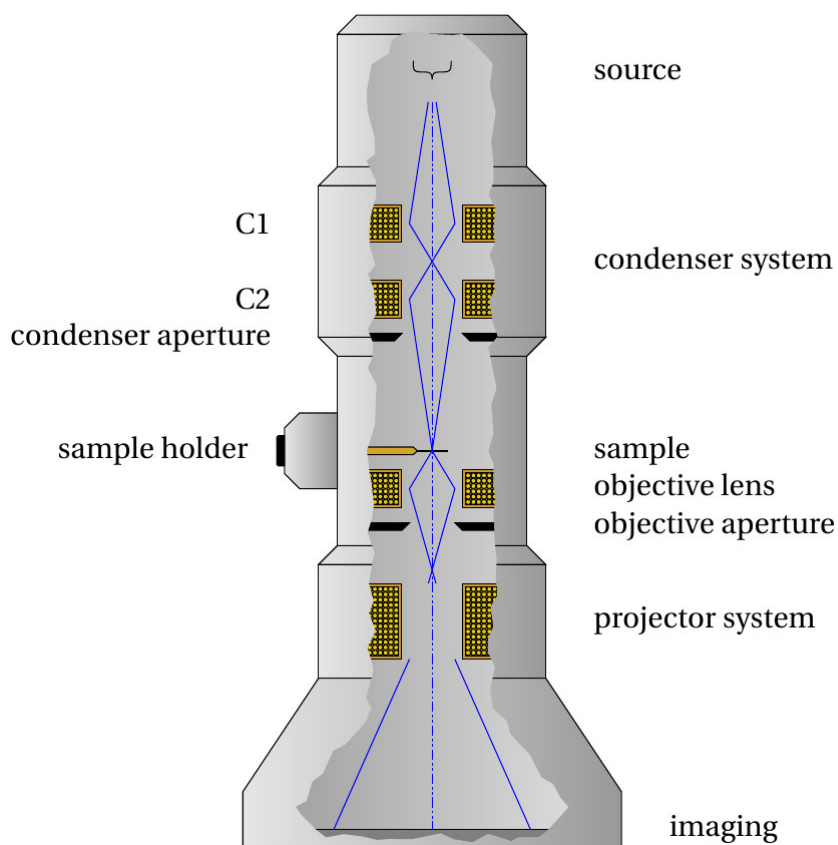


Figure 2.1: The basic design of a TEM. It is convenient to divide the TEM into four components from top to bottom along this column: the electron gun (source), the illumination system (C_1 , C_2), the objective lens/stage and the imaging/projector system. Created in TikZ by Eric Jensen [18, 19].

The objective lens and stage

This part of the TEM is the “heart” of the instrument. The stage is used to position the specimen holder in the correct position so that the objective lens can form images and diffraction patterns (DP) in a reproducible manner. In most TEMs, the holder is inserted from the side (side-entry). The TEM-holder can be tilted around one axis (single-tilt) or two axes (double-tilt). Furthermore, the objective lens is the most important lens in the TEM. It forms the images and DPs that are magnified later by other lenses. Lenses are further discussed below.

The TEM imaging system

The objective lens takes electrons emerging from the exit surface of the specimen, disperses them to create a DP in the back focal plane (BFP) and recombines them to form an image in the image plane. In diffraction mode, the imaging-system lenses are adjusted so that the BFP of the objective lens is the object plane for the intermediate lens. Thus, the DP is projected

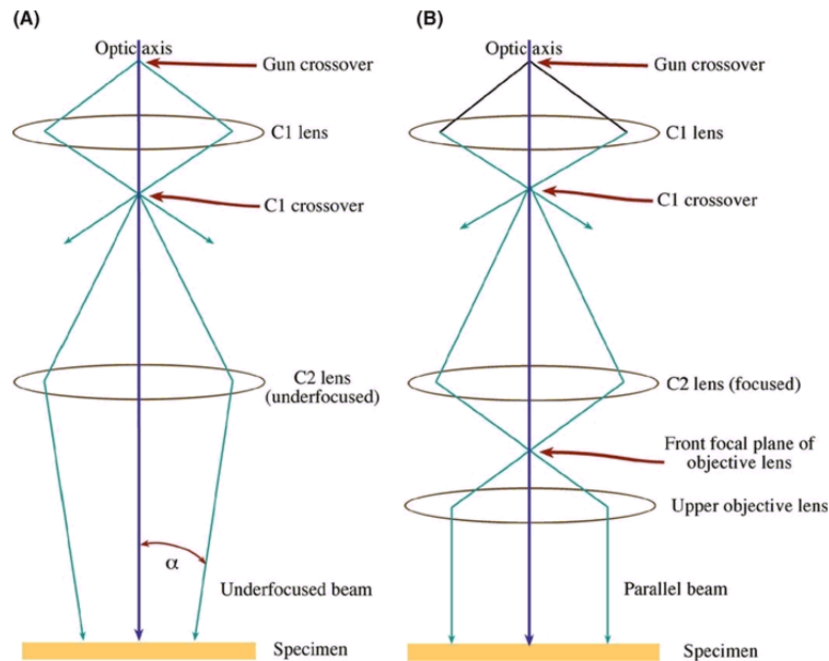


Figure 2.2: Parallel-beam operation of the TEM. In (A), the C_2 lens is under-focused. (B) displays the typical situation in most TEMs, where the C_1 and C_2 lenses are used to image the source at the FFP of the condenser-objective lens, hence creating a parallel beam at the specimen plane. For this reason, the upper objective lens is sometimes called C_3 . From [17].

onto the viewing screen or charged coupled device (CCD) by the projector system. In image mode, the intermediate lens is adjusted so that its object plane is the image plane of the objective lens. Thus, the image of the specimen is projected onto the viewing screen or CCD by the projector system.

Apertures

Apertures are used to select which electrons to pass on to the specimen by limiting the collection angle β , as sketched in figure 2.3. The condenser aperture is used to choose which electrons to pass on from the electron gun. The purpose is to exclude electrons that are too far away from the optic axis, because these are less coherent. This aperture is composed of electromagnetic lenses and deflectors. The deflectors are composed of coils that are able to tilt the electron beam off the optic axis. A pair of coils may shift the beam off the optic axis while still keeping the beam parallel to it.

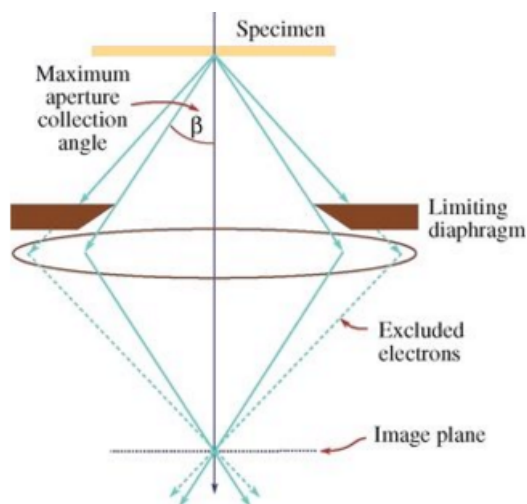


Figure 2.3: Schematic of how an aperture limits the angular spread of electrons entering the lens. Electrons that are too far away from the optic axis are excluded. From [17].

Electron lenses

The lenses are electromagnetic pole pieces that generate a symmetric magnetic field around the optic axis. Two parts are necessary to construct such a magnetic electron lens, both of which are shown in figure 2.4. The first is a cylindrically symmetric core of soft magnetic material such as soft iron with a hole drilled through it. This is called a *pole piece*, while the hole is called the *bore* of the pole piece. In most instruments, there are in fact two pole pieces (upper and lower). These may be part of the same piece of soft iron as in figure 2.4, or they may be two separate pieces. The distance between the upper and lower pole piece is called the *gap*. The bore-to-gap ratio is an important quantity that determines the focusing action of the lens. The second part needed in an electron lens is a coil of copper wire which surrounds each pole piece. A current is passed through this copper wire to create an axially symmetric magnetic field inside the bore. The magnetic field is inhomogeneous along the length of the lens, and it determines the electron trajectory through the Lorentz force,

$$\vec{F} = -e(\vec{E} + \vec{v} \times \vec{B}), \quad (2.5)$$

where $-e$ is the electron charge, \vec{v} is the electron velocity and \vec{E} and \vec{B} are the electric and magnetic fields inside the lens, respectively. Since the lens systems are finite, they cannot collect all the information emitted from a specimen. Hence, no perfect image can be formed of the specimen, because any point will form a Gaussian distribution. Furthermore, all the lenses in a TEM suffer from aberrations and astigmatism, which will be discussed next.

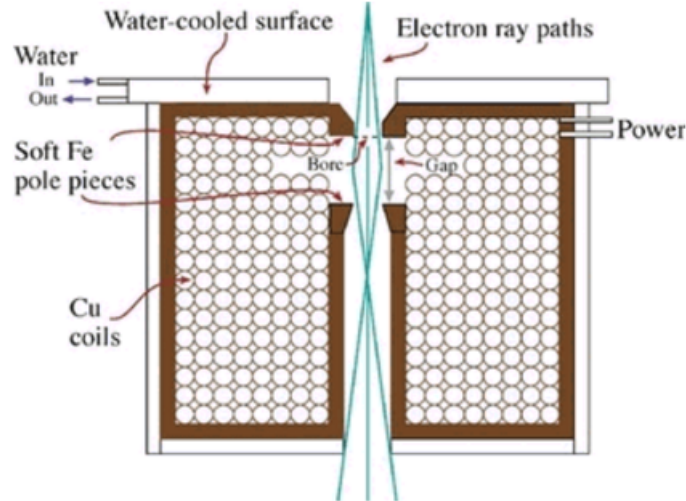


Figure 2.4: Schematic of a magnetic lens. The two main parts are a cylindrically symmetric core of soft magnetic material, the *pole piece*, and a coil of copper wire surrounding it. From [17].

2.1.3 Aberrations and astigmatism

The electromagnetic lenses in a TEM have several types of defects, and they are far from perfect. In fact, they are comparable to using the bottom of a soft-drink bottle as a magnifying glass. The most important types of defects are spherical aberration, chromatic aberration and astigmatism.

Spherical aberration occurs when the lens field behaves differently for off-axis rays. The further off-axis the electron is, the more strongly it is bent back towards the axis. This leads to a point object being imaged as a disk of finite size, which degrades the resolution. The error due to spherical aberration is given by

$$\delta = C_s \theta^3, \quad (2.6)$$

where θ is the angle of the electron ray to the optic axis. The radius of the spherically aberrated disk of intensity in the Gaussian image plane, under realistic conditions is

$$r_{sph} = C_s \beta^3. \quad (2.7)$$

State-of-the-art TEM instruments have spherical correctors, which compensate for C_s by creating a diverging lens which spreads out the off-axis beams so that they re-converge to a point rather than a disk in the Gaussian-image plane.

Chromatic aberration occurs due to a spread in frequency of the electrons when they leave the gun. This is most often not an important effect because the energy spread caused by the specimen itself is higher. A monochromator may be used to restrict the energy range. However, unless the specimen is very thin, it is pointless to correct chromatic aberration. Due to interaction with the specimen, electrons with a wide range of energies enter the objective lens. Electrons with lower energy are bent more strongly. Thus, electrons from a point in the object are blurred into a disk in the Gaussian image plane. The radius of this disk is

$$r_{chr} = C_c \frac{\Delta E}{E_0} \beta, \quad (2.8)$$

where C_c is the chromatic-aberration coefficient of the lens, ΔE is the energy loss of the electrons, E_0 is the initial energy of the beam, and β is the collection angle of the lens. Typically, ΔE due to the gun is ~ 1 eV, while ΔE due to the specimen is 15-25 eV. Thinner specimens give less chromatic aberration than thicker specimens. Thus, the best way to limit r_{chr} is to make thinner specimens.

Finally, astigmatism is caused by the fact that electrons sense a non-uniform magnetic field as they spiral around the optic axis. This non-uniformity arises because the soft-iron pole pieces are not perfectly cylindrical. Furthermore, there may be microstructural inhomogeneities in the soft iron. In addition, the apertures in the TEM disturb the lens fields. In short, a variety of imperfections causes the magnetic field to be slightly inhomogeneous, and this gives rise to astigmatism, which distorts the image according to

$$r_{ast} = \beta \Delta f, \quad (2.9)$$

where Δf is the maximum difference in focus induced by the astigmatism. It is fortunately easy to correct astigmatism. This is done by introducing octupoles that introduce a compensating magnetic field which balance the inhomogeneities that cause the astigmatism.

2.1.4 Imaging techniques

The process of imaging can be described as acquiring data of some type from a given region in the specimen. Usually, it is preferable to maximize the contrast. Perhaps the most intuitive type of contrast is the difference in intensity of electrons from different areas of the specimen. Several types of imaging modes can be used in the TEM, all giving rise to contrast

through different principles. E. g. DF-TEM, BF-TEM and HR-TEM. There are advantages and drawbacks to each of these techniques, and the theory and limitations associated with these techniques is presented below.

Amplitude contrast

To obtain amplitude contrast, an objective aperture is inserted into the focal plane. This restricts the electrons used in the image.

In BF imaging, the objective aperture is centered at the central, unscattered beam. Hence, areas that scatter strongly will appear dark while areas that scatter weakly will appear bright. For example, thicker regions will appear darker. Regions with a higher atomic number Z will also scatter more strongly and appear darker. Hence, both thickness and Z contributes to the contrast. For this reason, amplitude contrast is also called mass-thickness contrast. If one area of the specimen has a different crystal orientation, it will diffract more or less, and thus contrast is achieved between regions of different crystal orientation.

In DF imaging, the objective aperture is centered over some reflection different from the central reflection. In this manner, only electrons scattered to a specific angle by a specific set of planes will contribute to the final image. In a sense, the image is frequency filtered: the spatial frequency of a given set of planes is chosen.

STEM

In STEM, the lens is adjusted so that the incoming beam converges at the specimen forming a probe. The diameter of this probe can be down in the Å-regime. The probe is then scanned across the surface of the specimen. In this manner, a CBED pattern is formed for every position of the probe. These patterns are very sensitive to the symmetry of the crystal. For every probe position, the number of electrons scattered into a specific angular range are registered. An advantage of the STEM technique is that the image is not formed by any lenses. Hence, any aberration effects from the imaging and objective lens systems are avoided. On the other hand, the quality of the probe is determined by the condenser lens system, and thus this system ultimately determines the quality of the image. The resolution in a STEM image is determined by the size of the probe. For this reason, using a FEG based system is an advantage when performing STEM. A challenge in STEM is that the depth of focus is quite low, so that only the surface of the specimen will be in focus. There is also a channeling effect

where the electron beam will be channeled by the atomic columns. Hence, even though the surface is in focus, the beam does not spread too much when it passes through the specimen.

In HAADF-STEM, an annular detector is used to acquire the CBED patterns generated during STEM. A HAADF detector will measure the total intensity scattered into a certain range of angles. This intensity is registered for each position of the STEM probe. The size of the HAADF detector as well as the camera length determine the range of angles registered. The camera length is the effective distance between the specimen and the detector. It determines the distance between reflections in the DP. A short camera length will lead to high angle electrons being detected, while a long camera length will lead to low angle electrons being detected. Thus, using a short camera length means that most of the detected electrons have been Rutherford scattered, giving high Z -contrast [20].

High resolution TEM

In HR-TEM imaging, contrast is caused by the phase difference of the transmitted electrons, which again is caused by interference and diffraction effects in the electron beam. Based on this phase difference, information about the specimen's crystal structure can be determined. Due to the imperfections in the lenses in the TEM discussed above, each point in the specimen will be represented as an extended region in the image. Next, since each point in the specimen is different, it may be described by a specimen function, $f(x, y)$. The corresponding extended region in the image may be described as $g(x, y)$. Each point in the image $g(x, y)$ has contributions from several points in the specimen $f(x, y)$. In other words,

$$g(\vec{r}) = \int f(\vec{r}') h(\vec{r} - \vec{r}') d\vec{r}' = f(\vec{r}') \otimes h(\vec{r} - \vec{r}') \quad (2.10)$$

where $h(\vec{r})$ is the point spread function, i. e. the function that describes *how* a point in the specimen spreads into a disk. $g(\vec{r})$ is the convolution of $f(\vec{r})$ and $h(\vec{r})$. By the convolution theorem,

$$G(\vec{u}) = F(\vec{u}) \cdot H(\vec{u}). \quad (2.11)$$

Here, $G(\vec{u})$, $F(\vec{u})$ and $H(\vec{u})$ are the Fourier transforms of g , f and h , respectively. $H(\vec{u})$ is called the contrast transfer function (CTF), and it limits the frequency range of $G(\vec{u})$. The

effects of lens aberrations, apertures and wave attenuation are contained in $H(\vec{u})$. That is,

$$H(\vec{u}) = A(\vec{u}) \cdot E(\vec{u}) \cdot B(\vec{u}). \quad (2.12)$$

The aperture function $A(\vec{u})$ cuts off all values of u (spatial frequencies) above some value governed by the radius of the aperture. The envelope function is a complex function that depends on the lens itself, and may be more or less restricting than $A(\vec{u})$. Finally, the aberration function $B(\vec{u})$ can be expressed as

$$B(\vec{u}) = e^{i\chi(\vec{u})}, \quad (2.13)$$

where the phase distortion $\chi(\vec{u})$ is given by

$$\chi(\vec{u}) = \pi\Delta f \lambda u^2 + \frac{1}{2}\pi C_s \lambda^3 u^4, \quad (2.14)$$

where Δf is the overfocus, λ is the wavelength and C_s is the coefficient of spherical aberration.

Next, the specimen transmission function can in general be described as

$$f(x, y) = A(x, y)e^{-\phi_t(x, y)}, \quad (2.15)$$

where $A(x, y)$ is the amplitude and $\phi_t(x, y)$ is the phase, which depends on the thickness of the specimen. For application to HR-TEM, the analysis may be simplified by setting $A(x, y) = 1$. This is equivalent to setting the incident wave to unity. It can be shown that the phase only depends on the specimen potential, $V(x, y)$, which the electron sees as it passes through the specimen. Assuming the specimen has a small thickness t , it is justified to write

$$V_t(x, y) = \int_0^t V(x, y, z) dz. \quad (2.16)$$

$V_t(x, y)$ is thus a two-dimensional projection of the crystal structure. Next, in vacuum the wavelength of electrons λ is

$$\lambda = \frac{h}{\sqrt{2meE}}. \quad (2.17)$$

Inside the crystal this changes to

$$\lambda' = \frac{h}{\sqrt{2me(E + V(x, y, z))}}. \quad (2.18)$$

Hence, it is easily seen that the phase difference between an electron traveling outside the specimen in vacuum and an electron traveling inside the specimen per distance dz is given by

$$d\phi = 2\pi \frac{dz}{\lambda'} - 2\pi \frac{dz}{\lambda} = 2\pi \frac{dz}{\lambda} \left(\frac{\sqrt{E + V(x, y, z)}}{\sqrt{E}} - 1 \right). \quad (2.19)$$

$$d\phi = 2\pi \frac{dz}{\lambda} \left(\left(1 + \frac{V(x, y, z)}{E} \right)^{\frac{1}{2}} - 1 \right). \quad (2.20)$$

By Taylor expanding the square root this gives

$$d\phi = \pi \frac{dz}{\lambda E} V(x, y, z) = \sigma V(x, y, z) dz, \quad (2.21)$$

where

$$\sigma = \frac{\pi}{\lambda E} \quad (2.22)$$

is the interaction constant. The total phase shift is thus

$$\phi_t = \sigma \int V(x, y, z) dz = \sigma V_t(x, y). \quad (2.23)$$

Finally, if absorption is included in a function $\mu(x, y)$, the specimen transfer function is

$$f(x, y) = e^{-i\phi_t(x, y) - i\mu(x, y)} = e^{-i\sigma V_t(x, y) - i\mu(x, y)}. \quad (2.24)$$

In summary, the specimen is represented as a phase object. This is called the phase-object approximation (POA). If $V_t(x, y) \ll 1$, the exponential may be expanded. If higher order terms and $\mu(x, y)$ are neglected, the final result is

$$f(x, y) = 1 - i\sigma V_t(x, y). \quad (2.25)$$

The latter result is the weak phase-object approximation (WPOA). It is true if, for a very thin specimen, the amplitude of a transmitted wave function only depends linearly to the projected potential of the specimen. It is important to remember that “thin” is a rather relative

term, and depends on the Z -number of the material in question. For example, the WPOA fails for an electron wave passing through a single uranium atom, while it holds up to several nm for lighter materials.

By using the WPOA, the CTF is

$$T(\vec{u}) = 2E(\vec{u})A(\vec{u})\sin(\chi(\vec{u})), \quad (2.26)$$

known as the objective transfer function. Here, E is the envelope function which depends on the lens, while A is the aperture function. When the CTF is larger than zero, atoms will appear as bright spots. If the CTF is less than zero, atoms will appear as dark spots. Thus, depending on the microscope settings, i. e. the defocus and spherical aberrations, the contrast in the HR-TEM images may change. This is important to be aware of in order to interpret images correctly. Simulations may be necessary to properly understand these images.

Scanning precession electron diffraction

SPED is a technique in which a focused probe is rotated in a hollow cone around the optic axis above the specimen and de-rocked underneath the specimen, as sketched in figure 2.5. This produces a diffraction pattern which shares the same properties as a conventional pattern, but which contains a larger number of reflections because the intensities are integrated across the Bragg condition due to the rotation of the Ewald sphere as the beam is precessing. SPED can be used to characterize unknown structures [21]. By scanning the beam across a specimen and acquiring integrated diffraction patterns pixel by pixel, 4-dimensional datasets can be generated. In this manner, the crystal structure can be determined pixel by pixel by comparison with simulated patterns available in an online library [22]. From this it is also clear that the experimentalist is able to determine the orientation angle between two crystal grains, or to determine the size and shape of different precipitates in a matrix structure. Furthermore, by precessing the beam it has been shown that the data becomes more reliable due to a reduction of dynamical diffraction effects associated with local thickness changes as well as averaging over small out-of-plane tilt variations [23, 24].

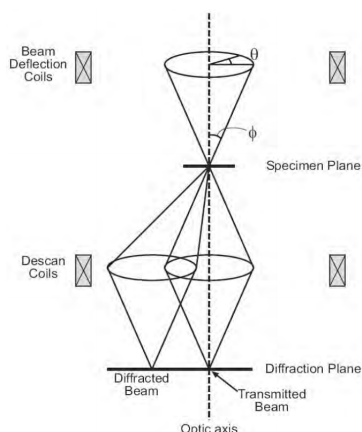


Figure 2.5: Schematic diagram demonstrating precession electron diffraction. First, the beam is tilted off zone by an angle ϕ utilizing the beam tilting coils and then serially precessed through an angle 2π . Underneath the specimen, a complementary de-tilt is performed by the de-scan coils, restoring the zone-axis pattern. From [25].

2.1.5 Energy dispersive spectroscopy

By illuminating atoms with electrons at a high energy, internal excitation of the atoms occur. These excitations occur between discrete energy levels that are characteristic of the atom. Shortly after the excitation, the atom will return to a lower energy state and excite a photon at a given frequency given by the energy difference between the high and low energy states. The X-ray spectrum emitted from a given material serves as a fingerprint that is used to determine the chemical composition of that material. In most TEMs, an EDS detector is present close to the specimen, allowing characterization of the composition. Parallel beam or convergent beam conditions may be utilized. In parallel beam mode, the composition of a large area is determined. In STEM mode, a map of the chemical composition can be constructed.

2.1.6 Electron energy loss spectroscopy

This section is mostly based on [17] and [26].

Introduction

In EELS, the energy distribution of electrons that have interacted with the specimen is analyzed. These electrons are initially monochromatic in the ideal case. If the electrons have high enough energy, and the specimen is thin enough (preferably less than 100 nm thick), the electrons are transmitted through the specimen with no reflection or absorption. In this

case, all the interaction takes place inside of the specimen. This allows for extraction of information about the internal structure by passing the electrons into a spectrometer. In order to analyze small volumes of interest, it is necessary to focus the electrons into a small area. The TEM is the perfect instrument for this purpose, and most TEMs also have electron lenses that can guide the electrons into a spectrometer.

The EELS spectrum

The primary goal of EELS is to separate electrons according to their kinetic energy using an electron energy-loss spectrometer to produce an EELS spectrum. This spectrum shows the scattering intensity as a function of the decrease in energy of the transmitted electron. There are several peaks that are present in all such spectrums.

First, there is the zero-loss peak, which represents all the electrons that have gone through the specimen without losing any energy. This is also known as the elastic peak, and involves electrons that have suffered negligible energy losses such as those that are scattered elastically in the forward direction or those that have scattered phonon modes. Some electrons may have passed through the material without being scattered at all. In the 5-50 eV region, the peaks due to transmitted electrons that have undergone interactions with outer-shell electrons occur. In the higher energy-loss range, edges due to electrons that have undergone interactions with inner-shell electrons occur. The reason for the term “edge” and not “peak”, is that these peaks in intensity are much sharper. A sharp rise in intensity occurs at the energy corresponding to the ionization threshold of a given inner-shell electron. These inner-shell binding energies depend on the atomic number of the atom, and thus the ionization edges in the EELS spectrum indicate which elements are present in the material.

Due to the high energy resolution of an EELS spectrometer, it is also possible to resolve the fine structure of the energy losses of the transmitted electrons. By investigating the details of the different edges in the high-loss part of the spectrum, additional information about the chemical and electronic structure of the material may be extracted. It is worth commenting on the importance of thin samples at this point. If the sample is not thin enough, the electrons may undergo multiple inelastic scattering events, which makes it more difficult to analyze the energy loss spectrum. If the sample is sufficiently thin, each edge corresponds to one excitation event. The multiple scattering phenomena occurs if the specimen is thicker than the mean free path of the electron, which is approximately 50-150 nm for outer-shell

excitations for 100 keV electrons. Specimens in this thickness range typically have a series of peaks at multiples of the plasmon energy. This is a rather unwanted effect, as it also typically distorts the overall shape of the EELS spectrum.

It is common to collect EELS spectra in the low-energy range as well as in the high-energy range. It is then necessary to align the zero-loss peak to the zero-loss position, and to use this alignment to also align the high-loss spectrum. The algorithms for this process is implemented in most software used for EELS analysis, such as HyperSpy. Such algorithms also involves deconvolution procedures that remove distortions in the spectrum due to plasmon losses and plural scattering.

In this work, the EELS spectrum has been used to estimate the oxygen concentration and the Mn oxidation state by looking at the fine structure of the O-K peak and the Mn L_3 and L_2 peaks. The details of how this is done is given in the methods section.

The EELS spectrometer

Most EELS spectrometers are magnetic-prism spectrometers. These instruments are quite complicated, and details about these instruments and the history of their development may be found in [26]. Briefly, a magnetic field is set up that deflects electrons a given amount depending on their energy. By changing the magnetic field strength, the spectrometer may detect electrons at different energies with a high energy resolution. Alternatively, electrostatic fields may be used to deflect the electrons, or a combination of electric and magnetic fields may be utilized together with monochromators to increase the energy resolution.

Differential scattering cross section

In order to understand the physics underlying electron scattering, it is necessary to be familiar with the *differential cross section*. A good introduction can be found in [27]. Briefly, this quantity contains information about how the incoming particles are scattered depending on their incident direction. It is customary to look at the particles emerging in a solid angle $d\Omega$ around some polar coordinates (θ, ϕ) . By monitoring the amount of particles scattered into a solid angle $d\Omega$, one can define

$$d\sigma(\text{into } d\Omega) = \frac{d\sigma}{d\Omega}(\phi, \theta) d\Omega. \quad (2.27)$$

The argument emphasizes that the cross section depends on the direction of observation. By integrating over all solid angles, the total cross section is thus obtained.

$$\sigma = \int \frac{d\sigma}{d\Omega}(\phi, \theta) d\Omega = \int_0^\pi \int_0^{2\pi} \sin(\theta) \frac{d\sigma}{d\Omega}(\phi, \theta) d\theta d\phi. \quad (2.28)$$

Hartree Slater Cross Sections

Looking at (2.62) and (2.59), it is clear that in order to describe scattering in a crystal, it is necessary to find $n_j(\boldsymbol{\rho})$. That is, to approximate the wave function for the atomic electrons. One approach to this is the Born approximation. Another complementary approach is the non-relativistic partial wave expansion, which is the one used in Hartree Slater Cross sections. In the EELS analysis performed in this work, the L-subshell cross section of Mn was studied by using Hartree Slater Cross sections. The ionization cross section for this subshell in Argon is [28]

$$\sigma_{L_s} = \int_{W_{min}}^{\infty} dW_{L_s} \frac{d\sigma_{L_s}}{dW_{L_s}}(L_s = 2s, 2p). \quad (2.29)$$

Here, $\frac{d\sigma_{L_s}}{dW_{L_s}}$ is the differential cross section for energy transfer. Its full expression can be found in [28]. Similar expressions may be found for other subshells in other elements, such as the Mn-L_{2,3} and O-K peaks [29, 30].

2.1.7 Geometrical phase analysis

One way to look at HR-TEM images is as a sum of lattice fringes. By Fourier transforming the image, the periodicities present are revealed and their amplitude and phase gives the strength and position of the lattice fringes present. If the crystal under investigation is perfect (which is never the case), the Fourier transform will only show Fourier components corresponding to Bragg reflections. This section reviews the GPA theory, and is based on [31].

Since no crystal is perfect, it is often the deviations from the ideal lattice which are of interest. There will be imperfections present due to strain and displacements in the specimen as well as imperfections in the imaging system. All of these non-ideal effects give rise to a diffuse intensity around each Bragg spot. These distributions of diffuse intensity around the Bragg spots contain information about grain size, strain fields, defects, displacement fields and so on.

Decomposition of the image

First, assume a perfect crystal. In such an ideal case, the image intensity at position \vec{r} can be written as a Fourier expansion over Bragg-periodicities,

$$I(\vec{r}) = \sum_{\vec{g}} H_{\vec{g}} e^{2\pi i \vec{g} \cdot \vec{r}}, \quad (2.30)$$

where $H_{\vec{g}}$ is the amplitude of the periodicity \vec{g} . $H_{\vec{g}}$ is complex in general,

$$H_{\vec{g}} = A_{\vec{g}}(\vec{r}) e^{iP_{\vec{g}}(\vec{r})}. \quad (2.31)$$

In Fourier space,

$$\hat{I}(\vec{k}) = \sum_{\vec{g}} \hat{H}_{\vec{g}}(\vec{k} - \vec{g}). \quad (2.32)$$

Thus, every Bragg spot in the Fourier transformation is convoluted with a function $\hat{H}_{\vec{g}}(\vec{k})$. The choice of $\hat{H}_{\vec{g}}(\vec{k})$ is not unique, and it is customary to define it so that $\hat{H}_{\vec{g}}(\vec{k}) = 0$ beyond the first Brillouin zone. Furthermore, it is chosen so that no information is excluded by the transformation.

Bragg filtering

If a mask is placed around the spots $\pm \vec{g}$ in reciprocal space followed by an inverse Fourier-transform, this is equivalent to filtering the image. The intensity distribution in this particular case will be

$$B_{\vec{g}}(\vec{r}) = \hat{H}_{\vec{g}}(\vec{r}) e^{2\pi i \vec{g} \cdot \vec{r}} + \hat{H}_{-\vec{g}}(\vec{r}) e^{-2\pi i \vec{g} \cdot \vec{r}}. \quad (2.33)$$

Assume $I(\vec{r})$ is real. Then, $I(\vec{r}) = I^*(\vec{r})$, that is,

$$\sum_{\vec{g}} H_{\vec{g}}(\vec{r}) e^{2\pi i \vec{g} \cdot \vec{r}} = \sum_{\vec{g}} H_{\vec{g}}^*(\vec{r}) e^{-2\pi i \vec{g} \cdot \vec{r}}. \quad (2.34)$$

By equating each phase component, it is clear that $H_{\vec{g}}(\vec{r}) = H_{-\vec{g}}^*(\vec{r})$. It is then easy to see that (2.33) can be rewritten as

$$B_{\vec{g}}(\vec{r}) = 2\Re \left[H_{\vec{g}}(\vec{r}) e^{2\pi i \vec{g} \cdot \vec{r}} \right] = 2\Re \left[A_{\vec{g}}(\vec{r}) e^{iP_{\vec{g}}(\vec{r})} e^{2\pi i \vec{g} \cdot \vec{r}} \right] \quad (2.35)$$

Since the amplitude is real, this reduces to

$$B_g(\vec{r}) = 2A_g(\vec{r}) \cos [P_g(\vec{r}) + 2\pi\vec{g} \cdot \vec{r}]. \quad (2.36)$$

This is a very important result. By computing $H_g(\vec{r})$, a set of lattice fringes can have their amplitude and phase plotted as a function of position. The amplitude images contain information about how the intensity of a given set of planes corresponding to a \vec{g} varies at different locations in the image. It is fair to call them the HR-TEM analogue of DF images.

Geometric phase

The regularity of any set of fringes over the image is described by the phase images. In other words, the phase images contain information about how the spacing of a given set of planes deviate from its ideal value at different locations in the image. For an ideal set of fringes, the position dependence of the amplitude and phase disappears.

$$B_g(\vec{r}) = 2A_g \cos [2\pi\vec{g} \cdot \vec{r} + P_g]. \quad (2.37)$$

Assuming a displacement field \vec{u} is present, (2.37) can be written as

$$B_g(\vec{r}) = 2A_g \cos [2\pi\vec{g} \cdot \vec{r} - 2\pi\vec{g} \cdot \vec{u}]. \quad (2.38)$$

Hence,

$$P_g(\vec{r}) = -2\pi\vec{g} \cdot \vec{u}. \quad (2.39)$$

Thus, it is clear that the phase field determines all of the components of the displacement field. If this procedure is repeated for each set of lattice planes, the vectorial displacement fields can be computed. If, instead, the reciprocal lattice vector changes slightly by a small amount $\Delta\vec{g}$, due to e. g. strain, (2.37) can be written as

$$B_g(\vec{r}) = 2A_g \cos [2\pi\vec{g} \cdot \vec{r} + 2\pi\Delta\vec{g} \cdot \vec{r}]. \quad (2.40)$$

Hence,

$$P_g(\vec{r}) = 2\pi\Delta\vec{g} \cdot \vec{r}. \quad (2.41)$$

The phase will have a uniform slope given by the variations of the lattice spacing. In other words, the magnitude of the slope of the phase is proportional to the change in lattice spacing. That is,

$$\vec{\nabla}P_g = 2\pi\Delta\vec{g}. \quad (2.42)$$

This last equation can be used to measure the strain fields in the sample. That is to say, departures of the lattice spacing from its average value in some selected reference region. Since the equation is vectorial, information about rotations of the lattice is also contained in this equation. In that case, Δg would be perpendicular to \vec{g} itself. The strain field components are given by the different spatial derivatives of the displacement field components, as outlined in [32]. From this it is seen that if the phase contains information about one of these fields it contains information about the other field as well. Thus, both the strain field and the displacement field may be derived from the phase by GPA.

2.2 Crystal structure and diffraction

The following section is based on material from [32].

2.2.1 Lattice translation vectors

A crystal is a form of solid state structure where the atoms form an infinite repetition of identical groups in a periodic array. This group is called the basis of the crystal. In three dimensions, the lattice can be described by three translation vectors \mathbf{a}_1 , \mathbf{a}_2 and \mathbf{a}_3 . These vectors have the property that if the lattice is transferred by an integral multiple of any of these vectors, it looks identical to itself. That is,

$$\mathbf{r}' = \mathbf{r} + u_1\mathbf{a}_1 + u_2\mathbf{a}_2 + u_3\mathbf{a}_3, \quad (2.43)$$

where $u_1, u_2, u_3 \in \mathbb{Z}$.

If two arbitrary points satisfying (2.43) look the same, the lattice is said to be primitive. This is the definition of primitive translation vectors \mathbf{a}_i . No cell can be defined in the crystal with a volume smaller than $V_c = |\mathbf{a}_1 \cdot \mathbf{a}_2 \times \mathbf{a}_3|$. The primitive translation vectors define the crystal axes, which form the edges of a primitive parallelepiped. This is an example of a primitive unit cell. Many different unit cells may be defined, and the choice of a unit cell is

not unique. The following convention is often used for the angles between the lattice vectors: $\mathbf{a}_1 \angle \mathbf{a}_2 = \gamma$, $\mathbf{a}_1 \angle \mathbf{a}_3 = \beta$ and $\mathbf{a}_2 \angle \mathbf{a}_3 = \alpha$.

2.2.2 Basis of the crystal structure

The basis is the group that is being repeated infinitely many times in the lattice. There may be one or several atoms in such a basis. The position of an atom j of the basis relative to the given basis point is

$$\mathbf{r}_j = x_j \mathbf{a}_1 + y_j \mathbf{a}_2 + z_j \mathbf{a}_3, \quad (2.44)$$

where $0 \leq x_j, y_j, z_j \leq 1$.

2.2.3 Lattice types

Crystal lattices can be carried into themselves by any lattice translation $\mathbf{T} = \mathbf{r} - \mathbf{r}'$ or by different symmetry operations such as rotations, inversions and mirror reflections. A lattice can for example have one-, two-, three-, four- and sixfold rotation axes. This means that the lattice is carried into itself by rotations of 2π , $\frac{2\pi}{2}$, $\frac{2\pi}{3}$, $\frac{2\pi}{4}$ and $\frac{2\pi}{6}$ around these axes, respectively. These are denoted by the symbols 1, 2, 3, 4 and 6.

An inversion operation consists of a rotation of π followed by reflection in a plane normal to the rotation axis ($\mathbf{r} \rightarrow -\mathbf{r}$). A mirror reflection is a reflection about a plane going through some lattice point.

In $3\mathbb{D}$ there are the additional operations of screw axes and glide planes. These are constructed through combining translation-, mirroring- and rotation-operations. A lattice that is invariant under a group of symmetry operations is said to belong to a planar group in $2\mathbb{D}$ or a space group in $3\mathbb{D}$. As indicated in table 2.1 below, there are 32 planar groups and 230 space groups.

2.2.4 The reciprocal lattice

Due to the periodicity of the crystal lattice, one can express any property of the lattice as a Fourier series. For example, the electron density can be expressed as

$$n(\mathbf{r}) = \sum_{\mathbf{G}} n_{\mathbf{G}} e^{i\mathbf{G} \cdot \mathbf{r}}, \quad (2.45)$$

Table 2.1: Overview of the different crystal systems, their Bravais lattices and their number of different point/space groups. From [33].

System	Axes	Unit Cell	#PGs	#SGs
Cubic	$a_1 = a_2 = a_3$ $\alpha = \beta = \gamma = 90^\circ$	P, I, F	5	36
Tetragonal	$a_1 = a_2 \neq a_3$ $\alpha = \beta = \gamma = 90^\circ$	P, I	7	68
Orthorhombic	$a_1 \neq a_2 \neq a_3$ $\alpha = \beta = \gamma = 90^\circ$	P, I, F, C	3	59
Trigonal/Rombohedral	$a_1 = a_2 = a_3$ $\alpha = \beta = \gamma \neq 90^\circ$	P	5	25
Hexagonal	$a_1 = a_2 \neq a_3$ $\alpha = \beta = \gamma = 90^\circ$	P	7	27
Monoclinic	$a_1 \neq a_2 \neq a_3$ $\alpha = \beta = \gamma = 90^\circ$	P, C	3	13
Triclinic	$a_1 \neq a_2 \neq a_3$ $\alpha \neq \beta \neq \gamma \neq 90^\circ$	P	2	2

$$n_{\mathbf{G}} = \frac{1}{V_c} \int_{V_c} dV n(\mathbf{r}) e^{-i\mathbf{G}\cdot\mathbf{r}}, \quad (2.46)$$

where \mathbf{G} is such that $n(\mathbf{r} + \mathbf{T}) = n(\mathbf{r}), \forall \mathbf{T}$. It can be proven that the vectors \mathbf{G} form a basis for the reciprocal lattice. The reciprocal lattice of a crystal is defined as the points spanned by the set of vectors

$$\mathbf{G} = u_1^* \mathbf{a}_1^* + u_2^* \mathbf{a}_2^* + u_3^* \mathbf{a}_3^*, \quad (2.47)$$

where u_1^*, u_2^* and $u_3^* \in \mathbb{Z}$, and

$$\mathbf{a}_1^* = 2\pi \frac{\mathbf{a}_2 \times \mathbf{a}_3}{V_c}, \quad (2.48)$$

$$\mathbf{a}_2^* = 2\pi \frac{\mathbf{a}_3 \times \mathbf{a}_1}{V_c}, \quad (2.49)$$

$$\mathbf{a}_3^* = 2\pi \frac{\mathbf{a}_1 \times \mathbf{a}_2}{V_c}, \quad (2.50)$$

where V_c is the volume of the unit cell in real space. The vectors defined by equation (2.47) are called the reciprocal lattice vectors, and they represent points in reciprocal space. Furthermore, simple geometric arguments can be used to prove that the reciprocal lattice

vector $[u_1^*, u_2^*, u_3^*] = [h, k, l] \perp (hkl)$ -plane [34], and that

$$|\mathbf{G}_{hkl}| = \frac{2\pi}{d_{hkl}}. \quad (2.51)$$

2.2.5 The Laue condition and the Ewald sphere

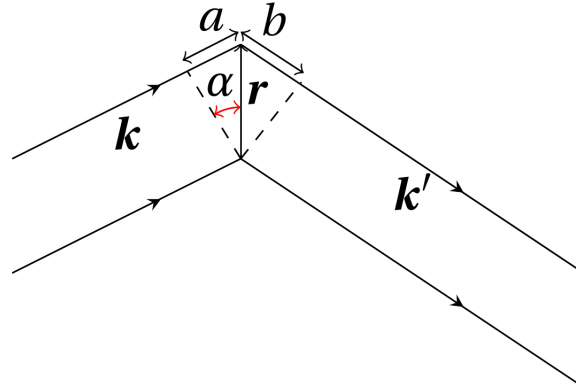


Figure 2.6: Figure used to explain the Laue condition. Created in TikZ [18].

An incoming wave with wave vector \mathbf{k} is scattered by atoms in two parallel planes separated by a distance $\mathbf{r} = \mathbf{d}$. The outgoing wave has wave vector \mathbf{k}' . The path difference between the two beams in the direction of \mathbf{k} is a and the path difference in the direction of \mathbf{k}' is b . One can see from picture 2.6 that a is the projection of \mathbf{d} in the direction \mathbf{k} , or $a = \mathbf{d} \cdot \hat{\mathbf{k}}$, where $\hat{\mathbf{k}} = \frac{\mathbf{k}}{|\mathbf{k}|}$ and $|\mathbf{k}| = \frac{2\pi}{\lambda}$. Similarly, b is the projection of \mathbf{d} in the direction $-\mathbf{k}'$, that is $b = -\mathbf{d} \cdot \hat{\mathbf{k}}'$.

Thus the total path difference $\Delta \mathbf{d}$ is

$$\Delta \mathbf{d} = a + b = \mathbf{d} \cdot (\hat{\mathbf{k}} - \hat{\mathbf{k}}'). \quad (2.52)$$

Whence, the total phase difference from the waves scattered from the two different planes is

$$\Delta \Phi = \frac{2\pi}{\lambda} \mathbf{d} \cdot (\hat{\mathbf{k}} - \hat{\mathbf{k}}') = -\mathbf{d} \cdot \Delta \mathbf{k}. \quad (2.53)$$

To achieve constructive interference, the phase difference needs to be a multiple of 2π . That is,

$$\Delta \Phi = -\mathbf{d} \cdot \Delta \mathbf{k} = 2\pi \cdot n. \quad (2.54)$$

Figure 2.6 makes it clear that $\mathbf{d} \parallel \Delta \mathbf{k}$. The fact that $\mathbf{G} \perp (hkl)$ -plane makes it clear that $\mathbf{d} \parallel$

$\Delta \mathbf{k} \parallel \mathbf{G}$. (2.54) then gives

$$|\Delta \mathbf{k}| = \frac{2\pi n}{|\mathbf{d}|} = |\mathbf{G}|. \quad (2.55)$$

Hence, the requirement is that $\Delta \mathbf{k}$ is a reciprocal lattice vector. This can be shown graphically, by drawing a sphere in reciprocal space with radius $|\mathbf{k}|$ around the start of \mathbf{k} terminating at a reciprocal lattice point, called the Ewald sphere. Points lying on this sphere give rise to diffraction. This is because the change in \mathbf{k} can be written out as a reciprocal lattice vector for such points. A demonstration of this in two dimensions can be seen in figure 2.7.

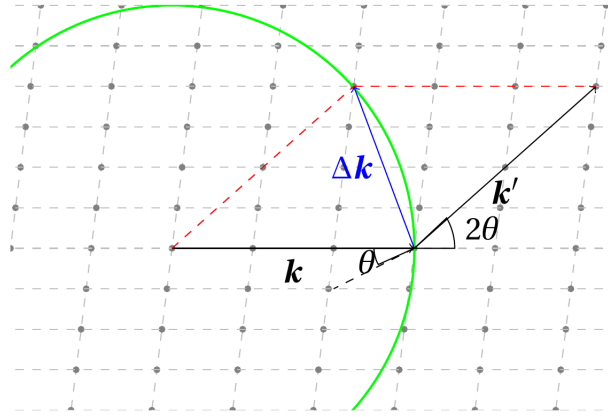


Figure 2.7: Ewald sphere intersecting a plane in reciprocal space. Created in TikZ [18].

2.2.6 The structure factor and the atomic form factor

By the use of Fourier theory, it is possible to write any periodic function in three dimensions as a Fourier series, as exemplified by equations (2.45) and (2.46). Next, the electron scattering in a volume dV at \mathbf{r} is proportional to $n(\mathbf{r})dV$ and the phase factor $e^{i\Delta\Phi}$. The phase factor is due to interference of the scattered wave components coming from different planes, and is given in equation (2.53) for $\mathbf{r} = \mathbf{d}$. Thus, the scattering amplitude over a volume V is

$$F = \int_V dV n(\mathbf{r}) e^{i\Delta\Phi} = \int_V dV n(\mathbf{r}) e^{-i\mathbf{r} \cdot \Delta \mathbf{k}}. \quad (2.56)$$

Now using equation (2.45) gives

$$F = \sum_{\mathbf{G}} \int_V dV n_{\mathbf{G}} e^{i\mathbf{r} \cdot (\mathbf{G} - \Delta \mathbf{k})}. \quad (2.57)$$

The integral averages to zero due to the phase factors unless

$$\Delta \mathbf{k} \approx \mathbf{G}. \quad (2.58)$$

Based on this, one can write the scattering amplitude from N different cells with volume V for some \mathbf{G} as

$$F_{\mathbf{G}} = N \cdot \int_V dV n(\mathbf{r}) e^{-i\mathbf{r} \cdot \mathbf{G}}. \quad (2.59)$$

This is the so called structure factor. Next, one assumes that the electron concentration can be written as a sum over the s atoms of the basis. That is,

$$n(\mathbf{r}) = \sum_j^s n_j(\mathbf{r} - \mathbf{r}_j). \quad (2.60)$$

This gives

$$F_{\mathbf{G}} = N \cdot \int_V dV \sum_j^s n_j(\mathbf{r} - \mathbf{r}_j) \cdot e^{-i\mathbf{r} \cdot \mathbf{G}} = \sum_j^s e^{-i\mathbf{G} \cdot \mathbf{r}_j} \int_V dV n_j(\boldsymbol{\rho}) e^{-i\mathbf{G} \cdot \boldsymbol{\rho}}, \quad (2.61)$$

where $\boldsymbol{\rho} = \mathbf{r} - \mathbf{r}_j$. Now, define the atomic form factor as

$$f_j = \int_V dV n_j(\boldsymbol{\rho}) e^{-i\mathbf{G} \cdot \boldsymbol{\rho}}. \quad (2.62)$$

Hence, by equations (2.44), (2.47) as well as (2.48), (2.49) and (2.50)

$$F_{\mathbf{G}} = \sum_j^s f_j e^{-i\mathbf{G} \cdot \mathbf{r}_j} = \sum_j^s f_j e^{-2\pi i \cdot (x_j h + y_j k + z_j l)}. \quad (2.63)$$

Notice from (2.59) that the structure factor is the Fourier transform of the electron density $n(\mathbf{r})$ of the lattice, while from (2.62) it is seen that the atomic form factor is the Fourier transform of the electron distribution $n_j(\boldsymbol{\rho})$ of the atom.

2.2.7 Diffraction patterns

A given reflection $|\mathbf{G}_{hkl}|$ corresponds to a given set of planes diffracting beams into the same angle θ . As a consequence, the electron beams converge in the focal plane of the TEM, which is a $2\mathbb{D}$ slice through reciprocal space. This $2\mathbb{D}$ slice is known as a diffraction pattern. The intensity of a given spot $|\mathbf{G}_{hkl}|$ is proportional to the structure factor (2.63).

A wave incident on a grate with openings approximately equal in size to the wavelength will give rise to diffraction. Crystal planes can be considered as grates, with a set distance given by

$$\frac{1}{|d_{hkl}|^2} = \frac{h^2}{a_1^2} + \frac{k^2}{a_2^2} + \frac{l^2}{a_3^2}, \quad (2.64)$$

where h, k and l are the indices of the planes.

Combining equations (2.55) and (2.64) gives

$$k_{hkl} = \frac{2\pi}{|d_{hkl}|} = 2\pi \sqrt{\frac{h^2}{a_1^2} + \frac{k^2}{a_2^2} + \frac{l^2}{a_3^2}}. \quad (2.65)$$

Furthermore, from the product rule in elementary vector calculus,

$$\cos(\phi) = \frac{h_1 h_2 + k_1 k_2 + l_1 l_2}{\sqrt{h_1^2 + k_1^2 + l_1^2} \sqrt{h_2^2 + k_2^2 + l_2^2}}. \quad (2.66)$$

These two equations are used to index diffraction patterns for crystals with known lattice parameters. All the reciprocal space vectors in the diffraction pattern are perpendicular to the zone-axis, i. e. the direction of the incoming electron beam. Deviations from the angle ϕ may occur in non-cubic materials.

2.2.8 Crystallographic properties of perovskites

A transition metal oxide (TMO) can crystallize into many different crystal structures. In this work, the perovskite structure is the one of interest. In general, perovskites can be described by their chemical composition, ABO_3 . A is either an alkaline earth metal or a rare earth metal, while B is a transition metal. The transition metal coordination is very important. In perovskites, the transition metal is surrounded by six oxygen atoms forming an octahedra. These octahedra can have different tilt angles, and how the different oxygen octahedra are tilted relative to each other is of great importance. See [35] for more on this. In figure 2.8, an ideal cubic perovskite with no tilting of the oxygen octahedra can be seen.

Furthermore, while oxygen always has charge -2, there is still a huge variety possible for the charge of the transition metal ion. This can be realized by choosing different doping levels x , e. g. in LSMO [11]. Goldschmidt [36], derived a tolerance factor in 1926 which gives

a rough estimate of whether or not an ABO_3 TMO crystallizes into a perovskite,

$$t = \frac{R_A + R_O}{\sqrt{2}(R_B + R_O)}, \quad (2.67)$$

where R_A , R_B and R_C are the radii of atoms A, B and C, respectively. If the tolerance factor is between 0.78 and 1.05, the perovskite structure is stable [11].

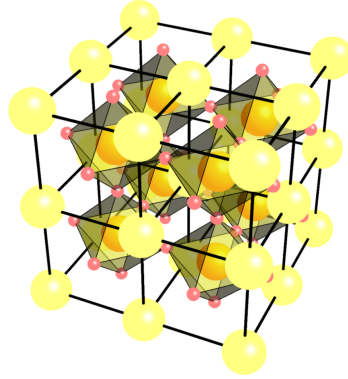


Figure 2.8: Cubic perovskite structure. In STO, the yellow atoms are Sr, the red atoms are oxygen and the orange atoms are Ti. Note that the oxygen form octahedra surrounding Ti. Constructed in Asymptote [37].

2.2.9 Thin film crystal structure

The control of functional properties in oxide thin films has been achieved through the development of thin-film deposition techniques and the development of high quality single crystalline substrate materials with single surface termination and well-controlled miscuts [7]. Deposition techniques such as PLD and molecular beam epitaxy (MBE) together with in-situ monitoring techniques such as RHEED have made this control possible. This type of deposition is called epitaxial growth. The word “epitaxy” is greek and stems from *e*pi which means above and *taxis* meaning “in an ordered manner.” Since the functional properties are strongly connected to the structure in perovskite materials, epitaxial growth can be used as a tool to tailor the material properties. If epitaxial growth is to occur, it is important that the crystal structure of the substrate material is relatively similar to that of the thin film material. This condition is satisfied for the materials used in the thin film systems in this work. Next, if the in-plane lattice parameters of the thin-film differs from that of the substrate, there are two possible outcomes. Either the thin film adapts to the in-plane lattice parameter of the substrate, or it may relax and create misfit dislocations in order to keep its original lattice

parameter. Films above a certain thickness will have the latter outcome because the strain energy then becomes similar to that of introducing misfit dislocations.

The above mentioned crystal structures for STO, LSMO and BTO are valid when these materials are in bulk form. This is reasonable for the bulk STO substrate, but the LSMO and BTO thin films may have distorted structures. The LSMO bulk rhombohedral lattice is incommensurate with the square surface unit cells of the STO-substrate, and is subjected to a tensile strain when deposited on STO(111) [38]. Furthermore, the LSMO thin film structure may be subject to a distortion of the unit cell when under strain, this reducing the symmetry of the unit cell [12, 38, 39, 40].

2.2.10 Dislocations

Dislocations are line imperfections [32]. They are often introduced in a thin film when it reaches a critical thickness and relaxes with respect to the substrate. Dislocations create strain and displacement fields in the thin film. There are two types of dislocations. Edge dislocations are produced when an extra lattice plane is inserted into the crystal, but does not extend through all of the crystal. The dislocation line is located along the end of this extra plane. This is demonstrated in figure 2.9 (a). A screw dislocation is created by translating one part of the crystal along an atomic plane by an integer multiple of the lattice parameter, but only doing so in part of the crystal. This is demonstrated in figure 2.9 (b).

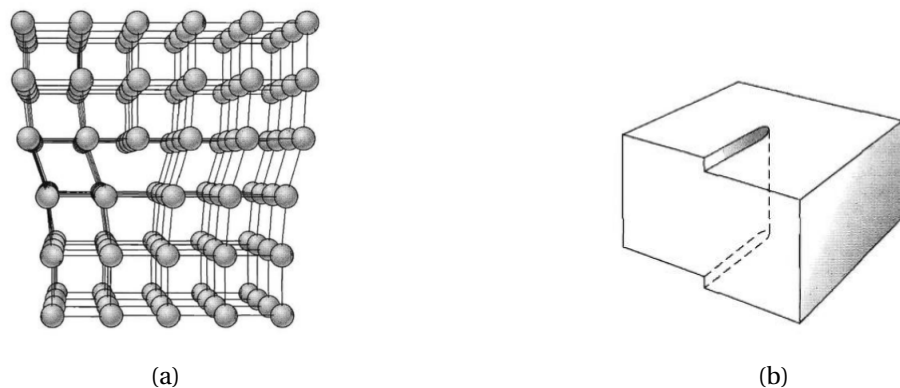


Figure 2.9: **(a)** Edge dislocation, produced by inserting an extra lattice plane into the crystal that does not extend all the way through it. **(b)** Screw dislocation, created by translating one part of the crystal along an atomic plane by an integer multiple of the lattice parameter. From [32].

A pseudo-periodic array of dislocations will create diffuse rings around the Bragg-reflections according to (2.68).

2.3 Ferroelectricity

This section is included because investigating the ferroelectric domain structure of the BTO thin film was of interest in this work. In order to give an introduction to ferroelectricity, some basic definitions must first be given. It is constructive to investigate how an electric field behaves within a crystal, and how it may give rise to an electric polarization. In order to understand how electrical polarization arises, one must understand the connection between an external electric field applied to a crystal $\mathbf{E}(\mathbf{r}, t)$ and the induced internal electric field in the crystal $\mathbf{P}(\mathbf{r}, t)$. It is also necessary to understand how a local electric field at each atomic site is related to the macroscopic polarization of the sample. Chapter 16 in [32] contains a good introduction to the electromagnetic theory of ferroelectricity.

2.3.1 Ferroelectric crystals

A ferroelectric crystal retains a dipole moment even in the absence of an external electric field. In such a crystal, the center of positive charge does not coincide with the center of negative charge. The unit cell must therefore have a reduced symmetry relative to e. g. the cubic phase. The most important criterion for ferroelectricity is the lack of inversion symmetry. This symmetry reduction is described by Landau's theory on phase transitions.

2.3.2 Landau theory

Landau theory is based on a symmetry-analysis of equilibrium behavior near a phase transition. A *system* cannot change continuously between two states of different symmetry [41, 42]. The thermodynamic state of two phases must be the same at their transition line, but the symmetry may be different. In Landau theory, an order parameter is defined that must be zero in the high symmetry state, and is changed to a finite value upon a transition to the state of low symmetry. In the case of ferroelectricity, the order parameter is the electric polarization. In the case of ferromagnetism, the order parameter is the net magnetization. A detailed treatment of Landau theory may be found e. g. in [43].

In a tetragonal crystal such as BTO, the polarization can point in two different directions, up or down, in the unit cell. There will be an energy barrier between these two polarization directions, which means an external electric field will not spontaneously switch the polarization of a material. Landau-Devonshire theory predicts hysteresis [43], as shown in figure 2.10.

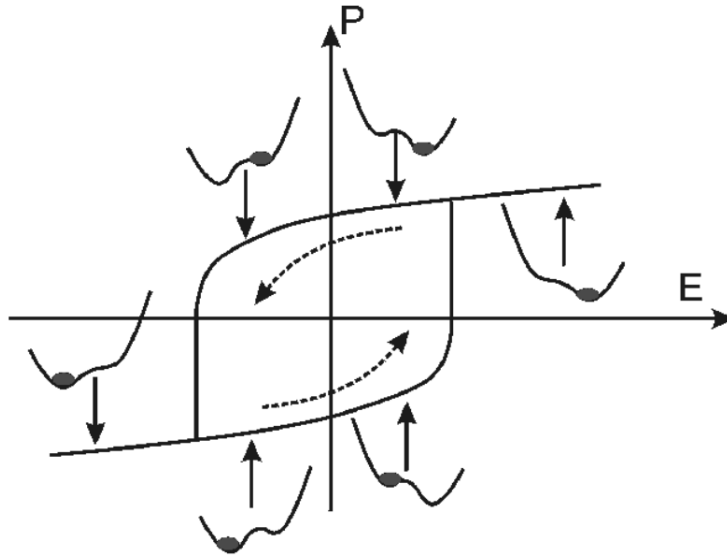


Figure 2.10: Schematic showing hysteresis behavior in an ideal ferroelectric. From [43].

2.3.3 Allowed domain structures in tetragonal thin films on (111) oriented substrates

Two types of ferroelectric domain structures are possible in tetragonal thin films on (111) oriented substrates [15, 44]. In one case, the domain walls are parallel to either $(\bar{1}10)_c$, $(0\bar{1}1)_c$ or $(\bar{1}01)_c$. This type of pattern is demonstrated in figures 2.11 (a) and (b). In the second case, the domain walls are parallel to either $(110)_c$, $(101)_c$ or $(011)_c$, demonstrated in figures 2.11 (c) and (d). In the first case, the domain walls are oriented parallel to $[111]$, as shown in figure 2.11 (b). In the second case, according to simple geometry as well as [45], the domain walls are skewed relative to $[111]$, as shown in figure 2.11 (d). The meaning of the directions d_i^\pm can be seen in figure 2.12. There is no critical film thickness for domain pattern formation in (111) oriented epitaxial ferroelectric films [15]. Note that for a given type of domain wall, only two domains are present. This means that the repeat sequence in the periodic structure thus formed consists of two domains. Also note that both of these types of domain walls are 90° head-to-tail domain walls.

It is of interest to investigate how these different types of domain structures would appear when observed along the $[1\bar{1}0]_c$ and the $[11\bar{2}]_c$ zone-axes. In order to do this it is useful to compile a table where the vector of intersection between the plane perpendicular to the zone-axis and the domain walls is given. When viewing the specimen along either of these zone-axes, there should be an irregularity parallel to some vector of intersection present in

one of these tables if there is a domain wall along any of these planes. This can simply be computed by the cross product of the zone-axis and the normal to the plane of the domain wall. Any irregularity that is along a direction not present in these tables is probably due to something else, such as a dislocation. Since BTO is tetragonal and not cubic, these computations are only approximate, but since the difference between a_{BTO} and c_{BTO} is small, the deviations from these computations should be small. All of these possibilities are listed in tables 2.2 and 2.3. Note that the domain wall is more visible if it is viewed edge-on, i. e. if its normal is perpendicular to the zone-axis.

Next, the domain boundaries represent a periodicity that is visible in the diffraction patterns. They should create a diffuse pattern around each STO, LSMO and BTO diffraction spot. The extent of this pattern should be inversely proportional to the periodicity of the domain structure. This distance is bigger than the distance between the atom planes. Hence, the extent of the pattern should be much smaller than the distance from the diffraction spot to the central beam. The periodicity of the domain structure is given by

$$\Lambda_D = \frac{2\pi}{\Delta q}, \quad (2.68)$$

where Δq is the distance from the diffraction spot to the pattern surrounding it and Λ_D is the size of the repeat structure (two domains) [46].

Such diffuse scattering may occur in several ways:

1. Diffuse scattering from the ferroelectric domain walls of BTO and/or the ferroelastic domain walls of LSMO and/or a pseudo-periodic array of dislocations. Gives a diffuse ring around the main beam.
2. Diffuse scattering from the ferroelectric domain walls of BTO and/or the ferroelastic domain walls of LSMO and/or a pseudo-periodic array of dislocations plus Bragg scattering from STO/LSMO/BTO. Gives a diffuse ring around the Bragg peaks of STO/LSMO/BTO.
3. Diffuse scattering from the ferroelectric domain walls of BTO and/or the ferroelastic domain walls of LSMO and/or a pseudo-periodic array of dislocations plus Bragg scattering from both STO, LSMO and BTO plus inelastic interactions between the beam and the sample with large Δq .

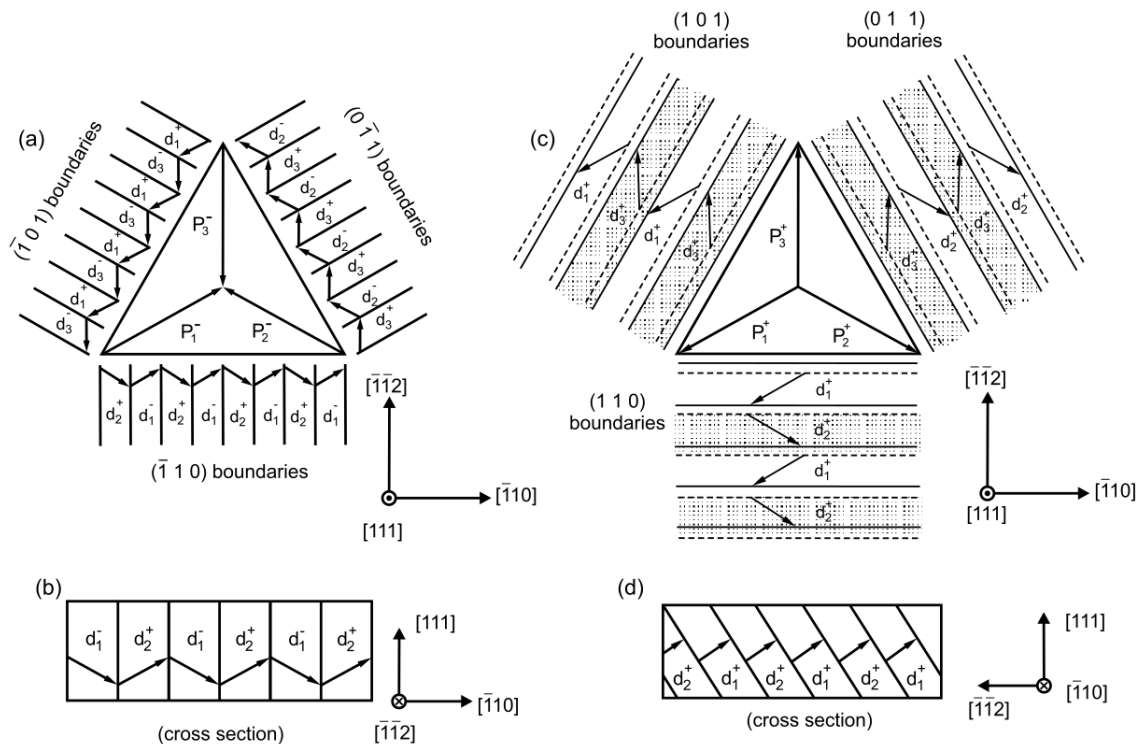


Figure 2.11: Schematic PV images **(a)** and **(c)** and CS images **(b)** and **(d)** of the two possible domain structures in (111) ferroelectric films with a cubic-tetragonal ferroelectric phase transition. The arrows point in the direction of spontaneous polarization in the domains. The symbols d_i^\pm denotes the six possible domain states. From [44].

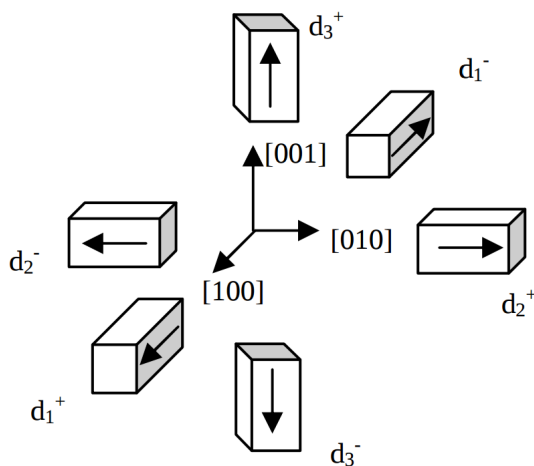


Figure 2.12: Orientations of unit cells for the tetragonal perovskite ferroelectric. The six unit cells with different polarization orientations are marked as d_i^\pm for $i = 1, 2, 3$ and \pm denotes positive or negative orientation. From [45].

Based on the above, one would expect to see quite complex patterns around both the STO, LSMO and the BTO diffraction spots. The fact that these spots lie close to each other in reciprocal space will make the patterns even more complex. How the electrons interact with

Table 2.2: Vectors of intersection between $(1\bar{1}0)_c$ and the domain walls.

Domain structure	Plane of domain walls	Vector of intersection	Angle to $[111]_c$
d_1^-/d_2^+	$(1\bar{1}0)_c$	Complete overlap	-
d_1^+/d_3^-	$(10\bar{1})_c$	$[111]_c$	0
d_2^-/d_3^+	$(01\bar{1})_c$	$[111]_c$	0
d_1^+/d_2^+	$(110)_c$	$[001]_c$	54.74°
d_1^+/d_3^+	$(101)_c$	$[11\bar{1}]_c$	70.53°
d_2^+/d_3^+	$(011)_c$	$[11\bar{1}]_c$	70.53°

Table 2.3: Vectors of intersection between $(11\bar{2})_c$ and the domain walls.

Domain structure	Plane of domain walls	Vector of intersection	Angle to $[111]_c$
d_1^-/d_2^+	$(1\bar{1}0)_c$	$[111]_c$	0
d_1^+/d_3^-	$(10\bar{1})_c$	$[111]_c$	0
d_2^-/d_3^+	$(01\bar{1})_c$	$[111]_c$	0
d_1^+/d_2^+	$(110)_c$	$[1\bar{1}0]_c$	90°
d_1^+/d_3^+	$(101)_c$	$[\bar{1}31]_c$	58.52°
d_2^+/d_3^+	$(011)_c$	$[3\bar{1}1]_c$	58.52°

the specimen is very dependent on its thickness. If the specimen is too thick, the last option listed above with the largest amount of interactions is most likely.

2.3.4 Observing ferroelectric domains in thin film systems using TEM

There will be contrast between the different ferroelectric domains due to the different unit cell orientations. This contrast may be phase contrast in HR-TEM images or diffraction contrast in BF-TEM, DF-TEM or ASTAR images. Thus, a series of alternating dark and bright stripes will be observed if there is a ferroelectric domain structure present. This is demonstrated in figure 2.13, where 90° domain walls are sketched.

The ferroelectric domains may also be observed in the diffraction patterns. In [48], the SAD patterns along the $[111]_c$ zone-axis from BTO/STO(111) in the presence of all three fer-

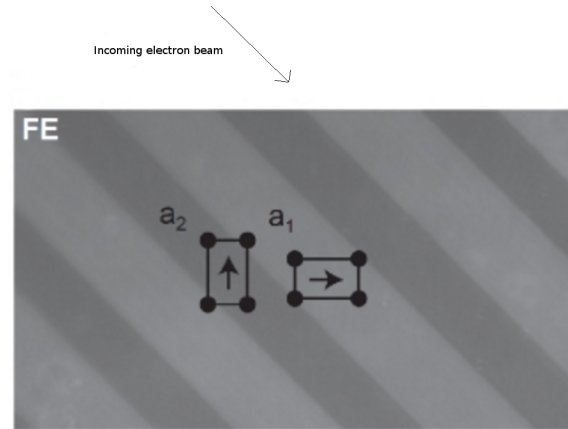


Figure 2.13: Viewing the domain structure in the TEM. Different domains have different orientations of their unit cells, and this may give contrast in the images. From [47].

roelectric domain states was computed. The result can be seen in figure 2.14, where the STO reflections are olive colored and the BTO reflections from the three different ferroelectric domains are red, blue and green. Note that the diffraction peaks due to different ferroelectric domains appear very close together. This makes it difficult to separate them without having high angular resolution in the diffraction patterns. Furthermore, other effects such as edge dislocations may give larger rotations in the lattice than the domain structure itself.

2.4 Ferroelastic domains in LSMO

Different ferroelastic domains in the rhombohedral phase can be described by pseudo-cubic unit cells that are compressed or elongated along the cubic $[111]_c$, $[11\bar{1}]_c$, $[1\bar{1}1]_c$ or $[\bar{1}11]_c$ directions [49]. When LSMO is deposited on STO(110) or STO(001) it forms ferroelastic domain structures [50]. It is therefore reasonable to expect that ferroelastic domain walls might be observed in LSMO deposited on STO(111). In the next two sections, equivalent $[1\bar{1}0]_c$ and $[11\bar{2}]_c$ zone-axes are derived in cubic and hexagonal coordinates for the four different domains. These observations are used later to simulate the SADPs of the different ferroelastic domains. Note that LSMO may be distorted due to stress and strain when deposited as a thin film. This leads to a reduction in symmetry, but does not necessarily remove the domain structure.

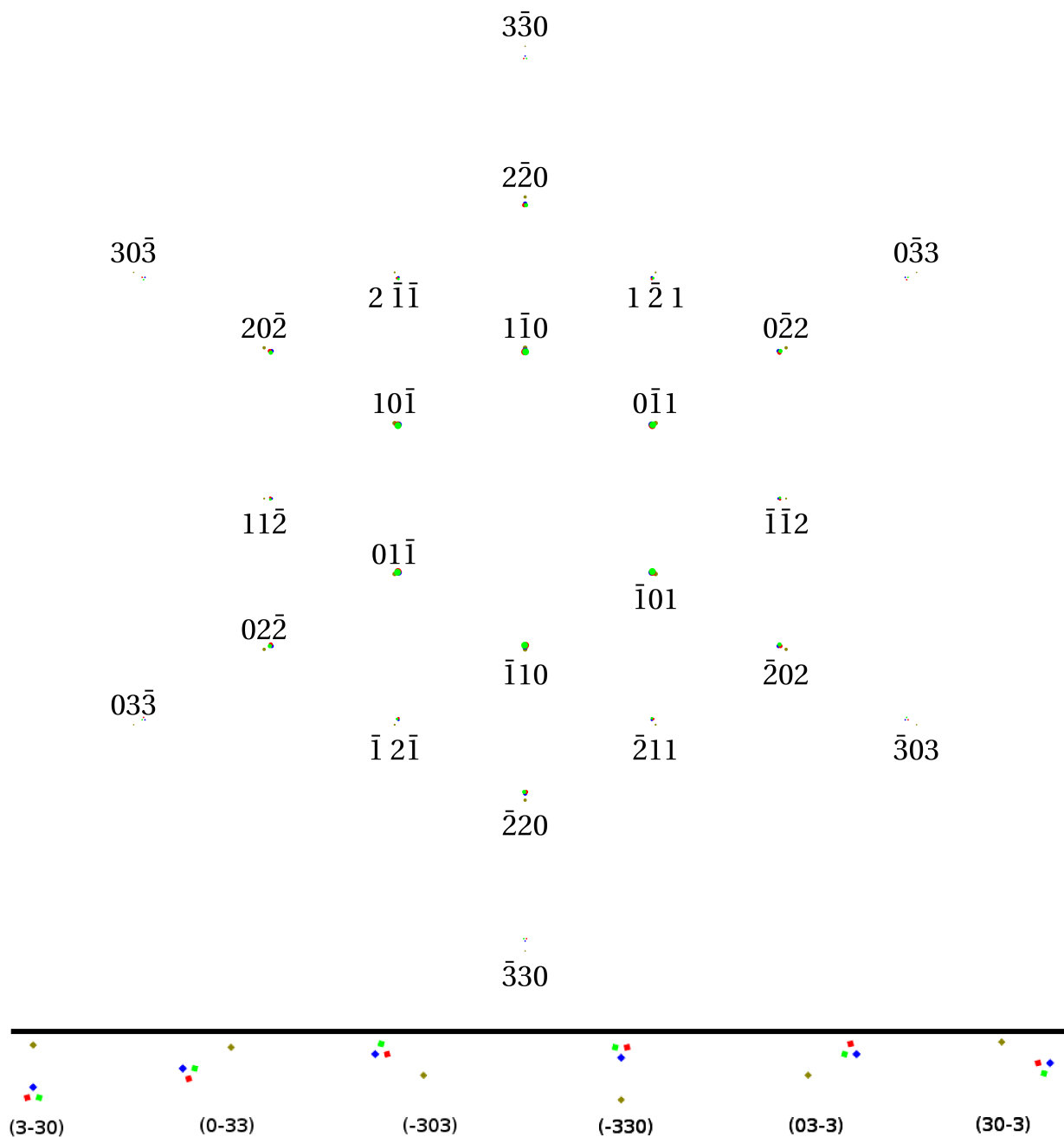


Figure 2.14: BTO/STO(111) [111] zone-axis diffraction pattern with all domains present constructed from theoretical equations using TiKZ [18]. The reflections from STO are olive colored, while the BTO reflections are blue, red and green. Underneath, a magnified view of reflections $(3\bar{3}0)$, $(0\bar{3}3)$, $(\bar{3}03)$, $(\bar{3}30)$, $(03\bar{3})$ and $(30\bar{3})$ is shown. Some (h, k, l) have been omitted due to time constraints. The derivation of this SAD pattern can be found in [48].

2.4.1 Orientation relationship between cubic and hexagonal axes

The relationship between a pseudo cubic unit cell and a hexagonal unit cell is [49]

$$\vec{a}_h = -\vec{a}_c + \vec{b}_c, \quad (2.69)$$

$$\vec{b}_h = -\vec{b}_c + \vec{c}_c, \quad (2.70)$$

$$\vec{c}_h = 2(\vec{a}_c + \vec{b}_c + \vec{c}_c). \quad (2.71)$$

Next, inverting (2.69)-(2.71) gives

$$\vec{a}_c = -\frac{2}{3}\vec{a}_h - \frac{1}{3}\vec{b}_h + \frac{1}{6}\vec{c}_h, \quad (2.72)$$

$$\vec{b}_c = \frac{1}{3}\vec{a}_h - \frac{1}{3}\vec{b}_h + \frac{1}{6}\vec{c}_h, \quad (2.73)$$

$$\vec{c}_c = \frac{1}{3}\vec{a}_h + \frac{2}{3}\vec{b}_h + \frac{1}{6}\vec{c}_h. \quad (2.74)$$

2.4.2 Ferroelastic domains seen from the $[1\bar{1}0]_c$ zone-axis

By comparing figure 2.15 (a) to figures 2.15, (b), (c) and (d), it can be seen that zone-axis $[1\bar{1}0]_c$ in domains R_2 (red), R_3 (orange) and R_4 (blue) correspond to zone-axes $[\bar{1}10]_c$, $[110]_c$ and $[\bar{1}\bar{1}0]_c$ in R_1 , respectively. Then equations (2.72)-(2.74) may be used to determine the corresponding zone-axes in the hexagonal LSMO system.

Domain R_1 :

$$\vec{a}_c - \vec{b}_c = -\vec{a}_h = [\bar{1}00]_{LSMO}. \quad (2.75)$$

Domain R_2 :

$$-\vec{a}_c + \vec{b}_c = \vec{a}_h = [100]_{LSMO}. \quad (2.76)$$

Domain R_3 :

$$\vec{a}_c + \vec{b}_c = -\frac{1}{3}\vec{a}_h - \frac{2}{3}\vec{b}_h + \frac{2}{6}\vec{c}_h \parallel [\bar{1}\bar{2}1]_{LSMO}. \quad (2.77)$$

Domain R_4 :

$$-(\vec{a}_c + \vec{b}_c) = \frac{1}{3}\vec{a}_h + \frac{2}{3}\vec{b}_h - \frac{2}{6}\vec{c}_h \parallel [12\bar{1}]_{LSMO}. \quad (2.78)$$

2.4.3 Ferroelastic domains seen from the $[11\bar{2}]_c$ zone-axis

Similarly, it can be seen in figures 2.16 that domains $R_1 - R_4$ along the $[11\bar{2}]_c$ zone-axis corresponds to zone-axes $[11\bar{2}]_c$, $[\bar{1}\bar{1}\bar{2}]_c$, $[\bar{1}\bar{1}\bar{2}]_c$ and $[1\bar{1}\bar{2}]_c$, respectively, in domain R_1 . Then equations (2.72)-(2.74) may be used to determine the corresponding zone-axes in the hexagonal LSMO system.

Domain R_1 :

$$\vec{a}_c + \vec{b}_c - 2\vec{c}_c = -\vec{a}_h - 2\vec{b}_h = [\bar{1}\bar{2}0]_{LSMO}. \quad (2.79)$$

Domain R_2 :

$$-\vec{a}_c - \vec{b}_c - 2\vec{c}_c = -\frac{1}{3}\vec{a}_h - \frac{2}{3}\vec{b}_h - \frac{2}{3}\vec{c}_h \parallel [\bar{1}\bar{2}\bar{2}]_{LSMO} \quad (2.80)$$

Domain R_3 :

$$-\vec{a}_c + \vec{b}_c - 2\vec{c}_c = \frac{1}{3}\vec{a}_h - \frac{4}{3}\vec{b}_h - \frac{1}{3}\vec{c}_h \parallel [1\bar{4}\bar{1}]_{LSMO} \quad (2.81)$$

Domain R_4 :

$$\vec{a}_c - \vec{b}_c - 2\vec{c}_c = -\frac{5}{3}\vec{a}_h - \frac{4}{3}\vec{b}_h - \frac{1}{3}\vec{c}_h \parallel [5\bar{4}\bar{1}]_{LSMO} \quad (2.82)$$

2.4.4 Ferroelastic domain-walls in LSMO

LSMO is a ferroelastic material, and twins form between different ferroelastic domains. These are summarized in table 2.4. According to table 2.4, the possible domain walls in the rhombohedral phase lie along $\{110\}_c$ type or $\{100\}_c$ type planes. Note that LSMO will be distorted and have a unit cell of reduced symmetry in thin film form, e. g. monoclinic. It is therefore reasonable to expect there to be small deviations from the domain wall orientations in bulk listed in table 2.4. In tables 2.5 and 2.6, the vectors of intersection between the $(1\bar{1}0)_c$ and $(11\bar{2})_c$ planes and the possible planes of the ferroelastic domain walls listed in table 2.4 are given. Note that a domain wall is more visible if it is viewed edge-on, i. e. if its normal is perpendicular to the zone-axis.

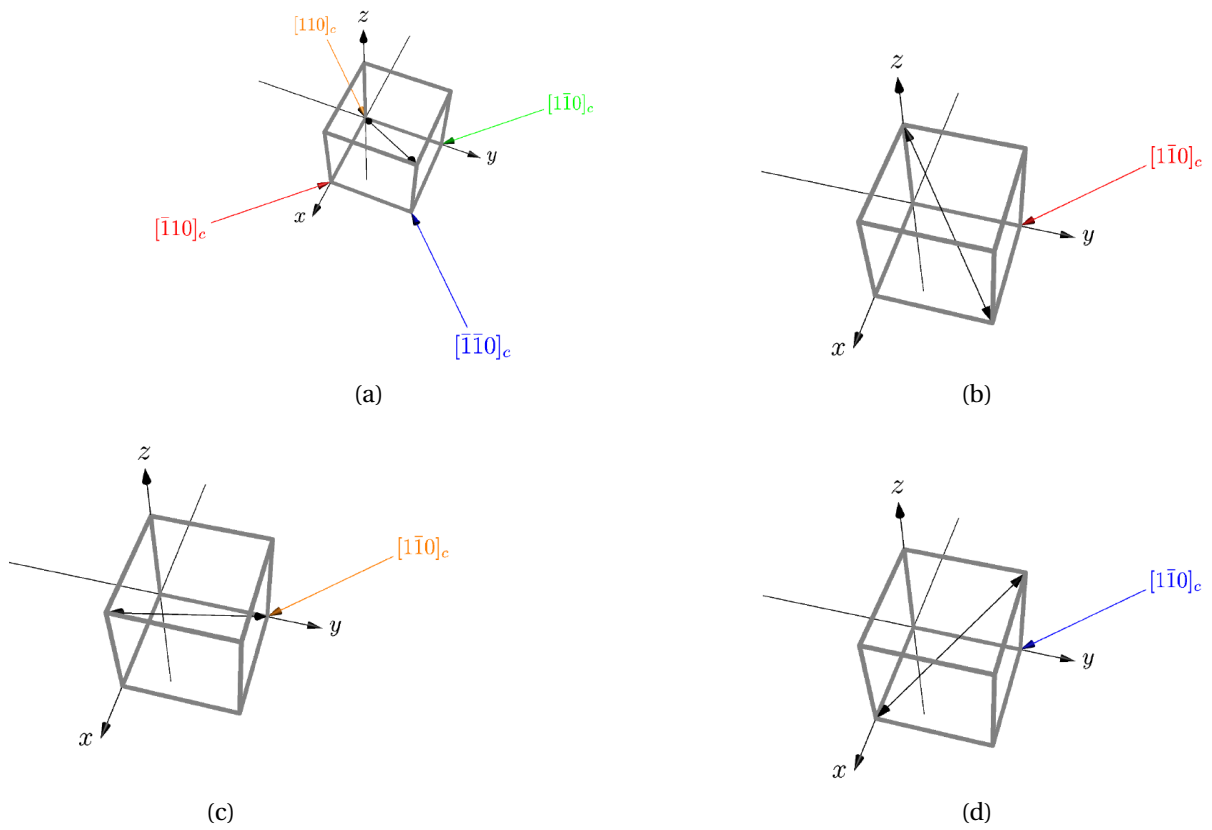


Figure 2.15: **(a)** Domain R_1 has its unique axis along $[111]_c$, indicated by the black double arrow. The $[1\bar{1}0]_c$ zone-axis in domain R_1 in green along with zone-axes equivalent to $[1\bar{1}0]_c$ in R_2 , R_3 and R_4 in red, orange and blue, respectively. **(b)** Domain R_2 has its unique axis along $[1\bar{1}\bar{1}]_c$. **(c)** Domain R_3 has its unique axis along $[1\bar{1}\bar{1}]_c$. **(d)** Domain R_4 has its unique axis along $[\bar{1}\bar{1}\bar{1}]_c$. Constructed in Asymptote [37].

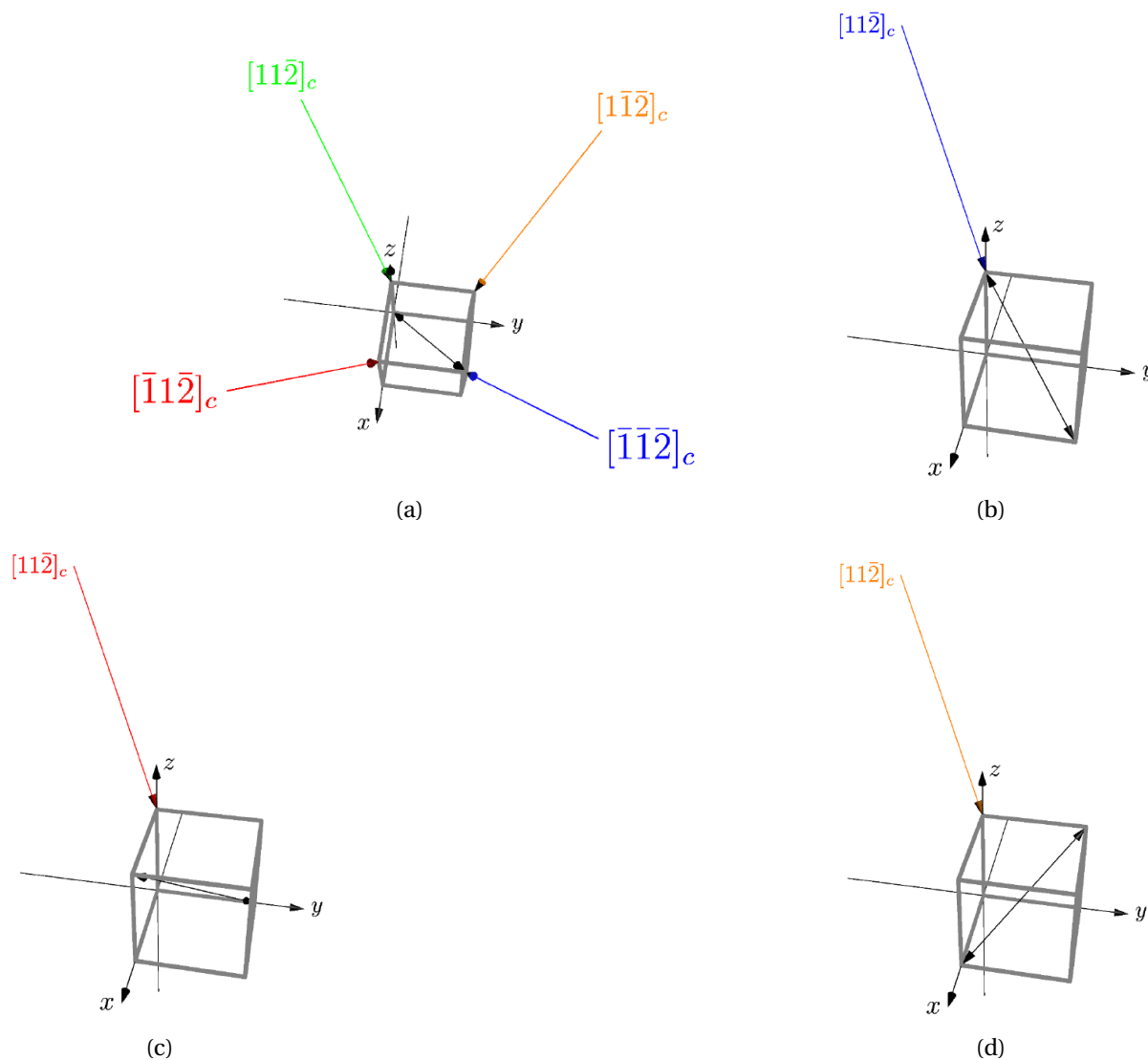


Figure 2.16: **(a)** Domain R_1 has its unique axis along $[111]_c$, indicated by the black double arrow. The $[11\bar{2}]_c$ zone-axis in domain R_1 is indicated in green along with zone-axes equivalent to $[11\bar{2}]_c$ in R_2 , R_3 and R_4 in blue, red and orange, respectively. **(b)** Domain R_2 has its unique axis along $[1\bar{1}\bar{1}]_c$. **(c)** Domain R_3 has its unique axis along $[1\bar{1}\bar{1}]_c$. **(d)** Domain R_4 has its unique axis along $[\bar{1}\bar{1}1]_c$. Constructed in Asymptote [37].

Table 2.4: Overview of possible deformation twins in the rhombohedral phase as a function of which domain states that meet. From [49].

Combination of domains	Orientation of the domain wall	
	{001} type	{110} type
$R_1 + R_2$	$(001)_c$	$(110)_c$
$R_1 + R_3$	$(010)_c$	$(101)_c$
$R_1 + R_4$	$(100)_c$	$(011)_c$
$R_2 + R_3$	$(100)_c$	$(01\bar{1})_c$
$R_2 + R_4$	$(010)_c$	$(10\bar{1})_c$
$R_3 + R_4$	$(001)_c$	$(1\bar{1}0)_c$

Table 2.5: Vectors of intersection between $(1\bar{1}0)_c$ and the possible domain walls in table 2.4. The rightmost column shows the angle between the intersection vector and the thin film normal.

Domain structure	Plane of domain walls	Vector of intersection	Angle to $[111]_c$
$R_1 + R_2, R_3 + R_4$	$(001)_c$	$[110]_c$	35.26°
$R_1 + R_3, R_2 + R_4$	$(010)_c$	$[001]_c$	54.74°
$R_1 + R_4, R_2 + R_3$	$(100)_c$	$[001]_c$	54.74°
$R_1 + R_2$	$(110)_c$	$[001]_c$	54.74°
$R_1 + R_3$	$(101)_c$	$[11\bar{1}]_c$	70.53°
$R_1 + R_4$	$(011)_c$	$[11\bar{1}]_c$	70.53°
$R_2 + R_3$	$(01\bar{1})_c$	$[111]_c$	0.00°
$R_2 + R_4$	$(10\bar{1})_c$	$[111]_c$	0.00°
$R_3 + R_4$	$(1\bar{1}0)_c$	Complete overlap	-

Table 2.6: Vectors of intersection between $(11\bar{2})_c$ and the possible domain walls in table 2.4. The rightmost column shows the angle between the intersection vector and the thin film normal.

Domain structure	Plane of domain walls	Vector of intersection	Angle to $[111]_c$
$R_1 + R_2, R_3 + R_4$	$(001)_c$	$[1\bar{1}0]_c$	90.00°
$R_1 + R_3, R_2 + R_4$	$(010)_c$	$[201]_c$	39.23°
$R_1 + R_4, R_2 + R_3$	$(100)_c$	$[021]_c$	39.23°
$R_1 + R_2$	$(110)_c$	$[1\bar{1}0]_c$	90.00°
$R_1 + R_3$	$(101)_c$	$[\bar{1}31]_c$	58.52°
$R_1 + R_4$	$(011)_c$	$[3\bar{1}1]_c$	58.52°
$R_2 + R_3$	$(01\bar{1})_c$	$[111]_c$	0.00°
$R_2 + R_4$	$(10\bar{1})_c$	$[111]_c$	0.00°
$R_3 + R_4$	$(1\bar{1}0)_c$	$[111]_c$	0.00°

2.5 Principal component analysis

The main objective of principal component analysis (PCA) is to cut down the dimensionality of a data set that consists of several interrelated variables, but at the same time preserve the variation present in the dataset. This is done by transforming to a new set of variables, called the principal components. These are not correlated, and ordered such that the first component contains most of the variation present in all the original variables. The subsequent components contain less variation, and most software allows the user to specify how many components to keep. In this manner, all the components which explain little variation can be cropped away, and this reduces the noise in the data set [31].

In order to investigate the number of components necessary to reproduce the data set, a Scree plot is utilized. This is a plot of the eigenvalue versus the index of the component. Eigenvalues of random noise form a straight line in the Scree plot. Thus, the components that carry significant information, i. e. the principal components, can be distinguished from the components associated with noise by looking for an abrupt change of slope in the Scree plot. The components after this change of slope are then filtered out. An example Scree plot can be seen in figure 2.17.

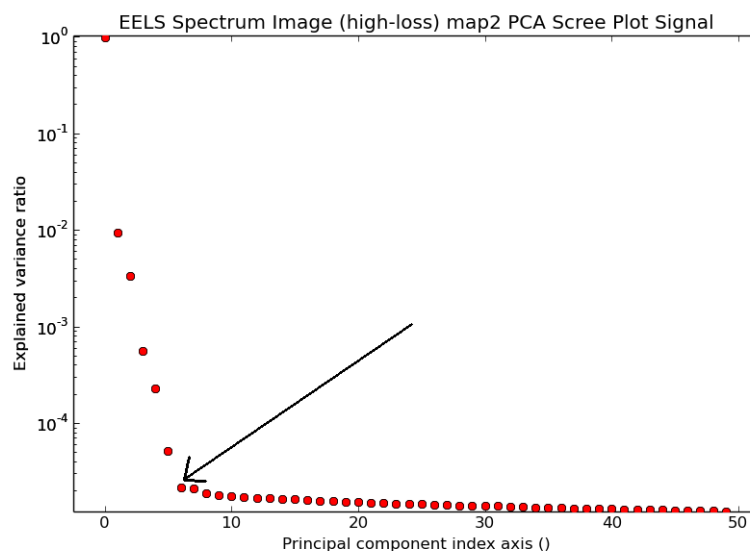


Figure 2.17: Scree-plot. The black arrow points to the change in slope. In this plot, at least 6 components should be retained.

Chapter 3

Applications of oxide thin films

One of the biggest areas of research in condensed matter physics is into strongly correlated electron systems in complex oxides [7, 8, 9, 10, 11]. A multitude of different properties have been detected in these materials, including colossal magnetoresistance [51], superconductivity [52] and the multiferroic effect [53]. The field is in a rapid development due to the implementation of improved deposition techniques such as High Oxygen Pressure Sputter Deposition [54, 55], PLD [56, 57] and Oxygen MBE [58]. Using these techniques, atomically flat surfaces with controlled termination can be created. Several interesting effects can be observed due to the interaction of different properties at the interface as well as additional lattice strain. In fact, superconductivity between insulating layers [59], magnetism between non-magnetic materials [60] or ferromagnetism between antiferromagnetic oxides [61] have all been observed. It is thus of great interest to characterize thin film systems with novel configurations such as BTO/LSMO/STO(111). In this chapter, examples of applications of ferroelectric thin films as well as experiments on complex oxide heterostructures, taken from the literature, are briefly presented.

3.1 Fe-RAM

The idea of using ferroelectric materials as a memory unit was proposed by MIT student Dudley A. Buck in 1952 [62]. A ferroelectric layer is used instead of a dielectric layer to produce NV memory units [5]. Integration of ferroelectric memories into a silicon Complementary Metal-Oxide-Semiconductor (CMOS) was demonstrated in 1987 [63]. Fe-RAM products were mass-produced from 1992. Subsequently, there has been an exponential growth in Fe-RAM capacity, and exponential decrease in CMOS transistor gate length to $0.13 \mu\text{m}$ [63].

Fe-RAM offers the same functionality as conventional flash memory, but has lower power usage and faster write performance as well as a much greater number of write-erase cycles [5, 63, 64]. Today, Fe-RAM is used in various applications such as electronic metering, automotive (e. g. smart air bags), printers, instrumentation, medical equipment, industrial microcontrollers and radio frequency identification [64].

Ferroelectric materials have a nonlinear relationship between the applied electric field and the electric polarization. This relationship comes in the form of a hysteresis loop, as demonstrated in figure 2.10. When the ferroelectric material is exposed to an external electric field, the dipoles align themselves to the field direction. However, even after the field is removed, this state is kept in the material. This means that the memory is NV, because the state is retained even if the electric field is removed. In this way, the polarization state can be used to encode 0 and 1 corresponding to the two possible directions of the polarization, and the memory is kept even when no power is supplied [64]. The very simplified memory cell seen in figure 3.1 consists of a capacitor connected to a plate and a bit line. The orientation of the dipole within the capacitor determines whether a 0 or 1 is stored. The dipole orientation can be set and reversed by applying a voltage across either line [64].

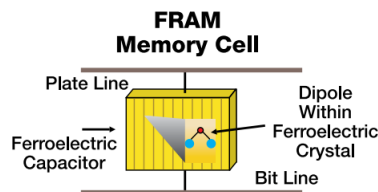


Figure 3.1: Schematic of a ferroelectric RAM cell. From [64].

Commercial Fe-RAM devices have been produced at 350 nm linewidth by Fujitsu and 130 nm linewidth at Texas Instruments, while flash memory is produced using semiconductor linewidths of 16 nm [65, 66]. The reason for having large Fe-RAM linewidths is size limitations such as the fact that materials stop being ferroelectric when they are too small and challenges with leakage currents [5]. However, these problems may be overcome, e. g. by strain engineering ferroelectric thin films utilizing the coupling between strain and ferroelectric phase transitions. Furthermore, due to their high dielectric constants, ferroelectric materials have great potential for reducing the total area of capacitors in memory devices [5].

3.2 Ferroelectric field effect transistors (Fe-FETs)

Fe-FETs are MOSFETs with a ferroelectric gate oxide instead of a dielectric gate oxide. An advantage of this type of cell is that the read operation is non-destructive. The main disadvantage is the fact that the current achievable retention time is very short for use in a NV memory. Even though a lot of research has been done on Fe-FETs with different designs and material combinations, the Fe-FET has not been commercialized [63].

3.3 Ferroelectric thin films in MEMS devices

Miniature systems containing devices or arrays of devices that combine electronics with sensors, transducers and actuators, which are fabricated by integrated circuit batch processing techniques, constitute the domain of Microelectromechanical Systems (MEMS) [67]. After the development of Fe-RAM, it was soon realized that ferroelectric thin films could add functionality in MEMS. A treatment of this topic may be found in [63].

3.4 Magnetoelectric coupling

In [11], a thin film system of $\text{La}_{0.5}\text{Sr}_{0.5}\text{MnO}_3/\text{BaTiO}_3/\text{STO}$ (001) (among other systems) was investigated. The goal was to see whether there is any magnetoelectric coupling at the interface between BTO and LSMO. That is, if there is any coupling between the ferromagnetic and ferroelectric order parameters. It was predicted that strong magnetoelectric coupling should occur near $x = 0.5$ in a LSMO/BTO(001) system in [68]. In that article, it was concluded that the different electron densities that occur as a result of switching the polarization in BTO would determine whether the dominant exchange mechanism in LSMO would be super-exchange or double-exchange. That is to say, the magnetic structure of the LSMO film could be switched from antiferromagnetic (AFM) to ferromagnetic depending on the electrical polarization in the BTO layer. The change in the resistance of such a device as a function of the electric polarization is called the tunneling electro resistance effect (TER). However, magnetoelectric coupling was not observed in [11].

The tunneling magneto resistance effect (TMR) is observed when two ferromagnets are separated by an insulator. There will be a tunneling current between them if their magnetizations are parallel. Whether there is conduction or not then corresponds to a 0 or a 1. The

tunneling current can be turned off by flipping the magnetization in one of the layers so that they become antiparallel using a magnetic field. One of the layers is pinned by an AFM layer. In the next section, two experiments exploiting magnetoelectric coupling at the interface between ferroelectric and ferromagnetic layers to combine the TMR and TER effects in order to create four state NV-RAM devices are discussed.

3.5 Four-state NV-RAM based on a multiferroic tunnel junction

In [69], multiferroic tunnel junctions (MFTJ) were used to create a four-state device by combining the TMR and TER effects. 20 nm LSMO was used as a magnetic layer, followed by 3.2 nm ferroelectric PbTiO₃ (PTO) and finally 40 nm cobalt deposited using RHEED controlled PLD and STO(001) substrates. It was observed that the magnetic anisotropy was dependent on the ferroelectric switching, and further that this anisotropy depends on the polarization sign. Hence, they concluded that the observed TER effect was in fact created by the LSMO/PTO interface. Furthermore, the temperature dependence of these effects was investigated. It was found that the exchange bias is stronger at low temperature and decreases upon heating the junction. Unfortunately, it vanishes at 140 K.

In figure 3.2, a ferromagnetic tunnel junction based on the TMR effect (a), a ferroelectric tunnel junction based on the TER effect (b), and a multiferroic tunnel junction combining the TER effect and the TMR effects (c), can be seen. There are few other ways to combine these properties, the reason being that very few materials have both of these properties at the same time. This is because ferroelectric materials in general require empty d-orbitals, while ferromagnetic materials in general require non-empty d-orbitals [7]. They are thus mutually exclusive, and the solution is to couple these properties at the interface between e. g. BTO and LSMO. However, leakage currents associated with the thin BTO-film is a big challenge [11, 70]. This problem is currently solved by conducting experiments at low temperatures, as in [69].

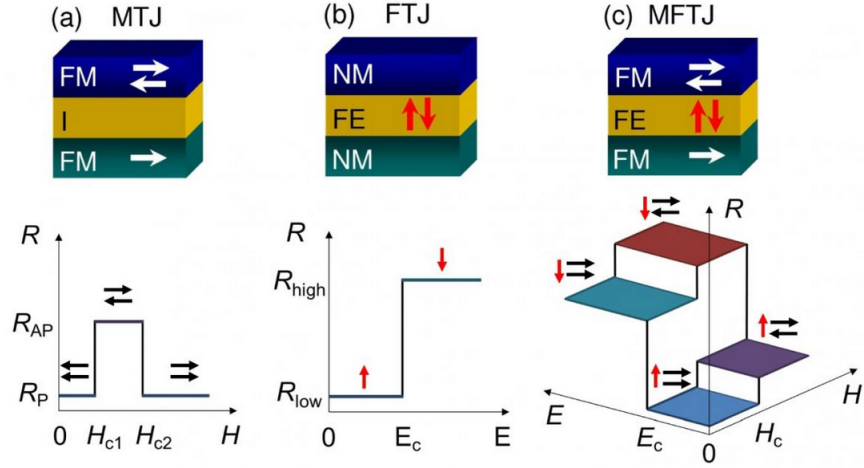


Figure 3.2: **(a)** Magnetic tunnel junction based on the TMR effect. The resistance changes depending on the direction of magnetic polarization, and the two different resistance values correspond to a 0 or a 1. **(b)** Ferroelectric tunnel junction based on the TER effect. The resistance changes depending on the direction of electric polarization, and the two different resistance values correspond to a 0 or a 1. **(c)** MFTJ. The resistance changes depending on the direction of electric and magnetic polarizations, and the four different resistance values correspond to 0, 1, 2 and 3. From [71].

In [70], another four-state NV memory device based on a MFTJ is demonstrated. The system used is a $\text{NiFe}/\text{BaTiO}_3/\text{La}_{0.7}\text{Sr}_{0.3}\text{MnO}_3$ deposited on $\text{STO}(001)$ with good memory characteristics due to a low switching field and larger tunneling magnetoresistance. By combining TER switching with the TMR effect, the device is demonstrated to have four possible states. The resistive change memory due to the ferroelectric switching has an ON/OFF ratio of 16 and the TMR effect is at 0.3 % at 8K. Due to leakage currents, the device must currently be operated at low temperatures.

In figure 3.3 (a) from [70], a resistance-voltage curve demonstrating NV resistance switching is demonstrated. The electroresistance OFF/ON ratio was measured to be 14 at 40 K. A positive pulse voltage is used to make the BTO polarization point toward NiFe, which sets the device in the low resistance state. A negative voltage is applied to drive the polarization to the opposite direction into the high resistance state. The voltage is applied to the bottom LSMO electrode, while the top electrode is grounded. However, due to leakage currents, these measurements had to be done at 40 K. The fact that ten identical hysteresis loops could be produced proves that the system is stable at this temperature.

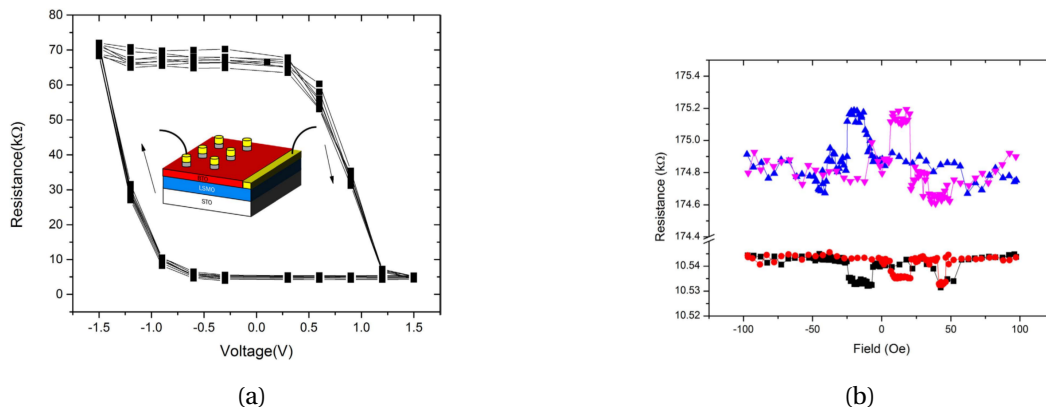


Figure 3.3: **(a)** Stability of OFF/ON electroresistance change in the devices. Resistance-voltage curves obtained at 40 K for 10 cycles shows a stable performance of the device. **(b)** Resistance changes with different magnetic fields at low temperature (8 K), tested on the NiFe/BTO/LSMO structure. From [70].

Finally, figure 3.3 **(b)** demonstrates how the system can combine different magnetic and electric polarizations to create four different states. According to [70], the curve was obtained by placing the NiFe/BTO/LSMO/STO(001) sample in the middle between two current-controlled electromagnets with the magnetic field parallel to the film direction. The purpose of this was to magnetize the LSMO and NiFe films in the same or opposite direction. The ferroelectric barrier is poled either upwards and downwards, while the magnetic field is changed from -100 Oe to 100 Oe. The upward polarization of BTO is drawn with squares, and the downwards with triangles in figure 3.3 **(b)**.

It is concluded in [70] that this MFTJ can produce four resistance states with low energy consumption. The result is reproducible, and was stable during an endurance test with 200 cycles. The results are thus promising for future high-density low power consumption NV-memories. By increasing the number of resistance states, more information can be stored. The biggest challenge that needs to be overcome is the leakage currents that prevent this device from working at room temperature.

3.6 Polar metals

Gauss law prohibits net electric fields from being set up inside a metal due to charge screening. In fact, the Coulomb potential from a point charge inside of a metal is

$$\phi = \frac{q}{4\pi\epsilon_0} e^{-k_s \cdot r},$$

where $\frac{1}{k_s}$ is the Thomas-Fermi screening length, which for example is 0.055 nm for copper [32]. Thus, it seems like an impossible task to create polar metals. However, recent developments, theoretical as well as experimental [12], indicate that this is indeed possible at room temperature in some thin film perovskite systems with a (111) oriented substrate. In [12], ANiO₃ perovskite nicleates are grown by RHEED-PLD on LaAlO₃(111) substrates. A conducting polar monoclinic oxide was achieved by geometrical stabilization of a polar tilt pattern. In order to ensure this result, a system with a conducting chemistry as well as a crystal structure that is insensitive to polar ionic displacements is required. This latter point provides a decoupling between the polar displacement mechanism and the electronic structure at the Fermi level. The article stresses the importance of the stronger substrate constraint of (111) oriented substrates compared to (001) oriented substrates in order to achieve a geometric stabilization of a non-equilibrium octahedral tilt-pattern. The motivation for creating materials systems with properties that traditionally have been considered mutually exclusive, such as polar conductors, is to accelerate the discovery of new types of multifunctional materials that may be used in electronic devices in the future.

Chapter 4

Methods

4.1 Thin film synthesis

The samples used in this work were synthesized by PLD by PhD student Torstein Bolstad at the Oxide Electronics Group at the Department of Electronics and Telecommunication (IET), NTNU. The synthesis of thin films is not the focus in this work, so the details will be omitted. Briefly, in the PLD technique a plasma is generated off a target by exposing it to an intense laser beam in short pulses [56]. The target consists of the same elements as the thin film, and is positioned relatively close to the substrate. The substrate is heated to facilitate diffusion of adatoms before nucleating. The target and the substrate reside in a vacuum chamber where a small amount of gas may be present, such as oxygen. The atoms in this gas will participate in the thin film growth. The growth of the thin film is monitored by RHEED, which is described in e. g. [72].

4.2 TEM Specimen preparation

In order to make the thin film samples electron transparent, mechanical polishing using a tripod polisher combined with PIPS was utilized to prepare PV and CS TEM specimens. These geometries are sketched in figure 4.1. One CS specimen was also made using a FIB. Table 4.1 contains an overview of the TEM specimens that were successfully prepared in this work. Since the specimen is very easily broken at any point during the preparation, especially during the last stages, only one out of four attempts at making specimens were successful. The film name is given by the growers in the Oxide Electronics Lab. The table also indicates specimen geometry and preparation method.

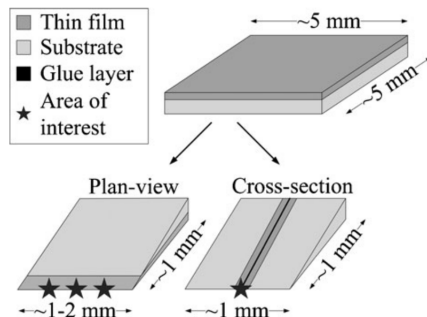


Figure 4.1: Illustration of the PV and CS geometries. The regions of interest (ROIs) are marked with stars. From [73].

Table 4.1: The thin film samples studied along with methods used to prepare TEM specimens from them. Failed or poor TEM specimens are omitted. All substrates are undoped.

Film name	Sample configuration	Geometry, method	Specimen name
P50904	BTO(10nm)/LSMO(10nm)/STO(111)	CS, FIB	10-10-CS
P60211	BTO(3nm)/LSMO(10nm)/STO(111)	CS, Tripod+PIPS	3-10-CS
P60403	BTO(3nm)/LSMO(10nm)/STO(111)	PV, Tripod	3-10-PV

4.2.1 Tripod polishing

The tripod polishing routine is a mechanical method that has shown to be promising for perovskite materials [73]. The tripod preparation process used in this work is similar to the procedure first proposed by Mosen [74].

Figure 4.2 shows the *Allied Multiprep System* used in this work. It provides a precise and reproducible way of preparing TEM specimens. The specimen is mounted on a pyrex stub fastened to a paddle as show in figure 4.2 (a). Then, the paddle is mounted on the arm of the system, which may be gradually lowered down on the rotating plate below, as shown in figure 4.2 (b). Different polishing media may be attached to the platen below the arm. Here, diamond lapping films (DLF) with different sizes of the diamond grains ($15\ \mu\text{m}$, $6\ \mu\text{m}$, $3\ \mu\text{m}$, $1\ \mu\text{m}$, $0.5\ \mu\text{m}$ and $0.1\ \mu\text{m}$) are used successively. A precise pressure may be applied by the arm. Furthermore, the rotation speed of the platen may also be specified. Finally, the orientation of the pyrex relative to the platen may be adjusted by two micrometer screws on the arm. A micrometer dial is used to monitor the amount of material removed *in situ*. The arm can be laterally moved by the system automatically in order to utilize more of the DLF and at the same time to reduce the probability of dislodged material to ruin the specimen. Continuous rinsing of the polishing media with water is possible through a flexible water tap, which reduces frictional heating as well as any chances of debris damaging the specimen.

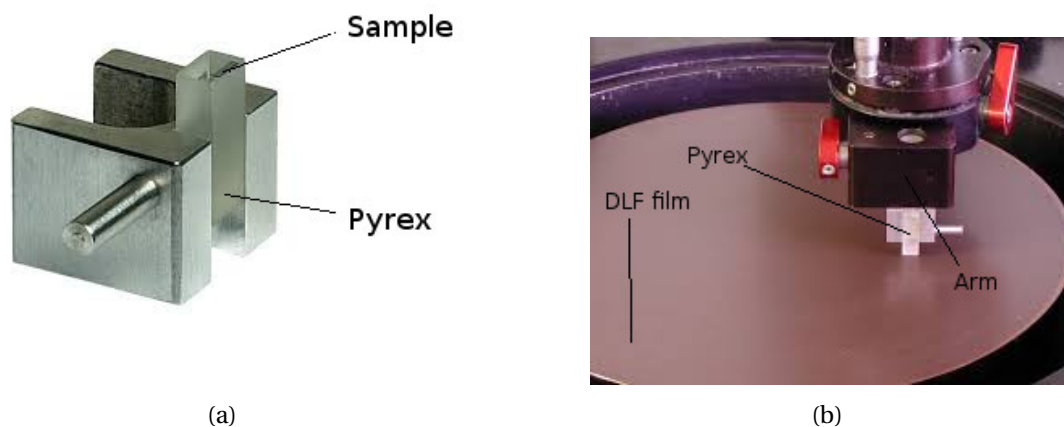


Figure 4.2: *Allied Multiprep System*, used to prepare TEM specimens. In (a), a paddle with a pyrex stub with a specimen on it is shown. In (b), the pyrex foot has been mounted on the arm with the DLF plate below.

4.2.2 Preparing plan-view specimens using a tripod polisher

First, the thin film sample was cut into small rectangular pieces with dimensions of approximately $1.5 \cdot 1 \text{ mm}^2$. A *Testbourne Model 60 Low Speed Diamond Wheel Saw* with an *Allied Wafering Blade* of thickness $150 \mu\text{m}$ was used. The pyrex stub was polished down $75 \mu\text{m}$ with a $6 \mu\text{m}$ DLF film, a 500 g load, a 50 rounds per minute (RPM) rotation speed, an oscillation speed of 2 and with a tilt of 0° . Then, the specimen was fastened to the pyrex stub using acetone soluble *Loctite Super Glue Precision* with the film side facing the pyrex. The tilt of the specimen was adjusted 4° relative to the pyrex. The load was changed to 200g , the rotation speed to 30 RPM and the oscillation speed to 1 . The substrate side of the specimen was then polished with a $15 \mu\text{m}$ DLF until the thickness of the specimen was $250 \mu\text{m}$. $6 \mu\text{m}$ DLF was used to polish the thickness down to $150 \mu\text{m}$ and $3 \mu\text{m}$ DLF to polish it down to $60 \mu\text{m}$. At this point, *Allied Green Lube Polishing lubricant* was deposited on the rotating plate and the load was changed to 0 g . A $1 \mu\text{m}$ DLF was used to polish the specimen until the polishing edge reached the ROI. Then, a $0.5 \mu\text{m}$ DLF was used for 15 seconds followed by a $0.1 \mu\text{m}$ DLF for 15 seconds. Between each step, the height and quality of the specimen were monitored in an optical microscope. Finally, a filth cloth was placed on top of the rotating platen and stained with *Allied $0.02 \mu\text{m}$ colloidal silica suspension*. The specimen was then polished for another 15 seconds. This resulted in making the edge even smoother and more pronounced. The colloidal silica particles were quickly removed using cotton sinks soaked in *Allied Micro Organic Soap* diluted to 2% in deionized (DI) water, and thoroughly rinsed

in DI water. Finally, a *Lift-out OMINI GRIDS 3-Post Shallow Downset Copper* TEM specimen holder was attached to the substrate side of the specimen with acetone resistant *Araldite epoxy glue*. The pyrex stub was then placed into an acetone solution to release the specimen and TEM-holder from the pyrex. It was also rinsed in ethanol. The end result can be seen in figure 4.3.

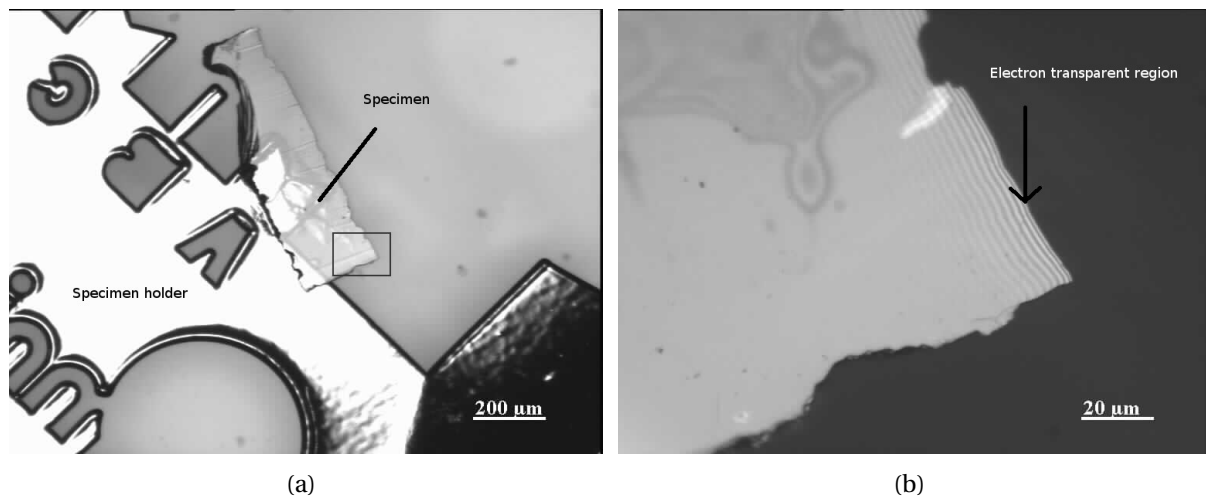


Figure 4.3: **(a)** Finished 3-10-PV specimen prepared from the P60403 thin film system mounted on a *Lift-out OMINI GRIDS 3-Post Shallow Downset Copper* TEM specimen holder. **(b)** Zoom-in on the region marked by a black square in **(a)**. Thickness fringes are clearly visible in the electron transparent region.

4.2.3 Preparing cross-sectional specimens using a tripod polisher and PIPS

In order to prepare CS specimens from the P60211 thin film system, a mechanical polishing procedure was followed. First, a 380 μm thick Si-wafer, polished on one side, was cut into rectangular pieces with width 1 mm and length 3 mm. Next, two rectangular strips were cut off the thin film system along $[1\bar{1}0]_c$. The thickness of the substrate plus thin films was measured to be about 0.5 mm. Each rectangular piece was 3 mm long and 1 mm wide. A *Testbourne Model 60 Low Speed Diamond Wheel Saw* with an *Allied Wafering Blade* of thickness 150 μm was used to cut the Si wafer and the thin film system, and care was taken to compensate for the saw-blade thickness in order to be able to prepare pieces of matching geometry.

The next step was to glue the two rectangular pieces from the Si-wafer and the two rectangular pieces from the thin film system into a sandwich using acetone resistant *Epoxy Bond 110 2-Part Adhesive* glue. Two components of the glue must be mixed together in a precise ratio of 1 part dark glue + 10 parts light glue, by weight. The polished sides of the Si-

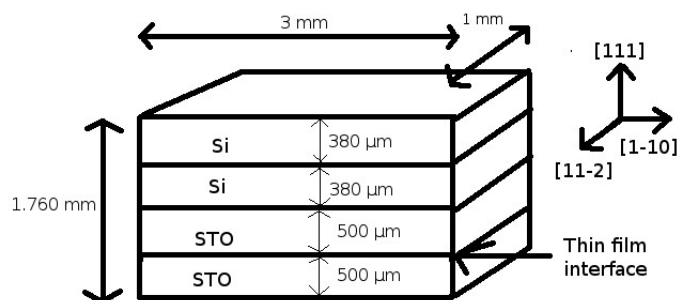


Figure 4.4: The specimen geometry after gluing the Si and thin film pieces together.

wafers were glued together, and the unpolished side of one Si-wafer was glued to STO. The geometry of the specimen at this point was 3 mm x 1 mm x 1.760 mm, and its configuration was as shown in figure 4.4.

The glue layer between the pieces must be very thin in order to make the specimen useful for observation in the TEM. This is achieved by putting the sandwich in a clamp holder, consisting of two steel plates connected by two screws. The plates and the screws have different thermal expansion coefficients, which leads to compression of the sandwich when heated. Thus, excess glue is pushed out and the glue layer becomes very thin. Two pieces of glass were cut out and applied on each side of the specimen to stabilize it and prevent any sliding during the compression. A piece of tape was placed under and over the specimen to protect it from direct contact with the clamp holder to reduce the probability of fracture in the specimen. Care was taken to make sure all layers were in contact with each other and that none of the layers were resting on the glass plates. The clamp was then placed on a hot plate at ~ 150 °C for ~ 5 minutes. The heat also causes the two components of the glue to react and the glue to harden.

After the heating process, the specimen was removed from the clamp holder and glass support. Mechanical polishing had to be utilized to fully free the specimen from the glass slides because some acetone resistant glue made it stick to the glass support. After the specimen was free, it was glued to a polished pyrex foot using acetone soluble *Loctite Precision Super Glue*. Next, it was left for 2 hours in order for the glue to harden completely.

It was then polished at zero tilt in the *Allied Multiprep System* using the polishing procedure outlined in subsection 4.2.2. However, a 0 g load was used during all the steps because the specimen is very fragile. The purpose of this first polishing step was to make the surface

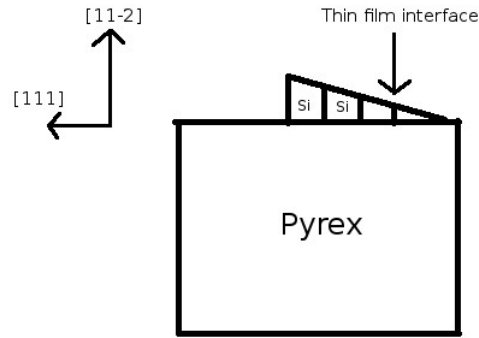


Figure 4.5: The specimen mounted on the pyrex foot. In this sketch, the polishing procedure with a 4° tilt has been initiated. Note that the specimen eventually will be electron transparent at the thin film interface as the polishing continues.

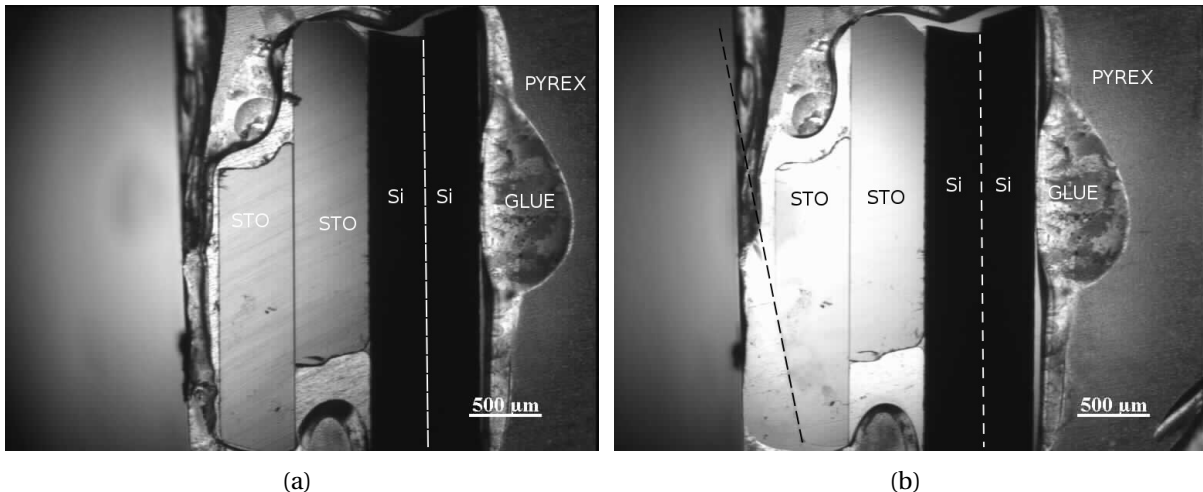


Figure 4.6: **(a)** The 3-10-CS specimen after polishing the second side with $3 \mu\text{m}$ DLF. The two Si-pieces can be seen on the right (dark pieces) while the two thin film pieces can be seen on the left (bright pieces). **(b)** The 3-10-CS specimen after polishing the second side with the $1 \mu\text{m}$ DLF. As can be seen, there is an angle between the polishing edge on the STO piece to the left, marked with a black dashed line, and the thin film interface. In both of these figures the $[11\bar{2}]_c$ direction is out of the plane of the figure.

of the specimen smooth and even.

Next, the specimen was freed from the pyrex by using acetone and then a quick rinse in ethanol. Then, it was re-attached to the pyrex with the polished side facing down and the glue was left to harden for 2 hours. The tilt of the pyrex was changed to 4 degrees. The specimen was then polished in the *Allied Multiprep System* using the polishing procedure outlined in subsection 4.2.2, but with a 0 g load. In figure 4.5, the specimen mounted on the wafer after some polishing steps is sketched. Note that as the polishing continues, the

specimen will eventually be electron transparent at the thin film interface. In figures 4.6, the condition of the specimen before the polishing edge reached the thin film interface can be seen. In figures 4.7, the condition of the specimen upon reaching the ROI can be seen. Interference fringes are visible, which indicates that the specimen is thin at the edge. Finally, the specimen is freed from the pyrex foot in acetone and rinsed in ethanol. No TEM-grid is used. Instead, the Si-end of the specimen is used as a support.

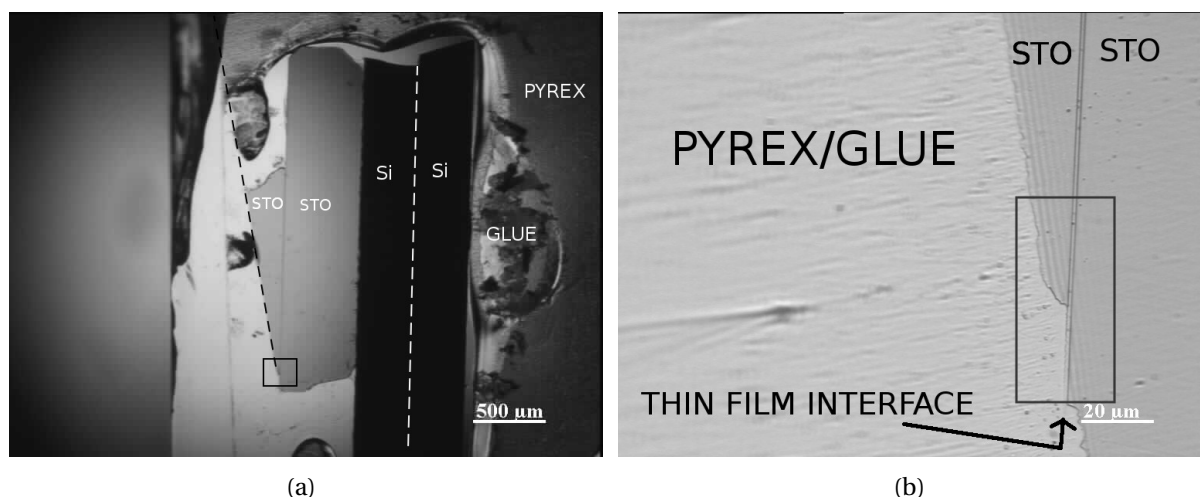


Figure 4.7: **(a)** 3-10-CS specimen after polishing the second side with the $0.5 \mu\text{m}$ DLF. The polishing edge, marked with a black dashed line, can be seen as it approaches the thin film interface. **(b)** 3-10-CS specimen zoomed in on the black square in **(a)**, after polishing the second side with a 4° tilt with $0.1 \mu\text{m}$ DLF. Note that the thin film is still intact on the entire even surface, giving a large ROI marked with a black rectangle. Unfortunately, this piece broke off, making a PIPS treatment necessary.

After an investigation in the TEM, it was clear that the specimen was still too thick in the ROI. This problem arose because the thinnest part, the even surface seen below the polishing edge in figure 4.7, broke off, as can be seen in figure 4.8. Therefore, an ion milling procedure was performed in a liquid nitrogen cooled *Model 695 Precision Ion Polishing System* (PIPS). In short, the specimen is then bombarded with a beam of argon ions, which mills it down to the desired thickness. The specimen is shown before and after milling in figure 4.8. First, the specimen was bombarded for one hour with 2 kV argon ions incident at 4 degrees, followed by one hour of bombardment with 1 kV argon ions incident at 4 degrees. As the specimen got thinner, the energy of the bombarding ions was reduced to 0.3 kV, then 0.2 kV and finally 0.1 kV for one minute each and in these last three steps with an angle of incidence of 8 degrees. Note that the nitrogen cooling and the low angle/ low-energy milling at the end of the milling were performed to minimize ion beam damage.

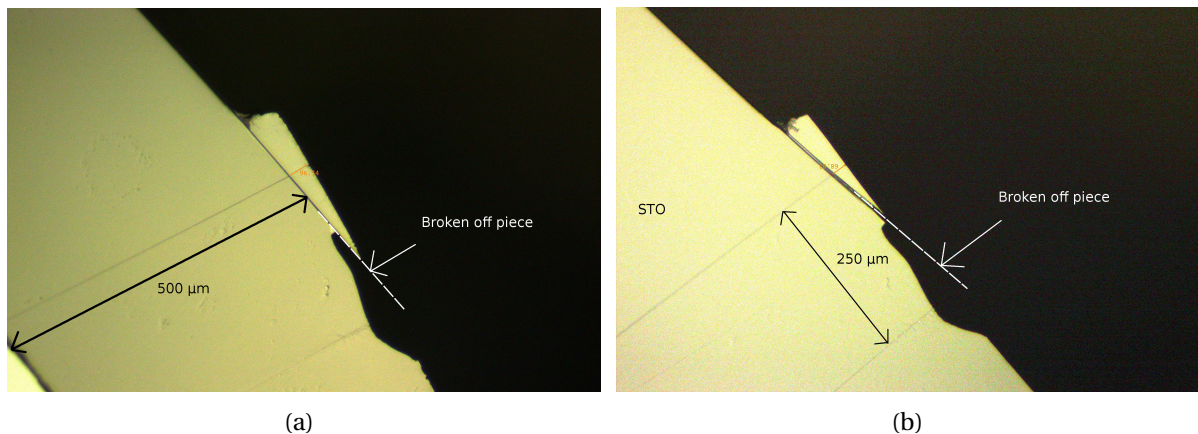


Figure 4.8: **(a)** The specimen mounted in the PIPS system before ion polishing. **(b)** The specimen after ion polishing. The scale in the images is indicated by the black double-arrows. The white dashed line indicates the location of the even surface in figure 4.7 (b), which is broken off. The specimens produced using tripod polishing are very fragile, and they must be handled with great care.

4.2.4 Preparing a cross-sectional specimen using FIB

A FEI Helios NanoLab DualBeam FIB at NTNU NanoLab was used to prepare the 10-10-CS specimen from the P50904 thin film system, using a standard lift-out technique. The FIB is an advanced instrument, and much training and experience is needed to use it properly. For this reason the specimen preparation in the FIB was done by Associate Professor II Per Erik Vullum. The details of this instrument is not the focus of this work, but some important details will be given.

Prior to the FIB preparation, a 40 nm thick Pt/Pd (80/20) (80 % Pt and 20 % Pd) layer was sputter coated on top of the sample to avoid sample charging during e-beam imaging, ion-beam imaging and sputtering. An additional ~ 200 nm thick protection layer of Pt was deposited by in-situ e-beam assisted deposition to avoid possible ion-beam damage in the thin films. A final ~ 2 μm thick protection layer of C was deposited by in-situ ion-beam assisted deposition. The coarse Ga⁺ ion-beam thinning was done at 30 kV acceleration voltage with a progressively finer beam, finishing with a 90 pA beam current. The sputtering angles, i.e. the angle between the ion-beam and the TEM specimen surface, were 2 degrees on either side of the sample. Final thinning was performed with 5 and 2 kV ion-beam acceleration voltages at 4 degrees angles between the ion-beam and the TEM specimen surfaces to minimize ion-beam damage.

4.3 TEM methods

The 3-10-PV and 3-10-CS specimens were characterized using a cold-FEG *Jeol-Jem 2100F* at 200 kV. HR-TEM images, BF-TEM images, EDS and SPED data were collected. To collect EDS data, an *Oxford Instruments INCA EDS* system was utilized. The *NanoMegas Digistar P1000* system combined with the *Gatan Digiscan II Model 768* and an *Allied Stingray 046B ASG* camera at the *Jeol-Jem 2100F* at 200 kV were used to collect SPED data using the parameters in table 4.2. SPED data was also collected from the 10-10-CS specimen.

To characterize the 10-10-CS specimen, a double corrected cold-FEG *Jeol-Jem ARM 200F* was utilized at 200 kV by Associate Professor II Per Erik Vullum. HR-TEM images, STEM-EELS and HAADF-STEM data were gathered. HAADF-STEM image stacks were collected using the parameters in table 4.3. The HAADF-STEM image stacks were first processed in the SmartAlign software [75]. This software aligns all the images in the stack to compensate for drift and reduce noise and then creates an average image. This is important, because a typical HAADF-STEM image stack has an acquisition time of about 40 seconds. During that time period, there can be a significant specimen drift and interference with the 50 Hz signal and its overtones from the power grid. The images were subsequently analyzed in the GPA software of Digital Micrograph [76].

Table 4.2: Parameters used for the SPED scans. The precession angle ϕ was 0.7° and the spot size was 0.5 nm for all the scans.

Sample	Figure	Area size	Step size	Dwell time	Convergence semi-angle	Camera length	Zone-axis
3-10-CS	5.23	256x128 nm ²	1.28 nm	40 ms	1.49 mrad	30 cm	[11 $\bar{2}$] _c
3-10-PV	5.19	768 nm ²	1.28 nm	20 ms	1.88 mrad	30 cm	[111] _c
10-10-CS	5.34, 5.35	128·44.8 nm ²	0.64 nm	40 ms	1.49 mrad	40 cm	[11 $\bar{2}$] _c
3-10-CS	5.37	128x64 nm ²	1.28 nm	40 ms	1.49 mrad	30 cm	[1 $\bar{1}$ 0] _c

Table 4.3: Parameters used for the HAADF image stack collection. The camera length was 1.5 cm, the dwell time 1.4 μ s, the inner collection angle 118 mrad and the outer collection angle 471 mrad for all the image stacks.

Image stack	Number of frames	Magnification	Zone-axis
5.9	25	10M	[1 $\bar{1}$ 0] _c
5.12	23	6M	[11 $\bar{2}$] _c
C.1	24	6M	[11 $\bar{2}$] _c
C.4	23	8M	[11 $\bar{2}$] _c
C.7	20	8M	[11 $\bar{2}$] _c

For the GPA analysis, the $(110)_c$ and $(001)_c$ reflections were chosen in the $[1\bar{1}0]_c$ zone-axis, while the $(111)_c$ and $(1\bar{1}0)_c$ reflections were chosen in the $[11\bar{2}]_c$ zone-axis. A cosine mask giving a spatial resolution of 0.592 nanometers was used, and the binning was set to 1. STO was used as a reference. The HAADF-STEM image stacks were also processed in the Ranger software [77], which fits Gaussians to the atomic columns.

STEM-EELS scans along the $[11\bar{2}]_c$ zone-axis were performed on the 10-10-CS specimen on the *Jeol-Jem ARM 200F. A Quantum GIF ER* with DualEELS was utilized to collect low-loss and high-loss spectra simultaneously. The parameters in table 4.4 were used.

Table 4.4: Parameters used for the STEM-EELS scans along the $[11\bar{2}]_c$ zone-axis on the 10-10-CS specimen. Map 3 had a pixel time of 50 ms while the other maps had a pixel time of 100 ms.

Convergence semi-angle	Collection Angle	Voltage	Camera length	Current
27.42 mrad	66.86 mrad	200 kV	1.5 cm	140 pA

4.4 SADP simulations of ferroelastic domains in LSMO

Using the bulk crystal data given in subsection 4.4.1, simulations of SADPs from a BTO, LSMO and STO in the $[11\bar{2}]_c$ and $[1\bar{1}0]_c$ zone-axes were performed for domain states LSMO- R_1 , LSMO- R_2 , LSMO- R_3 and LSMO- R_4 . The unit cell of BTO was kept static in these simulations.

4.4.1 Crystal structures

STO

STO belongs to the cubic crystal system and has space group $Pm\bar{3}m$ (221) in bulk at room temperature, as listed in table 4.5 [78, 79].

Table 4.5: Atomic coordinates in STO [78, 79]. STO has space group $Pm\bar{3}m$ (221), lattice parameter $a = 3.905 \text{ \AA}$ and angles $\alpha = \beta = \gamma = 90^\circ$.

Site	Element	X	Y	Z	Occupation
Sr	Sr	0	0	0	1
Ti	Ti	$\frac{1}{2}$	$\frac{1}{2}$	$\frac{1}{2}$	1
O	O	0	$\frac{1}{2}$	$\frac{1}{2}$	1

BTO

BTO belongs to the tetragonal crystal system and has space group P4mm (99) in bulk at room temperature, as listed in table 4.6 [80, 81].

Table 4.6: Atomic coordinates in BTO [80, 81]. BTO has space group P4mm (99), lattice parameters $a = b = 3.992 \text{ \AA}$ and $c = 4.036 \text{ \AA}$ and angles $\alpha = \beta = \gamma = 90^\circ$.

Site	Element	X	Y	Z	Occupation
Ba	Ba	0	0	0	1
Ti	Ti	$\frac{1}{2}$	$\frac{1}{2}$	0.518(2)	1
O1	O	$\frac{1}{2}$	$\frac{1}{2}$	0	1
O2	O	$\frac{1}{2}$	0	$\frac{1}{2}$	1

LSMO

LSMO belongs to the trigonal crystal system and has space group $R\bar{3}c$ (167) in bulk at room temperature, as listed in table 4.7 [82, 83]. It belongs to the rhombohedral lattice system with hexagonal axes.

Table 4.7: Atomic coordinates in LSMO [82, 83]. LSMO has space group $R\bar{3}c$ (167) in bulk form, lattice parameters $a = b = 5.503 \text{ \AA}$ and $c = 13.319 \text{ \AA}$ and angles $\alpha = \beta = 90^\circ$ and $\gamma = 120^\circ$.

Site	Element	X	Y	Z	Occupation
O1	O	0.454	0	$\frac{1}{4}$	1
Mn1	Mn	0	0	0	1
M1	0.700La + 0.300Sr	0	0	$\frac{1}{4}$	1

4.4.2 Simulation in E-MAPS

The online E-MAPS program [84] was used to simulate STO, LSMO and BTO along the $[1\bar{1}0]_c$ and $[11\bar{2}]_c$ zone-axes. In LSMO, the corresponding zone-axes for the different domains derived in equations (2.75)-(2.82) were used. For each domain, the SADPs from STO, BTO and LSMO were stacked together in an RGB image using ImageJ [85]. As can be seen in figures 4.9 and 4.10, the SADPs from the different domains have different super-reflections. By comparing experimental diffraction patterns to these simulated diffraction patterns, it is therefore possible to answer the following questions.

1. Are the thin films distorted from their bulk structure?
2. Which LSMO-domains are present in the thin film system?

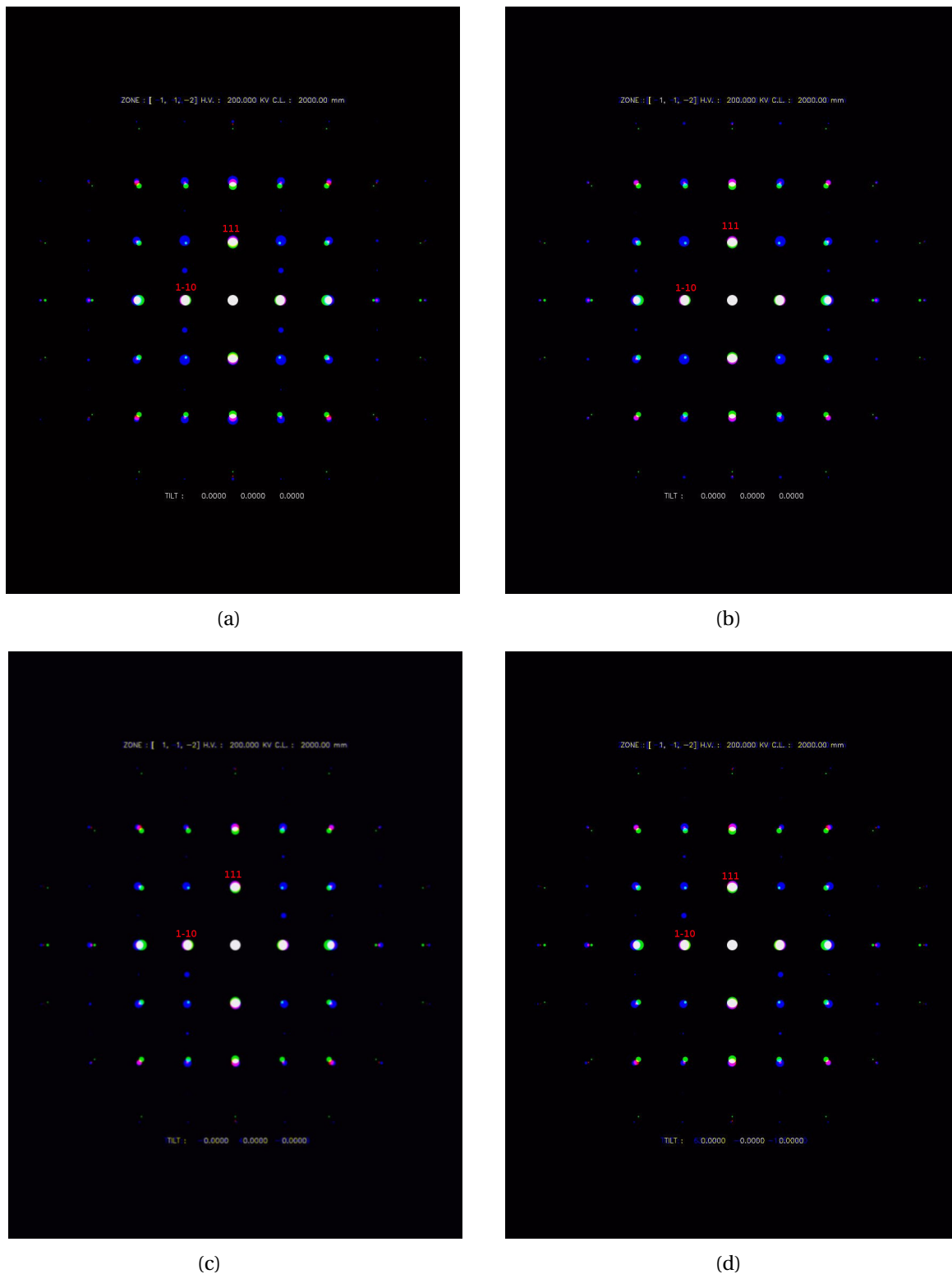


Figure 4.9: $[11\bar{2}]_c$ zone-axis diffraction patterns of STO, BTO and LSMO stacked together in an RGB image using ImageJ. Blue is LSMO, green is BTO and red is STO. White is complete overlap, and other colors mean some mixture of STO, LSMO or BTO. The different domains in LSMO are illustrated. (a) LSMO- R_1 , (b) LSMO- R_2 , (c) LSMO- R_3 and (d) LSMO- R_4 . The reflections are indexed in cubic coordinates in red. Note that the crystals were simulated as if they were in bulk. This simulation also ignores dynamical effects. Hence, the experimental diffraction patterns are expected to deviate from the simulated ones. Nevertheless, these ideal diffraction patterns are useful references. Deviations from these reveal strain effects, reduction in symmetry of the unit cells, dynamic effects and other non-idealities.

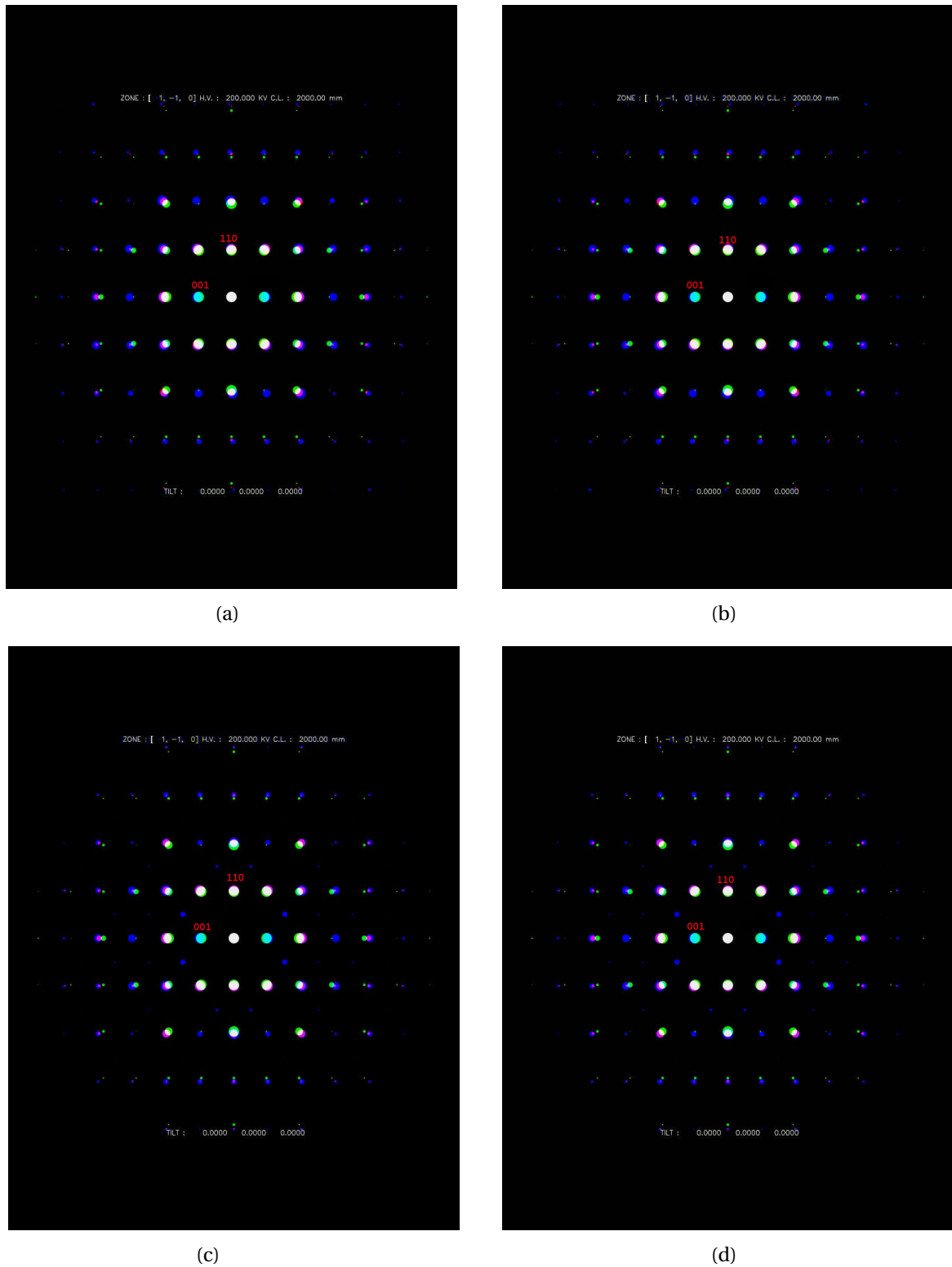


Figure 4.10: $[1\bar{1}0]_c$ zone-axis diffraction patterns of STO, BTO and LSMO stacked together in an RGB image using imageJ. Blue is LSMO, green is BTO and red is STO. White is complete overlap, and other colors mean some mixture of STO, LSMO or BTO. The different domains in LSMO are illustrated. (a) LSMO- R_1 , (b) LSMO- R_2 , (c) LSMO- R_3 and (d) LSMO- R_4 . The reflections are indexed in cubic coordinates in red. Note that the crystals were simulated as if they were in bulk. This simulation also ignores dynamical effects. Hence, the experimental diffraction patterns are expected to deviate from the simulated ones. Nevertheless, these ideal diffraction patterns are useful references. Deviations from these reveal strain effects, reduction in symmetry of the unit cells, dynamic effects and other non-idealities.

4.5 SADP simulations of ferroelectric domains in BTO

A simulation of SADPs of BTO/STO(111) with three different orientations of the BTO unit cell relative to the STO(111)-substrate was performed in CrystalKit [86]. That is to say, the crystal axes of BTO and STO are always parallel, but c_{BTO} can take on three different orientations. The interface between STO and BTO is specified to be $(111)_c$. After simulating these three different orientations of the BTO unit cell, the three resulting SADPs were stacked together in a RGB image using ImageJ. The simulation was performed along the $[111]_c$, $[11\bar{2}]_c$ and $[1\bar{1}0]_c$ zone-axes.

In figure 4.11, a very small split of the reflections from the different BTO domains can be observed. The simulation is consistent with the theoretically derived diffraction pattern in figure 2.14. Similar results were obtained for simulations along the $[1\bar{1}0]_c$ and $[11\bar{2}]_c$ zone-axes, as shown in figures 4.12 and 4.13, respectively. Hence, it is very challenging to resolve the ferroelectric domain structure by using diffraction contrast techniques such as ASTAR. Firstly, a very high resolution is needed in the diffraction patterns to separate the reflections due to different domains. Secondly, imperfections in the lattice such as dislocations may cause local strain variations that are larger than the variation due to a ferroelectric domain structure.

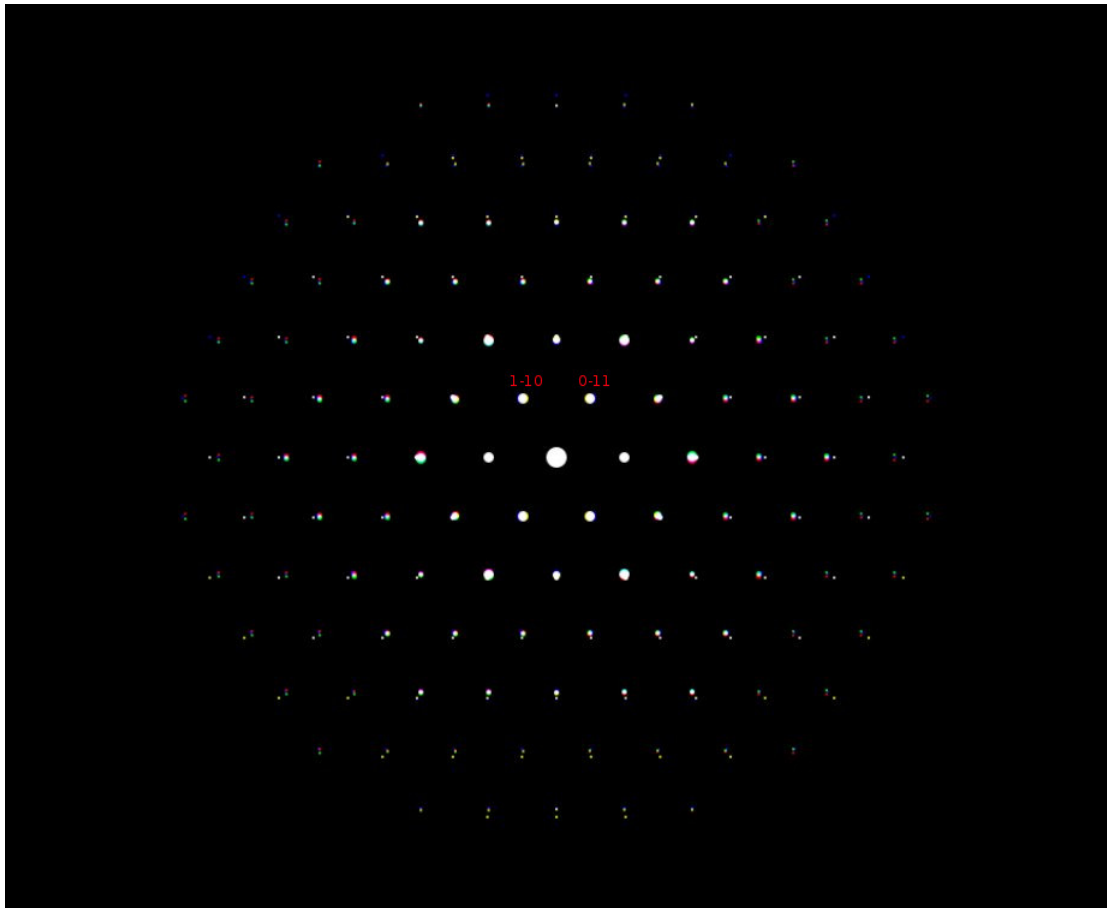


Figure 4.11: $[111]_c$ zone-axis CrystalKit simulation of SADP from BTO/STO(111) with three different orientations of the BTO unit cell present. After simulating the three different orientations of the BTO unit cell, the three resulting SADPs were stacked together in a RGB image using ImageJ. The three BTO domains are thus represented by blue, red and green, and other colors means some mixture of these. The reflections are indexed in cubic coordinates in red. A small separation of the BTO reflections can be seen.

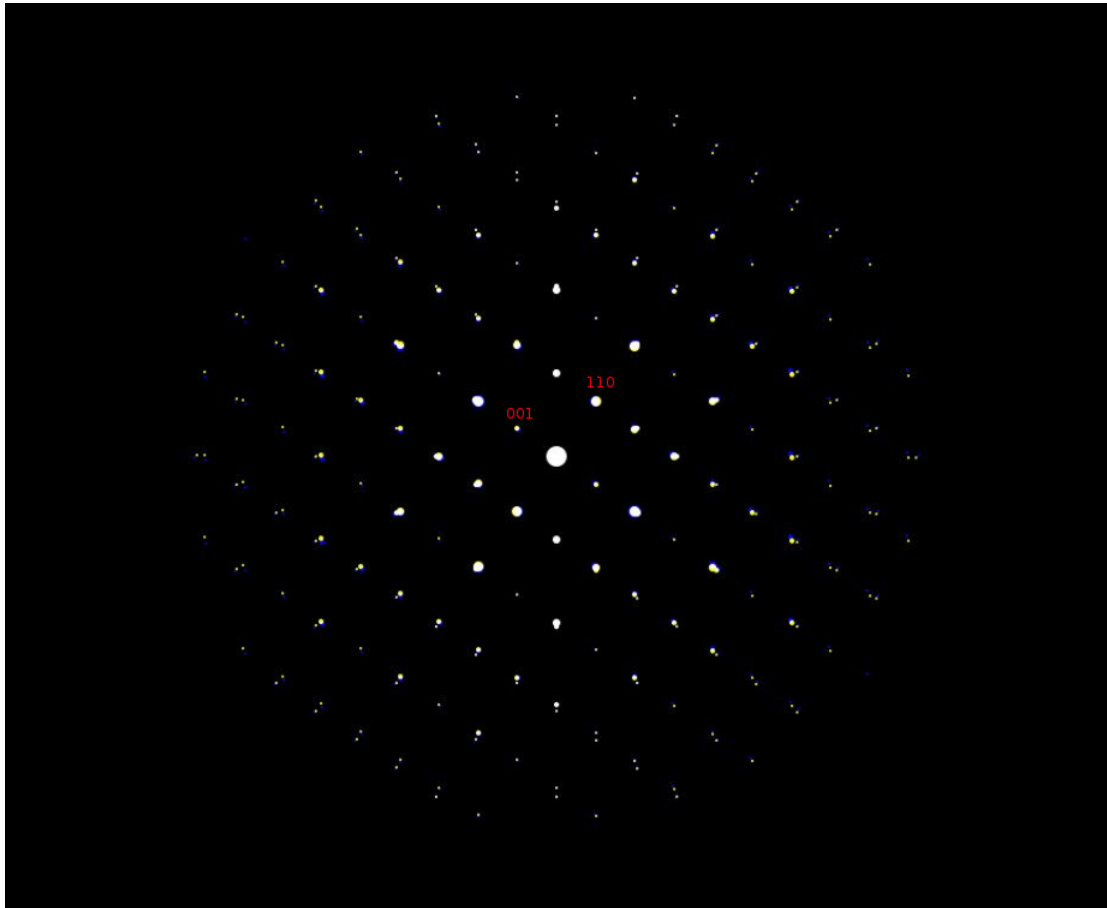


Figure 4.12: $[1\bar{1}0]_c$ zone-axis CrystalKit simulation of SADP from BTO/STO(111) with three different orientations of the BTO unit cell present. After simulating the three different orientations of the BTO unit cell, the three resulting SADPs were stacked together in a RGB image using ImageJ. The three BTO domains are represented by blue, red and green, and other colors means some mixture of these. The reflections are indexed in cubic coordinates in red. A separation of the reflections from the blue domain can be seen. The green and red domains overlap, giving a yellow color.

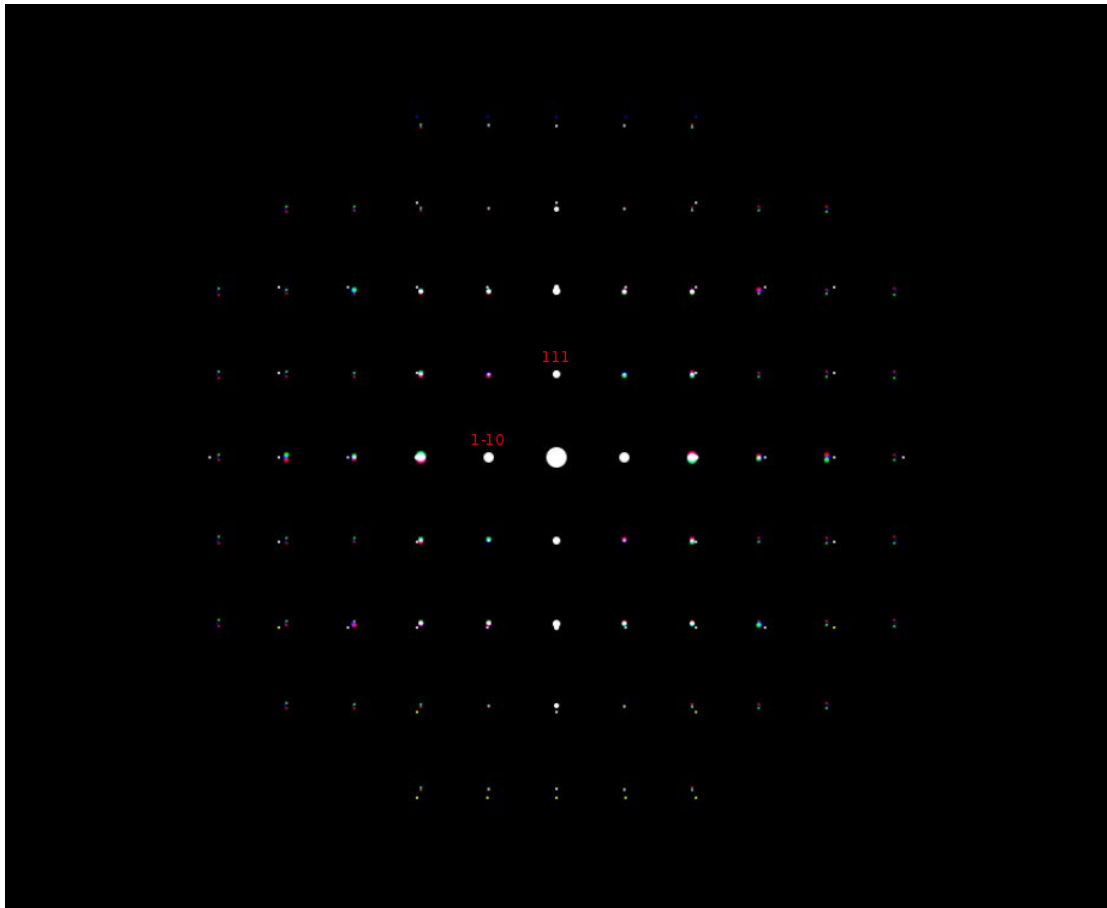


Figure 4.13: $[11\bar{2}]_c$ zone-axis CrystalKit simulation of SADP from BTO/STO(111) with three different orientations of the BTO unit cell present. After simulating the three different orientations of the BTO unit cell, the three resulting SADPs were stacked together in a RGB image using ImageJ. The three BTO domains are represented by blue, red and green, and other colors means some mixture of these. The reflections are indexed in cubic coordinates in red. A small separation of the BTO reflections can be seen.

4.6 HyperSpy Analysis

The HyperSpy software package [87] was used to analyze the EELS spectra acquired. The direction parallel to the film was integrated out to reduce noise. The EELS low-loss signals was convolved with the high-loss spectra to remove plural scattering. Hartree-Slater cross-sections were used to subtract the continuum background for the O-K and Mn-L peaks. PCA was used to reduce noise.

Two quantities were measured as a function of distance normal to the thin film interface. First, the ratio of the intensities of the Mn L_2 and L_3 edges, $R_{Mn} = \frac{I_{L_3}}{I_{L_2}}$. A customized script created by Magnus Nord, listed in Appendix A, was used for this. The script fits two Gaussians to these peaks and estimates the ratio of their intensity. This ratio gives an indication of the Mn oxidation state: a high ratio indicates a low Mn-oxidation state [88, 89, 90]. Using Gaussian fits to these edges is conventional [7]. The intensity can also be found by integrating in a window around the edge [89, 91]. The Gaussian components in HyperSpy are defined by [92]

$$f(x) = \frac{a}{\sqrt{2\pi c^2}} e^{-\frac{(x-b)^2}{2c^2}}, \quad (4.1)$$

where a , b and c are parameters in a Gaussian fit. The intensity of a given peak is equal to the area under the Gaussian,

$$I = \int_{x_1}^{x_2} \frac{a}{\sqrt{2\pi c^2}} e^{-\frac{(x-b)^2}{2c^2}} dx, \quad (4.2)$$

where x_1 and x_2 are appropriate limits for the peak. The a -parameter is used for the intensity. This is equivalent to choosing $x_1 = -\infty$ and $x_2 = \infty$, because

$$\int_{-\infty}^{\infty} \frac{a}{\sqrt{2\pi c^2}} e^{-\frac{(x-b)^2}{2c^2}} dx = a. \quad (4.3)$$

The ratio of the intensities may then be used to compute the Mn oxidation state. The transition metal L edges are caused by transitions to empty bound states or the continuum, and show two characteristic white lines due to transitions from $2p_{3/2}$ and $2p_{1/2}$ up to the $3d$ band. The ratio of these two lines, $\frac{I_{L_3}}{I_{L_2}}$, also known as the “white-line ratio”, should be 2 on the basis of the $2j + 1$ degeneracy [89]. However, deviations from this value frequently occurs [93, 94], and as mentioned above, the white-line-ratio depends on the oxidation state of the transition metal. In fact, a relation may be found for many transition metals. This method is called the “White-line ratio” method. In [91], the following relation was obtained from a fit

to the experimental data

$$V_{Mn} = 0.8311 \cdot \ln \left[\frac{24.9}{R_{Mn} - 1.648} \right], \quad (4.4)$$

where R_{Mn} is the white-line ratio and V_{Mn} is the Mn oxidation state.

Transition metals are capable of adopting a wide varieties of oxidation states. It is therefore important to be able to measure the Mn oxidation state, because different oxidation states leads to widely differing chemical and physical properties of the TM complex oxides [89, 95, 96, 97]. In [91], Hartree-Slater cross-sections were used to subtract the continuum background, as in this work. Furthermore, STEM-EELS data were collected, as in this work. However, a different microscope (*JEOL 300F*) was used at 300 kV instead of 200 kV. The collection angle was 1.1 mrad and the convergence angle was 0.85 mrad, quite different from the ones used here, see table 4.4. In addition, this ratio may depend on sample thickness. Furthermore, since (4.4) is a nonlinear equation, special care has to be taken for mixed valence compounds, such as LSMO. In fact, (4.4) will not lead to a correct average valence. In conclusion, equation (4.4) must be used with care, as it depends sensitively on experimental parameters and because it does not give a precise answer for mixed valence compounds [91]. It should only be used as a very coarse estimate.

The second quantity that was measured from the EELS spectra was the normalized intensity of the O-K A prepeak. The O-K peak is known to consist of three subpeaks A, B and C from lower to higher energy in bulk LSMO as well as in STO and BTO. A broadening of peak B combined with a weakening of peaks A and C has been correlated with oxygen vacancies [98]. The reason for this is that prepeak A is caused by a covalent interaction between O 2p and Mn 3d states in LSMO perovskite structures [88, 89]. It is also known to be sensitive to the Mn oxidation state [88]. This is because the bond between Mn and O becomes more ionic as the Mn oxidation state is decreased. Hence, the interaction between their orbitals decreases. It should be noted that this method is qualitative, because it is problematic to directly compare the O-K A prepeak of different materials such as STO, LSMO and BTO. This is because these peaks are different in these materials, even when they are stoichiometric. However, they all share the property that the prepeak A disappears when the oxygen vacancy concentration is very high. The integrated intensity of the prepeak A normalized over the total O-K intensity was therefore used as a measure of oxygen content, as in [88]. This is also implemented in the code in Appendix A.

Chapter 5

Results and discussion

In this chapter, experimental results are presented, analyzed and discussed. In total, three thin film systems were investigated, listed in table 4.1. One TEM specimen from each was studied.

5.1 Crystal structures

In figures 5.1 (a) and (c), BF-TEM images taken along the $[11\bar{2}]_c$ zone-axis from the 10-10-CS specimen using the *Jeol-Jem ARM 200F* and their corresponding FFTs in 5.1 (b) and (d) are presented, respectively. Two different types of regions are observed in the two images. That these regions are different is seen more clearly in the corresponding FFTs, where two different types of super-reflections can be seen. The super-reflections seen in figure 5.1 (b) are not present in any of the simulated diffraction patterns in figure 4.9, where the bulk spacegroup of LSMO, $R\bar{3}c$ (167), was assumed.

The super-reflections in figure 5.1 (b), not seen in the simulations, may be caused by a distortion of the crystal structure of LSMO relative to its bulk structure due to strain effects in the thin film. LSMO is subjected to a tensile strain when deposited on STO(111), because the pseudo-cubic lattice parameters of bulk LSMO is smaller than the lattice parameter of STO [38]. In studies of perovskite thin films deposited on (111) oriented perovskite substrates [12], as well as studies of LSMO/STO(001) [39, 40] and a study of $\text{La}_{0.67}\text{Sr}_{0.33}\text{MnO}_3/\text{STO}(110)$ [99], a monoclinic distortion has been observed in the thin film. It is therefore likely that the super-reflections seen in figure 5.1 (b) are due to such a monoclinic distortion.

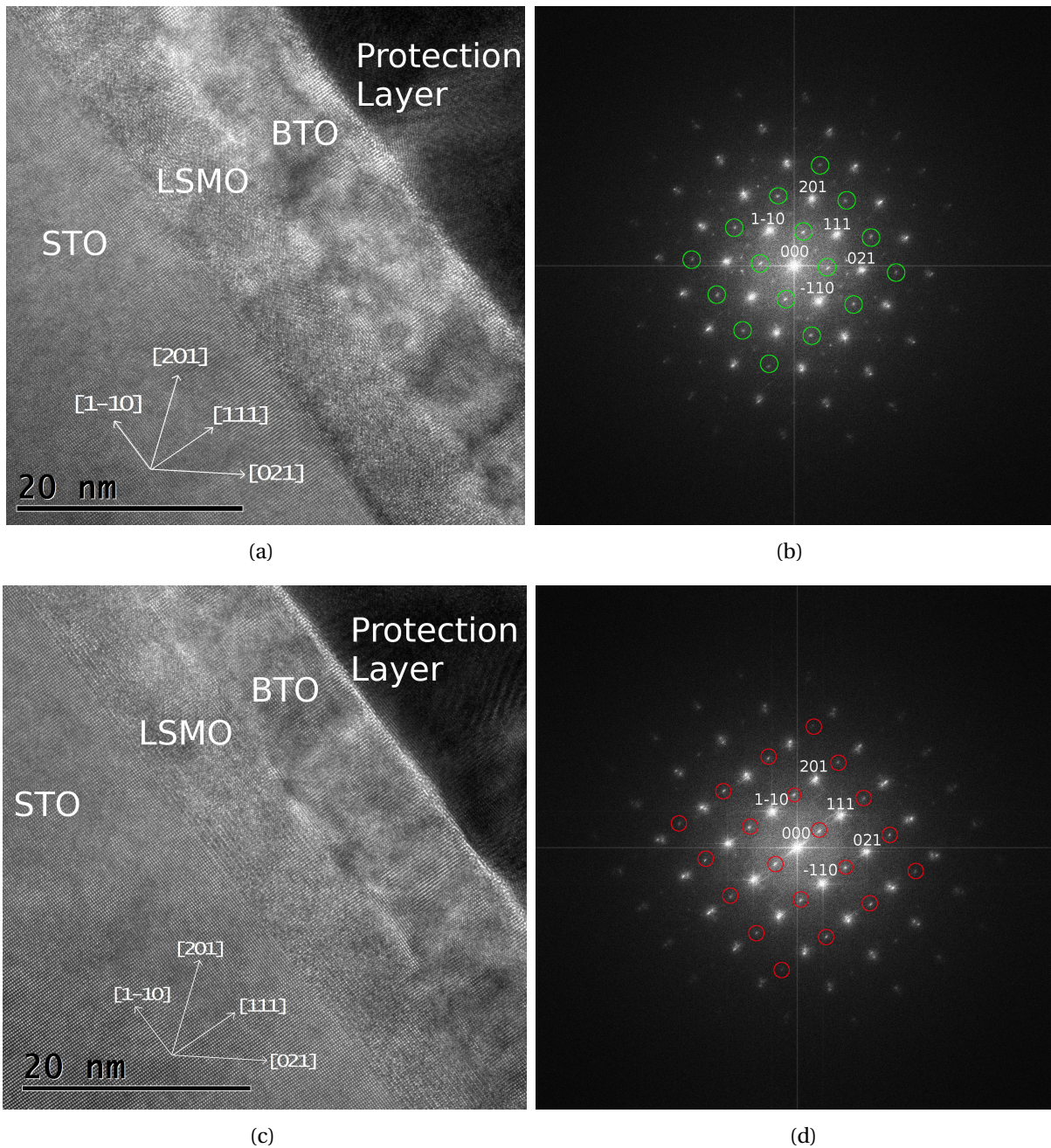


Figure 5.1: **(a)** BF-TEM image along the $[11\bar{2}]_c$ zone-axis with LSMO in the R_4 domain state. **(b)** FFT of figure **(a)**, showing super-reflections (marked with green circles) attributed to a reduction in symmetry due to a monoclinic distortion of LSMO. **(c)** BF-TEM image along the $[11\bar{2}]_c$ zone-axis with LSMO in the R_1 domain state. **(d)** FFT of figure **(c)**, showing super-reflections (marked with red circles) consistent with figure 4.9 **(a)**. All images were captured on the *Jeol-Jem ARM 200F* from the 10-10-CS specimen.

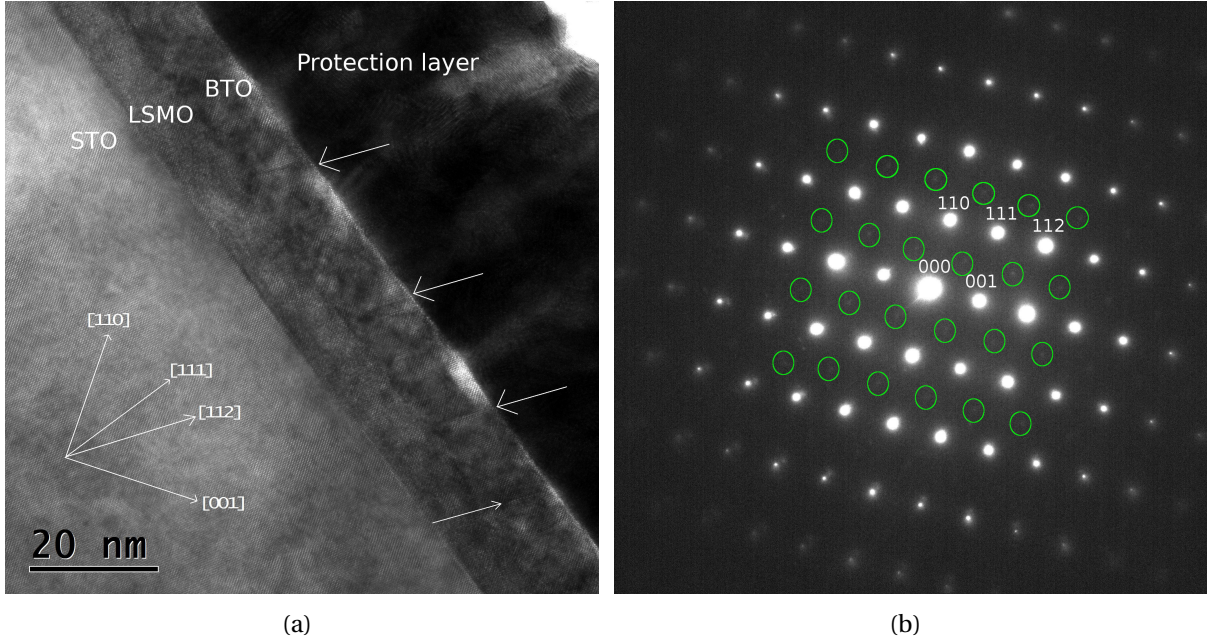


Figure 5.2: **(a)** BF-TEM image along $[1\bar{1}0]_c$ zone-axis taken on the *Jeol-Jem ARM 200F* from the 10-10-CS specimen. Note the bright spots on top of the BTO layer. These spots are located underneath bright areas in the Pt/Pd (80/20)-alloy protection layer. Hence, these artefacts are just due to damage from the FIB. The arrows point towards bright columns of atoms along $[112]_c$ which are due to edge dislocations. A ferroelectric domain wall in BTO should intersect $(1\bar{1}0)_c$ along $[111]_c$, $[001]_c$ or $[11\bar{1}]_c$, as listed in table 2.2. **(b)** Diffraction pattern with super-reflections (marked with green circles) similar to those found in the R_4 domain (if dynamical diffraction is taken into account), figure 4.10 **(d)**.

The super-reflections in figure 5.1 **(d)** are those one should expect from domain state R_1 (see section 2.4 for a definition) when LSMO has its bulk form, as can be seen upon comparison to figure 4.9 **(a)**.

Super-reflections were observed in [12], and were attributed to the octahedral tilt patterns. Furthermore, it was determined that a monoclinic distortion occurred and that the thin film had spacegroup 11. Spacegroup 11 has been observed in LSMO thin films in other studies [39]. Spacegroup 63 was observed in [40], while spacegroup 15 was observed in [99]. An exact determination of the spacegroup was not possible due to the limitations of this work, but based on the literature it seem to be very probable that LSMO has undergone a monoclinic distortion.

After measuring the orientation of a ferroelastic domain wall between these two regions, it was hypothesized that the region seen in figure 5.1 **(a)** corresponds to a R_4 domain. This is further explained in section 5.4. It is beyond the scope of this work to prove that the FFT pattern from the R_4 domain changes from that seen in figure 4.9 **(d)** to that seen in figure 5.1 **(b)**

when LSMO undergoes a monoclinic distortion, but it is inferred from the orientation of the domain wall as well as the identification of the R_1 domain, which appears to have the same FFTP when monoclinically distorted. However, as discussed in section 5.4, the identification of these domains is not certain, because the orientation of the domain walls in LSMO may change when LSMO is monoclinically distorted. Furthermore, it is not proven here that the SADP from R_1 is unchanged and that the SADP from R_4 changes as described above after a monoclinic distortion. However, this is a possible explanation for the observations. Further work is needed to confirm this hypothesis. For example, the precise crystal structure of monoclinic LSMO must be determined, and a theoretical study of the possible domain structures in monoclinic LSMO must be done. The two domains observed will be referred to as R_1 and R_4 , with the understanding that these domains are monoclinically distorted, and that this description of these domains is an unproven hypothesis.

In figure 5.2 (b), the $[1\bar{1}0]_c$ SAD pattern corresponding to figure 5.2 (a) from the 10-10-CS specimen can be seen. Super-reflections that would be suggestive of domain state R_4 upon comparison to figure 4.10 are visible (if dynamical diffraction is taken into account). This is in agreement with the hypothesis that R_1 and R_4 LSMO domains are present.

Note that there is a spread in the reflections in the FFTPs and SADP in figures 5.1 (b) and (d) and figure 5.2 (b). This is due to a relaxation of the BTO thin film in the 10-10-CS system. The weaker spots on the inside of the primary spots are due to the larger lattice parameters of BTO, and BTO relaxes both parallel to and perpendicular to the interface planes, as discussed in the GPA analysis in section 5.2.

Super-reflections may also be caused by a super-lattice structure induced by the electron beam. In [100], a super-lattice structure of oxygen-vacancy ordering in the direction perpendicular to the thin film interface was observed to emerge as the LSMO/STO(001) thin film was illuminated by electrons. This led to additional super-reflections. The two different domains observed in LSMO in this work could have oxygen-vacancy ordering in different directions, leading to different super-reflections in the FFTPs and SADPs. For example, according to this hypothesis, the R_1 domain would have a oxygen-vacancy ordering in the $[111]_c$ -direction, as suggested by figures 5.1 (c) and (d). The R_4 domain would have a oxygen-vacancy ordering in the $[201]_c$ and $[021]_c$ directions, as suggested by figures 5.1 (a) and (b). In the work done in [101], $\text{La}_{1-x}\text{Sr}_x\text{MnO}_{2.5}$ brownmillerite phases are described for $x = 0.25, 0.2$ and 0.4 .

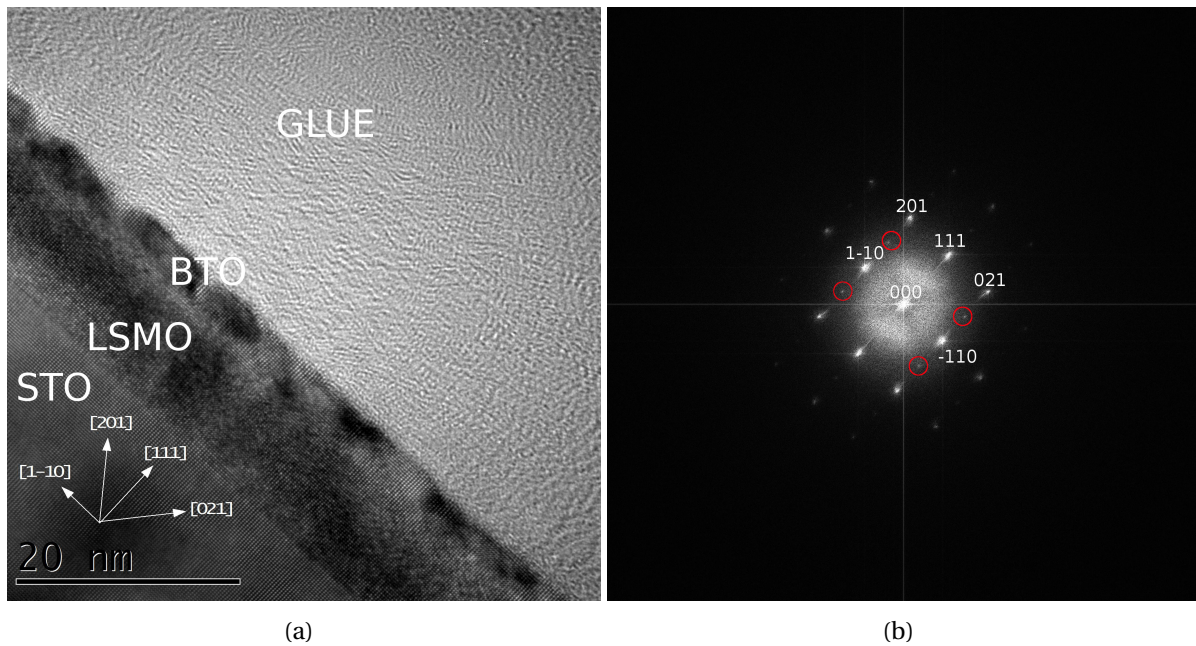


Figure 5.3: **(a)** $[11\bar{2}]_c$ zone-axis HR-TEM image of a R_1 -phase area acquired on the *Jeol-Jem 2100F* from the 3-10-CS specimen. A period doubling in the $[111]$ direction is present, visible as super-reflections marked by red circles in figure **(b)**, the FFT of figure **(a)**.

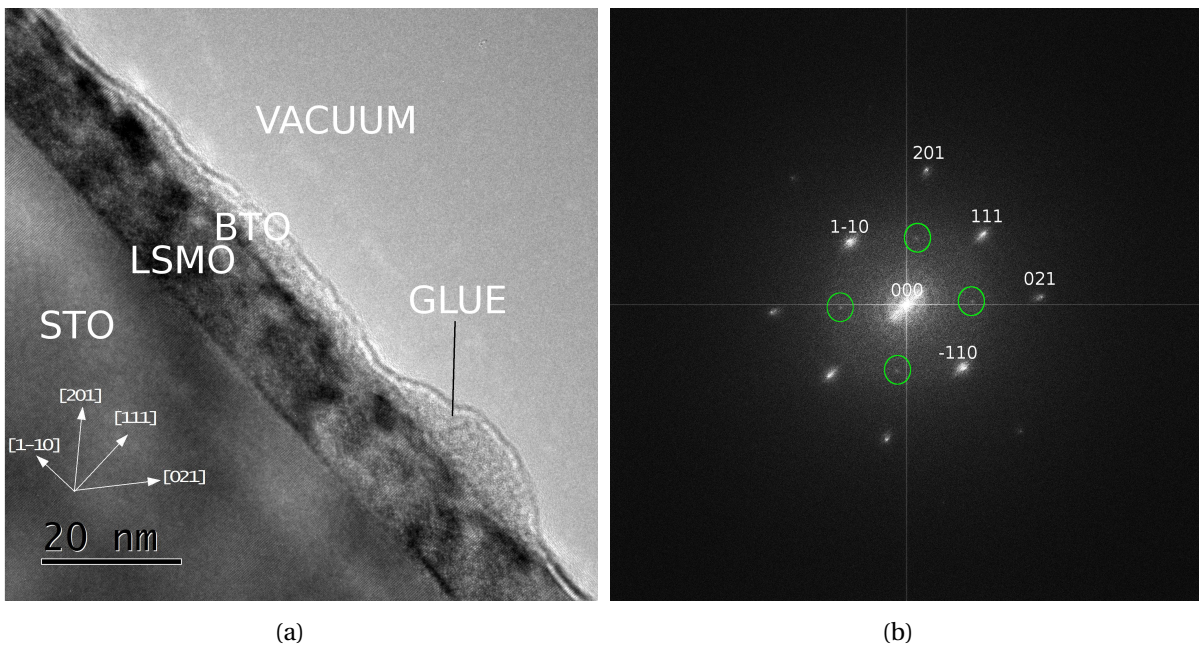


Figure 5.4: **(a)** $[11\bar{2}]_c$ zone-axis HR-TEM image of a R_4 domain area acquired on the *Jeol-Jem 2100F* from the 3-10-CS specimen. **(b)** FFT of figure **(a)**, showing super-reflections (marked with green circles) attributed to a monoclinic distortion of the R_4 domain.

For $x = 0.2$ and for $x = 0.25$, it was found that a monoclinic crystal structure of space group 11 was favored, and additional super-reflections were observed. These were attributed to oxygen-vacancy ordering. However, brownmillerite oxygen-vacancy super-structures order in the $[001]_c$ -direction. This is not consistent with the observed super-reflections in this work. It is shown in section 5.3 that there are a large amount of oxygen-vacancies present in LSMO. In conclusion, it is therefore likely that the oxygen-vacancies are disordered in the 10-10-CS specimen.

In figures 5.3 (a) and (b), a HR-TEM image and its corresponding FFT taken along the $[11\bar{2}]_c$ zone-axis from the 3-10-CS specimen can be seen. The FFTP in figure 5.3 (b), showing period doubling in the $[111]$ -direction, is identified as a R_1 domain pattern. In figure 5.4 (a), an area of LSMO in the R_4 domain state can be seen. The FFTP in figure 5.4 (b) clearly shows the super-reflections associated with a reduction in symmetry, which is probably due to a monoclinic distortion in a R_4 domain, as discussed above. Hence, it seems like the two hypothesized domains of LSMO observed in 10-10-CS, monoclinically distorted R_1 and R_4 domain states, are also present in 3-10-CS.

In figures 5.5 and 5.6, $[11\bar{2}]_c$ and $[1\bar{1}0]_c$ zone-axis SADPs, respectively, acquired from the 3-10-CS specimen, can be seen. Both of these show no super-reflections. This may seem contradictory to figures 5.3 and 5.4 (b), which show super-reflections in the FFTPs. However, the lack of super-reflections in the SADPs is probably due to a very weak signal from the thin films, because the LSMO film thickness is only 10 nm in total. The SAD aperture used has a diameter of 10 μm , and covers a region of ~ 150 nm in diameter. Hence, the fraction of illuminated area that contains thin film is too small to give a detectable signal. The reflections from the different thin films overlap. This indicates that the thin films are not relaxed, but rather are coherent with the substrate.

In figures 5.7 (a) and (b), a $[111]_c$ zone-axis HR-TEM image and a corresponding SADP from the 3-10-PV specimen are shown, respectively. The reflections seem to overlap in this SADP, indicating that the thin films are coherent with the substrate. That is to say, neither of the thin films are relaxed. This is consistent with the observations made on the 3-10-CS specimen. The observation that BTO is relaxed in the 10-10-CS, but not in 3-10-PV and 3-10-CS, is consistent with XRD measurements performed at the Oxide Electronics lab [102].

When the 3-10-PV specimen was observed along the $[110]_c$ zone-axis, as in figure 5.8 (a), super-reflections appeared in the SADP, as can be seen in figure 5.8 (b). This is in agreement

with the FFTs done on 3-10-CS, where super-reflections were observed along the $[1\bar{1}0]_c$ zone-axis. The reason for seeing super-reflections in SADPs from the 3-10-PV specimen, but not from the 3-10-CS specimen, is probably that the entire illuminated region contains thin film in the PV-sample, but not in the CS-sample. Thus, the signal from the thin films should be stronger in the PV-sample, so this is expected. The super-reflections are consistent with LSMO in the R_4 domain state (assuming dynamical diffraction), as seen in figure 4.10 (d).

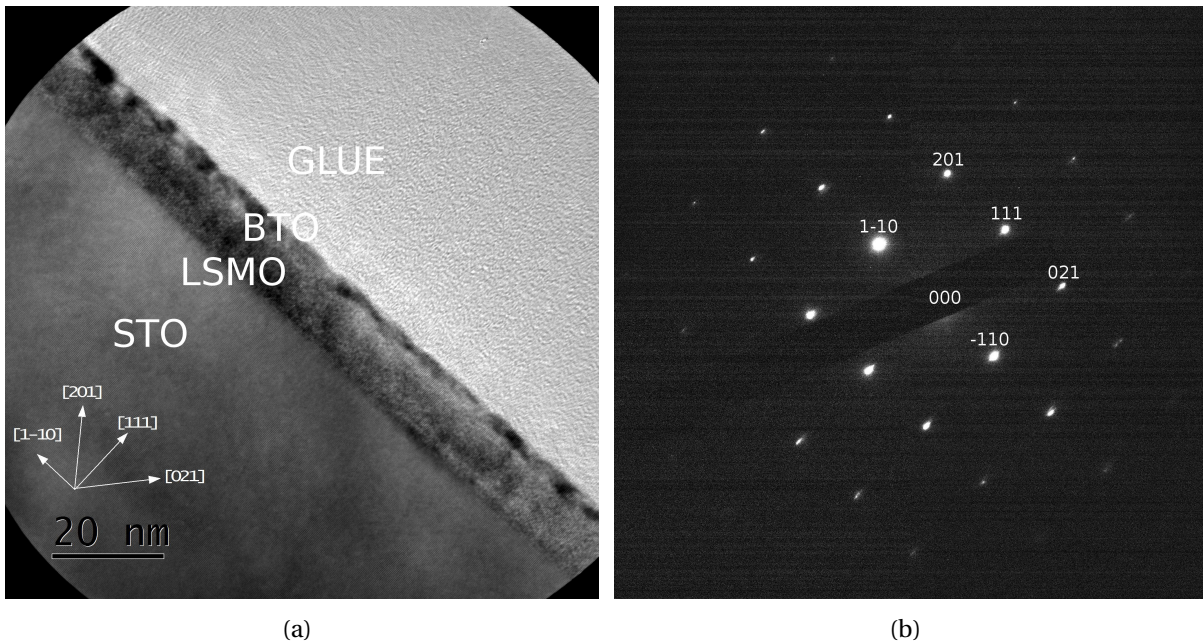


Figure 5.5: **(a)** $[11\bar{2}]_c$ zone-axis HR-TEM image acquired on the *Jeol-Jem 2100F* from the 3-10-CS specimen. **(b)** Diffraction pattern from figure (a). The Bragg reflections seem to overlap indicating that the thin films are not relaxed.

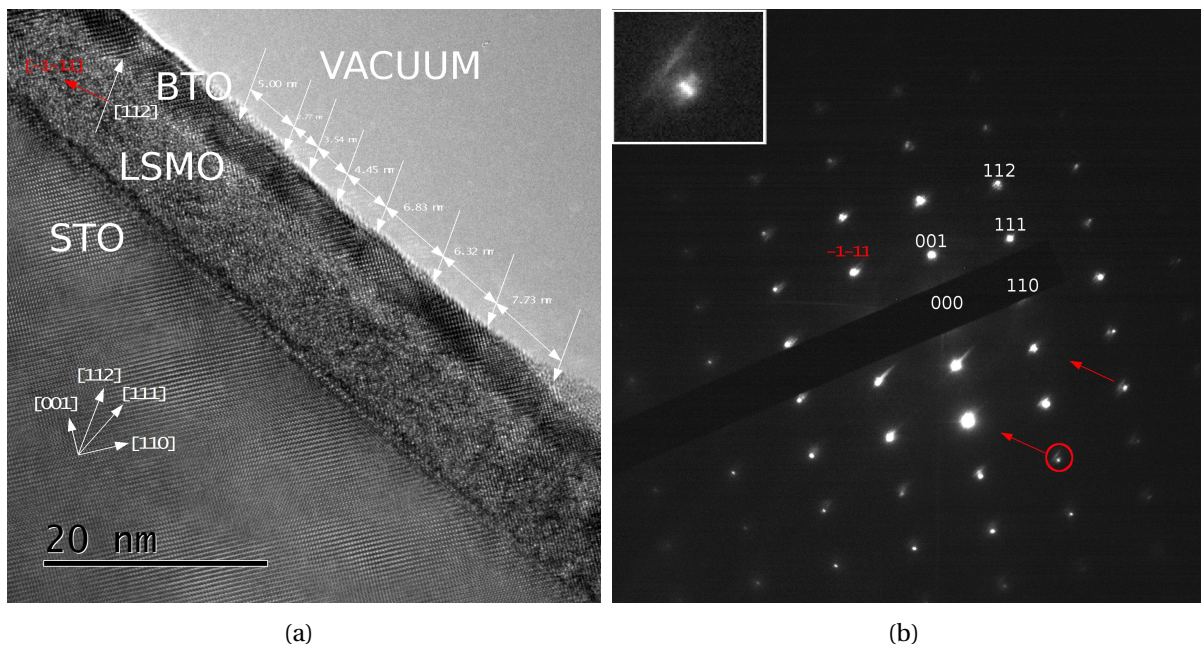


Figure 5.6: **(a)** HR-TEM image acquired along the $[1\bar{1}0]_c$ zone-axis on the *Jeol-Jem 2100F* from the 3-10-CS specimen. Contrast appear along $[112]_c$ in BTO. As in the 10-10-CS system (figure 5.2), the contrast is due to edge dislocations. The distance between the edge dislocations was measured to be $\sim 4\text{-}7$ nm. **(b)** Corresponding diffraction pattern. No super-reflections were seen and the reflections overlap, indicating that the thin films are not relaxed. In addition, additional reflections displaced in the $[\bar{1}\bar{1}1]_c$ direction relative to the Bragg spots can be seen. The white box in the top left corner is a zoom-in on the reflection marked with a red circle, and demonstrates such a displaced reflection. This indicates that the dislocations form a quasi-periodic array of inserted $(11\bar{1})_c$ planes. $\frac{\Delta q}{2\pi} = 0.025 \pm 0.005 \text{ \AA}^{-1}$ was measured, giving $\Lambda = 3.67 \pm 0.33$ nm. The red arrows point in the $[11\bar{1}]_c$ direction.

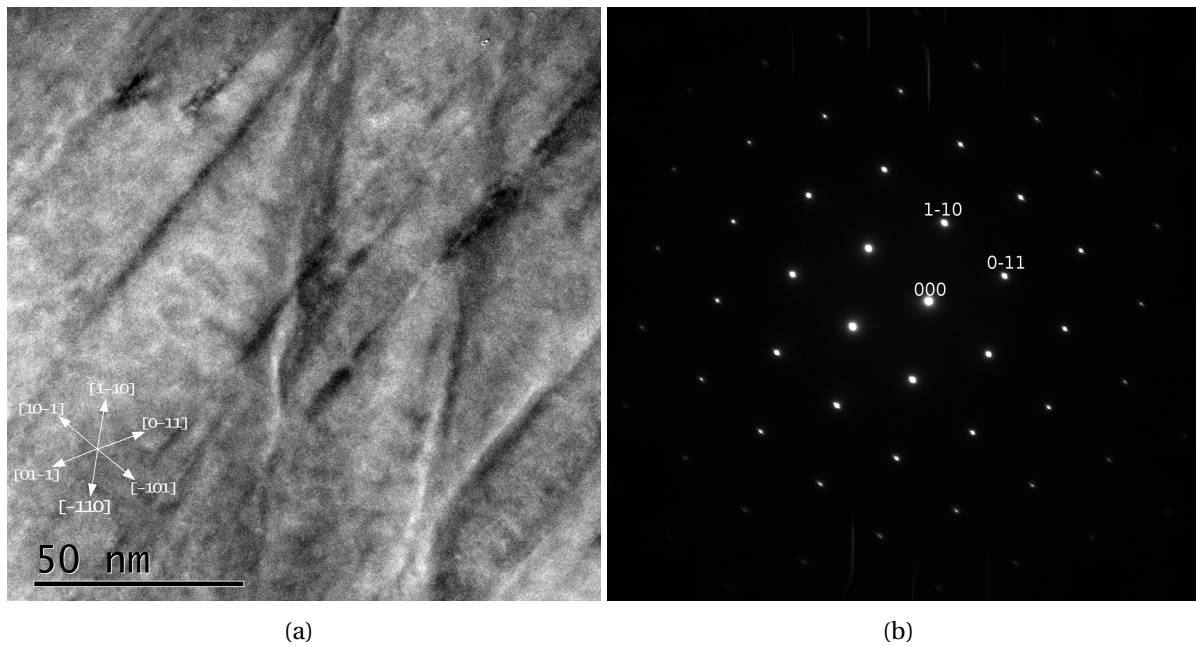


Figure 5.7: **(a)** $[111]_c$ zone-axis HR-TEM image acquired on the *Jeol-Jem 2100F* from the 3-10-PV specimen. **(b)** SAD pattern acquired from the area in **(a)**. The Bragg reflections seem to overlap indicating that the thin films are not relaxed.

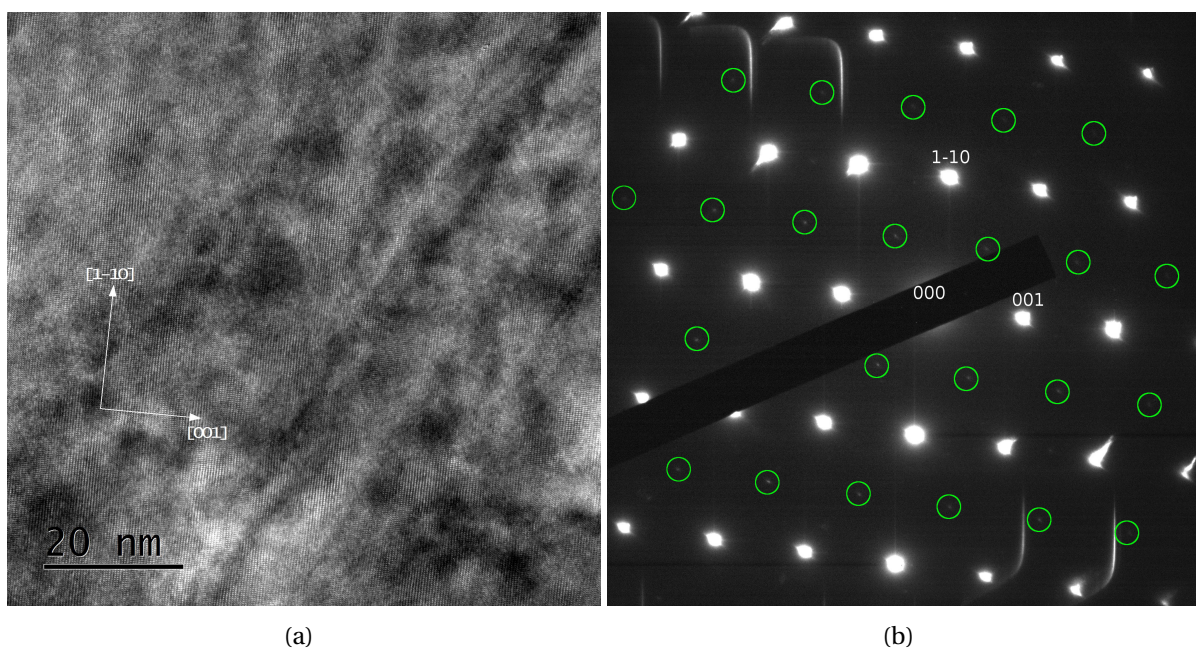


Figure 5.8: **(a)** $[110]_c$ zone-axis HR-TEM image acquired on the *Jeol-Jem 2100F* from the 3-10-PV specimen. **(b)** SAD pattern acquired from the area in **(a)**. Note the weak super-reflections present here, marked with green circles. The super-reflections are similar to those found in the R_4 domain (if dynamical diffraction is taken into account), figure 4.10 **(d)**. The lines in the DP in the top left and bottom right corners are artefacts due to problems with charging in the non-conducting specimen.

5.2 Thin film quality

It is important to be able to grow epitaxial thin films of high quality where e. g. the strain, dislocations and composition are carefully controlled. In order to characterize the quality of the thin films, HAADF-STEM image stacks as well as EDS and TEM images were acquired and analyzed.

5.2.1 GPA strain analysis

In figure 5.9 (a), a HAADF-STEM image stack from the 10-10-CS specimen can be seen. The black arrow points toward an edge dislocation in BTO, which is more easily seen in figure 5.9 (b), where an inverse FFT (IFFT) has been done using a mask on the $(110)_c$ reflections.

In figures 5.10 and 5.11, the strain fields and the displacements fields, respectively, computed using GPA, can be seen. LSMO appears to have a tensile strain of approximately 2.5% relative to the reference, STO, in the direction normal to the interface, as seen in figure 5.10 (a). Thus, assuming $a_{c,LSMO,bulk} = (3.876 \pm 0.003)\text{\AA}$ [83], the tensile strain of LSMO relative to its bulk state is

$$\frac{a_{c,LSMO,measured}}{a_{c,LSMO,bulk}} = \frac{1.025 \cdot a_{STO}}{a_{c,LSMO,bulk}} = \frac{1.025 \cdot 3.905}{3.876} \approx 1.033. \quad (5.1)$$

LSMO appears to be coherent with STO parallel to the surface, as seen in figure 5.10 (b). The BTO thin film is completely relaxed. There appears to be large displacement fields around the edge dislocations in BTO. This is seen in both of figures 5.11 (a) and (b).

The GPA-analysis was repeated on several HAADF image stacks acquired along the $[11\bar{2}]_c$ zone-axis. The same observations were made. Edge dislocations were observed in the BTO layer, as can be seen in figure 5.12 (a), or in figure 5.12 (b) where an IFFT has been done using a mask on the $(1\bar{1}0)_c$ reflections. LSMO was observed to be tensilely strained relative to STO in the direction normal to the interface and coherent with STO in the direction parallel to the interface, as can be seen in figure 5.13. There appears to be large displacement fields around the edge dislocations in BTO. This is seen in both of figures 5.14 (a) and (b). Additional HAADF-STEM image stacks confirming these observations can be found in Appendix C.

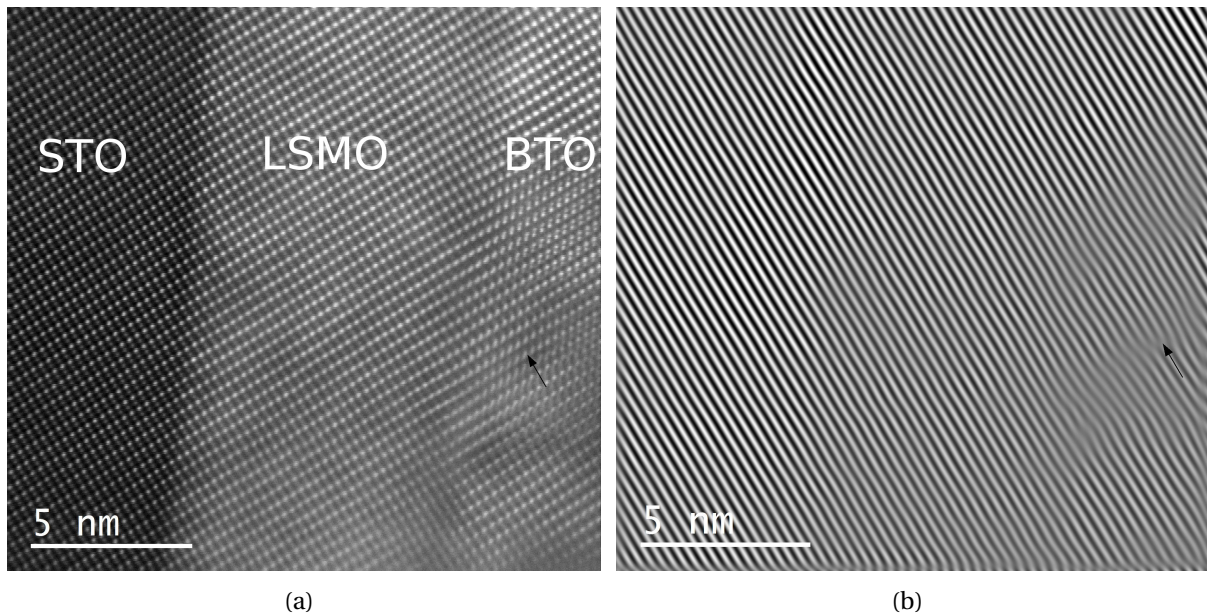


Figure 5.9: **(a)** HAADF-STEM image in $[1\bar{1}0]_c$ zone-axis made by summing several frames in an image stack using the SmartAlign software. **(b)** IFFT with mask on $(110)_c$ to show the dislocation. The black arrow points to edge dislocation in both images. The HAADF-STEM data were collected on the *Jeol-Jem ARM 200F* from the 10-10-CS specimen.

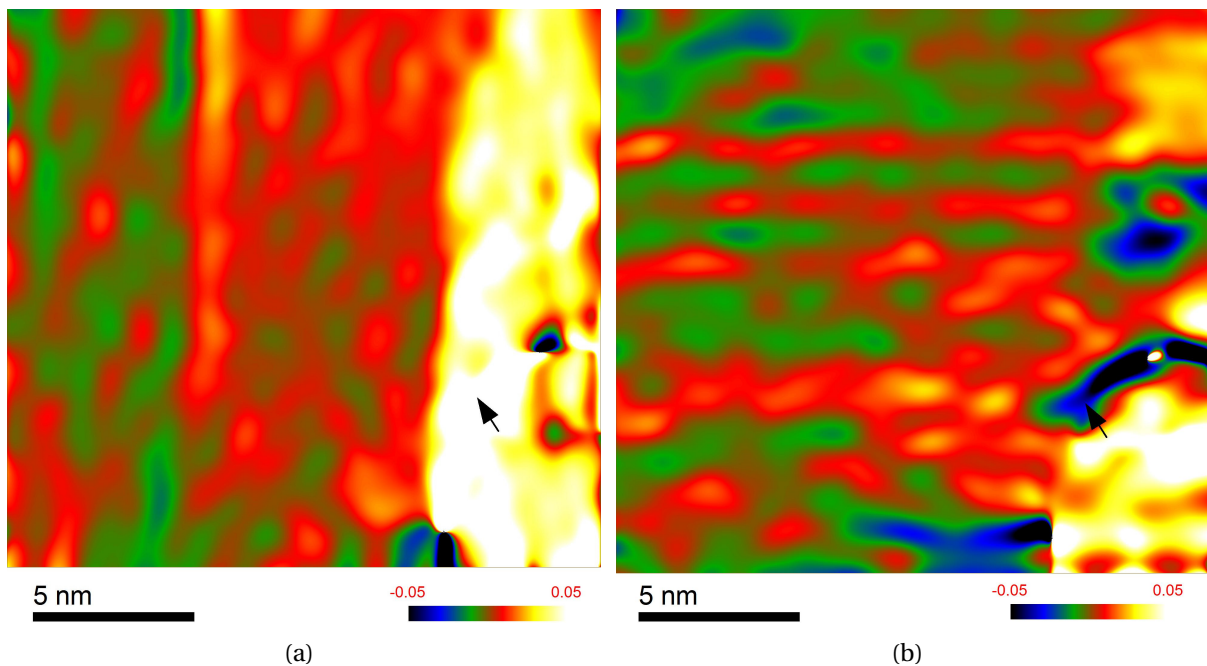


Figure 5.10: **(a)** GPA-computed strain field from figure 5.9 in the direction normal to the film. **(b)** GPA-computed strain field from figure 5.9 in the direction parallel to the film. The color bar displays the strain level from $\pm 5\%$ and the black arrow points to an edge dislocation in both images.

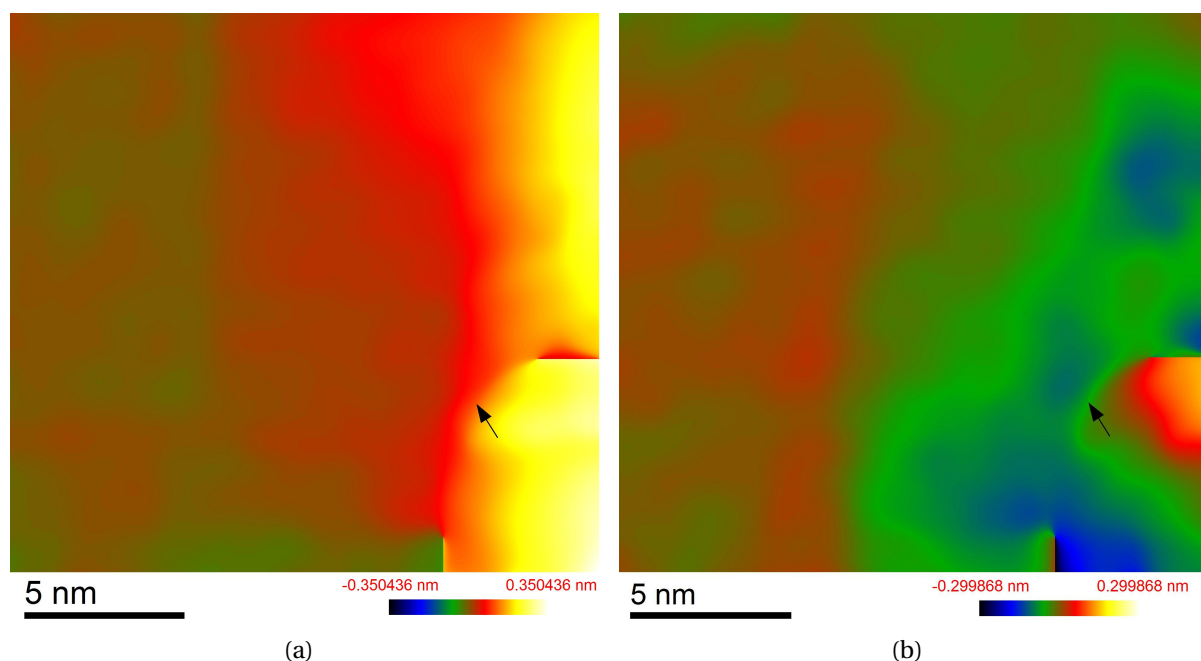


Figure 5.11: **(a)** GPA-computed displacement field from figure 5.9 in the direction normal to the film. **(b)** GPA-computed displacement field from figure 5.9 in the direction parallel to the film. The color bar displays the displacement field in nanometers and the black arrow points to an edge dislocation in both images.

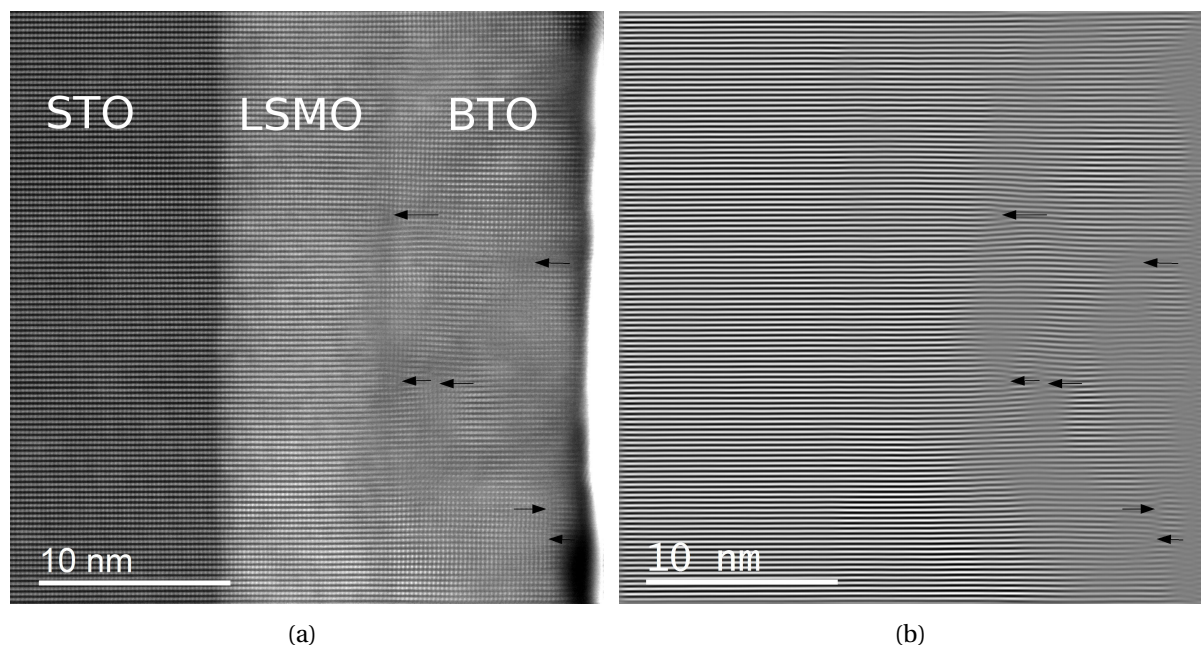


Figure 5.12: **(a)** HAADF-STEM image in $[11\bar{2}]_c$ zone-axis made by summing several frames in an image stack using the SmartAlign software. **(b)** IFFT with mask on $(1\bar{1}0)_c$ to show the dislocations. The black arrows point to edge dislocations in both images. The HAADF-STEM data were collected on the *Jeol-Jem ARM 200F* from the 10-10-CS specimen.

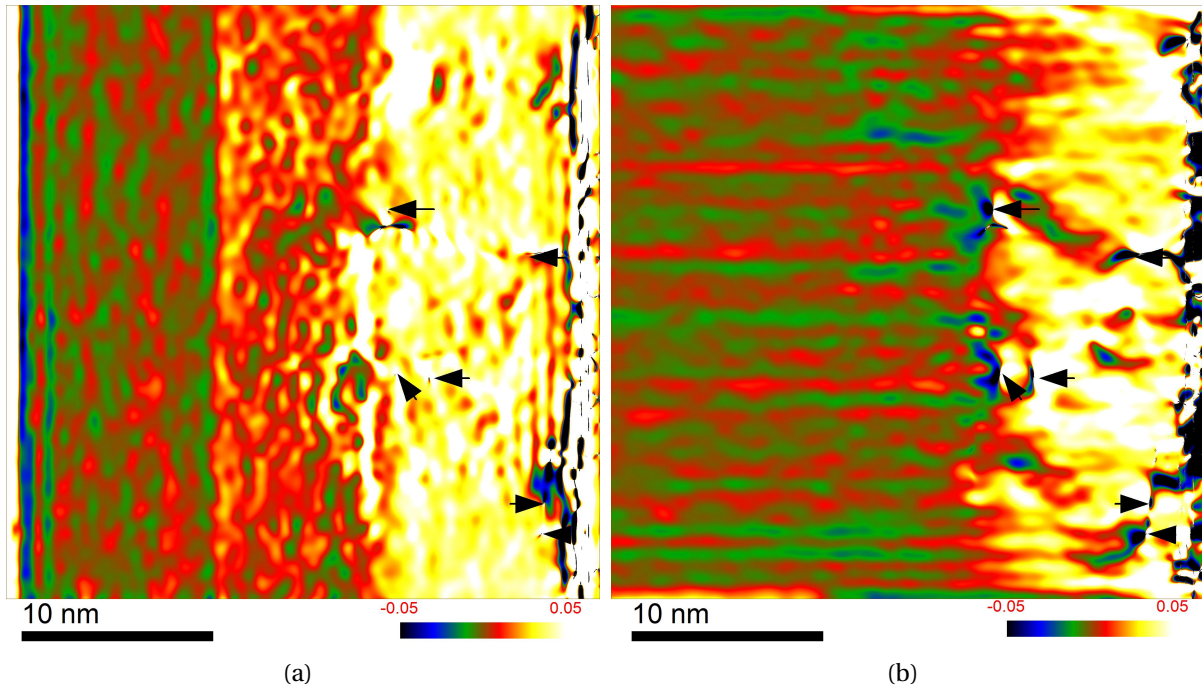


Figure 5.13: **(a)** GPA-computed strain field from figure 5.12 in the horizontal direction (normal to the film). **(b)** GPA-computed strain field from figure 5.12 in the vertical direction (parallel to the film). The color bar displays the strain level from $\pm 5\%$ and the black arrows point to edge dislocations in both images.

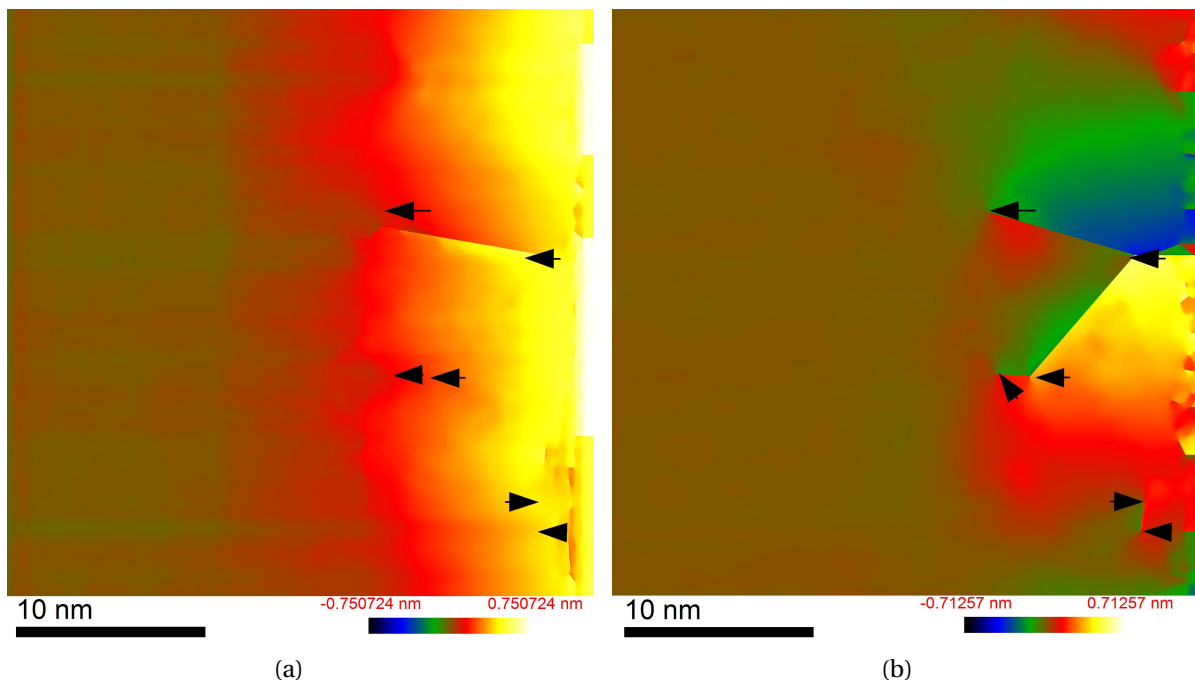


Figure 5.14: **(a)** GPA-computed displacement field from figure 5.12 in the horizontal direction (normal to the film). **(b)** GPA-computed displacement field from figure 5.12 in the vertical direction (parallel to the film). The color bar displays the displacement in nanometers and the black arrows point to edge dislocations in both images.

5.2.2 Artefacts in GPA

In [103], it was discovered that artefacts may occur in the GPA analysis in materials with compositionally distinct atom columns, such as the perovskites. If \vec{v} is the displacement vector between the two sub-lattices as observed from a given zone-axis, and \vec{g} is the vector chosen for the GPA analysis, the condition that $\vec{g} \cdot \vec{v} = n$, $n \in \mathbb{Z}$, is derived. If this condition is not met, anomalous results may be obtained in the GPA analysis.

In the perovskites, the A cation is displaced from the B cation by a vector $\vec{r} = [\frac{1}{2}, \frac{1}{2}, \frac{1}{2}]_c$. Since this vector is perpendicular to both $[1\bar{1}0]_c$ and $[11\bar{2}]_c$, $\vec{v} = [\frac{1}{2}, \frac{1}{2}, \frac{1}{2}]_c$ in both of these zone-axes.

In the $[1\bar{1}0]_c$ zone-axis, $g_1 = [110]_c$ and $g_2 = [001]_c$ were used. Hence,

$$\vec{g}_1 \cdot \vec{v} = 1 \in \mathbb{Z}. \quad (5.2)$$

$$\vec{g}_2 \cdot \vec{v} = \frac{1}{2} \notin \mathbb{Z}. \quad (5.3)$$

In the $[11\bar{2}]_c$ zone-axis, $g_3 = [111]_c$ and $g_4 = [1\bar{1}0]_c$ were used. Hence,

$$\vec{g}_3 \cdot \vec{v} = \frac{3}{2} \notin \mathbb{Z}. \quad (5.4)$$

$$\vec{g}_4 \cdot \vec{v} = 0 \in \mathbb{Z}. \quad (5.5)$$

In conclusion, the condition that was derived in [103] is not met in this work. For this reason, artefacts should be expected in the GPA images. Therefore, the GPA analysis was repeated with $\vec{g}_2 = [002]_c$ and $\vec{g}_3 = [222]_c$. However, this did not seem to have a large effect on the outcome of the GPA analysis. Therefore, the problems discussed in [103] does not seem to be present in the GPA analysis performed here.

5.2.3 Effect of the Pt/Pd (80/20)-alloy protection layer

It is known that interface reactions between LSMO and metal contacts can have an impact on structural, magnetic and chemical properties of the oxide [104]. Metals such as titanium and chromium are known to cause reduction reactions in LSMO. In [104], LSMO was deposited on STO(100) by RHEED-PLD. 10 and 20 nanometer LSMO thin films were used, and different metal layers (Au, Ti, Cr) were deposited on top of LSMO. Next, STEM-EELS and XRD was performed to characterize any changes induced by the metal layers. Deposition of Au, Ag, Pt or Cu (noble metals) had little effect on the thin film properties, while deposition of other types of metal layers had several effects reminiscent of the ones observed in this work. The deposition of Ti caused a tensile out-of-plane lattice constant of LSMO and a superlattice period-doubling in the out-of-plane direction. Furthermore, the white-line ratio and O-K edge were studied in [104], confirming a low Mn oxidation number and the presence of oxygen-vacancies. It was also observed that the number of oxygen-vacancies is higher at the interface to STO. The brownmillerite structure was pointed out as a crystal structure that could explain these observations. However, it was found that the oxidation reaction between the metal layer and LSMO could be stopped by inserting an epitaxial layer between LSMO and the metal. The thickness of the inserted layer had to be at least 4 nanometer thick to protect LSMO. Since a 10 nanometer BTO layer is deposited on top of LSMO in this work, oxidation by the metal layer should not be a problem. Furthermore, the protection layer is an alloy of Pt and Pd, and is thus not very oxidizing. In conclusion, the metal protection layer is probably not the cause of the observed oxygen-vacancies in LSMO. A more probable cause of the observed oxygen-vacancies is the electron beam itself, or beam knock-on damage in the FIB. The observations about the EELS fine structure and the XRD data in [104] are quite similar to the ones in this work. However, as discussed earlier the oxygen-vacancies in LSMO are probably disordered in the 10-10-CS specimen, because ordering should occur in the $[001]_c$ -direction, and no such ordering has been observed in this work.

The deposition of the metal layer seem to have some effect on the BTO layer. For example, in figure 5.2 (a), bright spots appear on the top of the BTO layer. These seem to appear under bright spots in the Pt/Pd (80/20)-alloy protection layer, and are due to damage in the FIB. LSMO does not seem to be affected by the metal layer in this image.

5.2.4 Composition

An EDS scan of the thin film area was performed on the 3-10-CS and 3-10-PV specimens in order to confirm that the thin films were present. That is, to make sure they were not accidentally removed during the specimen preparation. As can be seen in figures 5.15 and 5.16, the test indicates that all the expected elements were present.

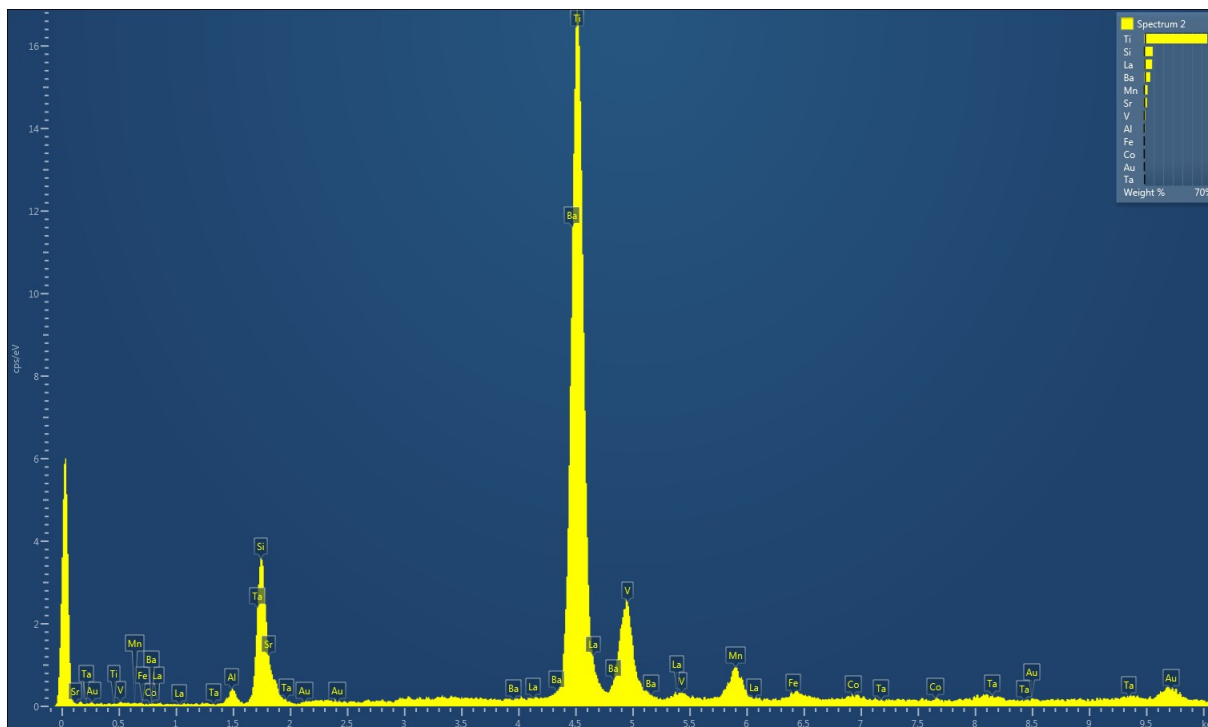


Figure 5.15: Confirming that the BTO and LSMO thin films are present in the 3-10-CS specimen. Ba, La and Mn are present. These can only come from the thin films. The Si is probably present due to the Si support of the specimen as well as the silica sol used during the tripod polishing. The EDS scan was performed on the *Jeol-JEM 2100F*.

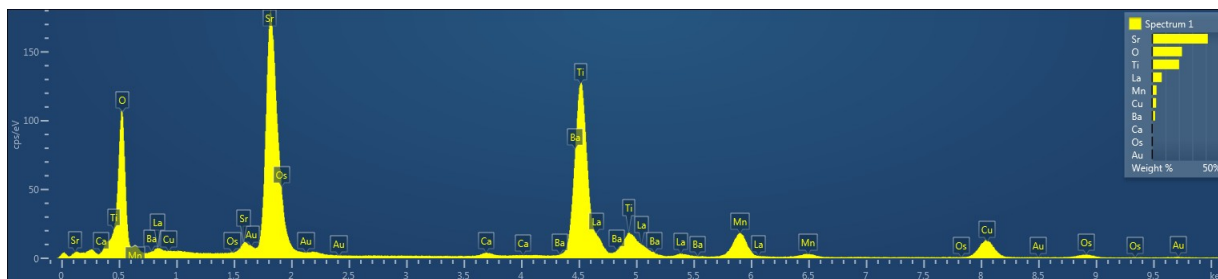


Figure 5.16: Confirming that the BTO and LSMO films are present in the 3-10-PV specimen. Ba, La and Mn are present. These can only come from the thin films. Cu is from the *Lift-out OMINI GRIDS 3-Post Shallow Downset Copper* TEM specimen holder. The EDS scan was performed on the *Jeol-JEM 2100F*.

However, the spectrum in figure 5.15 was taken with a negative X-tilt of the specimen. This means that the specimen holder was blocking the low-energy X-rays from reaching the detector. There are therefore some anomalies in the spectrum, such as the lack of an oxygen peak, and a low energy-resolution at low energies. Also note that the intensity is much lower in figure 5.15 than in figure 5.16. It could also be the Si support of the 3-10-CS specimen that is blocking the signal from the thin film system, giving a weaker signal.

The *Oxford Instruments INCA EDS* software system cannot be trusted to give a correct interpretation of all the peaks and the precise composition. Due to the overlap of the Si and Sr peaks, the Si peak in figure 5.15 may in fact be a Sr peak.

5.2.5 Dislocations

In figure 5.2 (a), a BF-TEM image along the $[1\bar{1}0]_c$ zone-axis from the 10-10-CS specimen can be seen. Several edge dislocations extending all the way through the BTO film can be seen along the $[112]_c$ direction, indicated by white arrows. These lines cannot be ferroelectric domain walls, because ferroelectric domain walls should intersect $(1\bar{1}0)_c$ along $[111]_c$, $[001]_c$ or $[11\bar{1}]_c$, as listed in table 2.2.

Since the edge dislocations seem to be along $[112]_c$, and since they appear to be atomically sharp, it is reasonable to assume that they are caused by inserted planes with normals perpendicular to the zone-axis. In that case, the normal of the inserted plane can be found by taking the cross product of the zone-axis and the direction of the dislocation line, because it must be perpendicular to both of these. Hence, $\vec{n} = [1\bar{1}0]_c \times [112]_c \parallel [11\bar{1}]_c$. This type of dislocation is sketched in figure 5.17.

In figure 5.6 (a), the 3-10-CS specimen is observed in the $[1\bar{1}0]_c$ zone-axis. There appears to be contrast between different types of regions in the BTO layer, marked with arrows. Since the border between these regions is along $[112]_c$, the contrast is probably due to edge dislocations, similar to those seen in figure 5.2 and sketched in figure 5.17. The distance between the edge dislocations was measured to be approximately 4-7 nm in figure 5.6 (a), or $\frac{2\pi}{\Delta q} = 3.67 \pm 0.33$ nanometers in figure 5.6 (b). Note that these edge dislocations do not appear to be atomically sharp, as in figure 5.2 (a) from 10-10-CS.

An initial overview image of the 3-10-PV specimen can be seen in figure 5.18 (a). Several lines are visible along the $[1\bar{1}0]_c$ -direction. Upon closer inspection, as in figure 5.18 (b), it was found that these lines are too narrow to be polishing lines. In addition, they were not

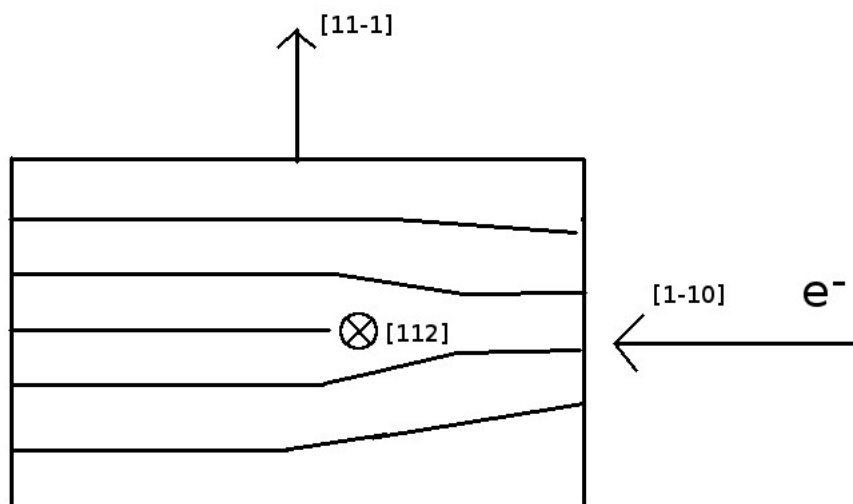


Figure 5.17: Edge dislocation caused by inserted $(11\bar{1})_c$ -plane terminating along $[112]_c$. This type of edge dislocation can be seen for example in figure 5.2 from 10-10-CS and in figure 5.6 (a) from 3-10-CS.

parallel to the polishing stripes on the specimen. An ASTAR scan was also performed on this region, as can be seen in figure 5.19. The lines were still visible in the ASTAR image, and small rotations of the diffraction pattern were observed upon crossing these lines. These small rotations are consistent with edge dislocations. These edge dislocations may be described by the sketch in figure 5.20 or the sketch in figure 5.21. The dislocation seen in figure 5.9 is viewed from a direction parallel to the dislocation line. Hence, it is easily seen that the inserted plane is a $(110)_c$ plane. Thus, this dislocation can also be described by the sketch in figure 5.20.

In figure 5.12 from 10-10-CS, edge dislocations are viewed from a direction parallel to the dislocation lines. Hence, it is easily seen that the inserted plane is a $(1\bar{1}0)$ plane.

In figure 5.22 (a), an area of LSMO- R_1 in the 3-10-CS specimen in the $[11\bar{2}]_c$ zone-axis can be seen. The film thickness is measured to be 13 nm, as it should be according to table 4.1. Upon performing a FFT and then inverse transforming with a mask on the $(111)_c$ and $(1\bar{1}0)_c$ reflections, figure 5.22 (b) is produced, in which several edge dislocations caused by inserted $(1\bar{1}0)_c$ -planes are marked in red. Hence, these types of dislocations are present even when BTO has a thickness of only 3 nm. Note that the CTF seems to change around the dislocations, making the interpretation of these images challenging. In figure 5.23, the result of doing virtual BF on an ASTAR data set collected from 3-10-CS along the $[11\bar{2}]_c$ zone-axis can be seen. Upon moving along the thin film in the BTO layer, small rotations of the diffraction pattern were observed, consistent with the observation of edge dislocations in this layer.

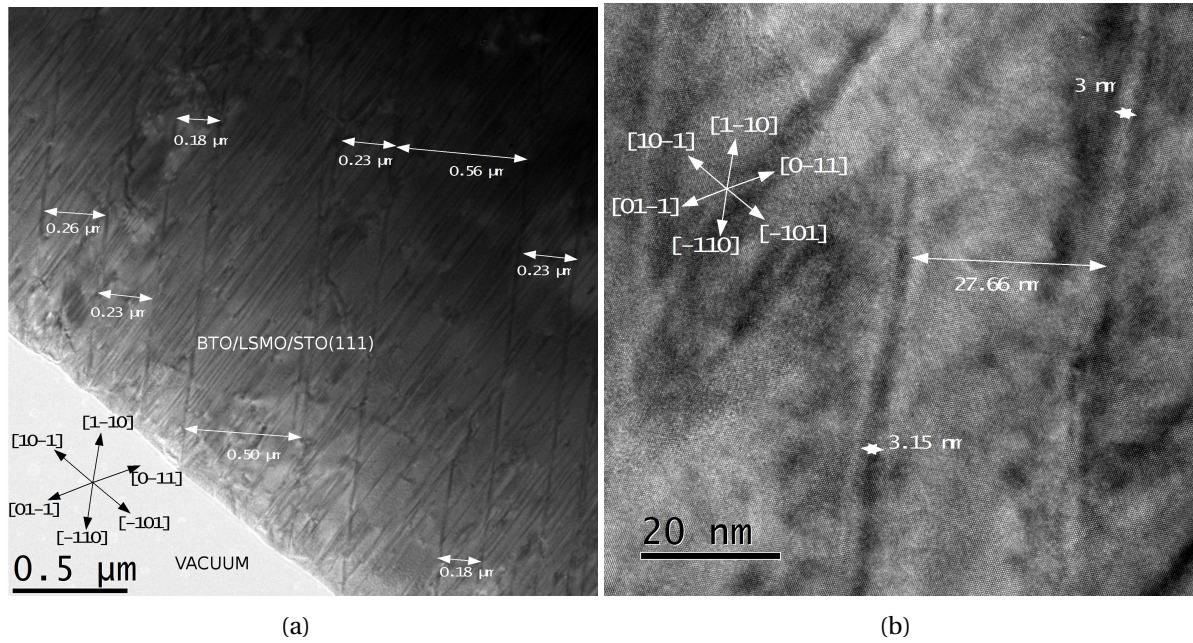


Figure 5.18: **(a)** and **(b)** are $[111]_c$ zone-axis HR-TEM images acquired on the *Jeol-Jem 2100F* from the 3-10-PV specimen.



Figure 5.19: ASTAR $[111]_c$ zone-axis virtual BF image, showing dark lines along $\langle 11\bar{2} \rangle_c$ and $\langle 1\bar{1}0 \rangle_c$. The ASTAR data was acquired on the *Jeol-Jem 2100F* from the 3-10-PV specimen.

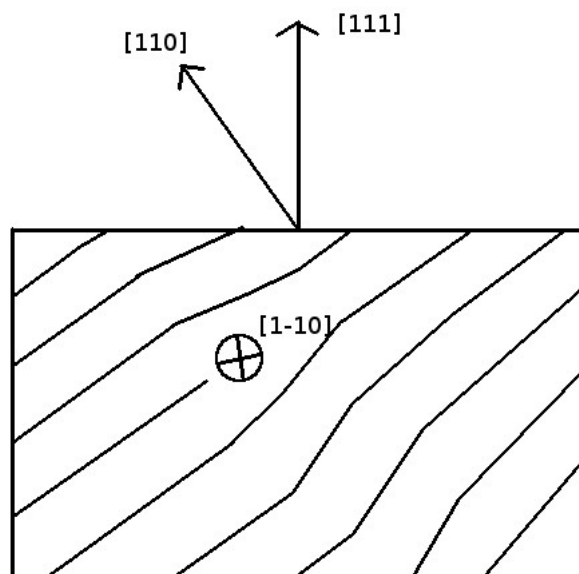


Figure 5.20: Edge dislocation caused by inserted $(110)_c$ -plane terminating along $[1\bar{1}0]_c$. This type of dislocation can be seen in the 3-10-PV specimen for example in figures 5.18 as lines along $[1\bar{1}0]_c$ and in the 10-10-CS specimen in figure 5.9.

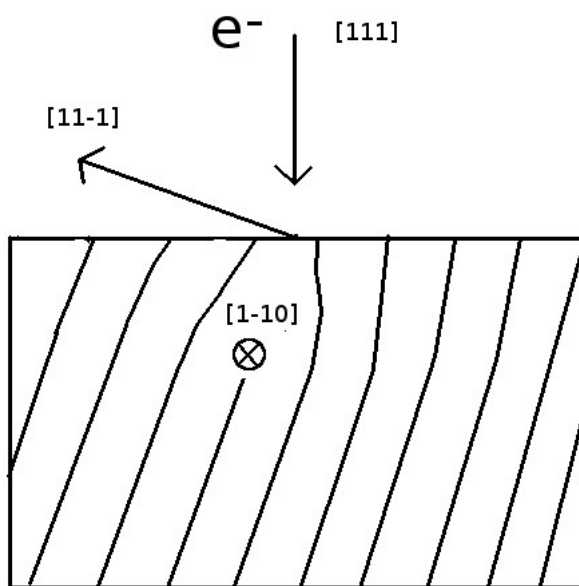


Figure 5.21: Edge dislocation caused by inserted $(11\bar{1})_c$ -plane terminating along $[1\bar{1}0]_c$. This type of dislocation can be seen for example in the 3-10-PV specimen in figures 5.18 as lines along $[1\bar{1}0]_c$.

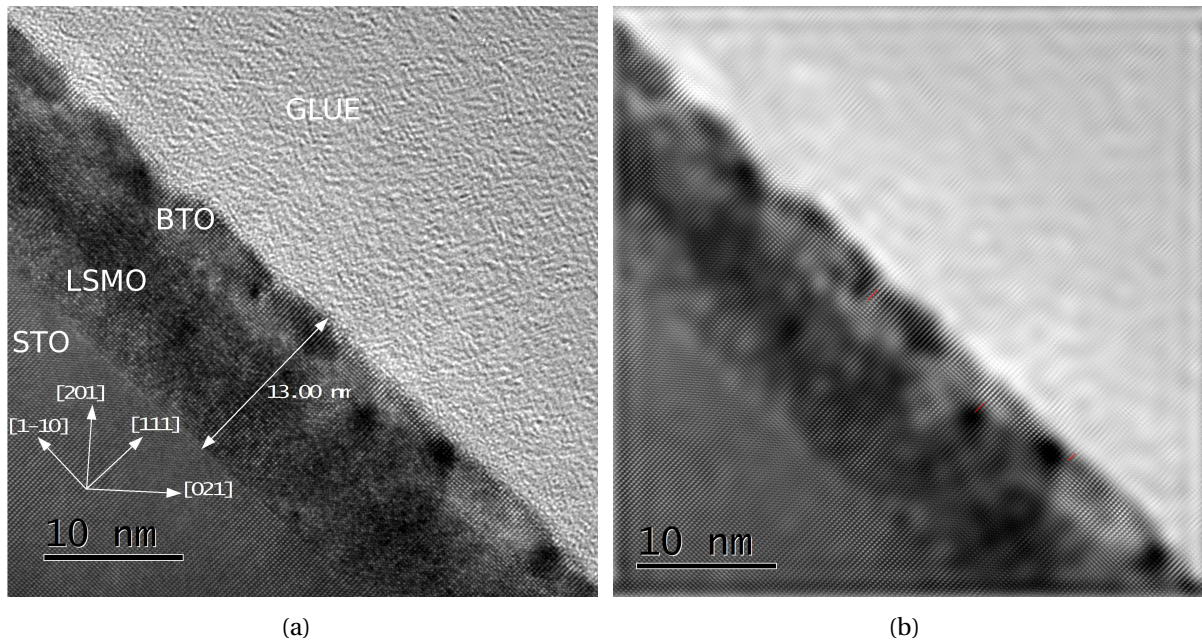


Figure 5.22: **(a)** HR-TEM image acquired along the $[11\bar{2}]_c$ zone-axis on the *Jeol-Jem 2100F* from the 3-10-CS specimen. **(b)** Filtered image, making it easier to see the edge dislocations, which are indicated by red lines.

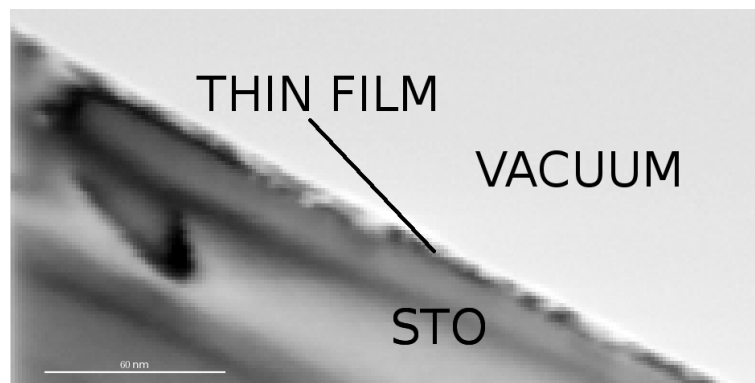


Figure 5.23: ASTAR virtual BF-image taken along $[11\bar{2}]_c$ zone-axis on the *Jeol-Jem 2100F* from the 3-10-CS specimen. Upon moving in the BTO layer, small rotations of the diffraction pattern occurred, confirming the presence of the edge dislocations seen in figure 5.22.

A sketch of an edge dislocation caused by an inserted $(1\bar{1}0)_c$ -plane is given in figure 5.24.

Edge dislocations along several different $\langle 1\bar{1}0 \rangle_c$ -directions and $\langle 11\bar{2} \rangle_c$ -directions were observed, as can be seen for example in figure 5.25 **(a)**. Furthermore, these directions are approximately equivalent in BTO. Thus, it is reasonable to conclude that edge dislocations corresponding to planes inserted along $\{\bar{1}\bar{1}1\}_c$ and $\{110\}_c$ must be present in general in this system.

In figures 5.26 **(a)** and **(b)**, the width of a stripe was measured to be ~ 2 nanometers. The contrast lines are in fact caused by the strain fields around the edge dislocations. When

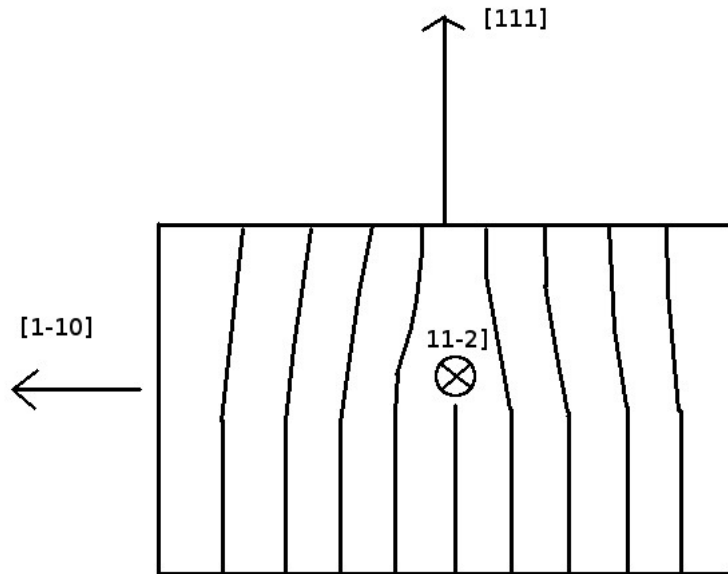


Figure 5.24: Edge dislocation caused by inserted $(1\bar{1}0)_c$ -plane terminating along $[11\bar{2}]_c$. This type of dislocation can be seen in figures 5.18 as lines along $[11\bar{2}]_c$, in figures 5.12 and in figures 5.22.

the inserted plane is skewed relative to $[111]_c$, the strain field should appear wider when viewed in that zone-axis. For example, the edge dislocations seen in figure 5.2 are less wide than those seen in figures 5.25 and 5.26. However, the dislocations along $\langle 11\bar{2} \rangle_c$ -directions appear to be just as wide as the dislocations along the $\langle 1\bar{1}0 \rangle_c$ -directions, even though the former dislocations are caused by inserted planes that contain $[111]_c$. Therefore, it is more likely that there is another reason why the strain fields around the edge dislocations are wider in the 3-10-PV specimen. For example, the fact that the thin film is not relaxed may cause a larger strain field around the dislocations. This is a more plausible explanation, because the edge dislocations were only atomically sharp in the 10-10-CS specimen, as can be seen in figure 5.2 (a), and this was the only specimen with a relaxed BTO thin film.

Finally, note that the edge-dislocations serve to relax the BTO lattice compared to LSMO and STO. However, as discussed earlier, the diffraction patterns from the 3-10-CS and 3-10-PV specimens show no splitting of the reflections due to relaxation. A possible explanation for this observation is that the BTO thin film is partially relaxed in 3-10-CS and 3-10-PV. However, due to the very small BTO thin film thickness of only 3 nanometers, as well as rotations of the BTO lattice due to dislocations giving a spread of the reflections, the signal from the BTO thin film is very weak. The observations of dislocations in BTO in these systems indicates that this is the case, and the earlier hypothesis that BTO is not relaxed must therefore be discarded. As mentioned earlier, XRD measurements performed on the same system show

that BTO is not relaxed when the thin film thickness is only 3 nanometers. This indicates that the thin film may have relaxed due to the TEM specimen preparation. Alternatively, the partial relaxation of BTO is not detected by XRD measurements.

5.2.6 Ion beam damage

In figure 5.6 (a), the LSMO layer appears to be quite amorphous. In general, several areas (not all) in the 3-10-CS specimen had such damage in the LSMO layer. It is probable that this amorphization is due to ion beam damage from the PIPS treatment, as discussed in [73]. It is therefore recommended to attempt to produce TEM specimens by using tripod polishing alone. This is very challenging, because a final PIPS treatment is often necessary to make the specimen electron transparent.

As discussed in section 5.3, a lot of oxygen-vacancies are present in the LSMO layer in the 10-10-CS specimen, prepared by FIB. However, no amorphous pollution such as that seen in figure 5.6 (a) was observed in the 10-10-CS specimen. This may indicate that the ion beam damage is more severe after a PIPS treatment. Since STEM-EELS data were not collected from 3-10-CS, the effect of the PIPS treatment on the EELS fine structure is not known.

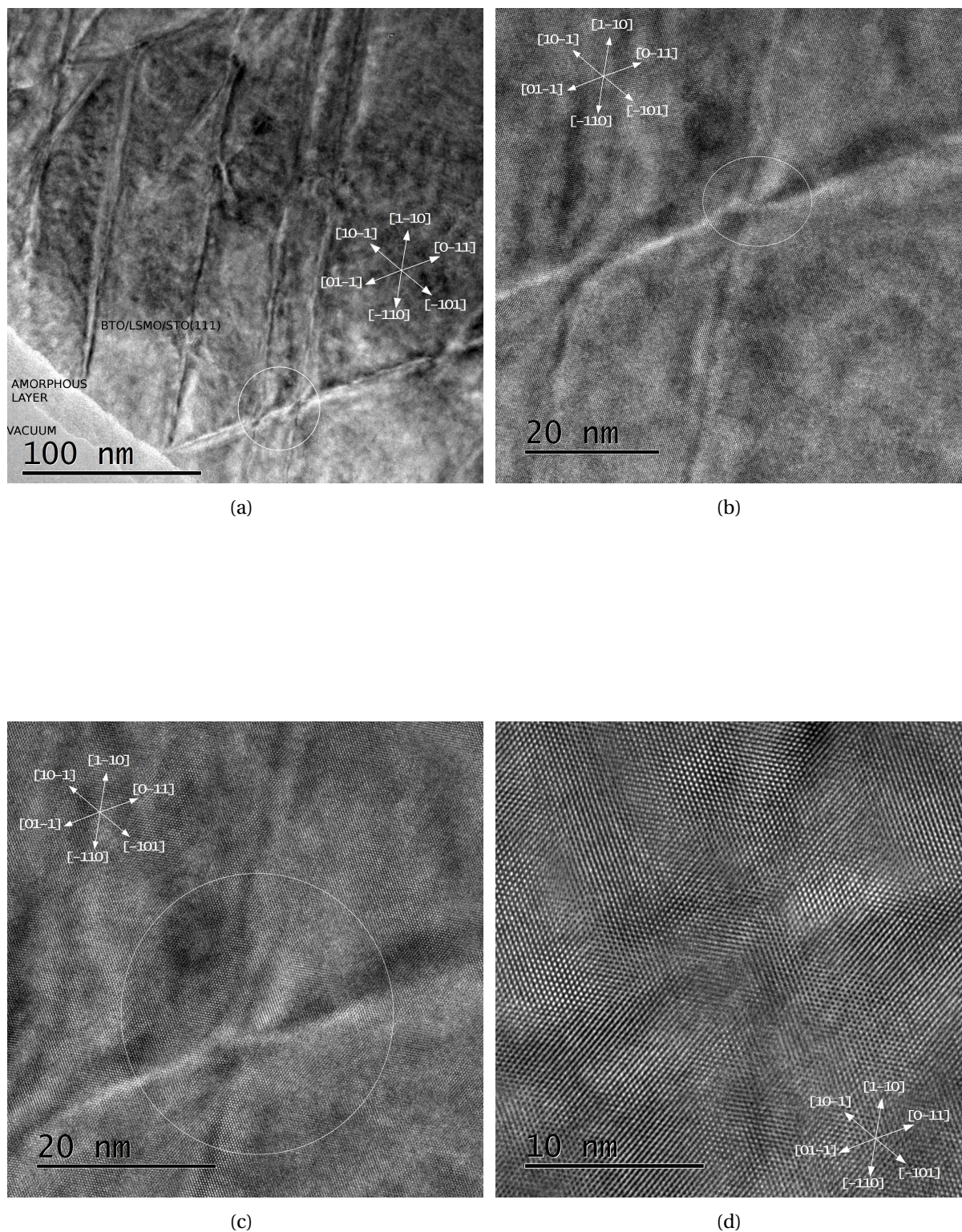


Figure 5.25: HR-TEM images taken along the $[111]_c$ zone-axis on the *Jeol-Jem 2100F* from the 3-10-PV specimen. Note that edge dislocations along $[0\bar{1}1]_c$, $[1\bar{1}0]_c$, $[1\bar{2}1]_c$ and $[11\bar{2}]_c$ are visible in these images. An amorphous layer is visible at the edge in figure (a). This is probably due to the glue used during the specimen preparation.

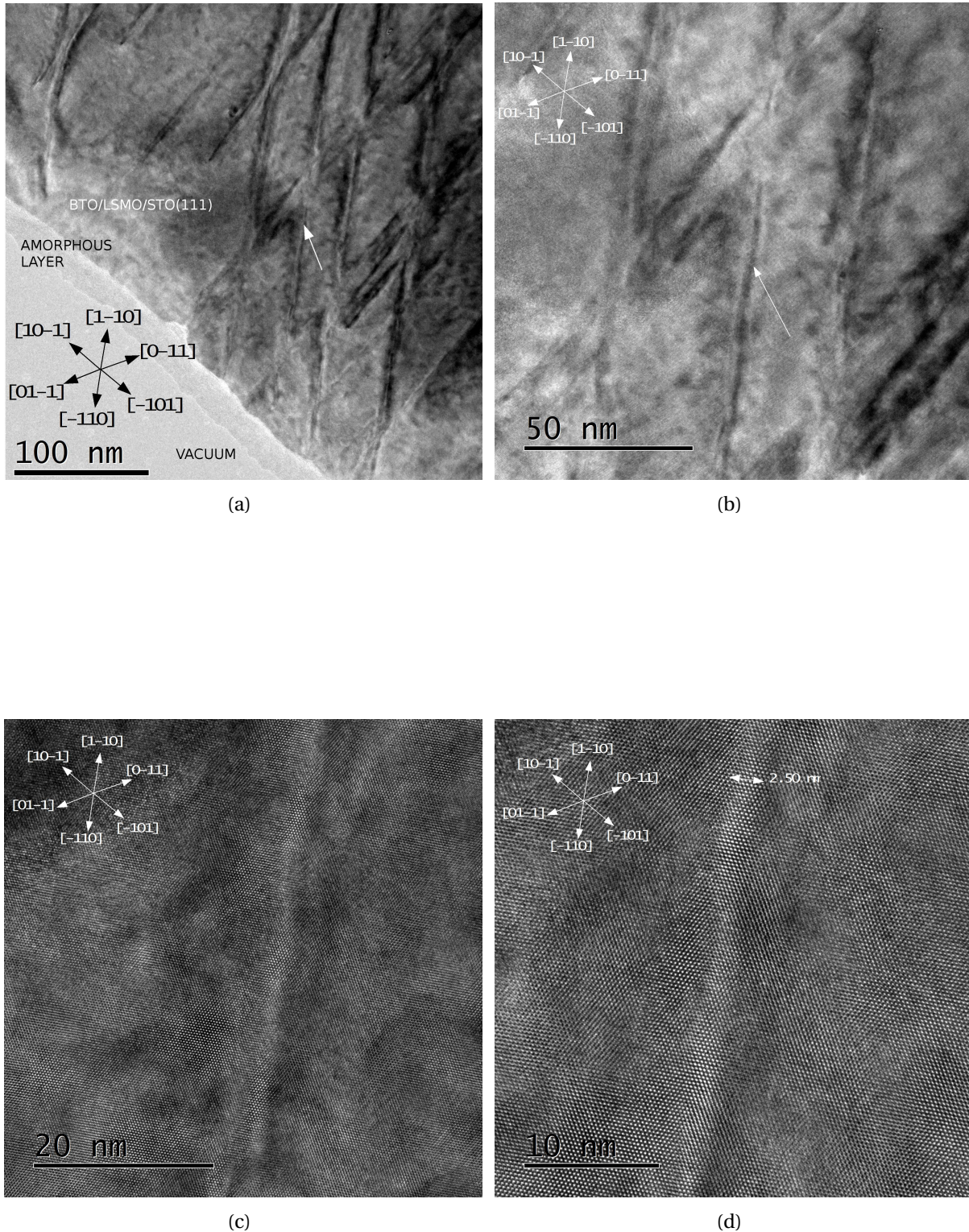


Figure 5.26: HR-TEM images taken along the $[111]_c$ zone-axis on the *Jeol-Jem 2100F* from the 3-10-PV specimen. Note that edge dislocations along $[1\bar{1}0]_c$ and $[1\bar{2}1]_c$ are visible in these images. An amorphous layer is visible at the edge in figure (a). This is probably due to the glue used during the specimen preparation. In figure (d), the width of the strain field around a dislocation line is measured to be around 2.5 nm.

5.3 EELS Analysis of Mn oxidation state and oxygen-vacancies in LSMO

Four EELS data sets were analyzed in this work. In figure 5.27, one of them is shown. On the left, a survey image with STO, LSMO and BTO from bottom to top can be seen. The green rectangle shows where the EELS data collection was performed. On the right, the spectra from STO, LSMO and BTO from bottom to top can be seen.

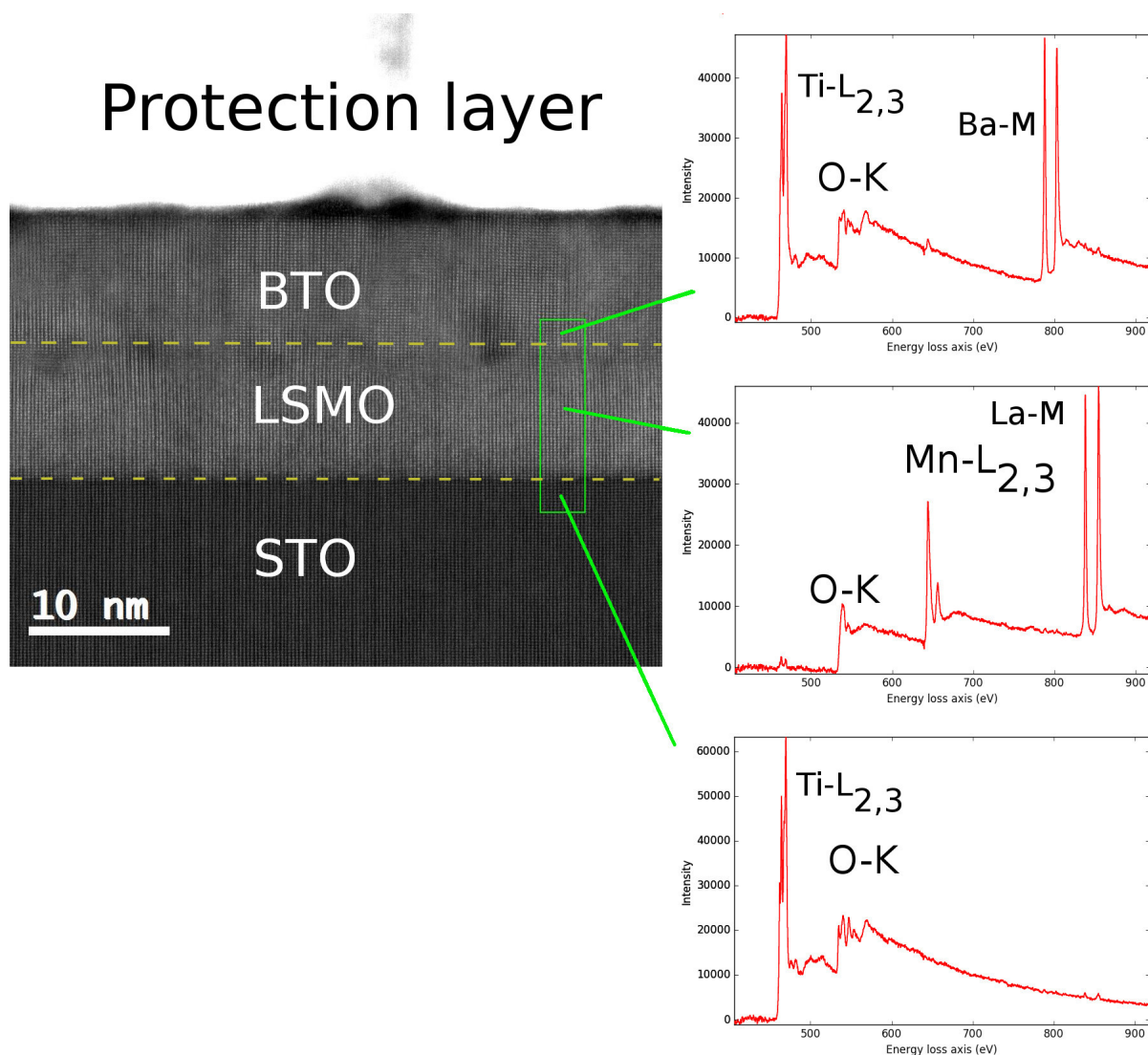


Figure 5.27: EELS high-loss image along the $[11\bar{2}]_c$ zone-axis from the 10-10-CS specimen. The direction parallel to the film was integrated out and PCA was used to reduce noise using HyperSpy. The image to the left is a survey image with STO, LSMO and BTO from bottom to top, while the green rectangle shows where the EELS data collection was performed. On the right, the spectra from STO, LSMO and BTO from bottom to top can be seen. The STEM-EELS data was collected on the *Jeol-Jem ARM 200F* from the 10-10-CS specimen.

In figure 5.28, the Mn L₃ and L₂ peaks from LSMO can be seen with a Gaussian fit in blue. In figure 5.29, the $\frac{I_{L_3}}{I_{L_2}}$ -ratio is plotted versus distance normal to the interface. The STO/LSMO interface is at $x \approx 3$ nm and the LSMO/BTO interface is at $x \approx 13$ nm. The ratio is higher at the STO/LSMO and LSMO/BTO interfaces. This means that the Mn oxidation state is lower at the interfaces, which implies that the density of oxygen-vacancies is higher there. This is consistent with the observations done in [88]. The ratio has a relatively constant value of $R_{Mn} = 4.4$ in LSMO (except for at the interfaces). According to (4.4), this gives an Mn oxidation state of $V_{Mn} = 1.83$. It should be noted that the minimum possible oxidation state of Mn is +2.3, so this value is clearly not correct. This is because the lowest possible oxygen concentration in a perovskite structure is +2.5 [49]. Hence, the oxidation state of Mn in $\text{La}_{0.7}^{3+}\text{Sr}_{0.3}^{2+}\text{Mn}^{V_{Mn}}\text{O}_{2.5}^{2-}$ is $-(0.7 \cdot (+3) + 0.3 \cdot (+2) + 2.5 \cdot (-2)) = +2.3$. The data used to obtain the fit in (4.4) cover the range of V_{Mn} all the way down to its lowest possible value in LSMO. That is to say, the fit in (4.4) should be valid in a sufficient range to use it in this work. Hence, the range of the fit is not an issue, and the incorrect V_{Mn} -value is rather related to the issues discussed in section 4.6. It is also interesting to note that a linear fit was obtained in [89], $R_{Mn} = a + b \cdot V_{Mn}$, $a = 5.0 \pm 0.4$ and $b = -0.73 \pm 0.11$, giving $V_{Mn} = 0.82$, which is clearly incorrect. In [7], it is remarked that this relation should be linear, in disagreement with [91]. In conclusion, it does not seem like it is possible to obtain a quantitatively correct estimation of the Mn oxidation state in 10-10-CS by using fits from the literature.

The stoichiometric oxidation state of Mn in LSMO is $-(0.7 \cdot (+3) + 0.3 \cdot (+2) + 3 \cdot (-2)) = +3.3$. Even though (4.4) does not give a precise Mn oxidation state, the low value obtained here indicates qualitatively that Mn has a much lower oxidation state than in stoichiometric LSMO.

In figure 5.30, the oxygen K-edges from (a) STO, (b) LSMO and (c) BTO are shown. As can be seen, the A pre-peak is present in both STO and BTO, but not in LSMO, confirming that there are several oxygen-vacancies in LSMO.

In figure 5.31, the normalized O-KA prepeak is plotted versus distance normal to the thin film interfaces, as in [88]. It shows a lower oxygen concentration in LSMO compared to STO and BTO, which is consistent with figures 5.29 and 5.30.

At this point, a comment on the tensile strain of LSMO perpendicular to the thin film interface (5.1) is appropriate. Simultaneously with the measurements performed on the 10-10-CS specimen on the *Jeol-JEM ARM 200F*, XRD was utilized by the Oxide Electronics Lab to

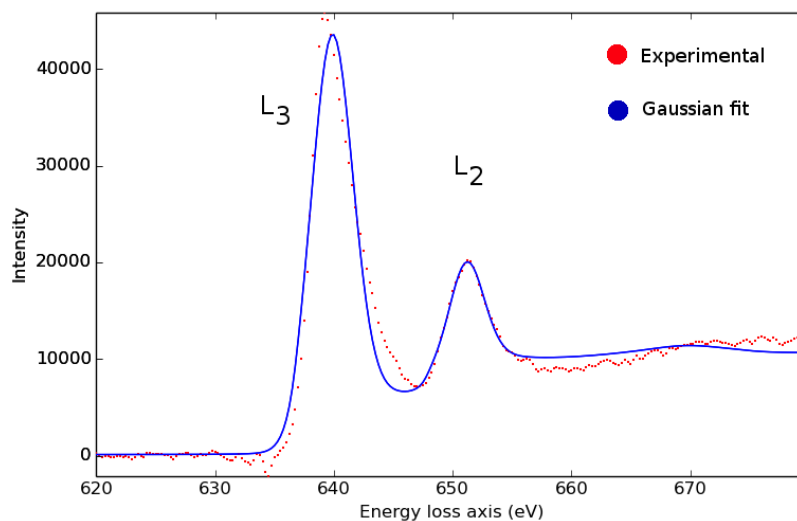


Figure 5.28: Mn L_3 and L_2 peaks from LSMO in figure 5.27. The blue graph is a Gaussian fit to the experimental data points in red.

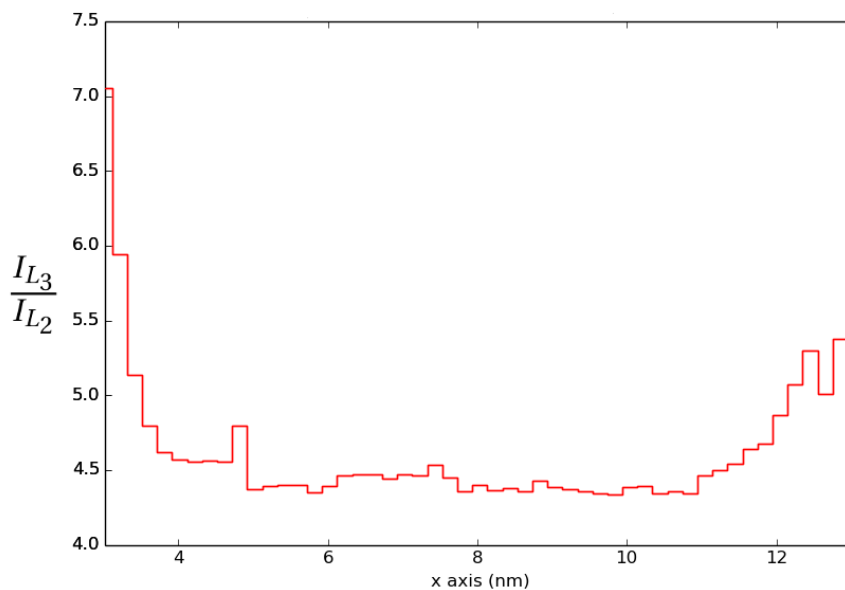


Figure 5.29: $\frac{I_{L_3}}{I_{L_2}}$ as a function of distance normal to the film interface. In this figure, the STO/LSMO interface is at $x \approx 3$ and the LSMO/BTO interface is at $x \approx 13$ nm. These coincide with the points where $\frac{I_{L_3}}{I_{L_2}}$ rises and drops abruptly. This indicates that the Mn oxidation state is lower at the interfaces.

investigate the same thin film systems. Their findings, which are unpublished at the moment of this writing, gave a compressive strain of LSMO in the direction perpendicular to the thin film interface, inconsistent with the result reached here [102].

One possible explanation of this disagreement with the XRD measurements could be the

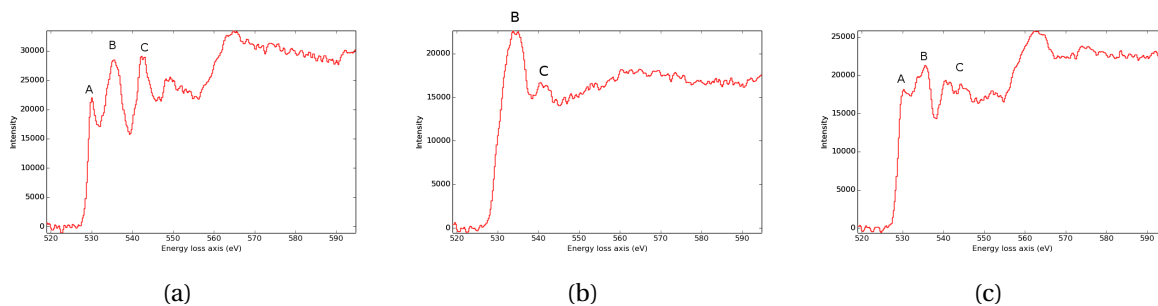


Figure 5.30: O-K edge from (a) STO, (b) LSMO and (c) BTO.

high concentration of oxygen-vacancies in the LSMO layer, which also leads to a lower Mn oxidation state. It is well known that different oxidation states of transition metals in oxides leads to widely differing physical and chemical properties [89, 95, 96, 97]. Since the 10-10-CS specimen was produced using FIB, there could be problems associated with using FIB for producing TEM specimens containing LSMO [73]. For example, beam knock-on damage where oxygen atoms are dislodged from the oxide due to the incoming Ga^+ ions [105]. Furthermore, there was a 2 month lag between specimen preparation and TEM characterization of the 10-10-CS specimen. During this time period, oxidation may have taken place gradually. In addition, it is known that the electron beam itself can cause damage in LSMO. In [106], it was found that the electron beam makes LSMO sub-stoichiometric by creating oxygen-vacancies. This is consistent with the findings done here. The loss of oxygen atoms were found to lower the oxidation state of Mn, and it was concluded that this may potentially lead to wrong interpretations of electronic, magnetic and structural properties. In particular, significant changes were observed in the fine structures of the O-K and Ti-L_{2,3} peaks. A low oxygen concentration could cause a phase transition in the LSMO layer, e. g. to the brownmillerite phase. In [100], electron beam induced phase transitions to the brownmillerite phase in LSMO thin films were investigated. The oxygen-vacancies induced by the electron beam first form an ordered brownmillerite structure, then a disordered structure [100]. It is also interesting to note that a significant increase of the out-of-plane lattice parameter was observed, as this might explain the tensile strain in LSMO normal to the interface observed in this work. It is also known that removal of oxygen leads to an increase in the size of the unit cell [107], because the oxygen atoms pulls the elements in the structure closer to each other through attractive Coulomb forces.

The O-K peaks in [100] were plotted before radiation, after the transition to the ordered brownmillerite phase and after the transition to the disordered phase, as can be seen in fig-

ure 5.32. Upon comparison to figure 5.30 (b), it seems like LSMO in this work has been transformed to a brownmillerite phase or to over-irradiated LSMO. As discussed earlier, the hypothesis that the additional super-reflections can be attributed to oxygen-vacancy ordering is not viable because the ordering should occur in the $[001]_c$ -direction in the brownmillerite phase. It is therefore more likely that the oxygen-vacancies in LSMO in the material studied here are disordered.

The EELS analysis was repeated for three additional EELS data sets. The results can be found in Appendix B. For the analysis of the O-K peak, the results in Appendix B support these findings. However, the data sets in Appendix B are not as good as the one shown in this chapter. That is to say, the energy range of the scans were cropped so that the tail of the L_2 peak is missing, and therefore the Gaussian fits to the L_2 peak were not useful.

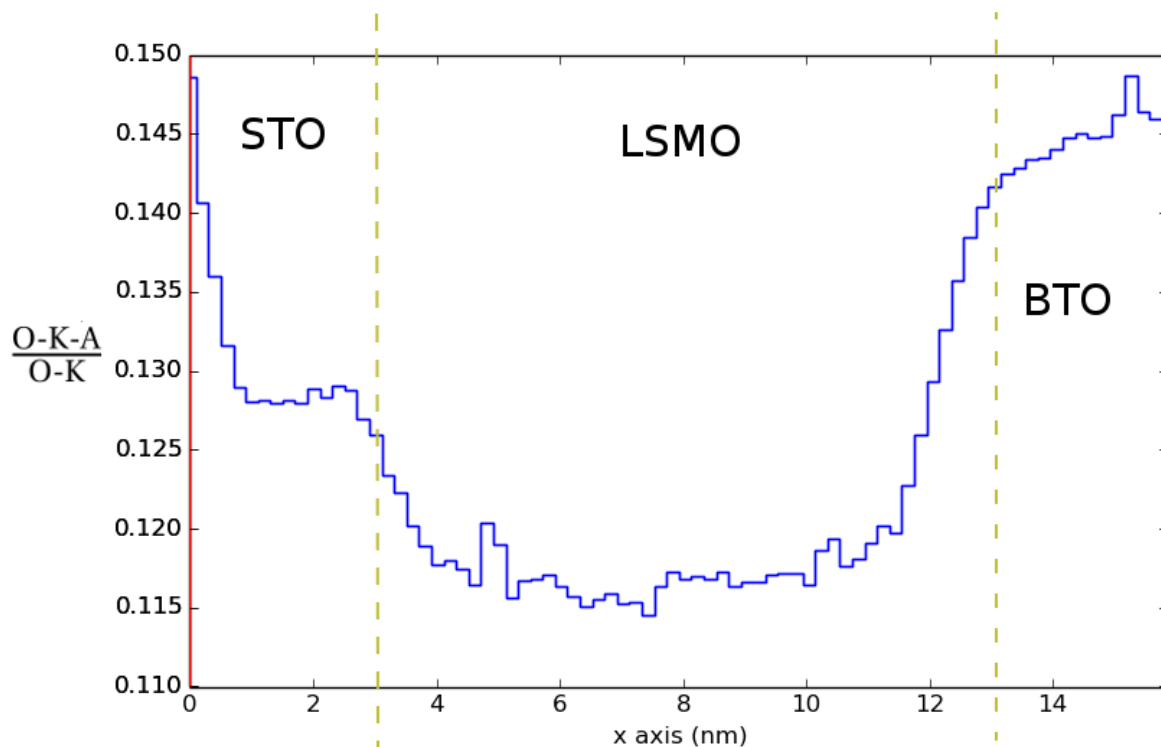


Figure 5.31: The integrated A prepeak intensity normalized over the entire O-K intensity as a function of distance normal to the thin film interface. As can be seen, the oxygen content is lowest in LSMO and highest in BTO. In this figure, the STO/LSMO interface is at $x \approx 3$ and the LSMO/BTO interface is at $x \approx 13$ nm.

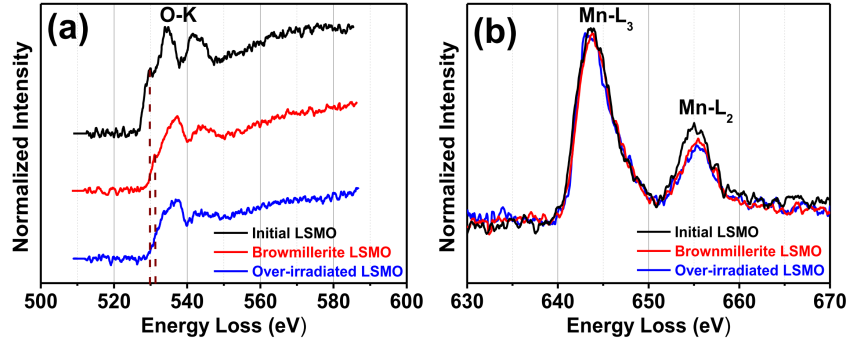


Figure 5.32: STEM-EELS spectra of (a) the O-K edge for three structural phases in LSMO induced by electron beam damage and (b) the Mn- $L_{2,3}$ edge. Upon comparison to figure 5.30 (b), it seems like LSMO in this work has been transformed to a brownmillerite phase or to over-irradiated LSMO. From [100].

5.4 Ferroelastic domain walls in LSMO

In figure 5.33 (a), a domain wall can be seen in the 10-10-CS specimen. In figure 5.33 (b), the domain wall is marked with a white line. As can be seen, the domain wall is approximately parallel to the $[021]_c$ -direction. This is consistent with it being a domain wall between domains R_1 and R_4 of $(100)_c$ type, as shown in table 2.6. Note that this domain wall is not viewed edge-on. The angle between the normal of the domain wall and $[11\bar{2}]_c$ is $\arccos\left[\frac{1}{\sqrt{6}}\right] = 65.91^\circ$. This means that the domain wall is skewed 24.09° relative to $[11\bar{2}]_c$. Thus, the domain wall should not be quite sharp, but have an extent $d = t \cdot \tan(24.09^\circ)$, where t is the specimen thickness. However, the domain wall appears to be atomically sharp. All the other types of ferroelastic domain walls listed in table 2.6 are skewed relative to $[11\bar{2}]_c$, except $R_3 + R_4$, but this type of domain wall is not consistent with the observed orientation. A possible explanation is that the orientations of the domain walls given in table 2.6 are no longer valid when LSMO has been monoclinically distorted. If this is true, the identification of the R_1 and R_4 domains is also put into doubt. Therefore, an investigation of how the LSMO domains changes when LSMO undergoes a monoclinic distortion must be done in order to properly understand the origin of the observed super-reflections in these two phases.

In figure 5.33 (c), an FFT of the entire region in 5.33 (a) is shown and in figure 5.33 (d) a SAD pattern from the entire region is shown. Both of the patterns show super-reflections from both the R_1 and R_4 domains, as they should. By doing a live FFT in Digital Micrograph,

it was observed that the R_4 pattern was present on the left and the R_1 pattern on the right. As a reminder, the R_4 pattern alone can be seen in figure 5.1 (b) and the R_1 pattern alone in figure 5.1 (d).

Finally, an ASTAR scan was done across the domain wall. The super-reflections corresponding to domain R_4 were selected using virtual DF imaging in HyperSpy, as shown in figure 5.34 (a). This resulted in the region on the right in figure 5.34 (b) being bright. The approximate orientation of the domain wall is marked with a white line in figure 5.34 (b). Next, the super-reflections corresponding to domain R_1 were selected, as shown in figure 5.35 (a). This resulted in the region on the left in figure 5.35 (b) being bright. The approximate orientation of the domain wall is marked with a white line in figure 5.35 (b), and it overlaps with the domain wall in figure 5.34 (b). Its angle to the normal was measured to be approximately $40^\circ \pm 4^\circ$. Note that this angle should be 39.23° according to table 2.6.

Figures 5.36 shows an area where a domain wall is located in the 3-10-CS specimen, seen from the $[11\bar{2}]_c$ zone-axis. In both images, the R_1 domain state is present in the upper left area, while the R_4 domain state is present in the lower right area. In 5.36 (a), a red rectangle produced in Digital Micrograph shows the region used to construct the FFT in figure 5.36 (b) using live FFT. This gives the super-reflections associated with domain state R_1 .

Similarly, when the red square is moved down to the R_4 area in figure 5.36 (c), super-reflections corresponding to the R_4 domain state appear, as can be seen in figure 5.36 (d). However, it was not possible to directly observe the domain wall in this specimen, as it was in 10-10-CS. The reason for this may be a lower TEM specimen quality, a lower quality of the thin film system or the lower resolution of the *Jeol-Jem 2100F* compared to the *Jeol-Jem ARM 200F*.

In figure 5.37, an ASTAR virtual DF image on a scan performed along the $[1\bar{1}0]_c$ zone-axis on the 3-10-CS specimen can be seen. By looking at figure 4.10, it is clear that the reflection selected in figure 5.37 (a) corresponds to a R_4 domain state. In figure 5.37 (b), a bright R_4 region appears on the lower right.

As discussed in earlier sections, several stripes were observed in the 3-10-PV specimen. However, these were attributed to edge dislocations. Their distance and spacing are not consistent with the distance and spacing between ferroelastic domain walls observed in the CS specimens. For example, in the 10-10-CS specimen, only one ferroelastic domain wall was found in a specimen with a ROI several μm wide. The situation was similar in the 3-10-CS

specimen. On the other hand, the observed stripes can be explained as edge dislocations with no contradictions.

Next, a comment on the energetics of ferroelastic domains. In bulk LSMO, the free energy in the four rhombohedral domains $R_1 - R_4$ is the same. However, when an external stress is applied, such as in a thin film system, the degeneracy is lifted and the domain state having its unique body diagonal closest to the stressed direction will lower or increase its energy relative to the other domain states [49]. If the unit cell of LSMO is larger than the unit cell of STO, which seems to be the case in 10-10-CS due to oxygen-vacancies, LSMO will align its unique body diagonal as parallel to the interface as possible [49]. However, these arguments are based on energetics related to strain. Due to the reduction of symmetry in LSMO to a monoclinic phase, there may have been a loss of inversion symmetry. Hence, the energetics related to ferroelectric polarization may have to be taken into account. A complete description of the energetics of the two domains observed in LSMO must take all these factors into account.

It is easier to tailor the properties of a homogeneous thin film system. There are stress and strain fields associated with ferroelastic domain walls [49]. In addition, the behavior of the thin film system could differ from one domain to another. It would therefore be best to avoid domain walls in LSMO in order to have better control over the properties of the system. As discussed in [7], strain engineering can be used to tailor the properties of the thin film by choosing different substrates. A suggestion for the future is to study how strain engineering can be used to induce a mono-domain state in LSMO.

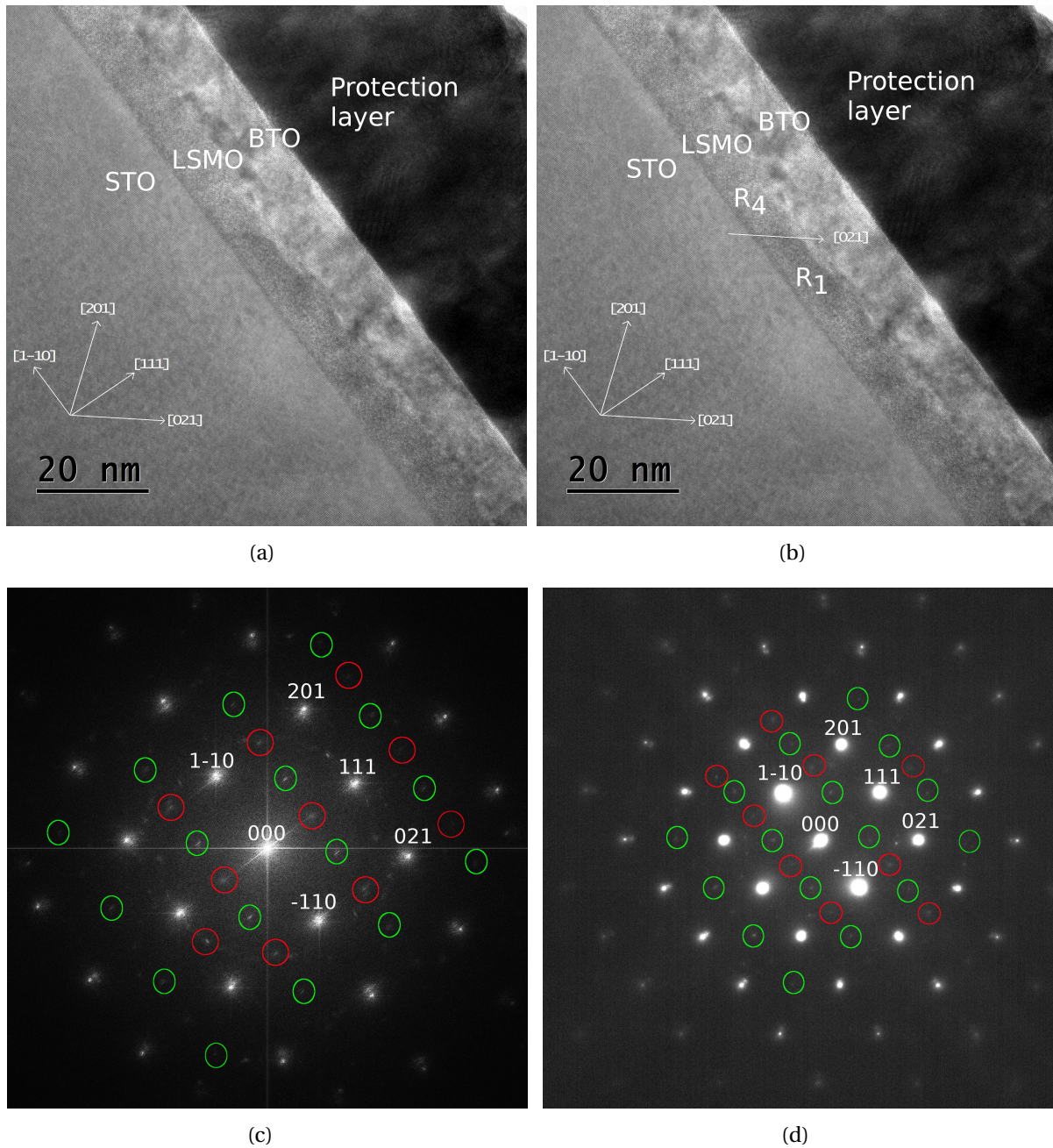


Figure 5.33: **(a)** BF-TEM image acquired along the $[11\bar{2}]_c$ zone-axis from the 10-10-CS specimen on the *Jeol-Jem ARM 200F*. Note the bright spots on top of the BTO layer. These spots are located underneath bright areas in the Pt/Pd (80/20)-alloy protection layer. Hence, these artefacts are just due to damage from the FIB. A ferroelectric domain wall in BTO should intersect $(11\bar{2})_c$ along $[111]_c$, $[1\bar{1}0]_c$, $[\bar{1}31]_c$ or $[3\bar{1}1]_c$, as listed in table 2.3. A ferroelastic domain wall is visible in the LSMO layer, indicated by an arrow. This domain wall separates a R_1 and a R_4 domain along $(100)_c$. Furthermore, it is observed that the R_4 domain has additional super-reflections not seen in the simulations, while the R_1 domain does not. These super-reflections are probably due to a reduction in symmetry due to a monoclinic distortion. **(b)** Figure (a) with an arrow along $[021]_c$ indicating the domain orientation. **(c)** FFT of figure (a). **(d)** SAD pattern from the region shown in (a). Note that there are super-reflections corresponding to both domain states R_1 and R_4 present, marked by red and green circles, respectively.

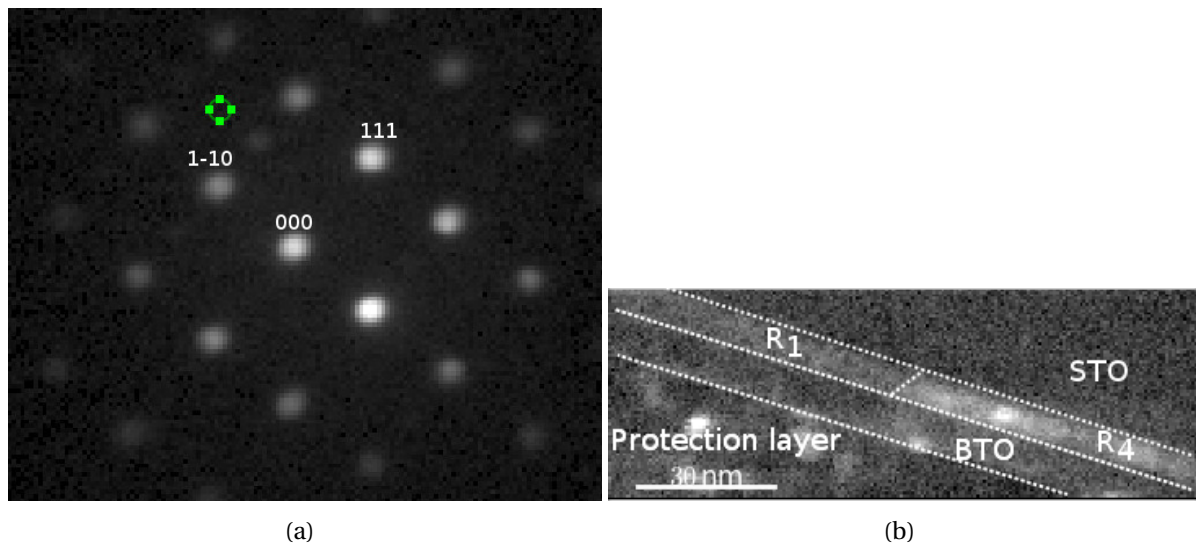


Figure 5.34: **(a)** Virtual DF used on ASTAR data, where a super-reflection from the R_4 domain is selected by the green software aperture. **(b)** The resulting virtual DF image. The region on the right is in the R_4 domain state, and appears brighter than the region on the left. The ASTAR data was acquired on the *Jeol-Jem 2100F* from the 10-10-CS specimen. Note that there is a small rotation between the DP and the image.

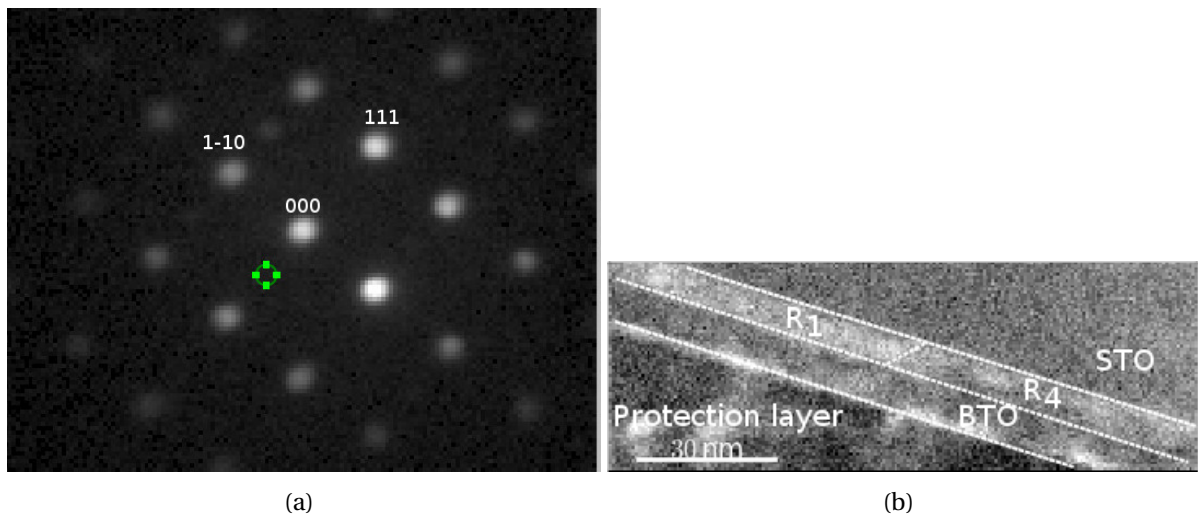


Figure 5.35: **(a)** Virtual DF used on ASTAR data, where a super-reflection from the R_1 domain is selected by the green software aperture. **(b)** The resulting virtual DF image. The region on the left is in the R_1 domain state, and appears slightly brighter than the region on the right (the signal was weak in this case). The ASTAR data was acquired on the *Jeol-Jem 2100F* from the 10-10-CS specimen. Note that there is a small rotation between the DP and the image.

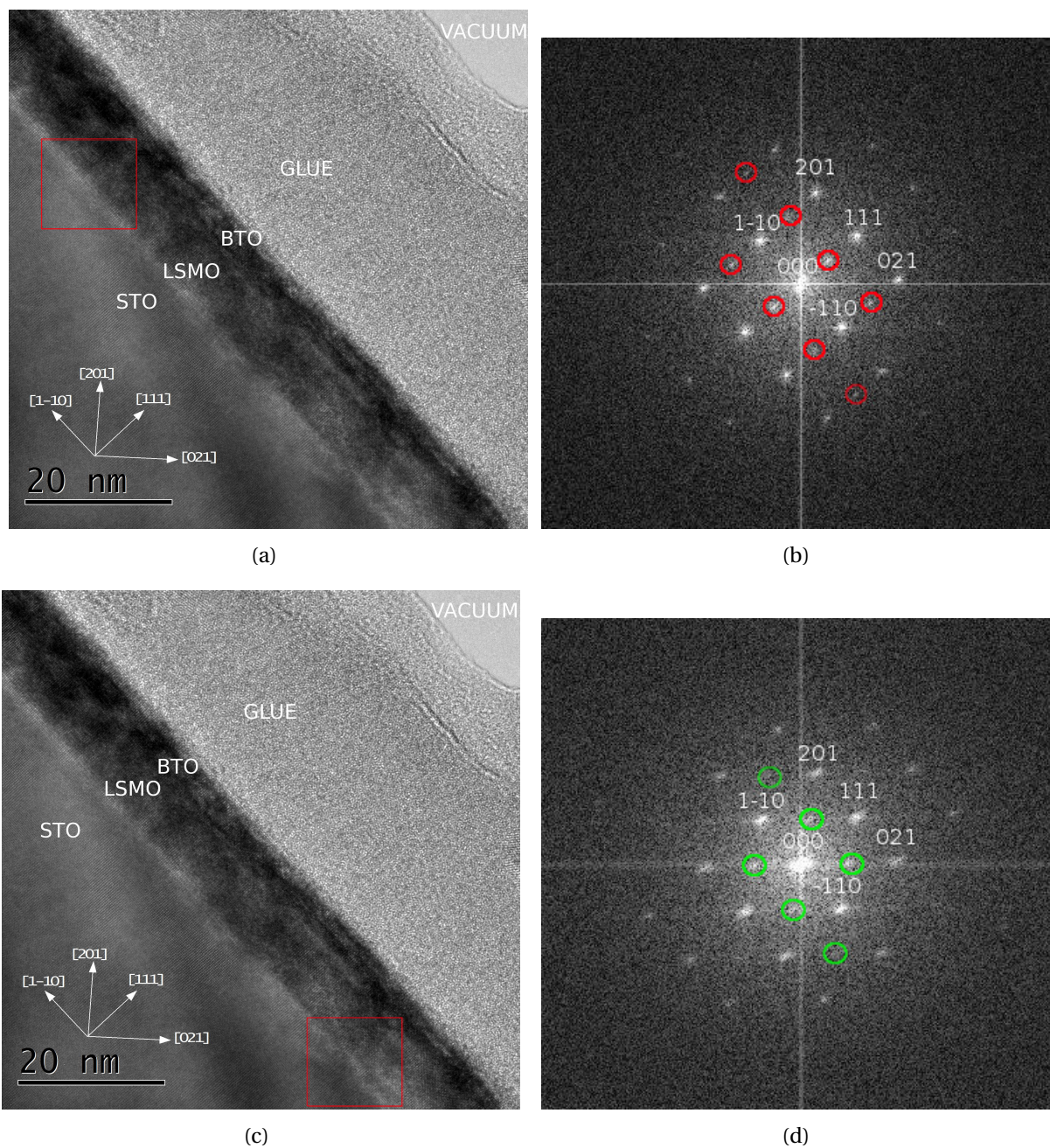


Figure 5.36: HR-TEM images acquired along the $[11\bar{2}]_c$ zone-axis on the *Jeol-Jem 2100F* from the 3-10-CS specimen. **(a)** The red square in the upper left is present in the R_1 domain state region. **(b)** The FFT corresponding to the area in **(a)**, showing super-reflections corresponding to the R_1 domain, marked with red circles. **(c)** The red square on the lower right is present in the R_4 domain state region. **(d)** The FFT corresponding to the area in **(c)**, showing super-reflections corresponding to the R_4 domain, marked with green circles.

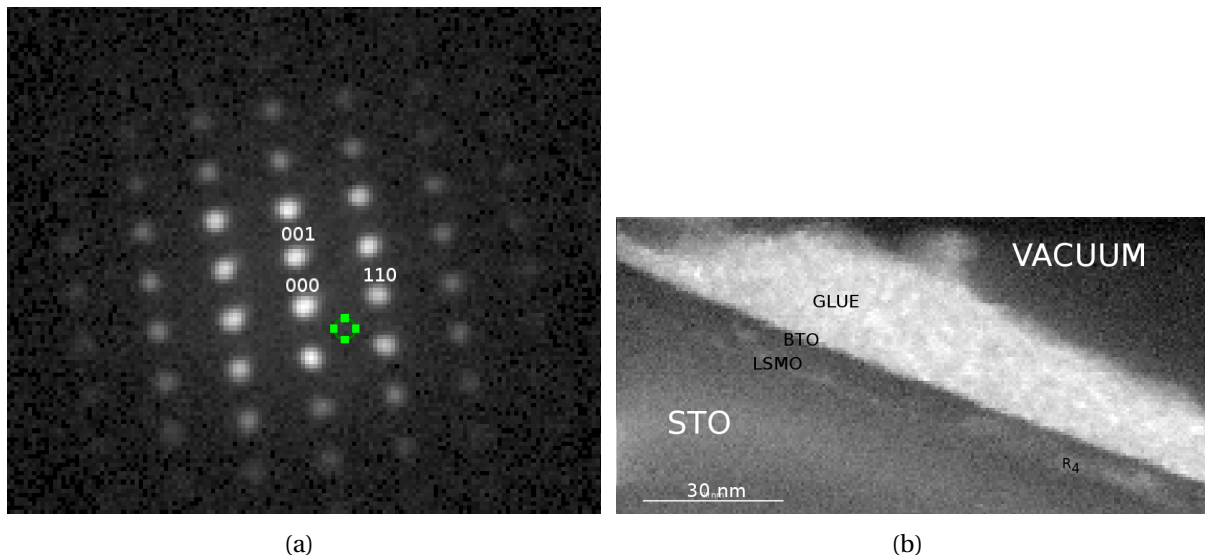


Figure 5.37: ASTAR DF image acquired along the $[1\bar{1}0]_c$ zone-axis on the *Jeol-Jem 2100F* from the 3-10-CS specimen. When selecting the R_4 reflection with the green software aperture, a region on the right glows up. Note that there is a small rotation between the DP and the image.

5.5 Ferroelectric domains in BTO

No ferroelectric stripe domains were observed in the 10-10-CS specimen. Contrast was observed along lines parallel to $[112]_c$ when the specimen was observed along $[1\bar{1}0]$, as can be seen in figure 5.2. However, the direction of these contrast lines is not consistent with the possible orientations of ferroelectric domain walls in tetragonal thin films on (111) substrates, as discussed earlier (see table 2.2). When the specimen was observed along the $[11\bar{2}]_c$ zone-axis, no clear contrast occurred along any direction, as can be seen in figure 5.33. A similar conclusion was reached for the 3-10-CS and the 3-10-PV specimens.

If ferroelectric stripe domains were present, they should be visible in phase contrast images. This was observed in [48]. Since no such structure was observed here, it is concluded that the BTO thin films are in a mono-domain state in all the specimens studied in this work. In [15], it was found that there is no critical film thickness for domain pattern formation in (111) oriented tetragonal ferroelectric thin films. This is one of the reasons for expecting there to be a domain structure, even in very thin films of 3 and 10 nanometer thicknesses. However, there may be other reasons for not having a domain structure, such as the LSMO thin film inserted in between STO(111) and BTO.

5.5.1 Mapping of the ferroelectric polarization

An attempt was done at mapping the evolution of the ferroelectric polarization as a function of distance from the thin film interface using Ranger [77]. The result can be seen in figure 5.38. Due to the large amount of dislocations in this specimen, as discussed above, it was not possible to map the displacement of the Ti columns in BTO. This can be seen more clearly in figures 5.39 (a) and (b), where the area in STO marked by a red rectangle in figure 5.38 and the area in BTO marked by a green rectangle in figure 5.38, can be seen, respectively. It is clear that the Ti columns are not detected at all in BTO. There are two reasons for this. Firstly, the displacement and strain fields around the dislocations decrease the quality of the image. Secondly, the atomic number of Ba is 56, the atomic number of Sr is 38 and Ti has atomic number 22. Since the contrast in HAADF-STEM scales as Z^2 [20, 108, 109, 110], the intensity from Ti is weaker relative to the intensity of Ba than relative to the intensity of Sr. In addition, a 50 Hz background noise, probably from the power line, was detected in the HAADF-STEM scans. However, it is of great interest to determine the evolution of the ferroelectric polarization close to the BTO/LSMO interface [111]. Thin films of higher quality or a better TEM specimen preparation procedure are needed for this purpose.

5.5.2 Dark-field imaging

A common method for imaging ferroelastic or ferroelectric domains is to use DF-imaging to select the different super-reflections corresponding to different domains [34]. This was done above for the ferroelastic domains in LSMO. However, as can be seen in figures 2.14, 4.11, 4.12 and 4.13, the reflections from different ferroelectric domains in BTO are extremely close to each other. As mentioned above, the BTO thin films were found to be in ferroelectric mono-domain states in this work. Thus, DF-imaging to select different domains was not needed. However, in [48], a ferroelectric domain structure was observed due to phase contrast. The reflections from different ferroelectric domains could not be selected for DF imaging, because they were too close to be resolved by any objective aperture, or even when using an arbitrarily small virtual objective aperture when performing virtual DF. Another challenge is that the spread of the diffraction spots due to strain and edge dislocations is larger than the reciprocal space distance between the reflections from different domains.

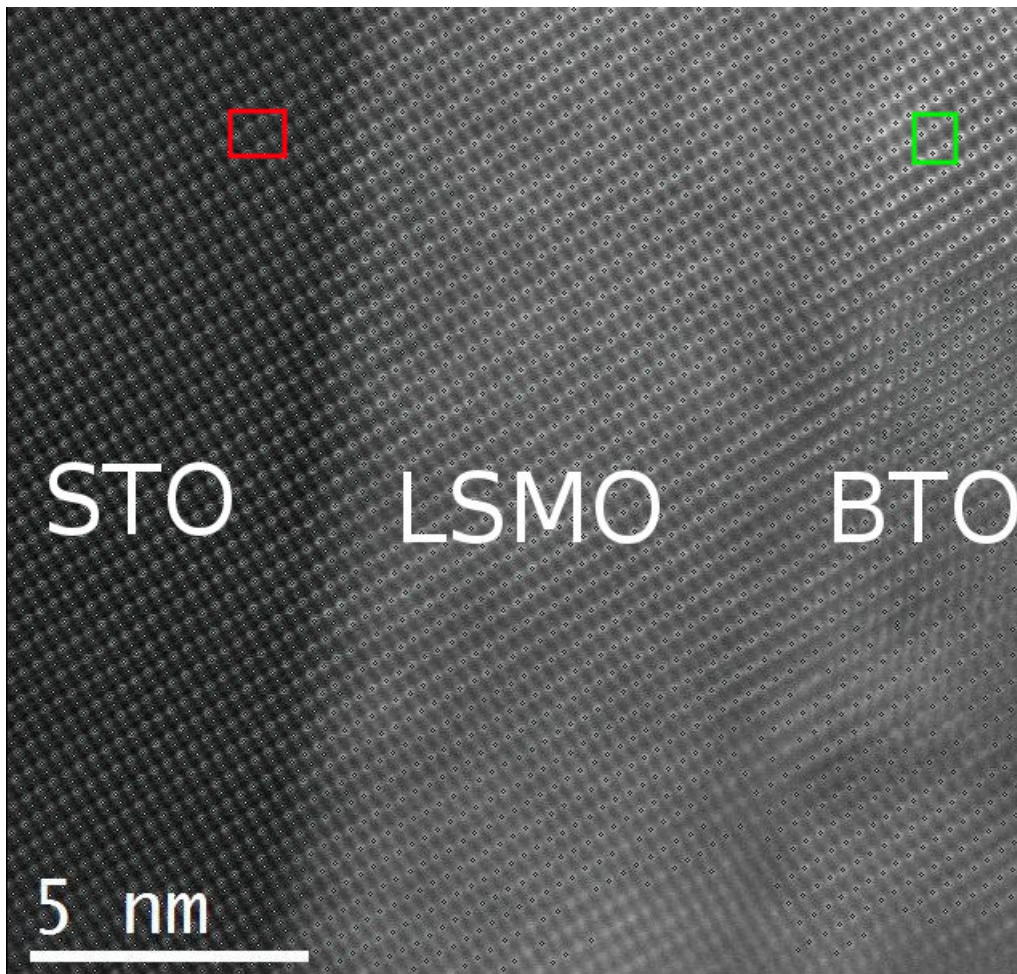


Figure 5.38: HAADF-STEM $[1\bar{1}0]_c$ zone-axis image, figure 5.9, processed in Ranger. Gaussians were fitted to the atomic positions. As can be seen, the Ti columns are detected in STO, but not in BTO.

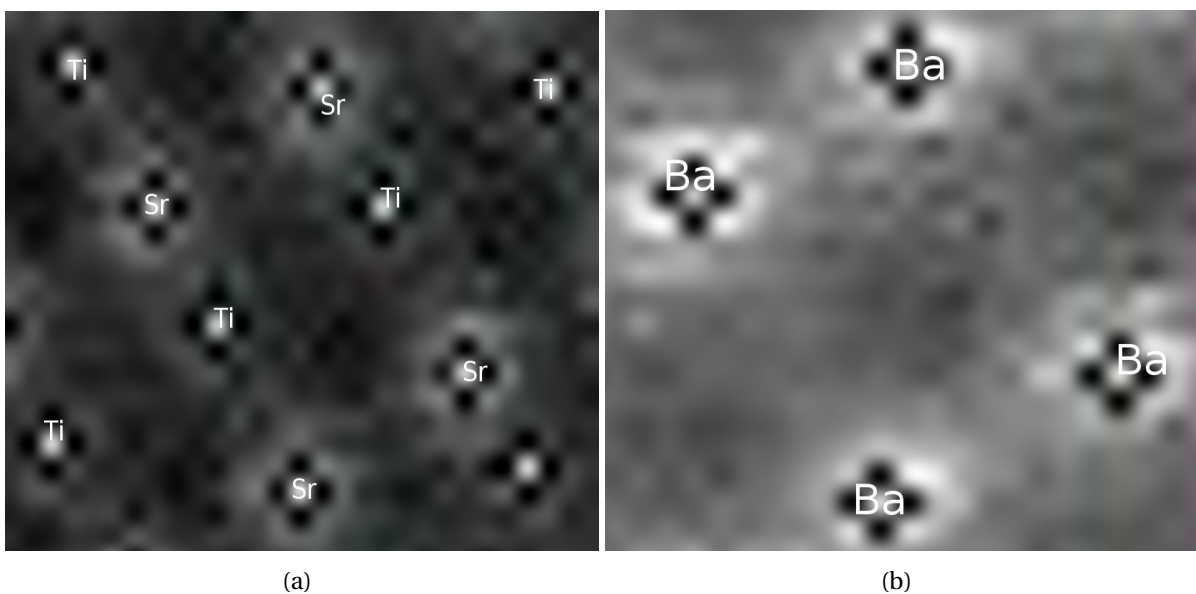


Figure 5.39: **(a)** Region in STO marked by red rectangle in figure 5.38. As can be seen, both the Sr and Ti columns are visible. **(b)** Region in BTO marked by green rectangle in figure 5.38. As can be seen, only the Ba columns are visible. Note that the shape of the peaks is due to a scaling of the image, and is an artefact of the image handling software.

Chapter 6

Conclusions

The main conclusions arrived at in this work are:

- Several misfit dislocations were observed in the BTO layer in all specimens. These were edge dislocations, created by inserted $\{110\}_c$ or $\{11\bar{1}\}_c$ planes.
- Some edge dislocations created a quasi-periodic contrast in the images that was reminiscent of ferroelectric stripe domains. However, their orientation was not consistent with the allowed ferroelectric structures, and on this basis it was concluded that the contrast was due to edge dislocations.
- Other edge dislocations were observed clearly, and there was no doubt that they were indeed edge dislocations.
- Due to the misfit dislocations and the strain and displacement fields around these, it was not possible to map the Ti column displacements in the BTO thin film.
- No ferroelectric stripe domains were observed in any of the thin film systems, and it was concluded that BTO is in a ferroelectric mono-domain state.
- It was observed in the SADP simulations of ferroelectric domains in BTO, as well as in the computation of the $[111]_c$ DP from [48], that the reflections corresponding to different ferroelectric domains appear very close to each other in reciprocal space. In fact, they were found to overlap in the experimental SADPs in [48]. This should be kept in mind if this technique is used to map ferroelectric domains in BTO in the future.

- The BTO thin film was relaxed in the 10-10-CS specimen. The SADPs and FFTPs indicate that the 3-10-CS and 3-10-PV specimens do not have relaxed thin films. However, since dislocations were observed in BTO in these specimens, the BTO thin films must be partially relaxed. A possible explanation is that the signal from the 3 nm BTO layer is too weak and too spread out to be detected.
- The LSMO thin film had additional super-reflections in the FFTPs and SADPs, attributed to a monoclinic distortion of the unit cell.
- Monoclinically distorted R_1 and R_4 domain states were hypothesized to be present. A domain wall between these was observed. However, even though this is a possible explanation of the two observed phases, further work is needed to confirm this.
- LSMO was coherent with STO parallel to the interface and tensilely strained perpendicular to the interface.
- The Mn oxidation state was lowered at the STO/LSMO and the LSMO/BTO interfaces, and was much lower than in stoichiometric LSMO throughout the thin film.
- The concentration of oxygen was lower in LSMO than in STO and BTO. The low oxygen concentration may have been caused by the FIB specimen preparation. However, it is also possible that it was caused by the electron beam, as this is a known mechanism for the creation of oxygen vacancies in LSMO. Oxygen vacancies could also have been created gradually during the two month storage time between specimen preparation and characterization.
- XRD measurements on these systems were inconsistent with the observed tensile strain in LSMO observed in the GPA analysis.
- The high Mn oxidation state combined with the high concentration of oxygen vacancies may have lead to the observed tensile strain.
- The observed super-reflections in the FFT patterns and SAD patterns are probably not caused by oxygen-vacancy ordering in LSMO. The observed directions of the super-reflections are not consistent with any known oxygen vacancy super-structure. It is more probable that these super-reflections are an intrinsic feature of the monoclinically distorted LSMO crystal structure. The oxygen vacancies are probably disordered.

Chapter 7

Further work

In order to further characterize the BTO/LSMO/STO(111) systems studied in this work, the work done here should be repeated for different thicknesses of the BTO layer in order to see how this affects the ferroelectric structure, the presence of misfit dislocations, film relaxation and strain as well as the EELS fine structure. It would be useful to collect CBED data in order to determine the space group of LSMO. A theoretical study of domain structures in monoclinically distorted LSMO must be done in order to understand the different domains observed in LSMO properly. It would also be interesting to collect HAADF-STEM data across a ferroelastic domain wall in LSMO, in order to study the strain and displacement fields in the different domains and at the domain wall. Next, it is recommended to anneal the sample in an oxygen rich atmosphere after the thin film synthesis and after the TEM specimen preparation in order to avoid oxygen vacancies. Furthermore, it is recommended to use a low voltage and shorter exposure times in the TEM to avoid electron beam induced oxygen vacancies. It is also recommended to study how different TEM specimen preparation techniques affect the specimen quality, as in [73]. Finally, the specimen should be characterized as soon as it is ready. If there is a lag between specimen preparation and characterization, its quality may deteriorate.

The challenge of mapping the ferroelectric polarization across the interface could be overcome if a sample with an even surface and few dislocations could be created. In this work, it was observed that even though the substrate was observed from a given zone-axis, the BTO thin film was not exactly in this zone-axis due to strain and rotations of the lattice in the thin film. The above mentioned recommendations could help create a specimen where this problem is solved. Furthermore, the HAADF-STEM contrast scales as Z^2 , which makes it difficult to detect Ti in BTO. It is therefore recommended to capture LAADF image stacks

as well in the future, because LAADF relies on diffraction contrast, and is useful for studying twinning, defects and deformed samples [112, 113]. 50 Hz scan noise in the HAADF-STEM images could be reduced by collecting image stacks with alternating scan directions in two perpendicular directions, and then processing in SmartAlign [114].

Bibliography

- [1] F. W. Brinkman, D. E. Haggan, and W. W. Troutman. A History of the Invention of the Transistor and Where It Will Lead Us. *IEEE Journal of Solid-State Circuits*, 32(12):1858–1865, 1997.
- [2] B. Lojek. *History of Semiconductor Engineering*. Springer, 2007.
- [3] G. E. Moore. Cramming more components onto integrated circuits. *Electronics*, 38(8):114–117, 1965.
- [4] W. Arden, M. Brillouet, P. Coge, M. Graef, B. Huizing, and R. Mahnkopf. More-Than-Moore. *International Technology Roadmap for Semiconductors*, 2005.
- [5] J. F. Scott. *Ferroelectric Memories*. Springer, 2000.
- [6] P. R. Gray, P. J. Hurst, S. H. Lewis, and R. G. Meyer. *Analysis and Design of Analog Integrated Circuits*. New York: Wiley, 5 edition, 2009.
- [7] E. Y. Tsymbal, E.R.A. Dagotto, C. Eom, and R. Ramesh. *Multifunctional Oxide Heterostructures*. Oxford University Press, 2012.
- [8] Y. Tokura and N. Nagaosa. Orbital Physics in Transition-Metal Oxides. *Science*, 288:462–468, 2000.
- [9] E. Dagotto. Complexity in Strongly Correlated Electronic Systems. *Science*, 309:257–262, 2005.
- [10] E. Dagotto and Y. Tokura. Strongly Correlated Electronic Materials: Present and Future. *MRS Bulletin*, 33:1037–1045, 2008.

- [11] D. Schumacher. *Interplay between magnetic and dielectric phenomena at transition metal oxide interfaces*. PhD thesis, Jülich, 2013. Zsfassung in engl. Sprache; Zugl.: Aachen, Techn. Hochsch., Diss., 2012.
- [12] T. H. Kim et. al. Polar metals by geometric design. *Nature Research Letter*, 533:68–72, 2016.
- [13] I. Hallsteinsen, J. E. Boschker, M. Nord, S. Lee, M. Rzchowski, P. E. Vullum, J. K. Grepstad, R. Holmestad, C. B. Eom, and T. Tybell. Surface stability of epitaxial $\text{La}_{0.7}\text{Sr}_{0.3}\text{MnO}_3$ thin films on (111)-oriented SrTiO_3 . *Journal of Applied Physics*, 113(18):183512, 2013.
- [14] I. Hallsteinsen, E. Folven, F. K. Olsen, R. V. Chopdekar, M. S. Rzchowski, C. B. Eom, J. K. Grepstad, and T. Tybell. Crystalline symmetry controlled magnetic switching in epitaxial (111) $\text{La}_{0.7}\text{Sr}_{0.3}\text{MnO}_3$ thin films. *APL Materials*, 3(6):062501, 2015.
- [15] A. E. Romanov, A. Vojta, W. Pompe, M. J. Lefevre, and J. S. Speck. Domain patterns in (111) oriented tetragonal ferroelectric films. *Physica status solidi*, 172(1):225–253, 1999.
- [16] G. Catalan, H. Béa, S. Fusil, M. Bibes, P. Paruch, A. Barthélémy, and J. F. Scott. Fractal Dimension and Size Scaling of Domains in Thin Films of Multiferroic BiFeO_3 . *Phys. Rev. Lett.*, 100:027602, 2008.
- [17] D. B. Williams and C. B. Carter. *Transmission Electron Microscopy*. Springer US, 2009.
- [18] TikZ. <https://en.wikibooks.org/wiki/LaTeX/PGF/TikZ>. Accessed: 2015-10-01.
- [19] Transmission electron microscope system. <http://www.texample.net/tikz/examples/transmission-electron-microscope/>. Accessed: 2016-05-01.
- [20] S. J. Pennycook. Structure Determination Through Z-Contrast Microscopy. *Advances in Imaging and Electron Physics*, 123:173–206, 2002.
- [21] W. Sinkler, L. D. Marks, D. D. Edwards, T. O. Mason, K. R. Poeppelmeier, Z. Hu, and J. D. Jorgensen. Determination of oxygen atomic positions in a Ga-In-Sn-O ceramic using direct methods and electron diffraction. *J. Solid State Chemistry*, 136(SC987804):145–149, 1998.

- [22] E. F. Rauch, J. Portillo, M. Veron, D. Bultreys, Y. Maniette, and S. Nicolopoulos. Automatic crystal orientation and phase mapping in TEM by precession diffraction. *Microscopy and Analysis Nanotechnology Supplement*, 22(6):S5–S8, 2008.
- [23] A. S. Eggeman, R. Krakow, and P. A. Midgley. Scanning precession electron tomography for three-dimensional nanoscale orientation imaging and crystallographic analysis. *Nature Communications*, 6:7267, 2015.
- [24] P. Moeck, S. Rouvimov, E. F. Rauch, M. Veron, H. Kirmse, I. Hausler, W. Neuman, D. Bultreys, Y. Maniette, and S. Nicolopoulos. High spatial resolution semi-automatic crystallite orientation and phase mapping of nanocrystals in transmission electron microscopes. 46(6):589–606, 2011.
- [25] C. Su-Yan Own. *System Design and Verification of the Precession Electron Diffraction Technique (Doctoral dissertation)*. Northwestern University, Illinois, 2005.
- [26] R. F. Egerton. *Electron Energy-Loss Spectroscopy in the Electron Microscope*. Plenum Press, 2nd edition, 1996.
- [27] J. Taylor. *Classical Mechanics*. University Science Books, 2005.
- [28] B. Choi. Hartree-Slater calculation of the cross section for L-shell ionization of argon by simple heavy charged particles. *Physical Review A*, 11(6):2004–2010, 1975.
- [29] R. Ludwig. *Energy-Filtering Transmission Electron Microscopy*, volume 71 of *Springer Series in Optical Sciences*. Springer Berlin Heidelberg, 1995.
- [30] C. C. Ahn. *Transmission Electron Energy Loss Spectrometry in Materials Science and the EELS ATLAS*. Wiley-VCH, 2nd edition, 2004.
- [31] M. J. Hytch. Geometric phase analysis of high resolution electron microscope images. *Scanning Microscopy*, 11:53–66, 1997.
- [32] C. Kittel. *Introduction to Solid State Physics, 8th Edition*. John Wiley and Sons, Inc., 2005.
- [33] T. Hahn et. al. *International Tables for Crystallography*, volume A. Springer, 5th edition, 2005.

- [34] E. Christiansen. *TEM Characterization of LFO Thin Films on STO (111) Substrates (Master's Thesis)*. NTNU, Department of Physics, 2015.
- [35] A. M. Glazer. The classification of tilted octahedra in perovskites. *Acta Crystallographica Section B*, 28(11):3384–3392, Nov 1972.
- [36] V. M. Goldschmidt. Die Gesetze der Krystallochemie. *Naturwissenschaften*, 14(21):477–485, 1926.
- [37] Asymptote. <http://asymptote.sourceforge.net/>. Accessed: 2015-09-20.
- [38] I. Hallsteinsen, E. Folven, F. K. Olsen, R. V. Chopdekar, M. S. Rzechowski, C. B. Eom, J. K. Grepstad, and T. Tybell. Crystalline symmetry controlled magnetic switching in (111) $\text{La}_{0.7}\text{Sr}_{0.3}\text{MnO}_3$ thin films. *APL Materials*, 3(6):062501, 2015.
- [39] A. Vailionis, H. Boschker, W. Siemons, E. P. Houwman, D. H. A. Blank, G. Rijnders, and G. Koster. Misfit strain accomodation in epitaxial ABO_3 perovskites: Lattice rotations and lattice modulations. *Physical review B*, 83:064101, 2011.
- [40] A. Vailionis, H. Boschker, Z. Liao, J. R. A. Smit, G. Rijnders, M. Huijben, and G. Koster. Symmetry and lattice induced strain accomodation near and away from correlated perovskite interfaces. *Applied Physics Letters*, 105(13):131906, 2014.
- [41] L. D. Landau. Theory of phase transformations II. *Phys. Z. Sowjetunion*, 11:545, 1937.
- [42] L. D. Landau. Theory of phase transformations II. *Zh. Eksp. Teor. Fiz.*, 7:627, 1937.
- [43] P. Chandra and P. B. Littlewood. *A Landau primer for ferroelectrics*, volume 105 of *Topics in Applied Physics*. Springer Berlin Heidelberg, 2007.
- [44] A. Tagantsev, L. E. Cross, and J. Fousek. *Domains in Ferroic Crystals and Thin Films*. Springer Verlag GmbH, 2010.
- [45] W. S. Oates and A. Gruverman. Polarization Switching in (111) Oriented PZT Thin Films. *ASME International Mechanical Engineering Congress and Exposition*, (13862):113–117, 2006.
- [46] R. Takahashi, O. Dahl, E. Eberg, J. K. Grepstad, and T. Tybell. Ferroelectric stripe domains in PbTiO_3 thin films: Depolarization field and domain randomness. *Journal of applied physics*, 104(6):064109, 2008.

- [47] T. H. E. Lahtinen, K. J. A. Franke, and S. Dijken. Electric-field control of magnetic domain wall motion and local magnetization reversal in multiferroic heterostructures. *Scientific Reports*, 2:258, 2012.
- [48] T. S. Holstad. *Project: TEM Characterization of BaTiO₃ Thin Films on Nb:SrTiO₃ (111) Substrates*. NTNU, Department of Physics, 2015.
- [49] P. E. Vullum. *Ferroelastic LaCoO₃-based Polycrystalline Ceramics - A Transmission Electron Microscopy and X-ray Diffraction Study (Doctoral dissertation)*. NTNU, Department of Physics, 2005.
- [50] N. Farag, M. Bobeth, W. Pompe, A. E. Romanov, and J. S. Speck. Rhombohedral LSMO films - a unique case of ferroelastic domain formation. *Phys. Stat. Sol.*, 202(4):R44–R46, 2005.
- [51] A. M. Haghiri and J. P. Renard. CMR manganites: physics, thin films and devices. *Journal of Physics D: Applied Physics*, 36(8):R127–R150, 2003.
- [52] J. G. Bednorz and K. A. Muller. Possible high T_c superconductivity in the Ba-La-Cu-O System. *Zeitschrift fur Physik B - Condensed Matter*, 64:189–193, 1986.
- [53] M. Fiebig. Revival of the magnetoelectric effect. *Journal of Physics D: Applied Physics*, 38(8):R123–R152, 2005.
- [54] U. Poppe, J. Schubert, R. Arons, W. Evers, C. Freiburg, W. Reichert, K. Schmidt, W. Sybertz, and K. Urban. Direct production of crystalline superconducting thin films of YBa₂Cu₃O₇ by high-pressure oxygen sputtering. *Solid State Communications*, 66(6):661–665, 1988.
- [55] A. Petraru, H. Kohlstedt, U. Poppe, R. Waser, A. Solbach, U. Klemradt, J. Schubert, W. Zander, and N. A. Pertsev. Wedgelike ultrathin epitaxial BaTiO₃ films for studies of scaling effects in ferroelectrics. 93(7):072902, 2008.
- [56] H. M. Christen and G. Eres. Recent advances in pulsed-laser deposition of complex oxides. *Journal of Physics: Condensed Matter*, 20:264005, 2008.
- [57] M. Brandt, H. Frenzel, H. Hochmuth, M. Lorenz, M. Grundmann, and J. Schubert. Ferroelectric thin film field-effect transistors based on ZnO/BaTiO₃ heterostructures. *Journal of Vacuum Science & Technology B*, 27(3):1789–1793, 2009.

- [58] D. G. Schlom, L. Q. Chen, X. Pan, A. Schmehl, and M. A. Zurbuchen. A thin film approach to engineering functionality into oxides. *Journal of the American Ceramic Society*, 91:2429–2454, 2008.
- [59] N. Reyren et. al. Superconducting interfaces between insulating oxides. *Science*, 317:1196–1199, 2007.
- [60] A. Brinkman, M. Huijben, M. van Zalk, J. Huijben, U. Zeitler, J. C. Maan, W. G. van der Wiel, G. Rijnders, D. H. A. Blank, and H. Hilgenkamp. Magnetic effects at the interface between non-magnetic oxides. *Nature Materials*, 6:493–496, 2007.
- [61] E. Dagotto, T. Hotta, and A. Moreo. Colossal magnetoresistant materials: the key role of phase separation. *Physics Reports*, 344:1–153, 2001.
- [62] D. A. Buck. *Ferroelectrics for Digital Information Storage and Switching (Master's Thesis)*. MIT, Department of Electrical Engineering, 1952.
- [63] N. Setter et. al. Ferroelectric thin films: Review of materials, properties and applications. *Journal of Applied Physics*, 100(5):051606, 2006.
- [64] <http://www.ti.com/lit/ml/szst014a/szst014a.pdf>. Accessed: 2015-11-07.
- [65] Micron Technology Inc. Micron Unveils 16-Nanometer Flash Memory Technology. <http://investors.micron.com/releasedetail.cfm?releaseid=777402>, 2013. Accessed: 2016-6-15.
- [66] Techinsights Inc. Samsung 16 nm 64 GB NAND Flash Memory Detailed Structural Analysis. <http://www2.techinsights.com/1/8892/2015-05-26/my16t>, 2015. Accessed: 2016-6-15.
- [67] C. Liu. *Foundation of MEMS*. Pearson, 2nd edition, 2012.
- [68] J. D. Burton and E. Y. Tsymlal. Prediction of electrically induced magnetic reconstruction at the manganite/ferroelectric interface. *Phys. Rev. B*, 80:174406, Nov 2009.
- [69] A. Quindeau, I. Fina, X. Marti, G. Apachitei, Ferrer. P., C. Nicklin, E. Pippel, D. Hesse, and M. Alexe. Four-state ferroelectric spin-valve. *Scientific Reports*, 5:9749, 2015.

- [70] H. M. Yau, Z. B. Yan, N. Y. Chan, K. Au, C. M. Wong, C. W. Leung, F. Y. Zhang, X. S. Gao, and J. Y. Dai. Low-field switching four-state nonvolatile memory based on multiferroic tunnel junctions. *Scientific Reports*, 5:12826, 2015.
- [71] E. Y. Tsymbal, A. Gruverman, M. Bibes, and A. Barthelemy. Ferroelectric and multiferroic tunnel junctions. *Materials Research Society Bulletin*, 37:138–143, 2012.
- [72] J. E. Boschker and T. Tybell. Qualitative determination of surface roughness by in situ reflection high energy electron diffraction. *Applied Physics Letters*, 100(15):151604, 2012.
- [73] E. Eberg, A. F. Monsen, T. Tybell, A. T. Van Helvoort, and R. Holmestad. Comparison of TEM specimen preparation of perovskite thin films by tripod polishing and conventional ion milling. *Journal of electron Microscopy*, 57(6):175–179, 2008.
- [74] A. Monsen. *TEM Characterization of LFO thin Films (Master's Thesis)*. NTNU, Department of Physics, 2006.
- [75] L. Jones. Smart Align. <http://lewysjones.com/software/smart-align/>. Accessed: 2016-04-15.
- [76] Gatan Inc. Digital Micrograph. <http://www.gatan.com/products/tem-analysis/gatan-microscopy-suite-software>, 2016.
- [77] L. Jones. Ranger. <http://lewysjones.com/software/ranger/>. Accessed: 2016-05-01.
- [78] SrTiO₃ Bulk Crystal Structure - Springer Database. http://materials.springer.com/isp/crystallographic/docs/sd_0554610. Accessed: 2016-02-01.
- [79] T. Tomio, H. Miki, H. Tabata, T. Kawai, and S. Kawai. Control of electrical conductivity in laser deposited SrTiO₃ thin films with Nb doping. *Journal of Applied Physics*, 76(10):5886–5890, 1994.
- [80] BaTiO₃ Bulk Crystal Structure - Springer Database. http://materials.springer.com/isp/crystallographic/docs/sd_1626717. Accessed: 2016-02-01.

- [81] M. B. Smith, K. Page, T. Siegrist, P. L. Redmond, E. C. Walter, R. Seshadri, L. E. Brus, and M. L. Steigerwald. Crystal structure and the paraelectric-to-ferroelectric phase transition of nanoscale BaTiO₃. *Journal of the American Chemical Society*, 130(22):6955–6963, 2008.
- [82] La_{0.7}Sr_{0.3}MnO₃ Bulk Crystal Structure - Springer Database. http://materials.springer.com/isp/crystallographic/docs/sd_0560732. Accessed: 2016-02-01.
- [83] M. C. Martin, G. Shirane, Y. Endoh, K. Hirota, Y. Moritomo, and Y. Tokura. Magnetism and structural distortion in the La_{0.7}Sr_{0.3}MnO₃ metallic ferromagnet. *Physical Review B: Condensed Matter*, 53:14285–14290, 1996.
- [84] The Frederick Seitz materials research laboratory. Web Electron Microscopy Applications Software (WebEMAPS), 2016.
- [85] National Institutes of Health. ImageJ. <http://imagej.nih.gov/ij/>. Accessed: 2015-11-15.
- [86] Total Resolution. Crystalkit. <http://www.totalresolution.com/CrystalKit.html>. Accessed: 2015-10-14.
- [87] HyperSpy. <http://hyperspy.org/>. Accessed: 2016-02-01.
- [88] M. Nord, P. E. Vullum, M. Moreau, J. E. Boschker, S. M. Selbach, R. Holmestad, and T. Tybell. Structural phases driven by oxygen vacancies at the L_{0.7}aSr_{0.3}MnO₃ hetero-interface. *Applied Physics Letters*, 106(4):041604, 2015.
- [89] M. Varela, M. Oxley, W. Luo, J. Tao, M. Watanabe, A. Lupini, S. Pantelides, and S. Pennycook. Atomic-resolution imaging of oxidation states in manganites. *Physical Review B*, 79:085117, 2009.
- [90] T. Riedl, T. Gemming, and K. Wetzig. Extraction of EELS white-line intensities of manganese compounds: Methods, accuracy and valence sensitivity. *Ultramicroscopy*, 106(4-5):284–291, 2006.
- [91] T. Haiyan, J. Verbeeck, A. Abakumov, and G. Van Tendeloo. Oxidation state and chemical shift investigation in transition metal oxides by EELS. *Ultramicroscopy*, 116:24–33, 2012.

- [92] HyperSpy Gaussian Component. http://hyperspy.org/hyperspy-doc/current/api/hyperspy._components.html#module-hyperspy._components.gaussian. Accessed: 2016-02-01.
- [93] R. D. Leapman and L. A. Grunes. Anomalous $\frac{L_3}{L_2}$ White-Line Ratios in the 3d Transition Metals. *Physical Review Letter*, 45:397–401, 1980.
- [94] P. A. Van Aken and B. Liebscher. Quantification of ferrous/ferric ratios in minerals: new evaluation schemes of Fe $L_{2,3}$ electron energy-loss near-edge spectra. *Physics and Chemistry of Minerals*, 29:188–200, 2002.
- [95] J. M. D. Coey, M. Viret, and S. von Molnar. Mixed-valence manganites. *Advances in Physics*, 48(2):167–293, 1999.
- [96] T. Wu, S. B. Ogale, J. E. Garrison, B. Nagaraj, A. Biswas, Z. Chen, R. L. Greene, R. Ramesh, T. Venkatesan, and A. J. Millis. Electroresistance and Electronic Phase Separation in Mixed-Valent Manganites. *Physical Review Letters*, 86:5998–6001, 2001.
- [97] J. Li. The electronic, structural and magnetic properties of $\text{La}_{1-1/3}\text{Sr}_{1/3}\text{MnO}_3$ film with oxygen vacancy: a first principles investigation. *Scientific Reports*, 6:22422, 2016.
- [98] L. Yao, S. Majumdar, L. Akaslompolo, S. Inkinen, Q. H. Qin, and S. Van Dijken. Electron-Beam-Induced Perovskite-Brownmillerite-Perovskite Structural Phase Transitions in Epitaxial $\text{La}_{2/3}\text{Sr}_{1/3}\text{MnO}_3$ Films. *Advanced Materials*, 26:2789–2793, 2014.
- [99] H. Boschker, J. Kautz, E. P. Houwman, W. Siemons, D. H. A. Blank, M. Huijben, G. Koster, A. Vailionis, and G. Rijnders. High temperature magnetic insulating phase in ultra thin $\text{La}_{0.67}\text{Sr}_{0.33}\text{MnO}_3$ (110) films. *Physical Review letter*, 109:157207, 2012.
- [100] L. D. Yao, S. Majumdar, L. Akaslompolo, S. Inkinen, Q. H. Qin, and S. Van Dijken. Electron Beam Induced Perovskite-Brownmillerite-Perovskite Structural Phase Transitions in Epitaxial $\text{La}_{2/3}\text{Sr}_{1/3}\text{MnO}_3$ Films. *Advanced Materials*, 26:2789–2793, 2014.
- [101] P. S. Casey, D. Barker, and M. A. Hayward. Charge and structural ordering in the brownmillerite phases: $\text{La}_{1-x}\text{SrMnO}_{2.5}$ ($0.2 < x < 0.4$). *Journal of Solid State Chemistry*, 179:1375–1382, 2006.
- [102] Private communication, Professor T. Tybell, 2016.

- [103] J. J. P. Peters, R. Beanland, M. Alexe, J. W. Cockburn, D. G. Revin, S. Y. Zhang, and A. M. Sanchez. Artefacts in geometric phase analysis of compound materials. *Ultramicroscopy*, 157:91–97, 2015.
- [104] N. Homonnay, K. J. OShea, C. Eisenschmidt, M. Wahler, D. A. MacLaren, and G. Schmidt. Interface Reactions in LSMO - Metal Hybrid Structures. *ACS Applied Materials and Interfaces*, 7:22196–22202, 2015.
- [105] A. Stanishevsky, B. Nagaraj, and R. Ramesh. Radiation damage and its recovery in focused ion beam fabricated ferroelectric capacitors. *Journal of Applied Physics*, 92(6):3275–3278, 2002.
- [106] M. Nord, P. E. Vullum, I. Hallsteinsen, T. Tybell, and R. Holmestad. Assessing electron beam sensitivity for SrTiO₃ and La_{0.7}Sr_{0.3}MnO₃ using Electron Energy Loss Spectroscopy. *Journal of Ultramicroscopy*, 2016. Not yet published.
- [107] S. B. Adler. Chemical Expansivity of Electrochemical Ceramics. *Journal of American Ceramic Society*, 84:2117–2119, 2001.
- [108] E. J. Kirkland, R. F. Loane, and J. Silcox. Simulation of annular dark field STEM images using a modified multislice method. *Ultramicroscopy*, 23:77–96, 1987.
- [109] R. Loane, P. Xu, and J. Silcox. Incoherent imaging of zone axis crystals with ADF STEM. *Ultramicroscopy*, 40:121–138, 1992.
- [110] M. Treacy. Optimising atomic number contrast in annular dark field images of thin films in the scanning transmission electron microscope. *Spectroscopic Electronics*, 7:511–523, 1982.
- [111] P. Yu et. al. Interface control of bulk ferroelectric polarization. *PNAS*, 109(25):9710–9715, 2012.
- [112] P. J. Phillips, M. De Graef, A. Agrawal, W. Windl, and M. J. Mills. Atomic-resolution defect contrast in low angle annular dark-field STEM. *Ultramicroscopy*, 116:47–55, 2012.
- [113] A. B. Dudekula, J. M. Rosalie, H. Somekawa, T. Miyawaki, A. Singh, and K. Tsuchiya. Application of STEM low angle annular dark field diffraction contrast to imaging of severely deformed alloys. *Microscopy*, 64(61):82, 2015.

[114] Private communication, L. Jones, 2016.

Appendix A

HyperSpy EELS-Analysis Code

```
import hyperspy.api as hs
import numpy as np

# Edge energy parameters, [Start background, end background, start edge, end edge]
s_ti_edge_E = [403., 452., 444., 500.]
s_o_edge_E = [519., 527., 519., 595.]
s_mn_edge_E = [590., 632., 620., 680.]

s = hs.load("EELS_Spectrum_Image_(high-loss)_map2.dm3")
s1 = s.sum(1)
s1 = s1.rebin((80,2048))

# Using PCA to reduce noise.
s1.change_dtype(float)
s1.decomposition()
s1 = s1.get_decomposition_model(7)
###

# Using low-loss signal to align the high-loss signal.
s_ll = hs.load("EELS_Spectrum_Image_(low-loss)_map2.dm3").sum(1)
s_ll = s_ll.rebin((80, s_ll.data.shape[1]))
s_ll.align_zero_loss_peak(subpixel=True, calibrate=True, also_align=[s1])

# Normalizing lowloss
s_ll_sum = s_ll.data.max()
s_ll.data /= s_ll_sum

s_ti = s1.isig[s_ti_edge_E[0]:s_ti_edge_E[3]]
s_o = s1.isig[s_o_edge_E[0]:s_o_edge_E[3]]
s_mn = s1.isig[s_mn_edge_E[0]:s_mn_edge_E[3]]

s_ti = s_ti.remove_background(
    signal_range=(s_ti_edge_E[0], s_ti_edge_E[1]), estimate_background=False)
s_o = s_o.remove_background(
    signal_range=(s_o_edge_E[0], s_o_edge_E[1]), estimate_background=False)
s_mn = s_mn.remove_background(
    signal_range=(s_mn_edge_E[0], s_mn_edge_E[1]), estimate_background=False)

s_ti = s_ti.isig[s_ti_edge_E[2]:s_ti_edge_E[3]]
s_o = s_o.isig[s_o_edge_E[2]:s_o_edge_E[3]]
s_mn = s_mn.isig[s_mn_edge_E[2]:s_mn_edge_E[3]]

# Restricting the curve fit of the Mn L2 and L3 peak to be within the LSMO layer.
# This range has to be adjusted for each scan, depending on the position of the LSMO layer.
```

```

s_mn = s_mn.inav[15:66]
s_l1 = s_l1.inav[15:66]
###

s_mn.add_elements(('Mn',))
s_mn.set_microscope_parameters(
    beam_energy=200, convergence_angle=27.42, collection_angle=66.86)

s_mn.save("mnl32_processed.hdf5", overwrite=True)
s_ti.save("til32_processed.hdf5", overwrite=True)
s_o.save("ok_processed.hdf5", overwrite=True)

m_mn = s_mn.create_model(l1=s_l1)

m_mn.pop(0) # Removing default power law.

m_mn['Mn_L3'].onset_energy.value = 635.5
m_mn['Mn_L2'].onset_energy.value = 648.
m_mn['Mn_L3'].onset_energy.assign_current_value_to_all()
m_mn['Mn_L2'].onset_energy.assign_current_value_to_all()

m_mn.set_signal_range(625.,632.)
m_mn.add_signal_range(658.,661.4)
m_mn.multifit()

m_mn.reset_signal_range()

m_mn['Mn_L3'].set_parameters_not_free()
m_mn['Mn_L2'].set_parameters_not_free()

g_L3 = hs.model.components.Gaussian()
g_L2 = hs.model.components.Gaussian()
g_L3.name = "L3"
g_L2.name = "L2"

m_mn.append(g_L3)
m_mn.append(g_L2)

m_mn.fit_component(g_L3, signal_range=(638.,642.5), only_current=False)
m_mn.fit_component(g_L2, signal_range=(649.4,653.5), only_current=False)

m_mn.set_signal_range(630.6, 658.)
m_mn.multifit()

m_mn.reset_signal_range()

s_L23_ratio = np.absolute(g_L3.A.as_signal()/g_L2.A.as_signal())
s_L23_ratio.save("mn_l23_ratio.hdf5", overwrite=True)

# Computing the normalized O-K-A pre-peak.
A = s_o.integrate_in_range(signal_range=(529.,532.))/s_o.integrate_in_range(signal_range=(527.,548.))

```

Appendix B

Additional EELS data

Additional data set 1

In figure [B.1](#) an overview image is shown. On the left, a survey image with STO, LSMO and BTO from bottom to top can be seen. The green rectangle shows where the EELS data collection was performed. On the right, the spectra from STO and LSMO from bottom to top can be seen.

In figure [B.2](#), the L_3 and L_2 peaks from LSMO can be seen. The Gaussian fits well for L_3 , but not very well for L_2 . In figure [B.3](#), the $\frac{I_{L_3}}{I_{L_2}}$ -ratio is plotted versus distance normal to the interface. Even though the ratio seem to increase towards the interface, its absolute value does not agree with figure [5.29](#). This is probably due to the poor fit in [B.2](#).

In figure [B.4](#), the oxygen K-edges from **(a)** STO and **(b)** LSMO are shown. As can be seen, the A pre-peak is present in STO, but not in LSMO.

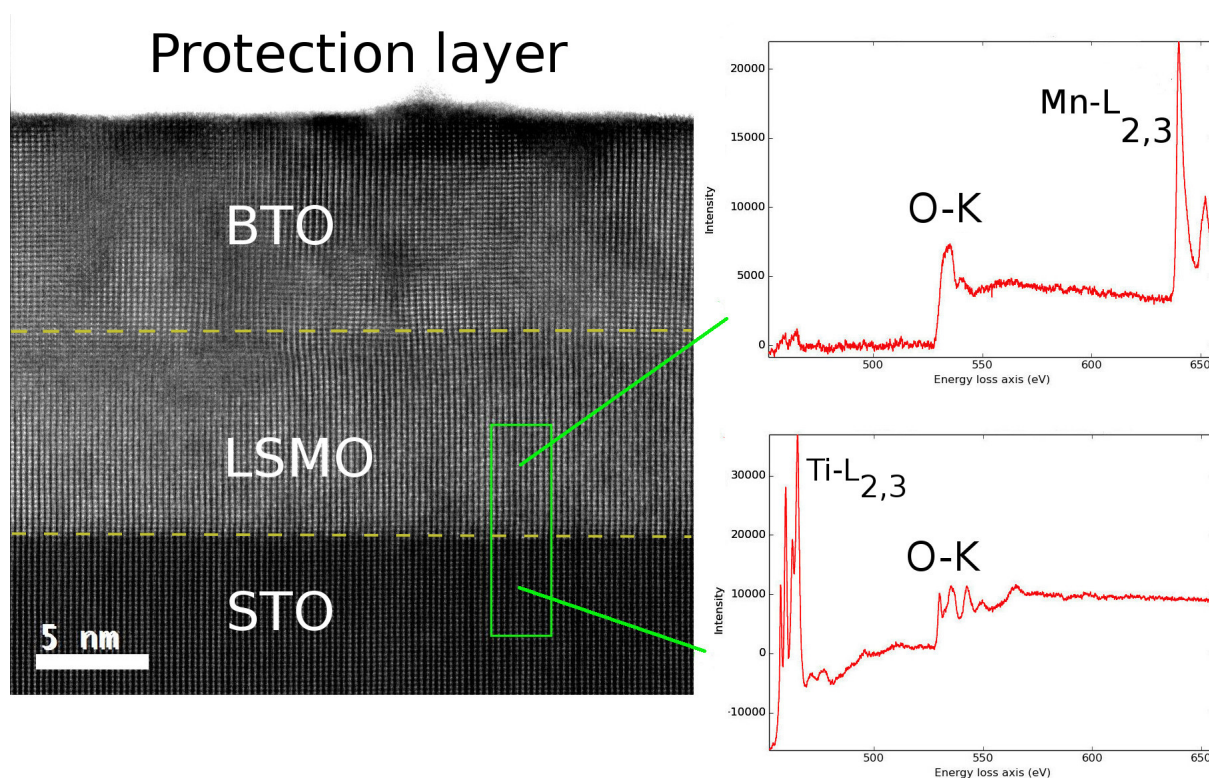


Figure B.1: EELS high-loss image along the $[11\bar{2}]_c$ zone-axis. The direction parallel to the film was integrated out. PCA was used to reduce noise using HyperSpy. The image on the left is a survey image with STO, LSMO and BTO from bottom to top, while the green rectangle shows where the EELS data collection was performed. On the right, the spectra from STO and LSMO from bottom to top can be seen. The STO/LSMO interface is around $x \approx 4$ nm. The STEM-EELS data was collected on the *Jeol-Jem ARM 200F* from the 10-10-CS specimen.

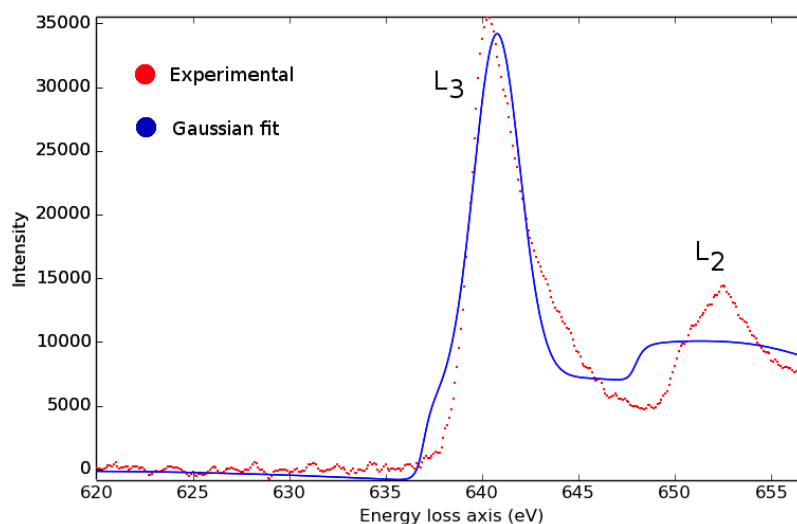


Figure B.2: Mn L_3 and L_2 peaks from LSMO in figure B.1. The blue graph is a Gaussian fit to the experimental data points in red. The fit is good for L_3 , but failed for L_2 . The reason for this is most likely that the signal was not collected to higher energies that ~ 657 eV, which means that the tail of L_2 is missing.

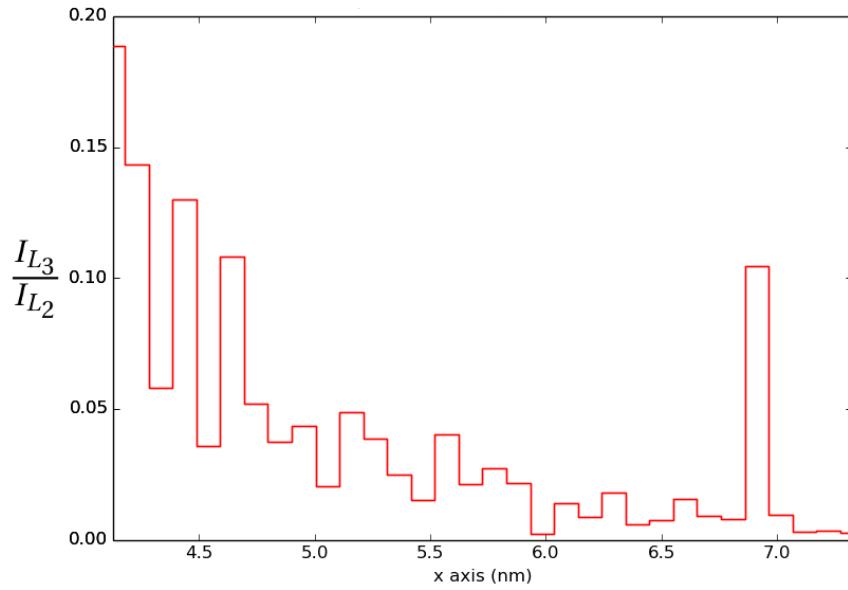


Figure B.3: $\frac{I_{L3}}{I_{L2}}$ as a function of distance normal to the film interface. The STO/LSMO interface is located at $x \approx 4$ nm. It can be seen that $\frac{I_{L3}}{I_{L2}}$ rises towards the interface, but since the fit in figure B.2 was poor, this plot cannot be trusted. In particular, the absolute value in LSMO does not agree with figure 5.29.

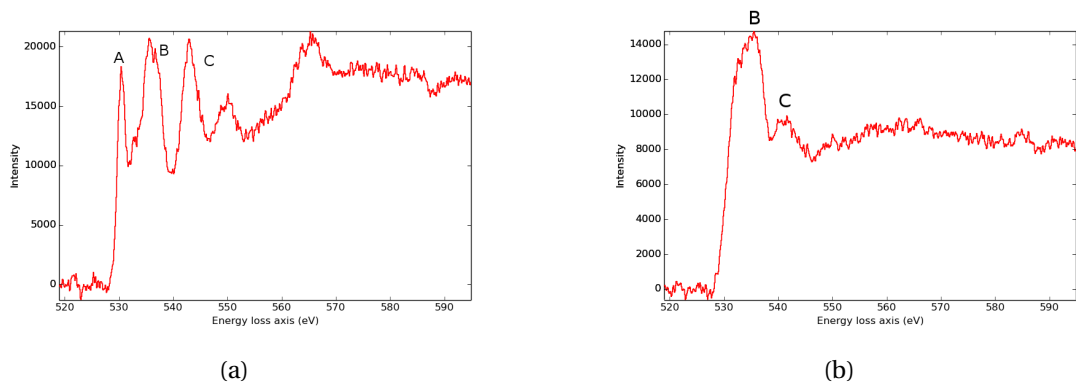


Figure B.4: O-K edge from **(a)** STO and **(b)** LSMO.

In figure B.5, the normalized O-K A prepeak is plotted versus distance normal to the thin film interfaces, as in [88]. It shows a lower oxygen concentration in LSMO compared to STO.

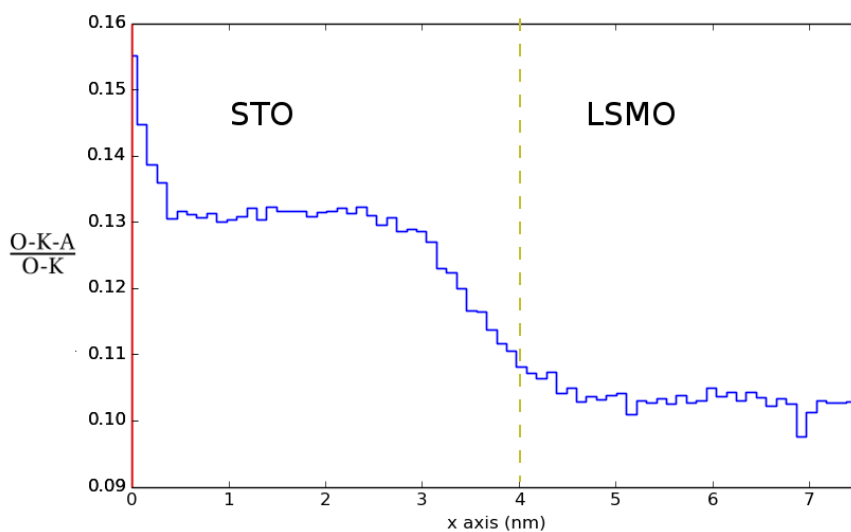


Figure B.5: The integrated A prepeak intensity normalized over the entire O-K intensity as a function of distance normal to the thin film interface. The STO/LSMO interface is located at $x \approx 4$ nm. As can be seen, the oxygen content is lowest in LSMO and highest in STO.

Additional data set 2

In figure B.6 an overview image is shown. On the left, a survey image with LSMO and BTO from bottom to top can be seen. The green rectangle shows where the EELS data collection was performed. On the right, the spectra from LSMO and BTO from bottom to top can be seen.

In figure B.7, the L_3 and L_2 peaks from LSMO can be seen. The Gaussian fits well for L_3 , but not very well for L_2 . In figure B.8, the $\frac{I_{L_3}}{I_{L_2}}$ -ratio is plotted versus distance normal to the interface. Even though the ratio seem to increase slightly towards the interface, its absolute value does not agree with figure 5.29. This is probably due to the poor fit in B.7.

In figure B.9, the oxygen K-edges from (a) LSMO and (b) BTO are shown. As can be seen, the A pre-peak is present in BTO, but not in LSMO.

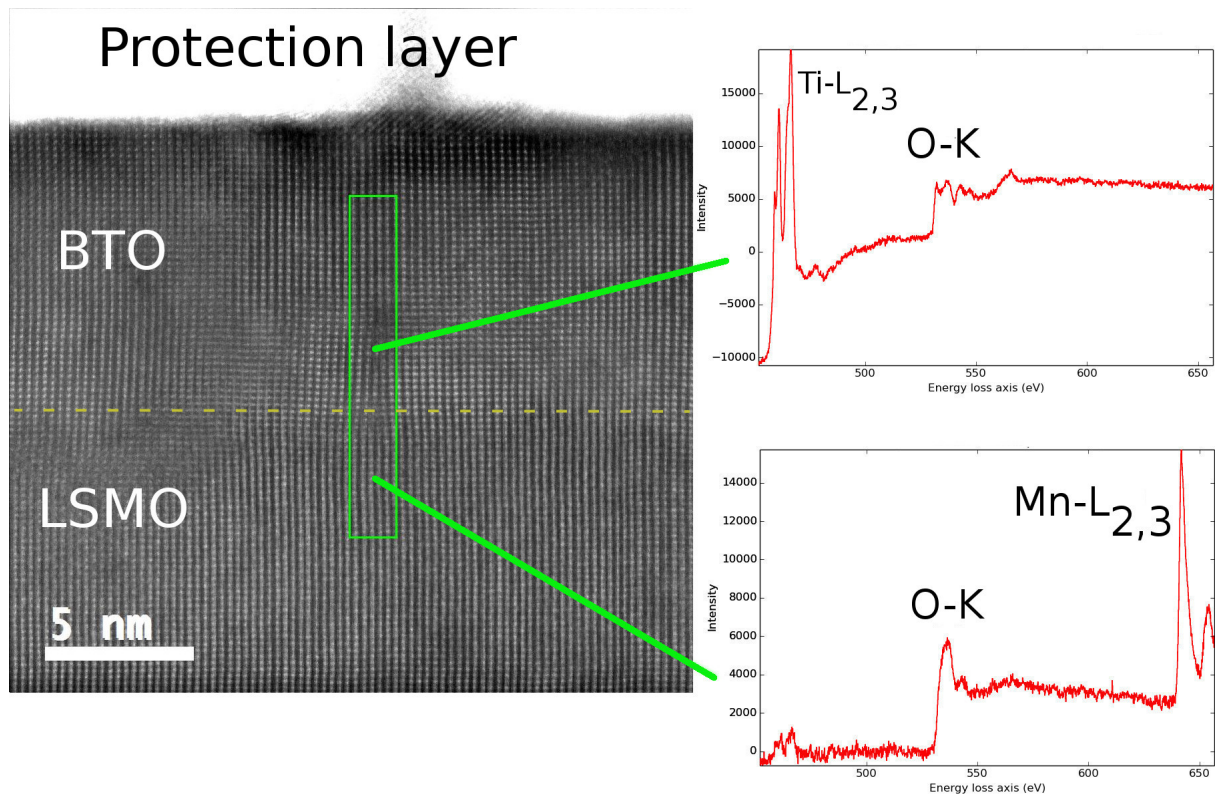


Figure B.6: EELS high-loss image along the $[11\bar{2}]$ zone-axis. The direction parallel to the film was integrated out. PCA was used to reduce noise using HyperSpy. The image on the left is a survey image with LSMO and BTO from bottom to top, while the green rectangle shows where the EELS data collection was performed. On the right, the spectra from LSMO and BTO from bottom to top can be seen. The LSMO/BTO interface is around $x \approx 3$ nm. The STEM-EELS data was collected on the *Jeol-Jem ARM 200F* from the 10-10-CS specimen.

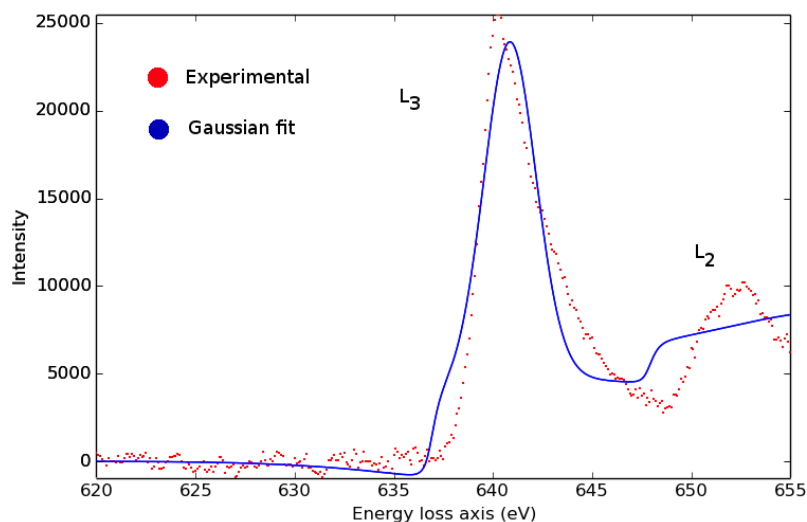


Figure B.7: Mn L_3 and L_2 peaks from LSMO in figure B.6. The blue graph is a Gaussian fit to the experimental data points in red. The fit is good for L_3 , but failed for L_2 . The reason for this is most likely that the signal was not collected to higher energies that ~ 655 eV, which means that the tail of L_2 is missing

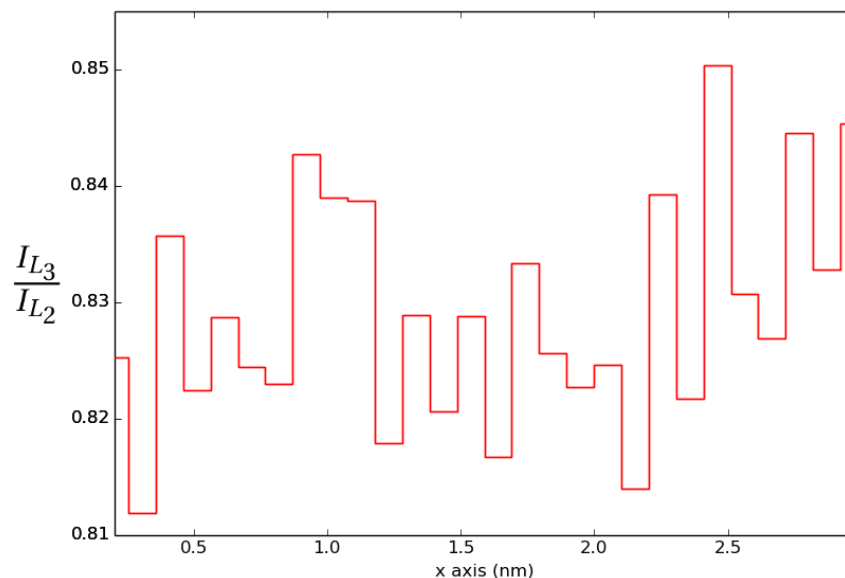


Figure B.8: $\frac{I_{L3}}{I_{L2}}$ as a function of distance normal to the film interface. The LSMO/BTO interface is located at $x \approx 3$ nm. There is a small rise in $\frac{I_{L3}}{I_{L2}}$ at the interface, but the signal is poor in this case, probably due to the poor fit achieved in B.7. In particular, the absolute value in LSMO does not agree with figure 5.29.

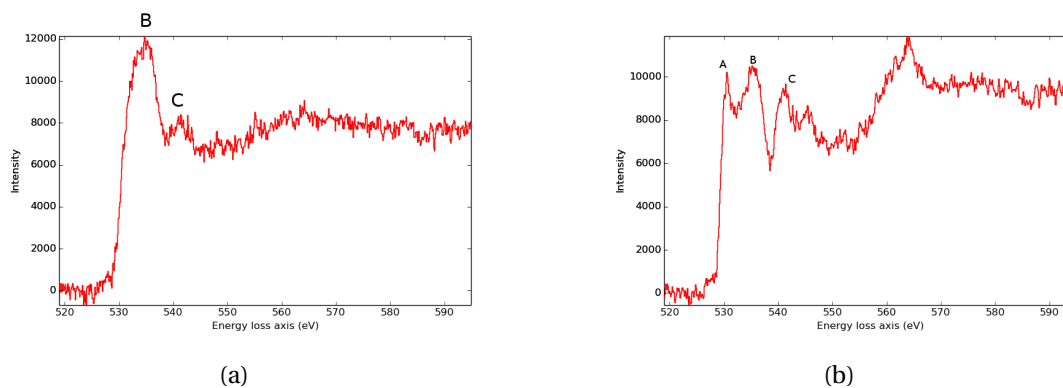


Figure B.9: O-K edge from (a) LSMO and (b) BTO.

In figure B.10, the normalized O-K-A prepeak is plotted versus distance normal to the thin film interfaces, as in [88]. It shows a lower oxygen concentration in LSMO compared BTO.

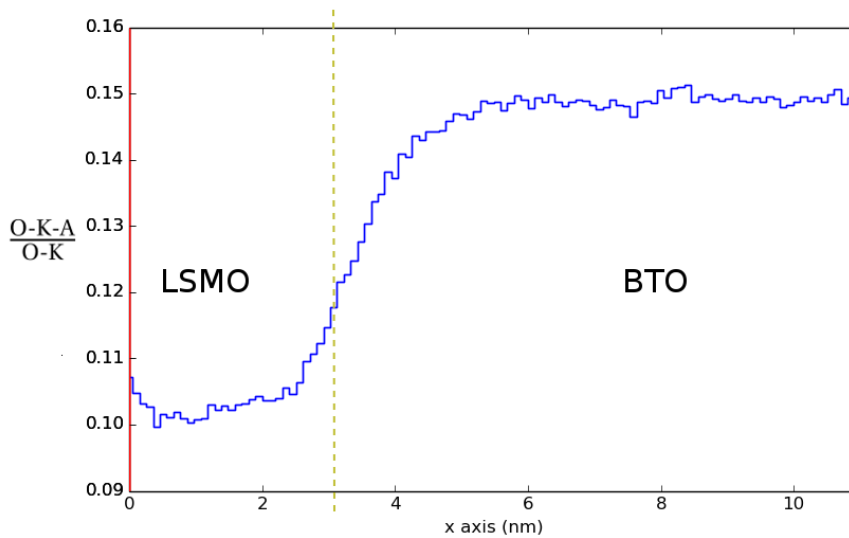


Figure B.10: The integrated A prepeak intensity normalized over the entire O-K intensity as a function of distance normal to the thin film interface. As can be seen, the oxygen content is lowest in LSMO and highest in BTO.

Additional data set 3

In figure B.11 an overview image is shown. On the left, a survey image with STO, LSMO and BTO from bottom to top can be seen. The green rectangle shows where the EELS data collection was performed. On the right, the spectra from STO and LSMO from bottom to top can be seen.

In figure B.2, the L_3 and L_2 peaks from LSMO can be seen. The Gaussian fits well for L_3 , but not very well for L_2 . In figure B.3, the $\frac{I_{L_3}}{I_{L_2}}$ -ratio is plotted versus distance normal to the interface. Its absolute value does not agree with figure 5.29. Furthermore, there is no increase towards the interface in this case. This is probably due to the poor fit in B.2.

In figure B.14, the oxygen K-edges from (a) STO and (b) LSMO are shown. As can be seen, the A pre-peak is present in STO, but not in LSMO.

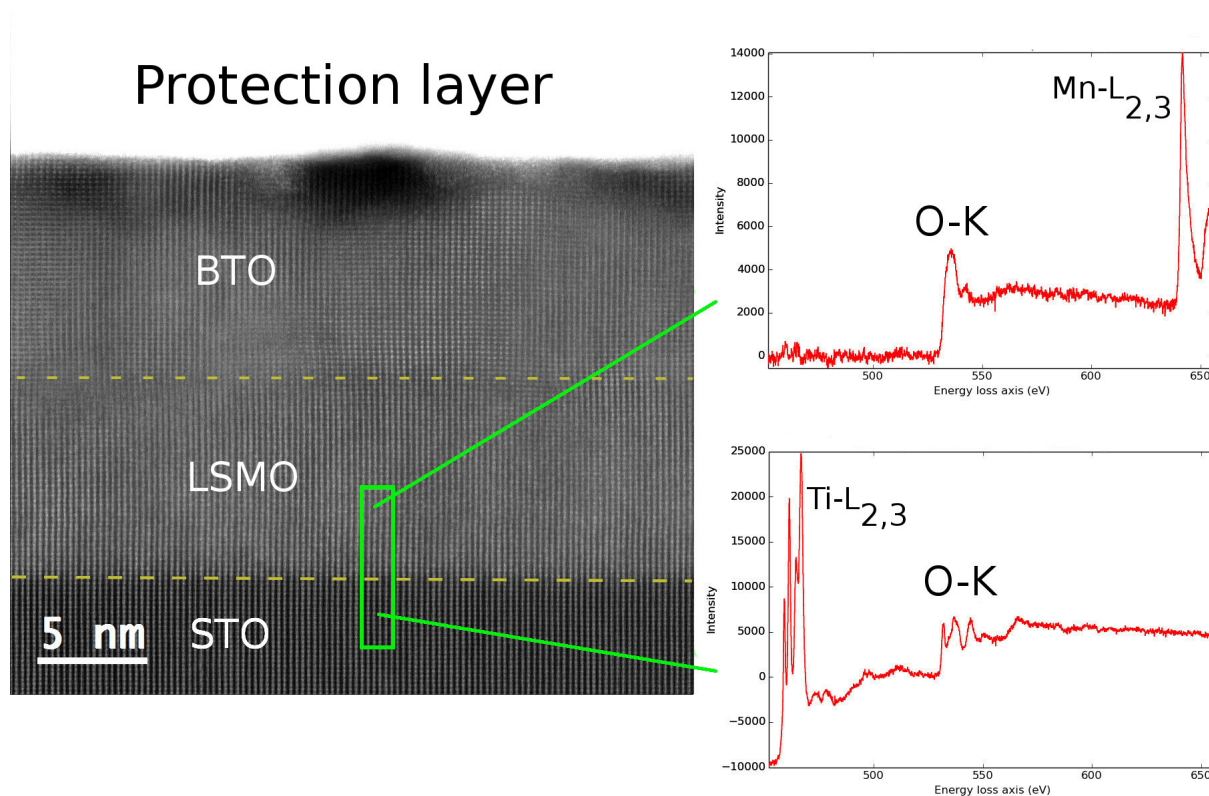


Figure B.11: EELS high-loss image along the $[11\bar{2}]$ zone-axis. The direction parallel to the film was integrated out. PCA was used to reduce noise using HyperSpy. The image on the left is a survey image with STO, LSMO and BTO from bottom to top, while the green rectangle shows where the EELS data collection was performed. On the right, the spectra from STO and LSMO from bottom to top can be seen. The STO/LSMO interface is around $x \approx 3.5$ nm. The STEM-EELS data was collected on the *Jeol-Jem ARM 200F* from the 10-10-CS specimen.

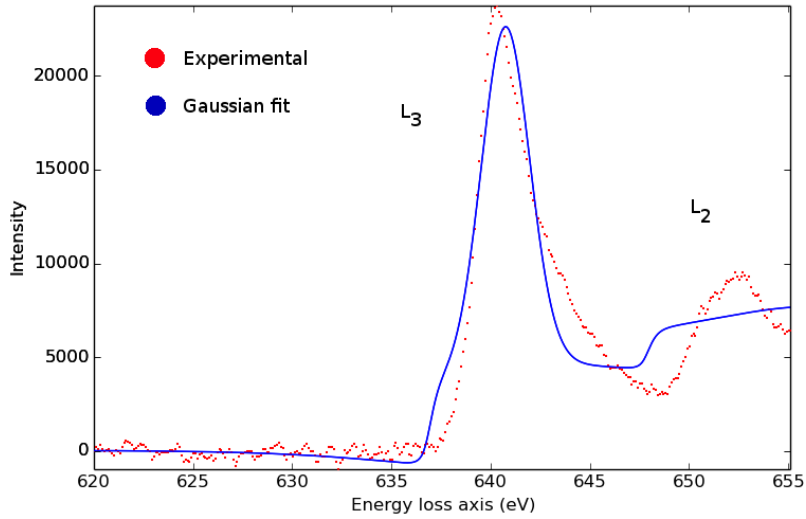


Figure B.12: Mn L_3 and L_2 peaks from LSMO in figure B.11. The blue graph is a Gaussian fit to the experimental data points in red. The fit is good for L_3 , but failed for L_2 . The reason for this is most likely that the signal was not collected to higher energies that ~ 655 eV, which means that the tail of L_2 is missing

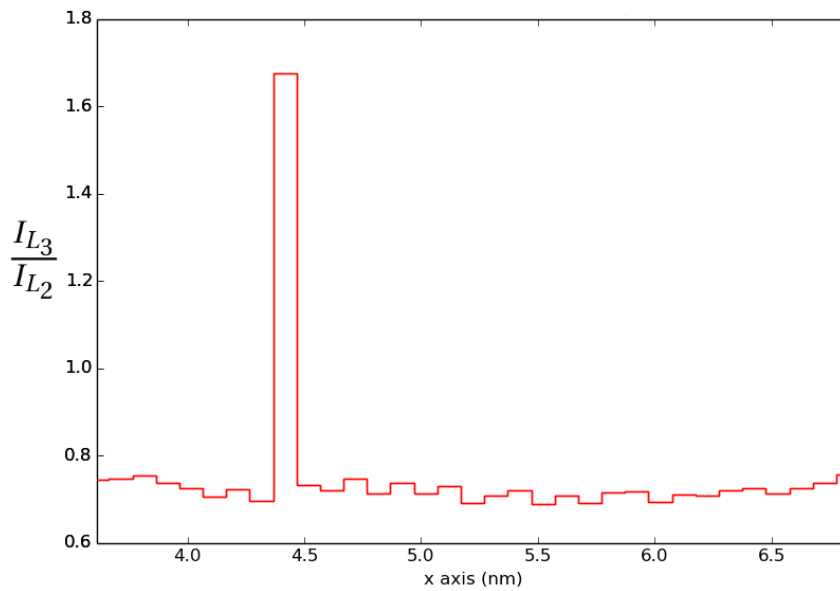


Figure B.13: $\frac{I_{L_3}}{I_{L_2}}$ as a function of distance normal to the film interface. No significant rise in $\frac{I_{L_3}}{I_{L_2}}$ was seen at the interface in this case, probably due to the poor fit achieved in B.12. In particular, the absolute value in LSMO does not agree with figure 5.29.

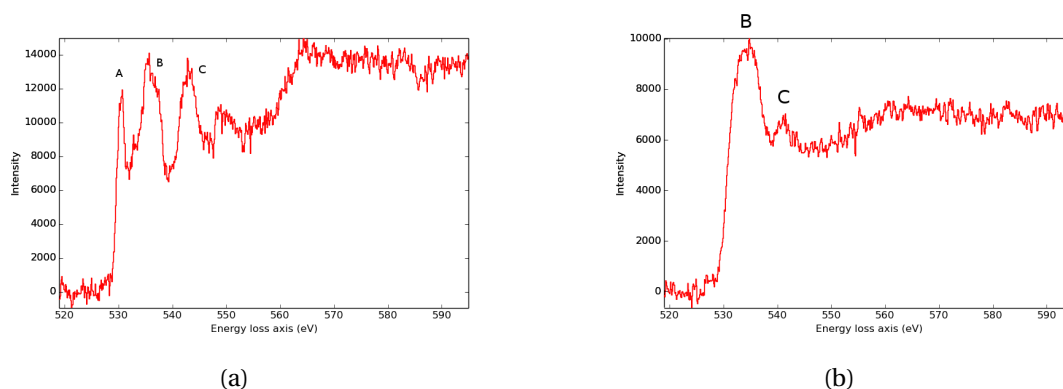


Figure B.14: O-K edge from (a) STO and (b) LSMO.

In figure B.15, the normalized O-K A prepeak is plotted versus distance normal to the thin film interfaces, as in [88]. It shows a lower oxygen concentration in LSMO compared to STO.

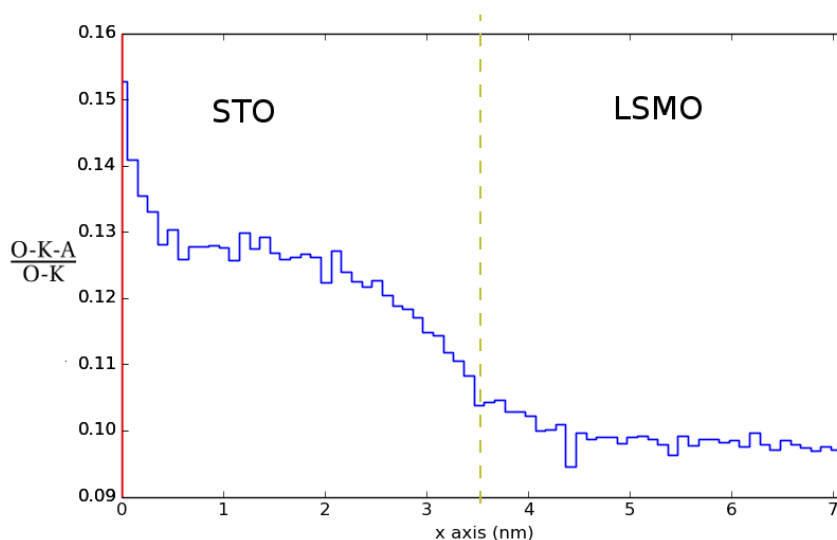


Figure B.15: The integrated A prepeak intensity normalized over the entire O-K intensity as a function of distance normal to the thin film interface. As can be seen, the oxygen content is lowest in LSMO and highest in STO.

Appendix C

Additional Image Stacks Analyzed in GPA

Additional HAADF-STEM image stacks acquired on the *Jeol-Jem ARM 200F* along the $[11\bar{2}]_c$ zone-axis were analyzed in SmartAlign and Digital Micrograph's GPA software. The results confirm the results demonstrated in the result section. Several misfit dislocations are present in BTO, which is completely relaxed. Furthermore, LSMO is coherent with STO parallel to the thin film interface, but tensilely strained perpendicular to the interface.

Additional image stack 1

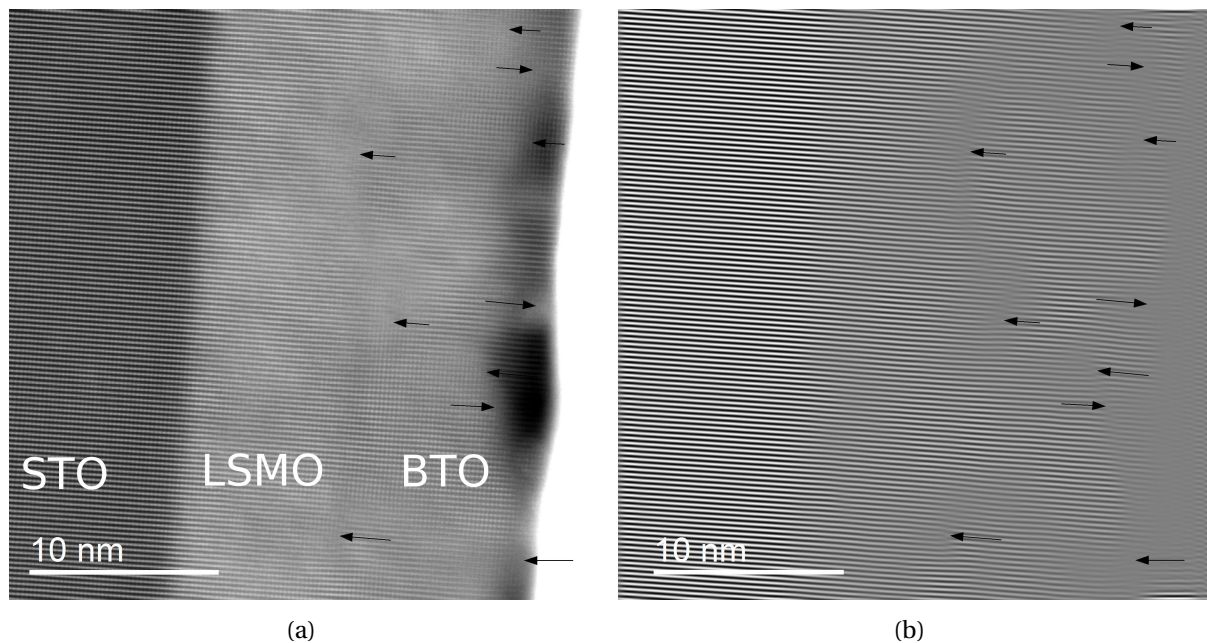


Figure C.1: **(a)** HAADF-STEM image made by summing several frames in an image stack using the SmartAlign software. **(b)** IFFT with mask on $(1\bar{1}0)_c$ to show the dislocations. The black arrows point to edge dislocations in both images. The HAADF-STEM data were collected on the *Jeol-Jem ARM 200F* from the 10-10-CS specimen.

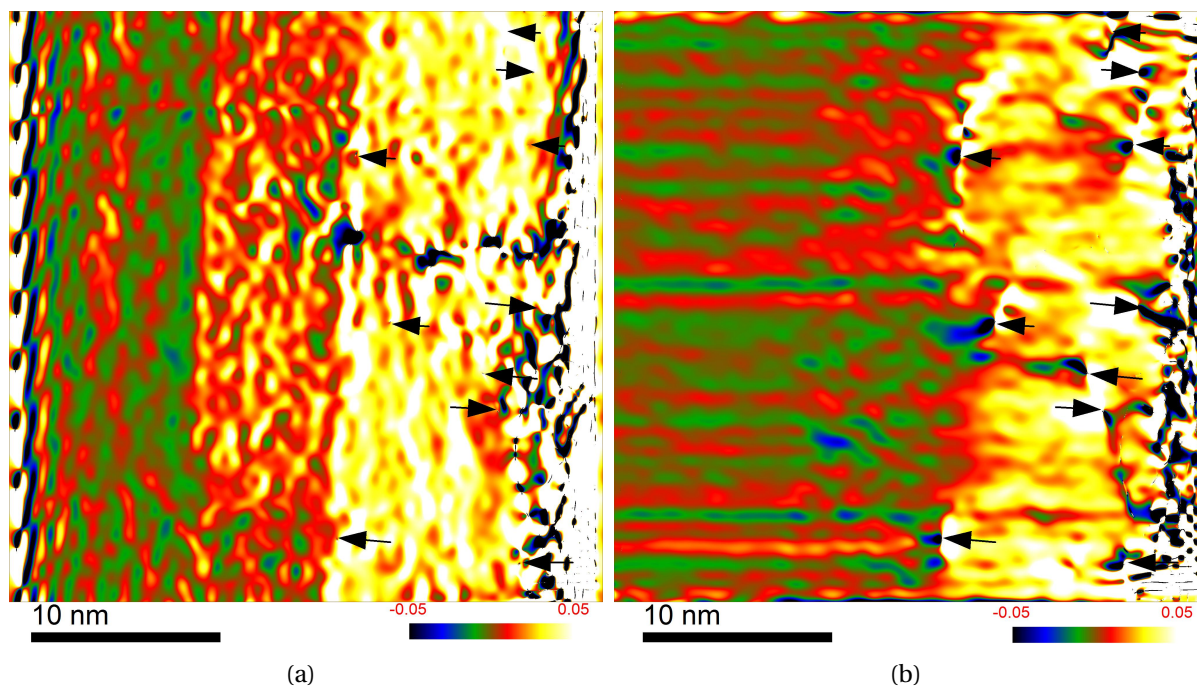


Figure C.2: **(a)** GPA-computed strain field from figure C.1 in the horizontal direction (normal to the film). **(b)** GPA-computed strain field from figure C.1 in the vertical direction (parallel to the film). The color bar displays the strain level from $\pm 5\%$ and the black arrows point to edge dislocations in both images.

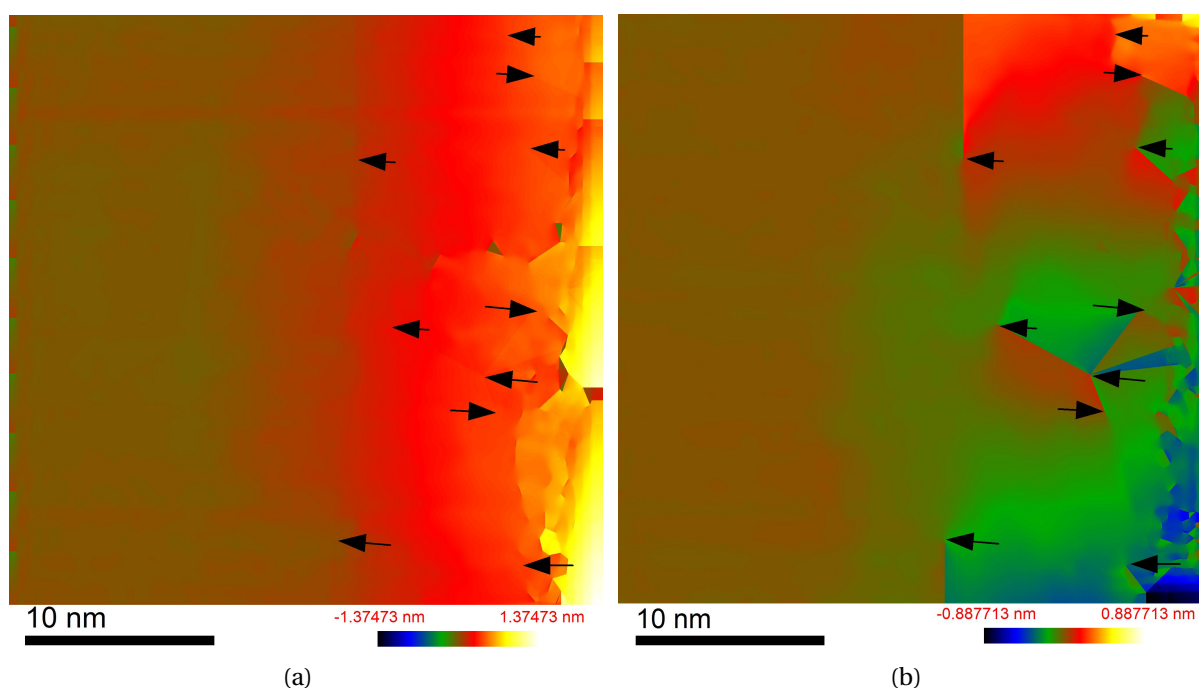


Figure C.3: **(a)** GPA-computed displacement from figure C.1 field in the horizontal direction (normal to the film). **(b)** GPA-computed displacement from figure C.1 field in the vertical direction (parallel to the film). The color bar displays the displacement in nanometers and the black arrows point to edge dislocations in both images.

Additional image stack 2

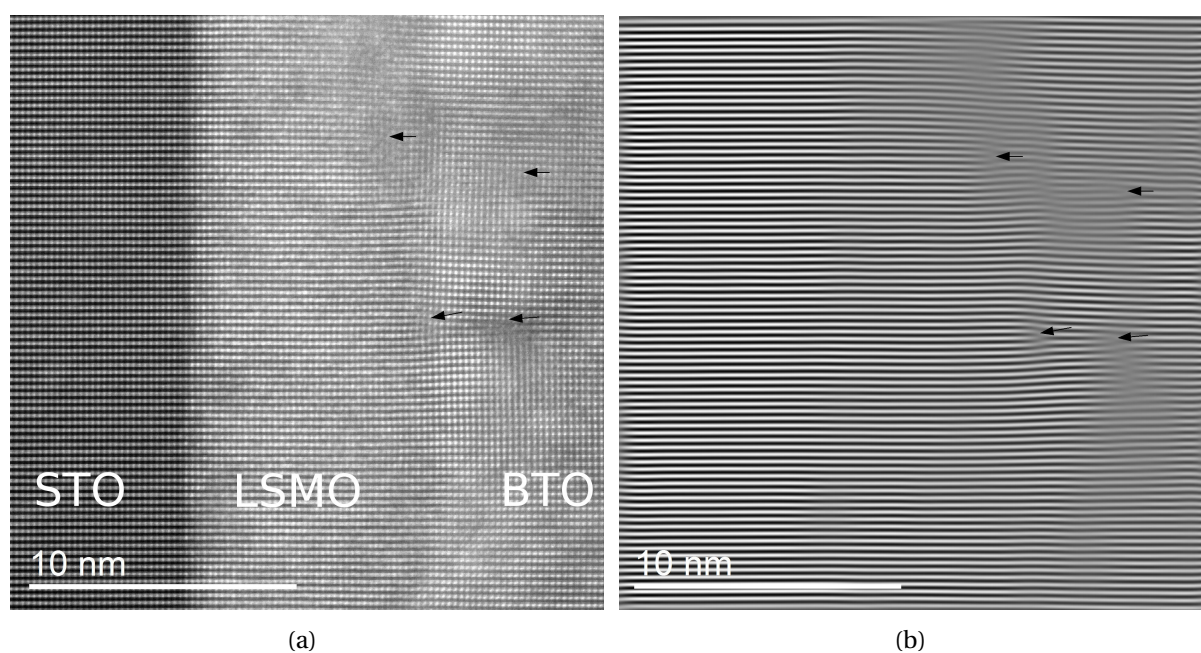


Figure C.4: **(a)** HAADF-STEM image made by summing several frames in an image stack using the SmartAlign software. **(b)** IFFT with mask on $(1\bar{1}0)_c$ to show the dislocations. The black arrows point to edge dislocations in both images. The HAADF-STEM data were collected on the *Jeol-Jem ARM 200F* from the 10-10-CS specimen.

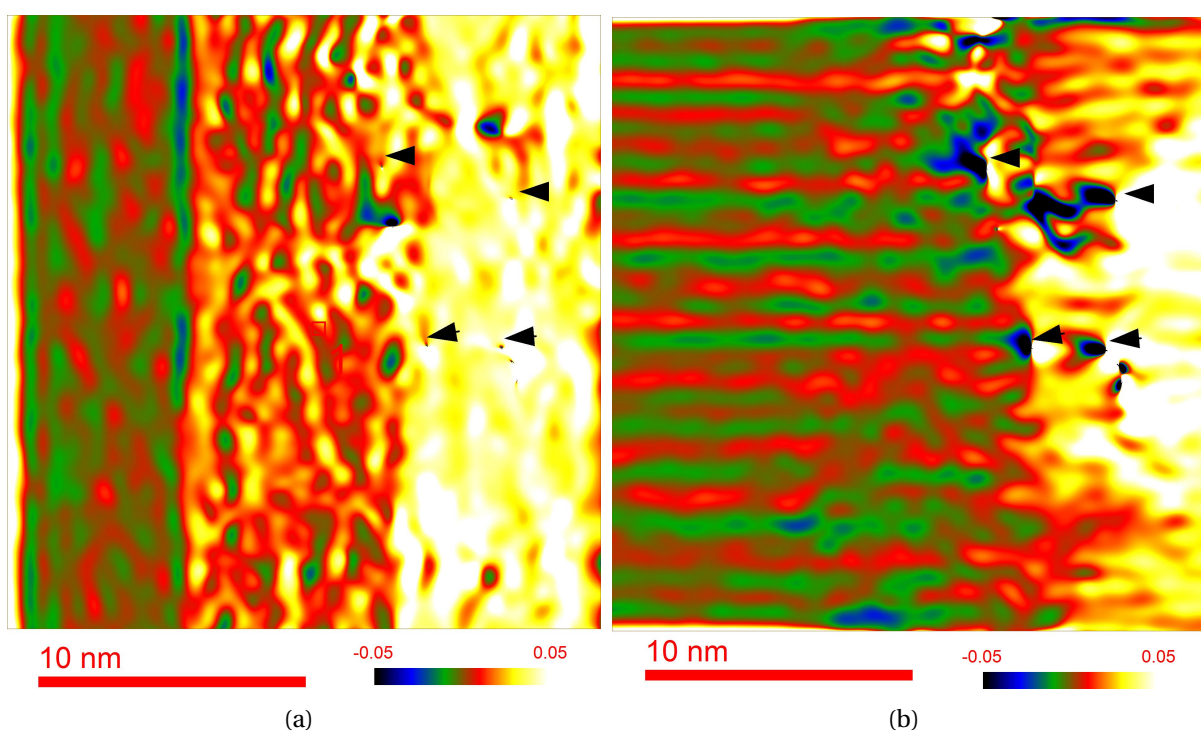


Figure C.5: **(a)** GPA-computed strain field from figure C.4 in the horizontal direction (normal to the film). **(b)** GPA-computed strain field from figure C.4 in the vertical direction (parallel to the film). The color bar displays the strain level from $\pm 5\%$ and the black arrows point to edge dislocations in both images.

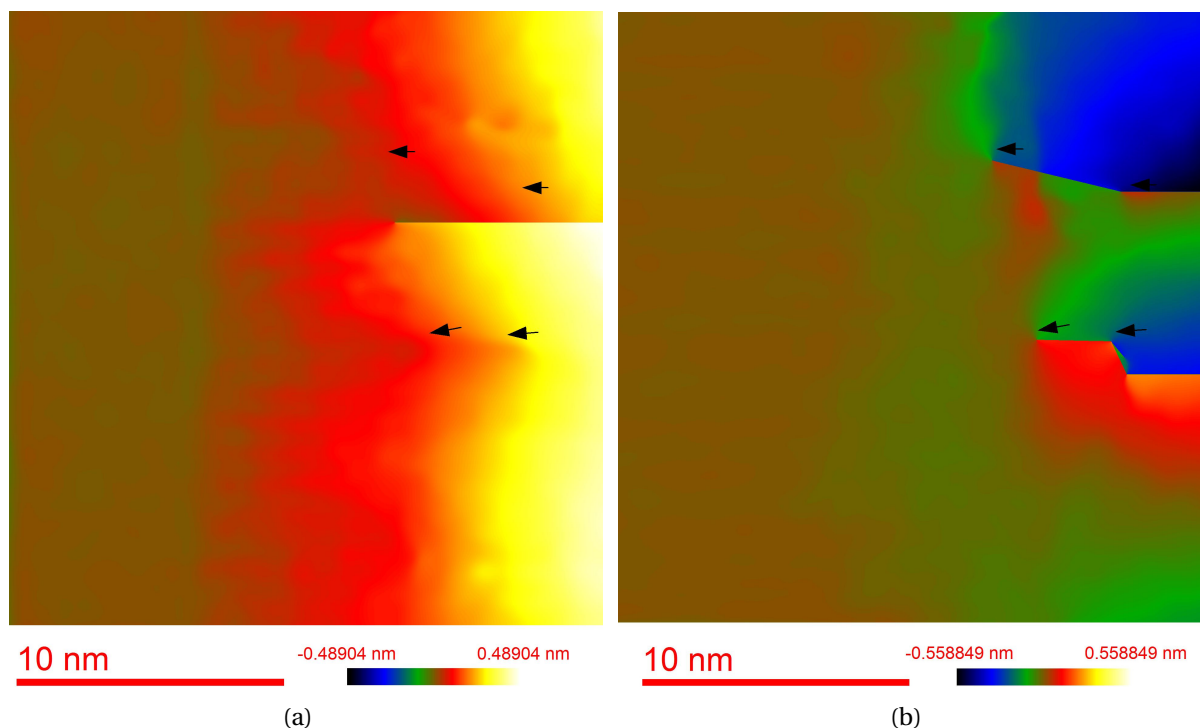


Figure C.6: **(a)** GPA-computed displacement field from figure C.4 in the horizontal direction (normal to the film). **(b)** GPA-computed displacement field from figure C.4 in the vertical direction (parallel to the film). The color bar displays the displacement in nanometers and the black arrows point to edge dislocations in both images.

Additional image stack 3

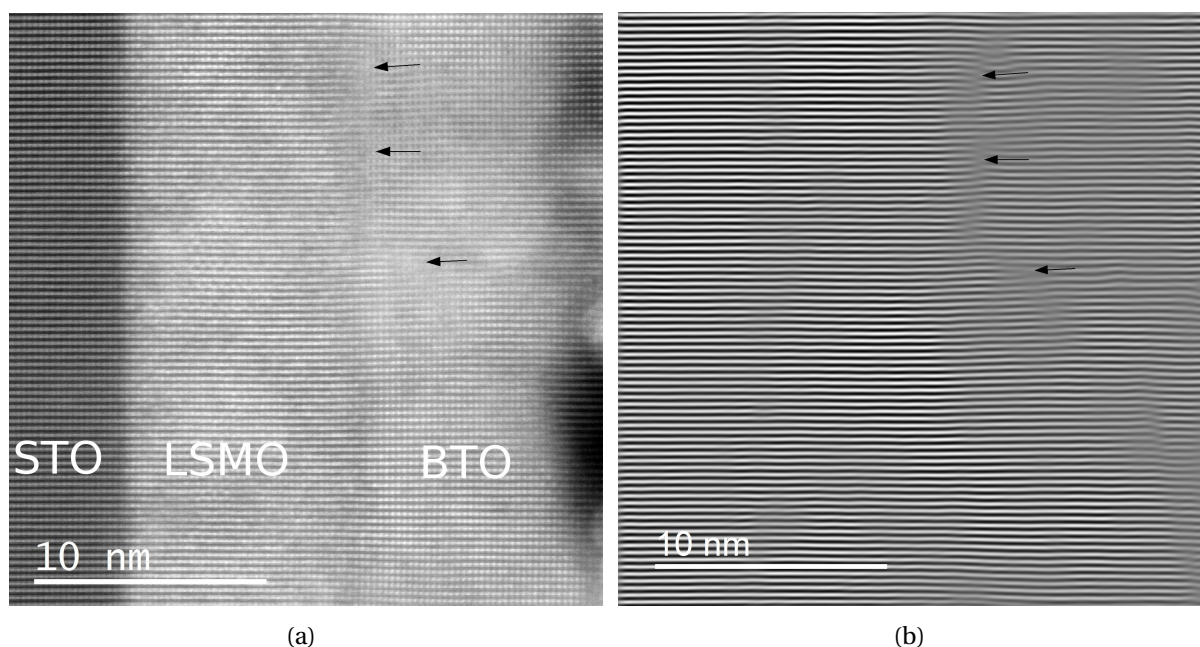


Figure C.7: **(a)** HAADF-STEM image made by summing several frames in an image stack using the SmartAlign software. **(b)** IFFT with mask on $(1\bar{1}0)_c$ to show the dislocations. The black arrows point to edge dislocations in both images. The HAADF-STEM data were collected on the *Jeol-Jem ARM 200F* from the 10-10-CS specimen.

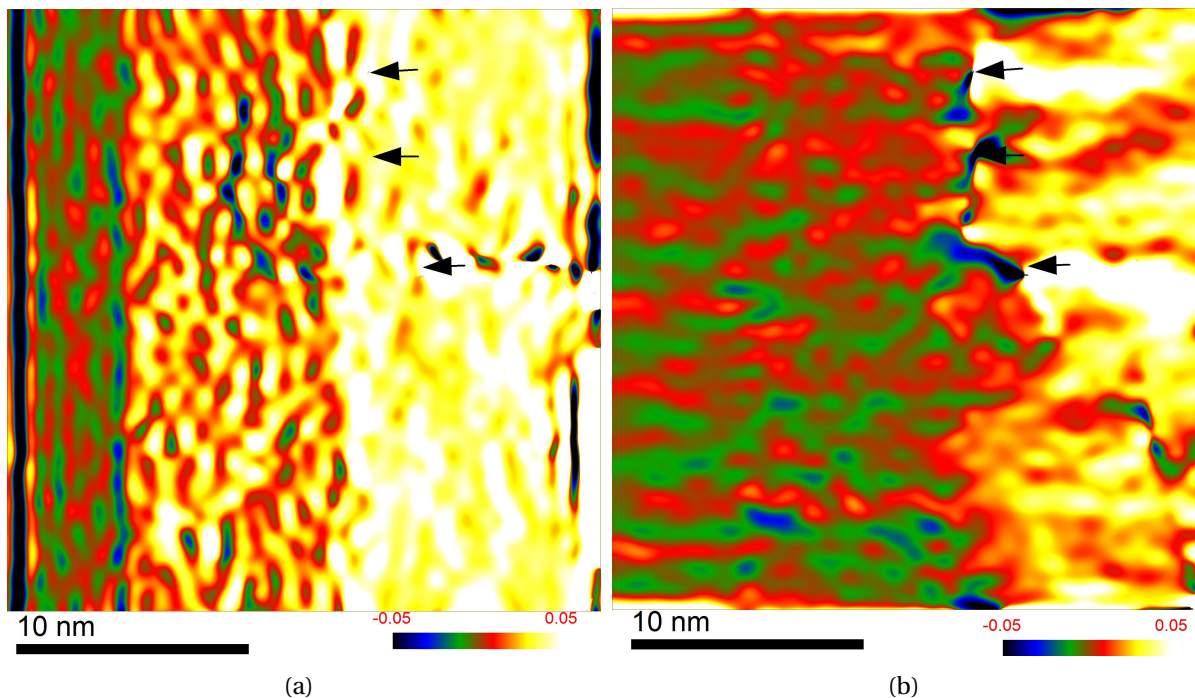


Figure C.8: **(a)** GPA-computed strain field from figure C.7 in the horizontal direction (normal to the film). **(b)** GPA-computed strain field from figure C.7 in the vertical direction (parallel to the film). The color bar displays the strain level from $\pm 5\%$ and the black arrows point to edge dislocations in both images.

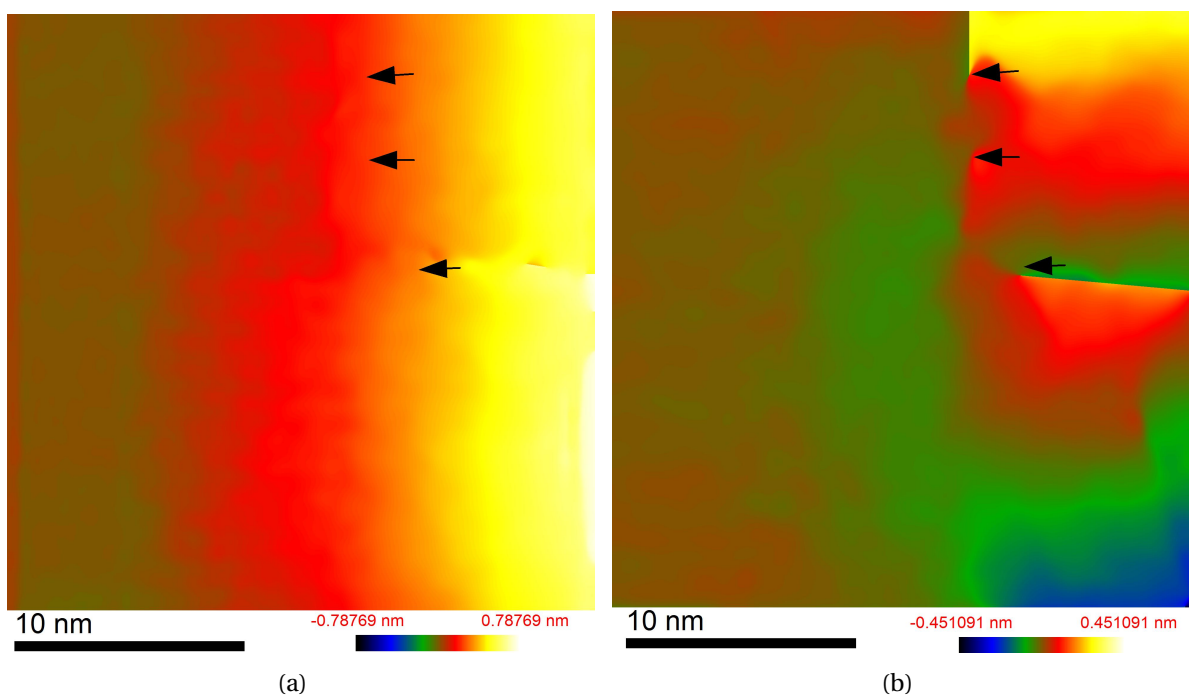


Figure C.9: **(a)** GPA-computed displacement field from figure C.7 in the horizontal direction (normal to the film). **(b)** GPA-computed displacement field from figure C.7 in the vertical direction (parallel to the film). The color bar displays the displacement in nanometers and the black arrows point to edge dislocations in both images.

